LBL-21442 Rev.
c.2

Lawrence Berkeley Laboratory
UNIVERSITY OF CALIFORNIA

EARTH SCIENCES DIVISION

RECEIVED
LAWRENCE
BERKELEY LABORATORY

JUN 2 1987

LIBRARY AND
DOCUMENTS SECTION

WELL TEST ANALYSIS IN FRACTURED MEDIA

K. Karasaki
(Ph.D. Thesis)

April 1987

TWO-WEEK LOAN COPY

This is a Library Circulating Copy which may be borrowed for two weeks.

Prepared for the U.S. Department of Energy under Contract DE-AC03-76SF00098

LBL-21442 Rev.
c.2

DISCLAIMER

This document was prepared as an account of work sponsored by the United States Government. While this document is believed to contain correct information, neither the United States Government nor any agency thereof, nor the Regents of the University of California, nor any of their employees, makes any warranty, express or implied, or assumes any legal responsibility for the accuracy, completeness, or usefulness of any information, apparatus, product, or process disclosed, or represents that its use would not infringe privately owned rights. Reference herein to any specific commercial product, process, or service by its trade name, trademark, manufacturer, or otherwise, does not necessarily constitute or imply its endorsement, recommendation, or favoring by the United States Government or any agency thereof, or the Regents of the University of California. The views and opinions of authors expressed herein do not necessarily state or reflect those of the United States Government or any agency thereof or the Regents of the University of California.

WELL TEST ANALYSIS IN FRACTURED MEDIA

Kenzi Karasaki

Earth Sciences Division
Lawrence Berkeley Laboratory
University of California
Berkeley, California 94720

Ph.D. Thesis

April 1987

This work was supported by the U.S. Department of Energy under Contract Number DE-ACO3-76SF00098.

WELL TEST ANALYSIS IN FRACTURED MEDIA

Kenzi Karasaki

Materials Science and Mineral Engineering
University of California, Berkeley

Abstract

In this study the behavior of fracture systems under well test conditions and methods for analyzing well test data from fractured media are investigated. Several analytical models are developed to be used for analyzing well test data from fractured media. Numerical tools that may be used to simulate fluid flow in fractured media are also presented.

Three types of composite models for constant flux tests are investigated. These models are based on the assumption that a fracture system under well test conditions may be represented by two concentric regions, one representing a small number of fractures that dominates flow near the well, and the other representing average conditions farther away from the well. Type curves are presented that can be used to find the flow parameters of these two regions and the extent of the inner concentric region.

Several slug test models with different geometric conditions that may be present in fractured media are also investigated. The type curves developed for each model can be used to estimate the flow parameters for such systems and certain geometric parameters such as the distance to controlling boundaries. Analyses of slug test results suffer problems of nonuniqueness more than other well tests.

A finite element model that can simulate transient fluid flow in fracture networks is used to study the behavior of various two-dimensional fracture systems under well test conditions. In some cases the system may not behave like a continuum on any scale of interest and conventional well testing methodology may not be applicable.

A mesh generator that can be used to model mass and heat flow in a fractured-porous media is presented. The mesh generator discretizes the arbitrary shaped matrix blocks into triangles or quadrilaterals. This model develops an explicit solution in the porous matrix as well as in the discrete fractures. Because the model does not require the assumptions of the conventional double porosity approach, it may be used to simulate cases where double porosity models fail. The effect of through-flow of heat and mass in the rock matrix, which is ignored in the conventional double porosity models, is significant.

Table of Contents

Table of Contents i

List of Figures v

List of Tables ix

Notation x

Acknowledgments xiv

CHAPTER 1: INTRODUCTION 1

CHAPTER 2: BACKGROUND

2.1. INTRODUCTION 3

2.2. GOVERNING EQUATION 4

2.3. INNER BOUNDARY CONDITIONS 8

2.3.1 Types of Disturbances 8

2.3.2 Mathematical Implementation of a Well 10

2.3.3 Skin Effect 11

2.3.4 Wellbore Storage 13

2.3.5 Partial Penetration 15

2.4 OUTER BOUNDARY CONDITIONS 17

2.5 OTHER CONDITIONS 19

2.5.1 Leakage from Neighboring Formations 19

2.5.2 Multilayered Reservoir 21

2.5.3 Composite Medium 23

2.5.4 Fractures 26

2.5.4.1 Double Porosity Medium 26

2.5.4.2 Single Fracture 29

2.5.5 Anisotropy 31

2.6 CONCLUSIONS 33

CHAPTER 3: ANALYTICAL SOLUTIONS FOR CONSTANT FLOW TESTS IN FRACTURED MEDIA

3.1. INTRODUCTION 34

3.2. COMPOSITE MODEL WITH LINEAR AND RADIAL FLOW 36

3.2.1 Model Description 39

3.2.2 Solutions 43

3.2.3 Example Applications 65

3.3. COMPOSITE MODEL WITH RADIAL FLOW 74

3.3.1 Model Description 75

3.3.2 Solutions 79

3.4. COMPOSITE MODEL WITH RADIAL AND SPHERICAL FLOW 88

3.4.1 Model Description 88

3.4.2 Solutions 92

3.5. CONCLUSIONS 100

CHAPTER 4: ANALYTICAL MODELS OF SLUG TESTS

4.1. INTRODUCTION 102

4.2. LINEAR FLOW MODEL 105

4.3. RADIAL FLOW MODELS 111

4.3.1 Interference Analysis of a Slug Test 111

4.3.2 Linear Constant Head Boundary 112

4.3.3 Radial Constant Head Boundary 122

4.3.4 Layered Aquifer with No Cross Flow 127

4.3.5 Linear-Radial Flow Model 132

4.4. SPHERICAL FLOW MODELS 142

4.4.1 Spherical Flow in a Homogeneous System 142

4.4.2 Radial-Spherical Composite Model 146

4.5. ANALYSIS OF SLUG TESTS AT NEVADA TEST SITE 154

4.5.1 Well Test Data Analysis 154

4.6. CONCLUSIONS 164

CHAPTER 5: NUMERICAL ANALYSIS

5.1. NUMERICAL MODEL 166

5.1.1 MESH GENERATOR 166

5.1.2 FRACTURE FLOW PROGRAM 170

5.2. NUMERICAL SIMULATION OF WELL TESTS 174

5.2.1 Well Tests in Continuous Fracture Systems 174

5.2.2 Well Tests in Discontinuous Fracture Systems 178

5.2.2.1 Case-4 184

5.2.2.2 Case-5 187

5.3 CONCLUSIONS 192

CHAPTER 6: A NEW FRACTURE AND MATRIX MESH GENERATOR

6.1. INTRODUCTION 196

6.2. CODE DESCRIPTION 198

6.3. EXAMPLE APPLICATION 203

6.4. CONCLUSIONS 210

CHAPTER 7: CONCLUSIONS

7.1. SUMMARY AND CONCLUSIONS 211

7.2. RECOMMENDATIONS 215

REFERENCES 218

APPENDIX A 231

APPENDIX B 234

List of Figures

Figure 2.1	Arbitrary volume of rock in a flow field bounded by surface S.	5
Figure 3.1	Flow to a well in a fracture-dominated system.	38
Figure 3.2	Linear-radial composite model.	40
Figure 3.3	Contour path for Laplace inversion.	46
Figure 3.4a	Dimensionless pressure for r_c <0.05 and α_c =0.1.	50
Figure 3.4b	Dimensionless pressure for r_c <0.05 and α_c =1.0.	51
Figure 3.4c	Dimensionless pressure for r_c <0.05 and α_c =10.	52
Figure 3.4d	Dimensionless pressure for r_c <0.05 and β=0.1.	53
Figure 3.4e	Dimensionless pressure for r_c <0.05 and β=1.0.	54
Figure 3.4f	Dimensionless pressure for r_c <0.05 and β=10.	55
Figure 3.5	Dimensionless pressure for α_c =1.0 and β=1.0.	57
Figure 3.6	Comparison between linear-radial and uniform flux solution.	63
Figure 3.7	Type curve matching with uniform flux solution.	67
Figure 3.8	Type curve matching with linear-radial solution.	68
Figure 3.9	Type curve matching for Example 2.	72
Figure 3.10	Radial composite model.	77
Figure 3.11	Comparison of inversion methods - Case 1.	85
Figure 3.12	Comparison of inversion methods - Case 2.	86
Figure 3.13	Radial-spherical composite model.	90
Figure 3.14	h_{D_1} vs. t_D for $\frac{\alpha_c}{\beta}$=1.	96

Figure 3.15	h_{D_1} vs. t_D for β=1. and r_c =0.05.	98
Figure 3.16	h_{D_1} vs. t_D for different values of r_c .	99
Figure 4.1	Type Curves for radial flow after Cooper et al. (1967).	104
Figure 4.2	Possible geometries that cause a linear flow.	106
Figure 4.3	Type curve for linear flow.	110
Figure 4.4a	Interference responses at $r_D = 10^2$.	113
Figure 4.4b	Interference responses at $r_D = 10^3$.	114
Figure 4.5a	Log-log plot of interference responses at $r_D = 10^2$.	115
Figure 4.5b	Log-log plot of interference responses at $r_D = 10^3$.	116
Figure 4.6a	Effects of linear constant head boundary for $\omega = 10^{-1}$.	118
Figure 4.6b	Effects of linear constant head boundary for $\omega = 10^{-4}$.	119
Figure 4.6c	Effects of linear constant head boundary for $\omega = 10^{-9}$.	120
Figure 4.7	Log-log plot of for $\omega = 10^{-4}$.	121
Figure 4.8a	Responses to a radial open boundary for $\omega = 10^{-4}$.	124
Figure 4.8b	Responses to a radial open boundary for $\omega = 10^{-9}$.	125
Figure 4.9	Log-log plot for $\omega = 10^{-9}$.	126
Figure 4.10a	Response of a two-layered aquifer for for $\omega = 10^{-4}$.	130
Figure 4.10b	Response of a two-layered aquifer for for $\omega = 10^{-9}$.	131
Figure 4.11a	Normalized head for linear-radial model ($\omega' = 10^{-3}$).	139
Figure 4.11b	Normalized head for linear-radial model ($\omega' = 10^{-4}$).	140
Figure 4.11c	Normalized head for linear-radial model ($\omega' = 10^{-9}$).	141
Figure 4.12	Normalized head for spherical flow model.	145
Figure 4.13a	Normalized head for radial-spherical model ($\omega' = 10^{-3}$).	151
Figure 4.13b	Normalized head for radial-spherical model ($\omega' = 10^{-6}$).	152
Figure 4.14	Location of Nevada Test Site and Ue-25c1 well.	155

Figure 4.15	Test intervals in Ue-25c1 well.	156
Figure 4.16	Slug test results in Ue-25c1 well.	157
Figure 4.17	Test 6 results matched with type curves after Cooper et al. (1967).	158
Figure 4.18	Type curve match with radial constant head boundary model (a) and spherical flow model (b).	163
Figure 5.1	Generation of fracture network.	168
Figure 5.2	Linear flow model in Long (1982) and well test model.	169
Figure 5.3	Comparison of analytical and numerical solutions.	172
Figure 5.4	Plot of numerical solution approaching steady state solution.	173
Figure 5.5a	Case 1 - pumping well at intersection.	175
Figure 5.5b	Injection test results for Case 1.	177
Figure 5.6a	Case 2 - pumping well at middle of fracture.	179
Figure 5.6b	Injection test results for Case 2.	180
Figure 5.7a	Continuous fracture system-large diameter well.	181
Figure 5.7b	Injection test results for the system in Figure 5.7a.	182
Figure 5.8	Fracture meshes for Case 4 and Case 5.	183
Figure 5.9	Injection test results for Case 4 at Group A observation wells.	185
Figure 5.10	Injection test results for Case 4 at Group B observation wells.	186
Figure 5.11	Iso-potential contour map for Case 4.	188
Figure 5.12	Injection test results for Case 5 at Group A observation wells.	189
Figure 5.13	Injection test results for Case 5 at Group B observation wells.	190

Figure 5.14	Injection test results for Case 5 at Group C observation wells.	191
Figure 5.15	Fracture mesh for Case 5 with only connected fractures shown.	193
Figure 5.16	Isopotential contour map for Case 5.	194
Figure 6.1	Fracture mesh generated by FMG.	199
Figure 6.2	Imaginary fracture elements and convex blocks.	200
Figure 6.3	Completed fracture-matrix mesh.	202
Figure 6.4	Transient pressure profiles at Node 302 and 421.	205
Figure 6.5	Transient temperature profiles at various nodes.	206
Figure 6.6	Comparison between permeable and impermeable rock matrix.	208
Figure 6.7	Comparison between conductive and nonconductive rock matrix.	209

List of Tables

Table 3.1	Reservoir and Buildup data for Example 1.	66
Table 3.2	Falloff Data from Krafla Well KJ-20 for Example 2.	71
Table 3.3	Parameters used to compare inversion methods.	84
Table 5.1	Geometric Parameters for Case4 and Case5.	184
Table 5.2	Principal Permeabilities and Axis Orientationfor Case4.	187
Table 5.3	Principal Permeabilities and Axis Orientationfor Case5.	192
Table 6.1	Input parameters for the example case.	204

Notation

A	area of flow	L^2
b	fracture aperture	L
B	formation volume factor	
c_f	formation compressibility	LT^2/M
c_t	total compressibility	LT^2/M
c_w	compressibility of water	LT^2/M
C_w	wellbore storage	L^2
g	acceleration of gravity	L/T^2
h	hydraulic head	L
h_D	dimensionless head	
h_i	initial head in formation	L
h_m	pressure head in rock matrix	L
h_s	normalized head, $\frac{h-h_i}{h_0-h_i}$	
h_w	pressure head in well	L
h_{w_s}	normalized head in well	
h_0	initial head in well	L
H	formation thickness	L
I_0	modified bessel function of the first kind, zeroth order	
I_1	modified bessel function of the first kind, first order	
J_0	bessel function of the first kind, zeroth order	

J_1	bessel function of the first kind, first order	
k	hydraulic conductivity	L/T
$\mathbf{k}$	hydraulic conductivity tensor	L/T
$\bar{k}$	geometric mean permeability	L^2
$\tilde{k}$	permeability	L^2
k_D	dimensionless hydraulic conductivity	
K	hydraulic conductivity (Chapter 5)	L/T
K_0	modified bessel function of the second kind, zeroth order	
K_1	modified bessel function of the second kind, first order	
L	length	L
m	mass generation rate per unit volume	M/L^3T
M	rate of generation of mass	M/T
n	number of fractures intersecting well	
$\mathbf{n}$	unit outward normal vector	
p	Laplace variable	
p_D	dimensionless pressure	
$\mathbf{q}$	volume flow rate per unit area	L/T
Q	well flow rate	L^3/T
r	radial distance	L
r_c	ratio of wellbore radius to inner region radius	
r_D	dimensionless radial distance	
r_e	distance to outer boundary	L
r_f	inner region radius	L
r_w	wellbore radius	L
r_w'	apparent wellbore radius	L

R	distance to discontinuity	L
s_f	pseudo-skin factor	
S	surface of arbitrary volume of rock (Chapter 2)	L^2
S	storativity	
S_s	storage coefficient	1/L
S_{s_D}	dimensionless storage coefficient	
t	time	T
t_D	dimensionless time	
t_p	production time	T
t_s	dimensionless time for slug tests	
t_0	shut-in time	T
T	transmissivity	L^2/T
x_D	dimensionless distance	L
Y_0	bessel function of the second kind, zeroth order	
Y_1	bessel function of the second kind, first order	
α	diffusivity	L^2/T
α_c	dimensionless diffusivity	
β	dimensionless transmissivity	
β	transmissivity ratio of Layer 2 to Layer 1 (Chapter 4.3.4)	
γ	Euler's constant (Chapter 3)	
γ	storage coefficient ratio of Layer 2 to Layer 1 (Chapter 4.3.4)	
Γ	contour integration path	
ϕ	porosity	
μ	fluid viscosity	M/LT

ω	dimensionless storage	
ρ	fluid density	M/L^3
σ	standard deviation	
θ	angle	radian
θ	time weighting parameter (Chapter 5)	

Subscripts

a	apparent
D	dimensionless
i	initial
f	based on fracture
s	dimensionless for slug test models
w	wellbore
0	initially applied value
1	region 1
2	region 2

Acknowledgements

First, I would like to thank Professor Witherspoon for his support and guidance throughout my graduate work at Berkeley. The international settings that he created around him made me feel at home, and at the same time it has been very stimulating. He has also been very patient with me. I owe him a great deal for what I have achieved here in Berkeley. I am very proud to be his student, and I feel it is a great responsibility of mine to inherit his enthusiasm in the field of hydrology like all the other many distinguished scholars he has graduated.

I would like to express my very special thanks to Dr. Jane Long. She has encouraged me, helped me, and advised me not only on my thesis work but in all aspects of my student life. She taught me how to write clearly, so my writing style is directly inherited from her. I am honored to be the first of many students who she will advise as a thesis committee member in years to come. Without her little "kick in my back," this thesis would have been delayed.

I would like to thank Professor Cook and Professor Udell for their critical review of this work. I would also like to express my gratitude to Dr. Charlie Wilson. The discussions I had with him helped me initiate this work.

I would like to thank my fellow colleagues, Dr. Howard Endo, Dr. Cheng-Hsien Lai and Dr. Ashock Verma for their useful discussions.

Throughout my student life, Ellen Klahn has helped me out on many occasions with paper work. Karla Savage helped me type-in equations onto Unix files and Diana Swantek drafted beautiful figures. I would like to thank all these people.

This work was supported by the U.S. Geological Survey, Denver, Nuclear Hydrology Program through the U.S. Department of Energy under contract No. DE-AC03-76SF00098.

Last but not least, I would like to thank my dear wife, Chisato. She has always been an inspiration to me. Without her this work would never have been completed. We worked together toward our goal. She was understanding and encouraging to me at times when I was feeling low. We persevered and enjoyed our student life together. I dedicate this thesis to my wife.

CHAPTER 1

INTRODUCTION

Problems concerning fluid flow in fractured media are commonly encountered in oil fields, geothermal fields, groundwater reservoirs, and other geologic media of engineering interest. In recent years, considerable attention has been focused on the storage of radioactive wastes in fractured rock. In such a system, fractures are the major conduits of groundwater. Therefore accurate characterization of the hydrologic behavior of the fractured rock mass is vital to the safety of such an operation.

In general, well testing is one of the most important methods for determining the flow properties of geologic media. Although well testing methodologies in porous media are well established, the analysis of such tests in fractured media requires that certain assumptions be made a priori about the behavior of the fracture network; i.e., the fracture system has to behave like an equivalent porous medium under well test conditions. However, not much is known about the conditions under which such an assumption can be employed and how much error is involved. The results of the tests may not be meaningful because the fracture system may in fact not behave like an equivalent homogeneous continuum.

In the present study we will investigate the behavior of fracture systems under well test conditions. As a background for this work, we will briefly discuss the theory behind well test analysis. We will review the state of the

art of the solutions for various well test problems. The reminder of this paper may be divided into two parts. The first part, Chapters 3 and 4, is mainly concerned with analytical solutions. In the second part, Chapters 5 and 6, we concentrate on numerical studies of well tests in fracture networks.

In Chapter 3, we propose that certain fracture systems might be represented by a composite model under well test conditions. We discuss the physical conditions which might lead to composite behavior in fractured rocks and present three models that may be used for analyzing well tests in these cases. Using the solutions presented, one may be able to estimate the geometry and the flow properties of the fracture that is intersecting the well as well as the average flow properties of the total system. In Chapter 4, we will attempt to supplement the available solutions for slug tests by considering the geometric conditions that may be present in fractured media. Analyses of field test results will also be presented.

The next two chapters are numerical studies of flow in fractured media. In Chapter 5, we will present a numerical model that simulates transient fluid flow in fracture networks. We will then perform numerical simulations of well tests in two-dimensional fracture systems using the model. In Chapter 6, we will develop a mesh generator which enables us to explicitly model fluid flow in a porous matrix as well as in discrete fractures. We will present one example simulation of heat and mass flow in a fractured porous medium and show how the results may differ from what could be obtained from a double porosity model.

CHAPTER 2

BACKGROUND

-Theory of Well Test Analysis-

2.1. Introduction

Well testing is a means of estimating the parameters and geometry of an underground flow system by inducing some artificial disturbance in a well and monitoring the response of the system. The response of the system is a function of the geometry and the flow parameters of the system. Therefore, given a conceptual model of the system, one can deduce the parameters appropriate to that model by analyzing the response. In this chapter, we will discuss the theory behind well test analysis. In doing so, we will review various models and the solutions to them that have been developed.

In order to estimate the flow parameters and geometry from the well test data, one must first establish a conceptual mathematical model for the behavior of the system. This is done by comparing the well test data to the behaviors of various known conceptual models subjected to the same test conditions. Any geologic information obtained through some other means may help this process. Once a model is adopted, the flow parameters and geometry may be calculated by using an analysis technique developed for the model. However, there may be a number of possible conceptual models with different combinations of geometry and flow parameters that cause the same observed response at a given point. For this reason, uniqueness is an

inherent problem in well test analyses. The degree of uncertainty can be reduced by having many observation points, although it is not usually practical to do so. Nonetheless, well testing is the most important tool we have for characterizing the hydrologic behavior of a system.

Let us first briefly discuss the construction of an equation that governs the fluid flow in a geologic medium for pressure transient tests. Then we examine various physical conditions which determine the boundary conditions for the governing equation. The governing equation and the initial and boundary conditions together define a boundary value problem. The solution of the boundary value problem describes the system behavior during the well tests.

2.2. Governing Equation

Consider an arbitrary volume of rock with porosity ϕ filled with fluid of density ρ bounded by surface S as shown in Figure 2.1. The law of conservation of mass states that, the sum of the net flux crossing the surface S plus the rate of generation of mass M must be equal to the rate of the mass accumulated in the domain, or

$$-\int\int \rho \mathbf{q}\cdot\mathbf{n}\, dS + M = \frac{\partial}{\partial t}\int\int\int \rho\phi\, dV \quad , \tag{2.1}$$

where $\mathbf{q}$ is volume flow rate per unit area and $\mathbf{n}$ is the unit outward normal. The Gauss theorem can be used to transform the surface integral on the left of Equation 2.1 to a volume integral:

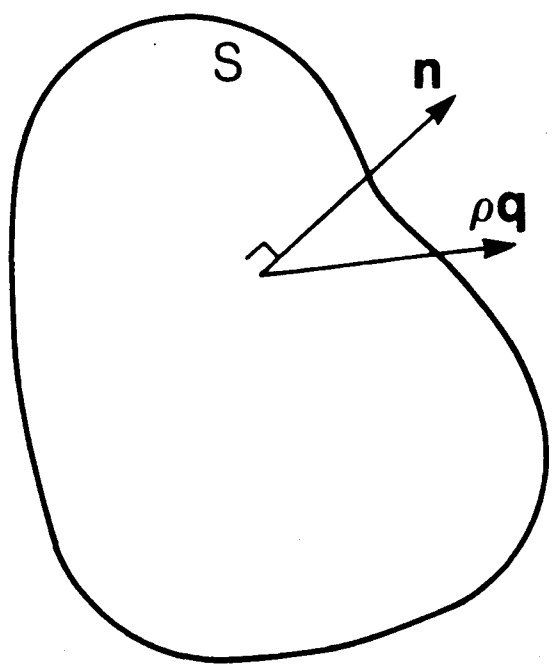

XBL 862-10665

Figure 2.1 Arbitrary volume of rock in a flow field bounded by surface S.

$$-\int\int\int \mathrm{div}(\rho \mathbf{q}) dV + M = \frac{\partial}{\partial t}\int\int\int \rho\phi dV \quad . \tag{2.2}$$

Because Equation 2.2 is valid for any choice of volume, it follows that

$$-\mathrm{div}(\rho \mathbf{q}) + m = \frac{\partial(\rho\phi)}{\partial t} \quad , \tag{2.3}$$

where m is the mass generation rate per unit volume. The right side of Equation 2.3 can be rewritten as:

$$\frac{\partial(\rho\phi)}{\partial t} = \rho S_s \frac{\partial h}{\partial t} \quad , \tag{2.4}$$

where S_s is defined as:

$$S_s = \rho g \left(c_f + \phi c_w\right) \quad , \tag{2.5}$$

where h is the hydraulic head as defined in Hubbert (1940) and g is the gravity constant, c_f is the formation compressibility and c_w is the water compressibility. A derivation of this storage coefficient can be found in Narasimhan (1975, 1982). For most subsurface flow in general,

$$\rho \mathrm{div}\mathbf{q} >> \mathbf{q} \cdot \nabla \rho \quad . \tag{2.6}$$

Therefore, Equation 2.3 simplifies to

$$-\mathrm{div}\ \mathbf{q} + m/\rho = S_s \frac{\partial h}{\partial t} \quad . \tag{2.7}$$

Pore geometry is too complex to allow rigorous extension of analytic expression of fluid motion at a pore volume level to a macroscopic level. Instead, an empirical expression derived by Darcy (1856) is used to describe the motion of fluid in a porous media:

$$\mathbf{q} = -\mathbf{k}\text{grad } h \quad , \tag{2.8}$$

where **k** is the hydraulic conductivity tensor. Substituting Equation 2.8 into Equation 2.7, we obtain:

$$\text{div } (\mathbf{k} \cdot \text{ grad } h \ ) + m / \rho = S_s \frac{\partial h}{\partial t} \quad . \tag{2.9a}$$

In most well test problems, involving homogeneous, horizontally isotropic media, radial symmetry can be assumed and the equation is expressed in a cylindrical coordinate system:

$$\frac{1}{r}\frac{\partial}{\partial r}(k_r \, r \frac{\partial h}{\partial r}) + \frac{\partial}{\partial z}(k_z \frac{\partial h}{\partial z}) + m / \rho = S_s \frac{\partial h}{\partial t} \quad . \tag{2.9b}$$

In an anisotropic system, if the coordinate system is chosen so that the principal directions of anisotropy coincide with the coordinate axis, Equation 2.9a can be written in a Cartesian coordinate system as:

$$k_x \frac{\partial^2 h}{\partial x^2} + k_y \frac{\partial^2 h}{\partial y^2} + k_z \frac{\partial^2 h}{\partial z^2} + m / \rho = S_s \frac{\partial h}{\partial t} \quad . \tag{2.9c}$$

Freeze and Cherry (1979) give a rigorous derivation of Equation 2.9. In the petroleum literature, Matthews and Russell (1967) discuss the derivation of its counterpart.

Well testing can be categorized by the types of disturbances and the geometries of the test. The differences in the types of disturbances and the geometries in general appear as the differences in the boundary conditions for Equation 2.9. Since Theis introduced his famous line source solution in 1935, which was later reintroduced by Jacob (1940), many researchers have pub-

lished solutions to well test problems for many different configurations and boundary conditions. In the petroleum literature, a complete bibliographical summary of well test analysis methods can be found in Earlougher (1977). In groundwater literature, Weeks (1977) summarized and tabulated the state of the art in hydrology. Javandel (1982) reviewed and summarized analytical methods available for solving groundwater flow problems. Solutions that have been published generally differ, mathematically speaking, by the way the boundary conditions are implemented on Equation 2.9. The following is a brief summary of various physical conditions that in turn give variations in well test problems, to most combinations of which researchers have provided with solutions.

2.3. Inner Boundary Conditions

2.3.1. Types of Disturbances

In general, there are four types of disturbances or inner boundary conditions that can be introduced in the test interval: constant flux, constant head, slug and pulse. Of the four, the constant flux test is the most commonly used and its analysis methods are the most widely investigated, especially in the petroleum literature.

In a transient constant flux test, flux going into or coming out of a test interval is kept constant and the head change as a function of time is monitored. Mathematically, constant flux at the well means that the first derivative of the hydraulic head is prescribed at the inner boundary, i.e.,

$$\left.\frac{\partial h(r,t)}{\partial r}\right|_{r=r_w} = \text{Constant} \tag{2.10}$$

Theis (1935) was the first to introduce the exponential integral solution using an analogy to heat conduction theory. In his solution, the well was treated as a line sink extending from the top to the bottom of the formation and the formation was assumed to be an infinite homogeneous slab. The majority of the published solutions are based on these assumptions, which are often referred to as the "Theis assumptions."

In a constant head test the hydraulic head in the interval is kept constant and the transient flow rate is monitored at the well. This boundary condition is expressed as:

$$h(r_w, t) = \text{Constant} \tag{2.11}$$

Because it is generally easier to accurately measure transient pressure than transient flow rate, constant head tests are not widely used. However, constant pressure tests have an advantage that they are not influenced by wellbore storage. Jacob and Lohman (1952) first introduced a type curve for transient flow rate in an infinite aquifer. More recently, constant head tests have received attention by several researchers (Ehlig-Economides 1979, Raghavan 1980). Doe and Remer (1982) suggested that constant head tests be used as an effective tool for testing low permeability rocks.

The slug test, or drill stem test, is the most inexpensive and simplest test of the four. For this reason, it is widely used. In this test, a column of reservoir fluid is instantaneously added to or removed from the well and

subsequent head change is monitored. Cooper, Bredehoeft and Papadopulos (1967) and Papadopulos, Bredehoeft and Cooper (1973) introduced a method for determining the transmissivity and the storage coefficient of an aquifer noting an analogy to heat transfer theory. The boundary condition for this type of test is expressed as:

$$\left.\frac{\partial h(r,t)}{\partial r}\right|_{r=r_w} = C \cdot \frac{dh_w(t)}{dt} , \tag{2.12}$$

where h_w is the pressure head in the well and C is a constant. In other words, the flow rate out of the test interval is proportional to the head change in the interval.

In a pulse test, periodic pulses are introduced in the well and the pressure responses to the pulses are monitored at another interval or other wells. The boundary condition, therefore, can be written as:

$$\left.\frac{\partial h(r,t)}{\partial r}\right|_{r=r_w} = f(t) \tag{2.13}$$

Pulses are usually generated by repetition of constant flow rate production/injection and shut-in periods. Johnson, Greenkorn and Woods (1966) first introduced pulse test methodology with multiple wells. Pulse tests are attractive because the test duration can be relatively short.

2.3.2. Mathematical Implementation of a Well

Theis (1935) approximated a producing well as a line sink. This boundary condition is expressed as

$$\lim_{r \to 0} r \frac{\partial h(r,t)}{\partial r} = \text{Constant} \tag{2.14}$$

However, a well is actually a finite size cylinder and line source/sink approximation introduces some errors. Van Everdingen and Hurst (1949) used a Laplace transformation to solve Equation 2.9 for a finite radius well. Mueller and Witherspoon (1965) presented type curves for dimensionless pressure for various dimensionless distances from a well. It has been shown that except for small values of dimensionless time ($t_D / r_D{}^2 \leq 0.5$) and for small values of dimensionless distances from the well ($r_D \leq 20$), the errors introduced by the approximation are negligible. In many practical cases, therefore, a physical well can be approximated as a line source (Ramey 1975). This approximation makes the equation more amenable to analytical solution. However, the line source approximation is not appropriate for slug tests as shown in Papadopulos (1967) and Papadopulos and Cooper (1967). In such cases the inner boundary condition must be imposed at a finite distance from the axis of the well.

A partially penetrating well is sometimes approximated as a spherical well using a "equivalent radius". Partial penetration is discussed in section 2.3.5.

2.3.3. Skin Effect

Due to some artificial causes or geological conditions, there sometimes exists an annulus where the material properties are different in the vicinity of the well. Hurst (1953) first termed the additional head loss caused by the lower permeability zone the "skin effect." Van Everdingen (1953) presented a

method to determine "infinitesimal skin effect" from pressure buildup test. He treated the damaged zone as a zone of infinitesimal thickness, which, together with a line-source approximation of a constantly producing well, made the mathematical treatment less complicated. In an analogy with heat transfer, skin is equivalent to a thin film resistance to heat flow on the inner surface of a cylindrical material. The solution to this problem is presented in Carslaw and Jaeger (1946).

With the presence of a skin effect, the flux across the sandface is proportional to the head difference between the well and the medium:

$$\left.\frac{\partial h}{\partial r}\right|_{r=r_w} = C \cdot (h_w - h \mid_{r=r_w}) \tag{2.15}$$

Hawkins (1956) suggested that a transient pressure drop in a finite thickness skin can be approximated by steady state pressure drop neglecting the storage effect of the skin. Therefore, an additional head loss due to a finite thickness skin of radius R and transmissivity T_1 in a medium of transmissivity T_2 for constant production Q is:

$$\Delta h = \frac{Q}{2\pi T_1}\ln\frac{R}{r_w} - \frac{Q}{2\pi T_2}\ln\frac{R}{r_w} \tag{2.16}$$

Agarwal, AL-Hussainy and Ramey (1970) reported that the steady-state skin effect concept becomes invalid for very short test times. When the storage effect of the skin zone cannot be neglected, the problem becomes the same as that of a radial composite reservoir. Sternberg (1973) used an approximate Laplace inversion scheme developed by Schapery (1961) and presented a

solution for pressure drawdown at a finite radius pumping well with a finite thickness skin. He compared the solution with that of Hawkins' (1956) and concluded that the steady-state approximation is quite adequate for the ranges of parameters he used. Ramey (1982) gave a review of the works on skin effects to that date.

The solution for a slug test with an infinitesimally thin skin was first presented by Ramey and Agarwal (1972). Ramey, Agarwal and Martin (1975) later presented type curves for estimating permeability and skin factor from slug test data. Faust and Mercer (1984) used a finite difference model to evaluate slug tests with finite thickness skin. Moench and Hsieh (1985) used numerical inversion scheme developed by Stehfest (1970) to develop type curves for the same problem.

2.3.4. Wellbore Storage

When the storage capacity of a well is significant, the inner boundary condition does not immediately or directly reflect the imposed disturbance. This effect is often referred to as wellbore storage, afterflow or unloading. The boundary condition for wellbore storage is analogous to that of a medium in contact with a well-stirred fluid or perfect conductor in heat transfer theory. For transient pressure testing, the inner boundary condition at the pumping well that includes wellbore storage effect can be expressed as:

$$\left.\frac{\partial h(r,t)}{\partial r}\right|_{r=r_w} = C_1 \cdot \frac{dh_w(t)}{dt} + C_2 , \qquad (2.17)$$

where C_1 and C_2 are constants relating to wellbore storage capacity and pumping rate, respectively. As can be seen from Equation 2.17, Equation 2.10 and Equation 2.12 are special cases of this more general boundary condition. For $C_1=0$, one obtains constant flux condition at the sandface as in Equation 10 and for $C_2=0$, it is the slug test boundary condition as expressed in Equation 2.12. Carslaw and Jaeger (1946) presented solutions for several heat transfer problems that involve the same boundary condition. Blackwell (1954) discussed a method to determine thermal constants using the Laplace transform solution.

In the petroleum literature, van Everdingen and Hurst (1949) first introduced the wellbore storage concept together with the finite radius well condition. Ramey (1965) discussed wellbore storage effects in gas wells. Agarwal, Al-Hussainy and Ramey (1970) presented a thorough investigation of wellbore storage and infinitesimal skin effects on pressure transient tests. They provided type curves to be used to determine a wellbore storage coefficient and a skin factor. Wattenbarger and Ramey (1970) investigated finite thickness skin condition with a finite difference model. McKinley (1971) presented type curves for pressure buildup data with no skin. Earlougher, Kersch and Ramey (1973) investigated effects of changing the wellbore storage coefficient. Earlougher and Kersch (1974) presented new type curves for estimating wellbore storage and skin factor defining new dimensionless variables. Gringarten et al. (1979) reviewed published works on wellbore storage and skin type-curves and proposed new efficient type curves using a new

dimensionless time variable.

Earlier works on interference tests have assumed that wellbore storage and skin effects at a pumping well have a negligible effect on the observation wells. More recently, Jargon (1976), Sandal et. al. (1978), Chu, Garcia-Rivera, and Raghavan (1980), and Tongpenyai and Raghavan (1981) investigated the effects of wellbore storage and skin at the producing well on interference test results. Ogbe and Brigham (1984) supplied solutions for interference test with wellbore storage and skin at both producing and observation wells.

2.3.5. Partial Penetration

Many well test solutions are developed assuming the well is completed from the top to the bottom of the formation. However, when a well does not penetrate to the bottom of the formation, or is completed in only a part of the formation, the inner boundary conditions discussed above must be prescribed in terms of r and z. The general boundary condition in Equation 2.17 is then expressed as:

$$\int_{z_1}^{z_2} \left. \frac{\partial h(r,z,t)}{\partial r} \right|_{r=r_w} dz = C_1 \cdot \frac{dh_w(t)}{dt} + C_2 , \qquad (2.18)$$

where z_1 and z_2 are the two end elevations of the opening of the well. Hantush (1957, 1961) originally solved a partial penetration problem using a superposition of continuous point source functions. Brons and Marting (1967) showed that a partially penetrated reservoir initially behaves like a

reservoir with a thickness equal to the well opening length and at later time behaves as one with the actual thickness. They also demonstrated that the conventional Horner (1951) method can be used to analyze late time buildup data and that the limited entry can be treated as a pseudo-skin factor. Odeh (1968) discussed a method to estimate the pseudo-skin factors caused by the restricted entry. Kazemi and Seth (1969) used a finite difference model to study the partial penetration problem in anisotropic formations. If the completion interval of a well is very short compared to the thickness of the formation, the pressure transient data have a long transition period characteristic of a spherical flow between the two cylindrical flow regime. Culham (1974) adopted the work of Moran and Finklea (1961) on wireline formation testing and presented an analysis method for the transition period data using the spherical flow equation. Gringarten and Ramey (1974) presented a solution applicable to the partial entry problem using Green's function (Gringarten and Ramey, 1973), but they were mainly interested in a uniform flux horizontal fracture. Raghavan and Clark (1975) developed a method to estimate vertical and horizontal permeability of a thick anisotropic formation from limited entry flow tests. They used the spherical wellbore radius approximation suggested by Rodriguez-Nieto and Carter. Javandel and Witherspoon (1979a, 1979b) presented analytical solutions for partial penetration in two layer-aquifers with a well partially open in either of the formations. Brigham, Peden and Ng (1980) and Joseph and Koederitz (1984) investigated wellbore storage and skin effects on spherical flow. The latter included

wellbore phase redistributions in the solution. Hsieh (1983) solved the three dimensional pressure field created by a continuous line segment source. He presented a three dimensional interference test method to be used for estimating the permeability ellipsoid. Tang (1985) presented a direct method to determine reservoir properties and skin of thick anisotropic formations. He observed that infinite thickness assumption is reasonable for analyzing limited entry well tests in thick reservoirs.

2.4. Outer Boundary Conditions

In the early time of a pressure transient test, a reservoir responds to the induced disturbance like an infinite system. Many well test analysis methods use this infinite acting period data. The boundary condition for an infinite system requires the pressure to be bounded or the disturbance not to reach to infinity:

$$\lim_{r \to \infty} h(r, t) = h_i \quad ,$$

where h_i is the initial pressure head.

If a test is run long enough, however, the effect of the outer boundary will be eventually felt. The distance to, the shape and the type of the boundary all affect the observed pressure transient. The types of outer boundary conditions are generally assumed to be either no-flow (closed) or constant head (open). In a radial system, the former can be expressed as:

$$\left. \frac{\partial h(r, t)}{\partial r} \right|_{r=R} = 0 \quad , \tag{2.19}$$

where R is the radius of the outer boundary, and the latter:

$$h\,(R\,,t\,) = Const. \tag{2.20}$$

Van Everdingen and Hurst (1949) presented transient pressure solutions in a cylindrical reservoir for both of the above outer boundary conditions. Miller, Dyes and Hutchinson (1950) demonstrated a method to determine average reservoir pressure from a buildup curve for a radial open outer boundary. Horner (1951) proposed a method to estimate the permeability from a new buildup plot: bottom hole pressure plotted against $\log\frac{t_p + \Delta t}{\Delta t}$, where t_p is the production time and Δt is the shut-in time.

The actual geometrical shapes of the outer limits of drainage regions are normally dictated by some geological feature such as faults and barriers, the water-oil interface for water drive reservoirs, and rivers and lakes in case of shallow aquifers. Water drive reservoirs are in many cases assumed to have circular open outer boundaries. On the other hand, faults and other barriers usually result in a combination of linear no-flow boundaries.

When a reservoir is produced by multiple wells simultaneously, each well acts on a drainage area whose shape is dependent on the well pattern and pumping rates. If those wells are located in a regular pattern and the production/injection scheme is symmetrical, typical drainage areas can be assumed to be rectangular or have some regular shape. The unsteady pressure behavior of such systems, in general, can be obtained by superimposing solutions for an infinite medium. Matthews, Brons, and Hazebroek (1954)

presented dimensionless pressure for wells at different locations in various rectangular shapes and developed a method for calculating the average pressure in such bounded reservoirs. Dietz (1965) proposed a simpler method for estimating the average pressure of a bounded reservoir that has reached pseudosteady state. Earlougher et al. (1968) presented a solution for a bounded square system and showed that the solution can be superimposed to generate drawdown functions for any rectangular system. Ramey and Cobb (1971) compared various pressure buildup analysis techniques and showed how to use them in a closed square system. Denson, Smith and Cobb (1976) developed a method to determine the drainage volume and the effective porosity of a bounded reservoir whose approximate geometry is known. Recently, Streltsova and McKinley (1984) presented solutions and methods of analyzing buildup tests with differently shaped outer boundaries. They investigated effects of the length of flow period prior to shut-in on buildup curves. While the works mentioned above dealt with regularly shaped boundaries such as rectangles and circles, Kuo (1985) investigated effects of irregularly shaped boundaries on pressure distribution. He used a superposition of series of image wells along a irregularly shaped boundary.

2.5. Other Conditions

2.5.1. Leakage from Neighboring Formations

Most of the welltest solutions are developed assuming that there is no flow either from the top or the bottom of the formation. This assumption is

adequate if the overlying and the underlying formations are virtually impermeable. However, there are cases when there is a leakage from a different aquifer separated by low permeability aquitard. Hantush and Jacob (1955) published a solution for pressure distribution around a well discharging at a constant rate in an infinite aquifer with leakage from the neighboring formation. The leakage rate was assumed to be proportional to drawdown at any point in the pumped formation. Therefore, leakage can be represented by the mass generation term m in Equation 2.9:

$$m = C \cdot (h_i - h) , \tag{2.21}$$

where C is a constant. Hantush (1959) later presented solutions for the related problem for a constant drawdown well with each of infinite, open and closed outer boundaries. In a later paper, Hantush (1960) modified the Hantush and Jacob solution to include the storage effects of the aquitard. Neuman and Witherspoon (1968) solved for the drawdown in the aquitard enclosed by two leaky aquifers. Leaky aquifers were a major concern to researchers investigating the aquifer natural gas storage problem. Witherspoon, Mueller, and Donovan (1962), Witherspoon and Neuman (1967), and Witherspoon, Javandel, Neuman, and Freeze (1967) have all contributed to this area of study.

The works mentioned thus far made either or both of the following two assumptions: (i) the storage effect of the aquitard is negligible, and (ii) there is no drawdown in the unpumped aquifer. Only Neuman and Witherspoon (1969a, 1969b) presented a complete solution to the leaky aquifer problem

without these two assumptions. They constructed separate governing equations for each of the two aquifers and the aquitard and solved them simultaneously while requiring continuity of head and mass flux across the boundaries. Their solution, however, was based on the assumption that the flow in the aquitard is vertical and flow in the aquifer is horizontal. Therefore, the leakage term can be described by

$$m = C \cdot \left. \frac{\partial h_2}{\partial z} \right|_{z=\text{interface}} \tag{2.22}$$

where h_2 is the head in the aquitard. Javandel and Witherspoon (1968) validated this assumption using a finite element method. More recently, Javandel and Witherspoon (1980, 1983) solved for the pressure distribution in two layer-aquifers with a partially penetrating well open in either of the formations.

2.5.2. Multilayered Reservoir

A multilayered reservoir problem is distinguished from a leaky aquifer problem in that a well is open to multiple formations as opposed to a single formation. Multilayered models can be categorized into two groups depending on whether crossflow between formations is allowed. When no crossflow is considered, the formations communicate with each other only at the well. Then the boundary condition in Equation 2.17 can be rewritten as:

$$\sum_{i=1}^{n} k_j \left. \frac{\partial h_j(r,t)}{\partial r} \right|_{r=r_w} = C_1 \cdot \frac{dh_w(t)}{dt} + C_2 , \tag{2.23}$$

where the subscript j denotes j-th formation. There are two types of formation crossflow representation: (i) pseudo-steady state flow and (ii) rigorous three dimensional flow. The first assumes that the flux across the interface is proportional to the pressure difference between two neighboring formations and that the flow in each formation is horizontal. This condition can be included in the mass generation term in Equation 2.9a:

$$m = C_1 \cdot (h_{j-1} - h_j) + C_2 \cdot (h_j - h_{j+1}) . \tag{2.24}$$

For the second flow representation, the governing equation Equation 2.9b in three dimensional form without the mass generation term has to be constructed for each formation. The subsequent set of equations must be solved simultaneously requiring continuity in the pressure and flux across the interface, i.e.:

$$h_j(r, z_j - 0, t) = h_{j+1}(r, z_j + 0, t) , \tag{2.25}$$

and

$$\left.\frac{\partial h_j}{\partial z}\right|_{z=z_j-0} = \left.\frac{\partial h_{j+1}}{\partial z}\right|_{z=z_j+0} . \tag{2.26}$$

Most of the works on the multilayered reservoir problem are found in petroleum literature. Lefkovits, Hazebroek, Allen, and Matthews (1961) first presented a solution for arbitrary number of layers communicating at the well but with no formation crossflow. Russell and Prats (1962) developed a solution for two layer system allowing for three dimensional crossflow with a well producing at a constant pressure. Kazemi (1970) studied a multilayered

system with transient crossflow using a finite difference model. Woods (1970) looked at the behavior of a two layer system under a pulse test. Others (Earlougher, Kersch and Kunzman, 1974; Raghavan, Topaloglu, Cobb, and Ramey, 1974; Chu and Raghavan, 1981; Streltsova, 1984) investigated multilayered system behavior with various combinations of boundary conditions. Recently, Bremer, Winston and Vela (1985) presented a solution for a two layer system with pseudo-steady crossflow. Most of the studies concluded that the behavior of a multilayered system is similar to that of a single layer with equal permeability thickness product. Ehlig-Economides and Joseph (1985) gave a complete account for the published works on multilayered system and tabulated them in the chronological order listing the features of each model. They also introduced a most general model of a multilayered reservoir with pseudo-steady state crossflow and proposed a method to determine individual layer properties using simultaneously acquired pressure and flow rate transient data.

2.5.3. Composite Medium

When there is an abrupt discontinuity in the material properties in the radial direction from a well, the reservoir is called a composite medium. A composite reservoir can often be man-induced. Fluid injections or combustion in secondary or tertiary recovery projects create radial fluid banks of different fluid properties of water, steam, chemicals, gas, or oil. An oil reservoir with a producing well surrounded by a region saturated with gas may be

represented by a composite medium as well. Drilling may create a damaged zone around a well. When the radius of such zone is thin, it is called a skin and it may be included in the inner boundary condition as discussed in the previous section. However, when the radius of the damaged zone is large and the storage of the zone can not be neglected, it should be treated as a composite medium. Some geologic settings may represent a composite medium. Benson and Lai (1986) successfully matched interference data in a geothermal reservoir with a composite model and suspected an existence of high permeability fractured region. They introduced a method to estimate the inner region radius from multiple observation well data. Witherspoon, Javandel and Martin (1985) used a composite medium solution to analyze a brine injection problem in the caprock of a salt dome. In this unusual case the caprock was so much more permeable than the surrounding rock that it behaved like a "bath tub."

An analytical model of a composite medium consists of a separate governing equation for each medium. The required condition at the media interface $r = R$ is the continuity up to the first derivative:

$$h(R-0,t) = h(R+0,t) \tag{2.27}$$

and

$$k\frac{\partial h}{\partial r}\bigg|_{r=R-0} = k\frac{\partial h}{\partial r}\bigg|_{r=R+0} . \tag{2.28}$$

Hurst (1960) first presented a solution for a line source located in the center

of the inner region of an infinite composite reservoir, while Loucks (1961) worked with a finite well condition. Jones (1962) extended the solution to multi-phase system. Larkin (1963) later introduced a more general solution using the Green's function presented by Jaeger (1944). His solution allowed an arbitrary number of line sources at any locations in the inner region. However, he did not evaluate the integrals in his solution. Carter (1966) investigated the effects of no-flow outer boundary. Odeh (1969) proposed a semi-log plot analysis method for a composite reservoir. He considered the case where the ratio of storage capacity in the two regions was unity. Ramey (1970) presented an approximate solution to the same problem as Hurst's using the Boltzmann transformation. Onyekonwu and Horne (1983) presented a solution to a spherical composite medium. Streltsova and McKinley (1984) investigated the effect of flow time on buildup curves in a composite reservoir. Satman (1985) included wellbore storage and skin at the active well in the composite model. Brown (1985) used the derivative curve method introduced by Bourdet and Alagoa (1984) to present a similar solution. Other works on finite thickness skin that consider inner region storage effects (Sternberg, 1973; Faust and Mercer, 1984; Moench and Hsieh, 1985) are also directly related to a composite reservoir problem.

Numerical studies on composite reservoirs include Bixel and van Poollen (1967), Kazemi, Merrill, and Jargon (1972), and Merrill Kazemi, and Gogarty (1974). The last two works investigated a reservoir with a moving front of an injected fluid bank that has a different mobility and a specific storage

from the reservoir fluid.

2.5.4. Fractures

2.5.4.1. Double Porosity Medium (Naturally Fractured Reservoir)

When a reservoir is extensively and uniformly fractured and the permeability of the rock matrix is small compared to that of the fracture system and the storage capacity of the rock matrix is large compared to that of the fracture system, the reservoir can be represented by a double porosity model. In a double porosity model, the fracture system is assumed to form a continuum as well as the rock matrix. Hence, Equation 2.9 can be used to describe the flow in the fracture system. While the rock matrix is assumed not to contribute to the overall flow capacity of the reservoir, it is assumed to interact with the fracture system and to behave as the fluid source to the fracture system.

There are two approaches to express this fracture-matrix interaction term. One is to assume a quasi-steady state between the rock matrix and the fractures. That is, to assume the flux between the fracture and the rock matrix is proportional to the pressure difference between the local fracture pressure and the average rock matrix pressure. The fluid generation term in Equation 2.9, therefore, is expressed as:

$$m = C_1 \cdot \frac{dh_m(t)}{dt}, \tag{2.29}$$

where $h_m(t)$ is the pressure head in the rock matrix. The flow between the

rock matrix and the fracture is described by:

$$\frac{dh_m(t)}{dt} = C_2 \cdot (h - h_m(t)) , \tag{2.30}$$

where C_1 and C_2 are constants.

Barenblatt, Zheltov, and Kochina (1960) first introduced the double porosity concept in hydrology. Warren and Root (1963) modified their work and presented two parameters to characterize the naturally fractured reservoir. Both groups assumed a quasi-steady state flow in the rock matrix. Many other works with similar assumptions followed these two pioneering works. Odeh (1963) presented a case when the behavior of a double porosity medium is identical to that of a homogeneous medium. Kazemi and Seth (1969) introduced a solution for interference tests. Mavor and Cinco-Ley (1979) included wellbore storage and skin effects in their solution. Bourdet and Gringarten (1980) and Gringarten (1984) introduced new dimensionless groups and presented type curves for analyzing well test data from naturally fractured reservoirs. Da Prat, Cinco-Ley and Ramey (1981) presented a solution for constant pressure tests in naturally fractured reservoirs. They concluded that ignoring the presence of a constant flow rate period in a type-curve match can lead to erroneous estimates of the dimensionless outer radius of a naturally fractured reservoir.

A second approach is to assume a quasi-steady state flow in the rock matrix. The transient flow in the rock matrix is described by Equation 2.9 and the fluid generation term in the equation for the flow in the fracture is

now:

$$m = C_1 \cdot \frac{\partial h_m(z,t)}{\partial z}, \tag{2.31}$$

where z is the space variable for the rock matrix. The flow in the rock matrix is generally assumed to be one dimensional. It should be noted that a double porosity reservoir model is mathematically analogous to that of a reservoir with leakage from an adjacent formation as can be seen from the equations above.

Kazemi (1969) first used a finite difference method to analyze transient flow in the rock matrix. His results substantiated the conclusions of the earlier works with the quasi-steady state assumption except for the shape of the pressure curve during the transition period between the first and second straight line. De Swaan (1976) constructed an analytical model for transient matrix flow and presented approximate solutions for limiting cases. Najurieta (1980) extended de Swaan's (1976) work and obtained approximate solutions for all time using Schapery's (1961) approximate Laplace inversion method. Bourdet and Gringarten (1980) first identified the existence of a semilog half slope during the transition time period. Streltsova (1983) and Serra, Reynolds, and Raghavan (1983), and Reynolds et al. (1985) used a slab like matrix block to describe the interaction with the fracture in their model which is analogous to a layered reservoir model. Lai, Bodvarsson, and Witherspoon (1983) presented a solution that considers a transient flow between fractures and cube-shaped rock matrix blocks. Moench (1984) investigated

the effects of fracture skin at the fracture-matrix block interface. Ershaghi and Aflaki (1985) extended the analysis of Lai et al. on the transition time period data. In a recent paper, Cinco-Lay and Samaniego (1985) studied the effects of multiple matrix block size.

2.5.4.2. Single Fracture

In some cases, a well is intercepted by a single fracture. One such example is a hydraulically fractured well. Hydraulic fracturing is often performed as part of a well stimulation scheme in order to enhance the productivity in hydrocarbon and geothermal reservoirs. It is believed that hydraulic fracturing generally produces a single vertical fracture especially in deep wells. However, in shallow formations, a horizontal fracture may be formed. It is also possible that a well may intersect a fracture of natural origin. In either case, it is often necessary to account for the physical geometry near the well in considering the behavior of the well under well test conditions.

Gringarten and Ramey (1974) solved for the pressure distribution created by a uniform flux horizontal fracture with impermeable upper and lower boundaries. Their solution employed Green's functions and the product solution method presented by Gringarten and Ramey (1973). Their solution is also applicable to the limited entry problem. Using a similar method, Gringarten, Ramey and Raghavan (1974) presented solutions for uniform flux and infinite conductivity vertical fracture models. In the unform flux fracture model, the flux per unit length of the fracture is

assumed to be constant, whereas in the infinite conductivity fracture model, it is assumed that there is no pressure drop along the fracture. In their model, the fracture is treated as a plane source located along the x-axis. Because radial symmetry is no longer preserved, the governing equation for the vertical fracture model is cast in Cartesian coordinates. Gringarten et al. also presented type curves for a closed square reservoir in comparison with the previous finite difference solution by Russell and Truit (1964). Gringarten and Witherspoon (1972) extended the works of Gringarten and Ramey and Gringarten et al. on the uniform flux horizontal and vertical fracture in isotropic formations to anisotropic formations. They reported that the uniform flux solution gives good results in a case where a well intersects a natural fracture. Raghavan (1977) gave a summary of the work to that date on the well behavior intercepted by fractures.

Although the infinite conductivity assumption is adequate in some cases, fractures in reality have finite conductivities and storage capacities. Cinco-Ley, Samaniego-V, and Dominguez-A (1978) presented a solution for a well intersecting a finite conductivity vertical fracture. In a later paper, Cinco-Ley and Samaniego-V (1981) identified four flow periods in the transient flow of a vertically fractured well. They demonstrated that there exists a "bilinear" flow period between a fracture linear flow period and a formation linear flow period. In the bilinear flow period the flow in the fracture and in the formation are both linear and in this case the dimensionless pressure plotted against the dimensionless time on a log-log plot exhibits a one-quarter

slope. Rosato, Bennett, Reynolds, and Raghavan (1982) developed buildup curves for a well with a finite conductivity fracture using a finite difference model. Bennett, Rosato, Reynolds, and Raghavan (1983) used a similar method to investigate the effects of variable fracture conductivity and unequal fracture wing length. They observed that the bilinear flow period characterized by a one-quarter slope may be obscured by a variable conductivity fracture.

2.5.5. Anisotropy

Many well test solutions are obtained assuming the horizontal permeability to be isotropic. This assumption simplifies the governing equation and the subsequent solution scheme considerably; e.g., Equation 2.9a reduces to Equation 2.9b, in which only one space variable r in the horizontal direction is necessary to describe the flow because of a radial symmetry. However, there are cases when the horizontal permeability varies as a function of the direction. Such anisotropy can be caused by the deposition process or fracturing in a preferential orientations. To describe the flow in an anisotropic formation Equation 2.9c should be used instead of Equation 2.9b. The governing equation and the boundary conditions, however, can be converted to those for an isotropic formation by using a transformation of coordinates. Transformations of the coordinates are given by:

$$x = \hat{x}\sqrt{k_x / \bar{k}}$$

$$y = \hat{y}\sqrt{k_y / \bar{k}} \tag{2.32}$$

$$z = \hat{z}\sqrt{k_z / \bar{k}} \quad ,$$

where $\bar{k} = (k_x\, k_y\, k_z)^{\frac{1}{3}}$.

Papadopulos (1965) solved for the pressure distribution caused by a continuous line source in an infinite anisotropic aquifer using the transformation of the coordinates. Hantush (1966a) presented solutions for leaky and non-leaky anisotropic aquifers with various inner boundary conditions using a similar method. Hantush (1966b) introduced procedures for analyzing data from pumping tests using the solutions presented by Hantush (1967a). In his method, observations in two rays of observation wells are necessary if the principal directions of anisotropy are known and three rays are necessary if the directions are not known. Hantush and Thomas (1966) presented the use of an equal drawdown curve for analyzing interference data from multiple observation wells. Ramey (1975) demonstrated an analysis of actual oil field data with the method presented by Papadopulos (1965). Kucuk and Brigham (1979) presented analytical solutions to elliptical flow problems that are applicable to anisotropic reservoirs. They solved the flow equation with a finite radius well condition, under which a circular well is transformed to an elliptical well through a coordinate transformation. Their solutions are also applicable to infinite conductivity vertically fractured wells. Walter (1983) presented a methodology to estimate the formation anisotropy with a three-well array. He proposed to perform two aquifer tests by sequentially pumping two of the wells. Hsieh (1983) solved for pressure distribution in a homo-

geneous anisotropic three dimensional medium with a finite continuous line source. He presented a methodology to determine the permeability ellipsoid from a series of cross hole injection tests.

2.6. Conclusions

We have briefly discussed the theory behind well test analysis. We have also reviewed the state of the art of the solutions for well test problems. We have discovered that there are only few models that have been developed specifically for fracture systems. Most of the well test solutions were developed primarily for porous media, although they are also applied to fractured media. Naturally fractured reservoir models or double porosity models assume that the fracture system behaves like a porous medium. There has been little work done on whether the fracture system indeed behaves like a porous medium under well test conditions. Single fracture models are also applied to a fractured medium. However, the rationale for this is that the observed data seems to match well with the model. There has been little work to support the assumption theoretically. Thererfore, it has become clear that more work is necessary to better understand the behavior of a fracture system subjected to well test conditions. Also, only few models have been studied for slug test boundary conditions. In the following chapters, attempts will be made to fill some of these gaps.

CHAPTER 3

ANALYTICAL SOLUTIONS FOR FLOW TO WELLS IN FRACTURED MEDIA

3.1. Introduction

The presence of natural fractures complicates the interpretation of well tests. One of the reasons for this is that the fractures are generally much more permeable than the rock matrix. Thus the rock mass responds to the induced well test conditions more slowly than the fracture system. Also flow near the well is mainly controlled by the fractures intersecting the well and, depending on the geometry of the fractures, may represent a different flow regime from that of the system as a whole. For this reason the standard radial flow solutions are sometimes inadequate in analyzing well test data for a well intercepting fractures.

Double porosity models have been introduced to analyze such well test data. The double porosity models originated by Barenblatt et al. (1960) and extended by many others (Warren and Root, 1963; Odeh, 1963; Kazemi and Seth, 1969) treat naturally fractured porous systems by superimposing two continua, one for the fracture system and another for the porous matrix. These models successfully account for the dual nature of the naturally fractured system. However, models of this kind do not treat the fractures near the well explicitly. The models assume a priori that the fracture system can be approximated by a single continuum. If there is only a small number of

fractures intersecting the pumping well, the single continuum approximation may not be appropriate because the conditions of the well test cause flow to converge into the few fractures that intersect the well. These fractures will also experience a large gradient. The properties and the geometries of these few fractures therefore control flow in the vicinity of the active well. The characteristics of fractures close to the well must be accounted for especially if the hydraulic parameters of these fractures are significantly different from the average values for the entire system.

On the other hand, if a reservoir is extensively fractured and if a large number of fractures intersect the well, the fracture system probably can be approximated as a single continuum. Whether a fracture system can be approximated by a continuum in this way depends on the geometry of the fracture system as well as the scope of the test.

In this chapter we present solutions for flow to wells in fractured media that account for the difference in the flow regime around the active well from that of the system as a whole. The proposed analytical models are composite systems with two concentric regions. The inner region is composed of a finite number of fractures whose flow characteristics and properties are different from the average values for the entire system. In the outer region it is assumed that the flow takes place in a sufficient number of fractures so that the classical porous medium approximation applies. First, we look at a model in which a linear flow takes place in the inner region and a radial flow in the outer region. Next we present an analytical Laplace inversion solution

to a radial composite model. Solutions in the past have been obtained either by an approximate Laplace inversion (Sternberg, 1973; Streltsova and McKinley, 1984) or by a numerical Laplace inversion (Satman, 1985). Third, we investigate a radial-spherical flow combination.

3.2. Composite Model With Linear and Radial Flow

When a well intercepts a few vertical fractures or when the flow near the well is restricted to be entirely in channels within fractures of any orientation, the flow near the well may be more linear than radial, that is, the cross sectional area available to flow does not change with the radial distance. In such cases, the system can be described by a concentric composite model, in which the flow is assumed to be linear in the inner region and radial in the outer region.

Single fracture models have been originally developed in order to analyze the pressure transients of hydraulically fractured wells. Gringarten et al. (1974) introduced the infinite conductivity solution and the uniform flux solution for a single vertical fracture intersecting a well. Their solutions can be used to find the fracture length as well as the formation permeability. Later, Cinco-Ley, et al. (1978) solved the finite conductivity vertical fracture problem and introduced a method to obtain the fracture conductivity. It has been reported that the uniform flux solution gives good results for a well intersecting a natural vertical fracture (Gringraten et al., 1972; Gringraten and Witherspoon, 1972; Raghavan, 1977).

In the single vertical fracture models, fluid enters the fracture from the fracture faces and no fluid enters from the ends. However, for the case when a pumping well intersects a natural fracture or an artificial fracture which is part of an interconnected network of fractures, which is significantly more permeable than the matrix, the fluid enters the fracture primarily from intersections with other fractures, i.e., the ends, rather than from the faces. The fluid then flows linearly into the well (Figure 3.1). Moreover, the formation linear flow period (Gringarten and Ramey, 1974; Gringarten et al., 1975; Cinco-Ley et al., 1976) provides evidence that the fluid entering the fracture flows linearly. Therefore, it seems plausible to construct a model which assumes a linear flow region around the well that intersects vertical fractures.

The proposed model is a composite system with two concentric regions. The inner region contains a finite number of fractures and flow is assumed to be linear. The outer region is the classical porous medium where only radial flow takes place. Similar composite models have been examined previously (Larkin, 1963; Bixel and van Poollen, 1967; Ramey, 1970) but none has considered a linear-radial flow combination. The solution is presented in a series of type curves, so that the flow properties of the fracture system can be determined by curve matching. A field example is presented to demonstrate the type curve matching technique that can be used to characterize the fracture as well as the average system parameters.

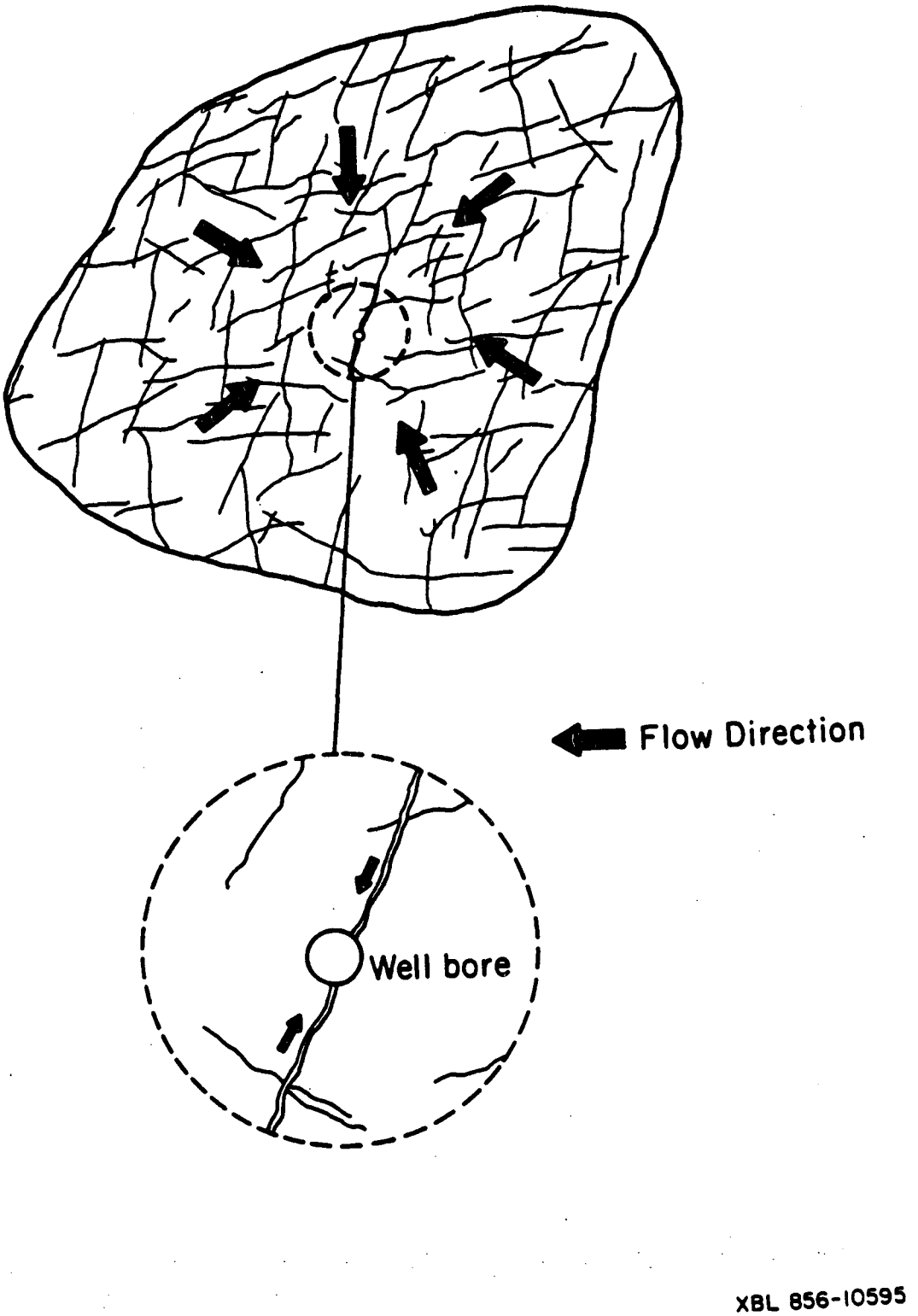

Figure 3.1 Flow to a well in a fracture-dominated system.

3.2.1. Model Description

An isothermal system in a homogeneously fractured formation of uniform thickness H and radially infinite extent is considered. The well is pumped at a constant rate Q. It is assumed that all hydraulic parameters are independent of pressure, and no wellbore storage or damage is considered. The conceptual model of the well test in this system consists of two zones. In the outer region, the flow is radial, and the hydraulic conductivity and storage coefficient for the region are k_2 and S_{s_2}, respectively. In the inner region, the flow is assumed to be linear. There is a finite number (n) of fractures in the region with the same hydraulic aperture b, hydraulic conductivity k_1 and storage coefficient S_{s_1}. These values must be volumetrically averaged to obtain flow parameters for the inner region as a whole.

The fractures are assumed to be vertical and to extend from the top to the bottom of the formation. The well is located in the center of the inner region. The radius of the well is r_w, and the radius of the boundary between the inner and outer regions is r_f. The latter is the radius required before the radial flow regime takes over the system response under well test conditions. Therefore, in practice, r_f is related to, but not exactly equal to, the exact fracture length. It is assumed that there is an infinitesimally thin ring of infinite conductivity between the two regions so that the otherwise incompatible boundaries can be matched. Figure 3.2 illustrates the model. The details of the solution are given below and the final result can be found in Equation 3.2.28. We then examine the assymptotic behavior in small and

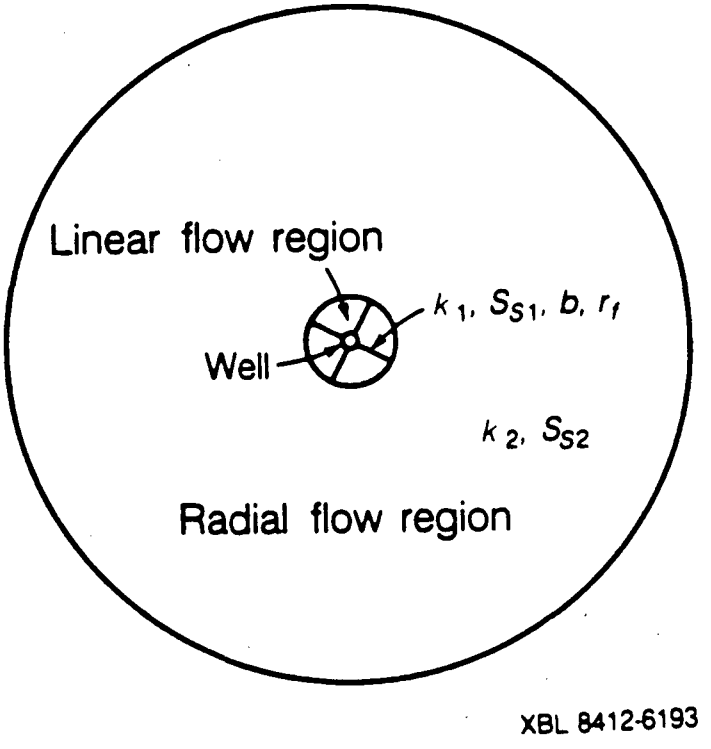

Figure 3.2 Linear-radial composite model.

large time in order to provide simpler solutions and check the results.

The governing equation for the inner region is that for one dimensional unsteady-flow,

$$\frac{\partial^2 h_1}{\partial r^2} = \frac{1}{\alpha_1} \cdot \frac{\partial h_1}{\partial t}, \tag{3.2.1a}$$

where the hydraulic diffusivity, $\alpha = k/S_s$. For the outer region the usual radial flow equation describes the flow.

$$\frac{\partial^2 h_2}{\partial r^2} + \frac{1}{r} \cdot \frac{\partial h_2}{\partial r} = \frac{1}{\alpha_2} \cdot \frac{\partial h_2}{\partial t}. \tag{3.2.1b}$$

The initial conditions and the boundary conditions for constant rate injection test are

$$h_1(r, 0) = h_i \qquad (r_w \leq r \leq r_f) \tag{3.2.2}$$

$$h_2(r, 0) = h_i \qquad (r_f \leq r \leq \infty) \tag{3.2.3}$$

$$-nk_1 bH \frac{\partial h_1}{\partial r} = Q \qquad (r = r_w). \tag{3.2.4}$$

For the continuity at the boundary of the inner and outer region, we have

$$h_1 = h_2 \qquad (r = r_f) \tag{3.2.5}$$

$$nk_1 b \frac{\partial h_1}{\partial r} = 2\pi r k_2 \frac{\partial h_2}{\partial r} \qquad (r = r_f). \tag{3.2.6}$$

The following dimensionless parameters are defined:

$$h_D = \frac{2\pi k_2 H (h_i - h)}{Q}, \tag{3.2.7a}$$

$$t_D = \frac{\alpha_2 t}{r_w^2} \cdot \frac{r_w^2}{r_f^2} = \frac{\alpha_2 t}{r_f^2} , \tag{3.2.7b}$$

$$r_D = \frac{r}{r_f} , \tag{3.2.7c}$$

$$r_c = \frac{r_w}{r_f} , \tag{3.2.7d}$$

$$\alpha_c = \frac{\alpha_1}{\alpha_2} , \tag{3.2.7e}$$

$$\beta = \frac{nbk_1}{2\pi r_f \, k_2} . \tag{3.2.7f}$$

Substituting into Eqs.(3.2.1a) and (3.2.1b) we obtain

$$\frac{\partial^2 h_{D_1}}{\partial r_D^2} = \frac{1}{\alpha_c} \frac{\partial h_{D_1}}{\partial t_D} \tag{3.2.8}$$

$$\frac{\partial^2 h_{D_2}}{\partial r_D^2} + \frac{1}{r_D} \frac{\partial h_{D_2}}{\partial r_D} = \frac{\partial h_{D_2}}{\partial t_D} . \tag{3.2.9}$$

In terms of the dimensionless parameters the initial and boundary conditions become

$$h_{D_1}(r_D , 0) = 0 \quad (r_c \leq r_D \leq 1) \tag{3.2.10}$$

$$h_{D_2}(r_D , 0) = 0 \quad (1 \leq r_D \leq \infty) \tag{3.2.11}$$

$$\frac{\partial h_{D_1}}{\partial r_D} = - \frac{1}{\beta} \quad (r_D = r_c) \tag{3.2.12}$$

$$h_{D_1} = h_{D_2} \quad (r_D = 1) \tag{3.2.13}$$

$$\frac{\partial h_{D_1}}{\partial r_D} = \frac{1}{\beta} \cdot \frac{\partial h_{D_2}}{\partial r_D} \qquad (r_D = 1) \tag{3.2.14}$$

3.2.2. Solutions

Laplace transforms can be used successfully to solve the equations simultaneously. The subsidiary equations are:

$$\frac{d^2\bar{h}_{D_1}}{dr_D^2} = \frac{p}{\alpha_c}\bar{h}_{D_1} \tag{3.2.15}$$

$$\frac{d^2\bar{h}_{D_2}}{dr_D^2} + \frac{1}{r_D} \cdot \frac{d\bar{h}_{D_2}}{dr_D} = p\bar{h}_{D_2} . \tag{3.2.16}$$

The transformed boundary conditions are

$$\frac{d\bar{h}_{D_1}}{dr_D} = -\frac{1}{\beta p} \qquad (r_D = r_c) \tag{3.2.17}$$

$$\bar{h}_{D_1} = \bar{h}_{D_2} \qquad (r_D = 1) \tag{3.2.18}$$

$$\frac{d\bar{h}_{D_1}}{dr_D} = \frac{1}{\beta}\frac{d\bar{h}_{D_2}}{dr_D} \qquad (r_D = 1) . \tag{3.2.19}$$

The general solutions for Eqs.(3.2.15) and (3.2.16) are of the form:

$$\bar{h}_{D_1} = \mathrm{A}\cosh(\sqrt{p/\alpha_c} \cdot r_D) + \mathrm{B}\sinh(\sqrt{p/\alpha_c} \cdot r_D) \tag{3.2.20}$$

$$\bar{h}_{D_2} = \mathrm{C}\, I_0(\sqrt{p} \cdot r_D) + \mathrm{D}\, K_0(\sqrt{p} \cdot r_D) \tag{3.2.21}$$

where I_0 and K_0 are modified bessel functions of zeroth order of the first and second kind, respectively. The coefficient C in Eq.(3.2.21) is found to be nil since we expect the solution to be bounded for $r_D \rightarrow \infty$. Eqs.(3.2.20) and

(3.2.21) are substituted into Eqs.(3.2.17), (3.2.18) and (3.2.19), and the following set of equations are obtained.

$$A\sqrt{p/\alpha_c}\sinh(\sqrt{p/\alpha_c}\cdot r_c) + B\sqrt{p/\alpha_c}\cosh(\sqrt{p/\alpha_c}\cdot r_c) = -\frac{1}{\beta p}$$

$$A\cosh\sqrt{p/\alpha_c} + B\sinh\sqrt{p/\alpha_c} = DK_0(\sqrt{p}) \tag{3.2.22}$$

$$A\sqrt{p/\alpha_c}\sinh\sqrt{p/\alpha_c} + B\sqrt{p/\alpha_c}\cosh\sqrt{p/\alpha_c} = -\frac{D}{\beta}\sqrt{p}K_1(\sqrt{p})$$

Eqs.(3.2.22) are solved for A,B and D.

$$A = \frac{\sqrt{\alpha_c}}{\beta p\sqrt{p}\,\Delta}\times$$

$$\times\left[\sqrt{\alpha_c}K_1(\sqrt{p})\sinh\sqrt{p/\alpha_c} + \beta K_0(\sqrt{p})\cosh\sqrt{p/\alpha_c}\right]$$

$$B = -\frac{\sqrt{\alpha_c}}{\beta p\sqrt{p}\,\Delta}\times \tag{3.2.23}$$

$$\times\left[\sqrt{\alpha_c}K_1(\sqrt{p})\cosh\sqrt{p/\alpha_c} + \beta K_0(\sqrt{p})\sinh\sqrt{p/\alpha_c}\right]$$

$$D = \frac{\sqrt{\alpha_c}}{p\sqrt{p}\,\Delta}$$

where

$$\Delta = \sqrt{\alpha_c}K_1(\sqrt{p})\cosh\left[\sqrt{p/\alpha_c}\cdot(1-r_c)\right] +$$

$$+\beta K_0(\sqrt{p})\sinh\left[\sqrt{p/\alpha_c}\cdot(1-r_c)\right]$$

Substituting A,B and D back into Eqs.(3.2.20) and (3.2.21), the solutions in the Laplace domain are obtained:

$$\bar{h}_{D_1} = \frac{\sqrt{\alpha_c}}{\beta p \sqrt{p}\ \Delta} \left\{ \sqrt{\alpha_c} K_1(\sqrt{p}\ ) \sinh \left[\sqrt{p/\alpha_c} \cdot (1-r_D) \right] + \right.$$

$$\left. + \beta K_0(\sqrt{p}\ ) \cosh \left[\sqrt{p/\alpha_c} \cdot (1-r_D) \right] \right\} \tag{3.2.24}$$

$$\bar{h}_{D_2} = \frac{\sqrt{\alpha_c}}{p \sqrt{p}\ \Delta} K_0(\sqrt{p}\ \cdot r_D) \tag{3.2.25}$$

Inversion of $\bar{h}_{D_1}$

Instead of attempting to invert $\bar{h}_{D_1}$ directly, we apply the Mellin's inversion theorem to $p\bar{h}_{D_1}$. The reason for this becomes clear when we try to evaluate the contour integral around the origin.

$$L^{-1}\{p\bar{h}_{D_1}\} = \frac{1}{2\pi i} \int_{\gamma - i\infty}^{\gamma + i\infty} p\bar{h}_{D_1} e^{pt_D}\, dp$$

$$= \frac{1}{2\pi i} \int_{\gamma - i\infty}^{\gamma + i\infty} \frac{\sqrt{\alpha_c}\, e^{pt_D}}{\beta\sqrt{p}\ \Delta} \left\{ \sqrt{\alpha_c} K_1(\sqrt{p}\ ) \sinh \left[\sqrt{p/\alpha_c} \cdot (1-r_D) \right] + \right.$$

$$\left. + \beta K_0(\sqrt{p}\ ) \cosh \left[\sqrt{p/\alpha_c} \cdot (1-r_D) \right] \right\} dp \tag{3.2.26}$$

The integrand has a branch point at $p = 0$. We consider the contour Γ in Figure 3.3. Since there are no singularities within Γ,

$$\oint_{\Gamma} = \int_A^B + \int_B^C + \int_C^D + \int_D^E + \int_E^F + \int_F^A = 0\ ,$$

so that

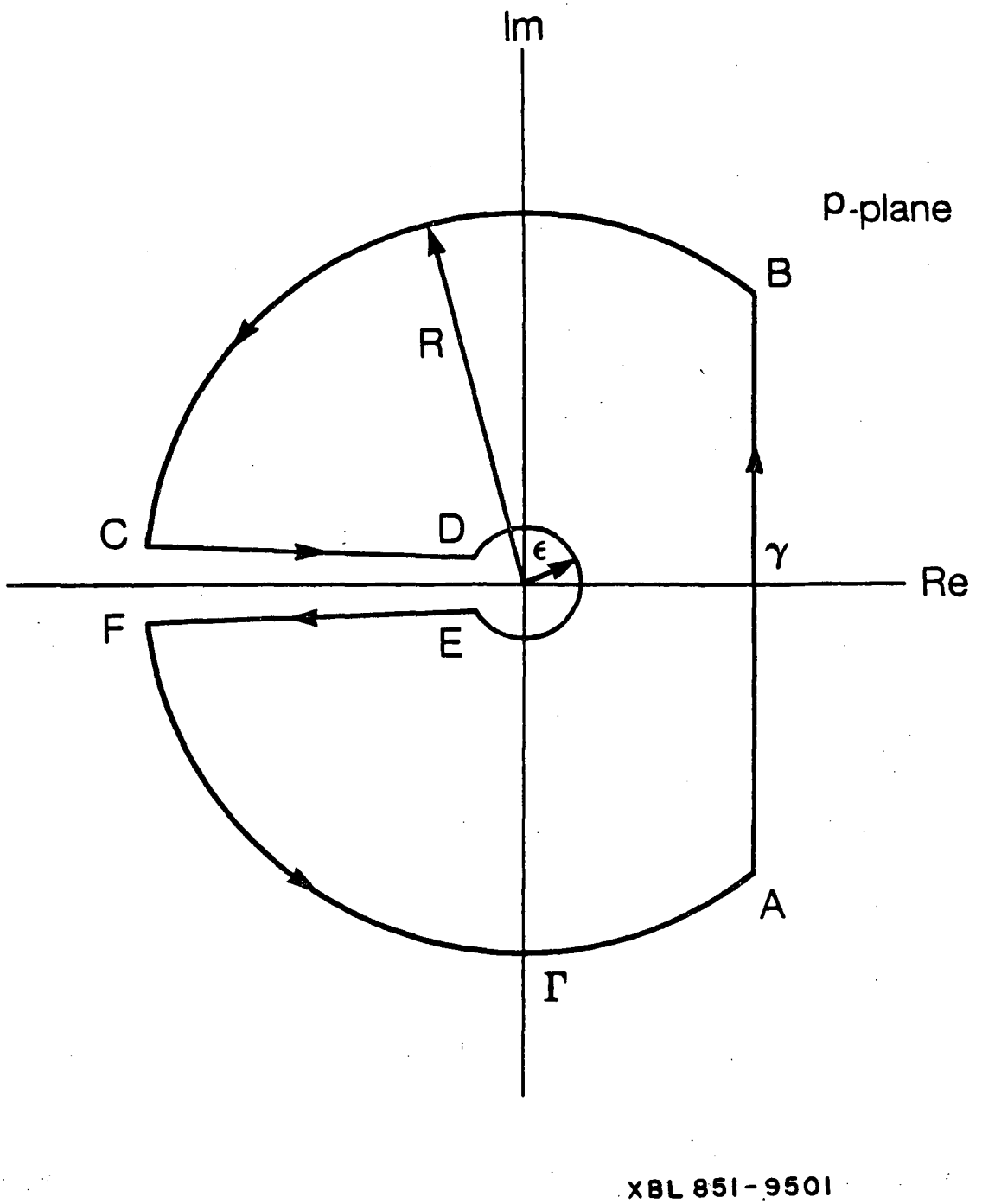

Figure 3.3 Contour path for Laplace inversion.

$$\int_A^B = -\left(\int_B^C + \int_C^D + \int_D^E + \int_E^F + \int_F^A \right).$$

Therefore,

$$L^{-1}\{p\bar{h}_{D_1}\} = \lim_{\substack{R \to \infty \\ \epsilon \to 0}} \frac{1}{2\pi i} \int_A^B$$

$$= -\frac{1}{2\pi i} \lim_{\substack{R \to \infty \\ \epsilon \to 0}} \left(\int_B^C + \int_C^D + \int_D^E + \int_E^F + \int_F^A \right),$$

where R is the radius of the outer circle and ϵ the radius of the inner. It can be shown that

$$\lim_{R \to \infty} \int_B^C = \lim_{R \to \infty} \int_F^A = 0 .$$

Also, by letting $p = \epsilon e^{i\theta}$ and taking the limit as $\epsilon \to 0$,

$$\lim_{\epsilon \to 0} \int_D^E = 0 .$$

The proof for this can be found in Appendix A. Here, it becomes clear why we chose to invert ph_{D_1} instead of h_{D_1}. Had we chosen to invert h_{D_1}, the integral $\lim_{\epsilon \to 0} \int_D^E$ would have become unbounded and therefore the inversion procedure would have failed.

On CD, let $p = \mu^2 e^{i\pi}$ and on EF let $p = \mu^2 e^{-i\pi}$ and using the identity,

$$K_\nu(ze^{\pm\frac{1}{2}\pi i}) = \pm\frac{1}{2}\pi i e^{\pm\frac{1}{2}\nu\pi i}\left[-J_\nu(z) \pm iY_\nu(z)\right],$$

we obtain

$$\frac{1}{2\pi i}\lim_{\substack{R\to\infty\\ \epsilon\to 0}}\int_C^D = \frac{\sqrt{\alpha_c}}{\beta\pi i}\int_0^\infty e^{-\mu^2 t_D}\frac{\Lambda + i\Omega}{\Psi + i\Theta}d\mu$$

$$\frac{1}{2\pi i}\lim_{\substack{R\to\infty\\ \epsilon\to 0}}\int_E^F = \frac{\sqrt{\alpha_c}}{\beta\pi i}\int_0^\infty e^{-\mu^2 t_D}\frac{-\Lambda + i\Omega}{-\Psi + i\Theta}d\mu \quad ,$$

where

$$\Lambda = -\sqrt{\alpha_c}\,J_1(\mu)\sin\left(\frac{1-r_D}{\sqrt{\alpha_c}}\mu\right) - \beta J_0(\mu)\cos\left(\frac{1-r_D}{\sqrt{\alpha_c}}\mu\right) \tag{3.2.27a}$$

$$\Omega = \sqrt{\alpha_c}\,Y_1(\mu)\sin\left(\frac{1-r_D}{\sqrt{\alpha_c}}\mu\right) + \beta Y_0(\mu)\cos\left(\frac{1-r_D}{\sqrt{\alpha_c}}\mu\right) \tag{3.2.27b}$$

$$\Psi = -\sqrt{\alpha_c}\,J_1(\mu)\cos\left(\frac{1-r_c}{\sqrt{\alpha_c}}\mu\right) + \beta J_0(\mu)\sin\left(\frac{1-r_c}{\sqrt{\alpha_c}}\mu\right) \tag{3.2.27c}$$

$$\Theta = \sqrt{\alpha_c}\,Y_1(\mu)\cos\left(\frac{1-r_c}{\sqrt{\alpha_c}}\mu\right) - \beta Y_0(\mu)\sin\left(\frac{1-r_c}{\sqrt{\alpha_c}}\mu\right) \tag{3.2.27d}$$

Therefore

$$L^{-1}\{p\bar{h}_{D_1}\} = -\frac{1}{2\pi i}\lim_{\substack{R\to\infty\\ \epsilon\to 0}}\left(\int_C^D + \int_E^F\right)$$

$$= \frac{2\sqrt{\alpha_c}}{\pi\beta}\int_0^\infty e^{-\mu^2 t_D}\frac{\Lambda\cdot\Theta - \Omega\cdot\Psi}{\Psi^2 + \Theta^2}d\mu\,.$$

Simplifying and using the recurrence formula;

$$J_\nu(z)Y_\nu'(z) - Y_\nu(z)J_\nu'(z) = \frac{2}{\pi z},$$

we get:

$$L^{-1}\{p\bar{h}_{D_1}\} = \frac{4\alpha_c}{\pi^2}\int_0^\infty \frac{e^{-\mu^2 t_D}}{\mu} \cdot \frac{\cos\left(\frac{r_D - r_c}{\sqrt{\alpha_c}}\mu\right)}{\Psi^2 + \Theta^2} d\mu$$

Finally, by the convolution theorem we obtain

$$h_{D_1} = \frac{4\alpha_c}{\pi^2}\int_0^{t_D}\int_0^\infty \frac{e^{-\mu^2\tau}}{\mu} \cdot \frac{\cos\left(\frac{r_D - r_c}{\sqrt{\alpha_c}}\mu\right)}{\Psi^2 + \Theta^2} d\mu d\tau$$

$$= \frac{4\alpha_c}{\pi^2}\int_0^\infty \frac{1 - e^{-\mu^2 t_D}}{\mu^3} \cdot \frac{\cos\left(\frac{r_D - r_c}{\sqrt{\alpha_c}}\mu\right)}{\Psi^2 + \Theta^2} d\mu$$

$$(r_c \leq r_D \leq 1) \qquad (3.2.28)$$

Equation 3.2.28 can be used to evaluate dimensionless pressure drops h_{D_1} and h_{D_2} at r_D as a function of t_D for a given set of the parameters α_c, β and r_c. Figures 3.4a-f present several log-log plots of h_{D_1} vs. t_D at $r_D = r_c = 0.01$ for ranges of α_c and β. All of the curves have a characteristic initial half-slope straight line portion, which is evidence of linear flow.

For large β, the curves have a transitional unit slope. This is because the higher permeability inner region is drained much more quickly than the

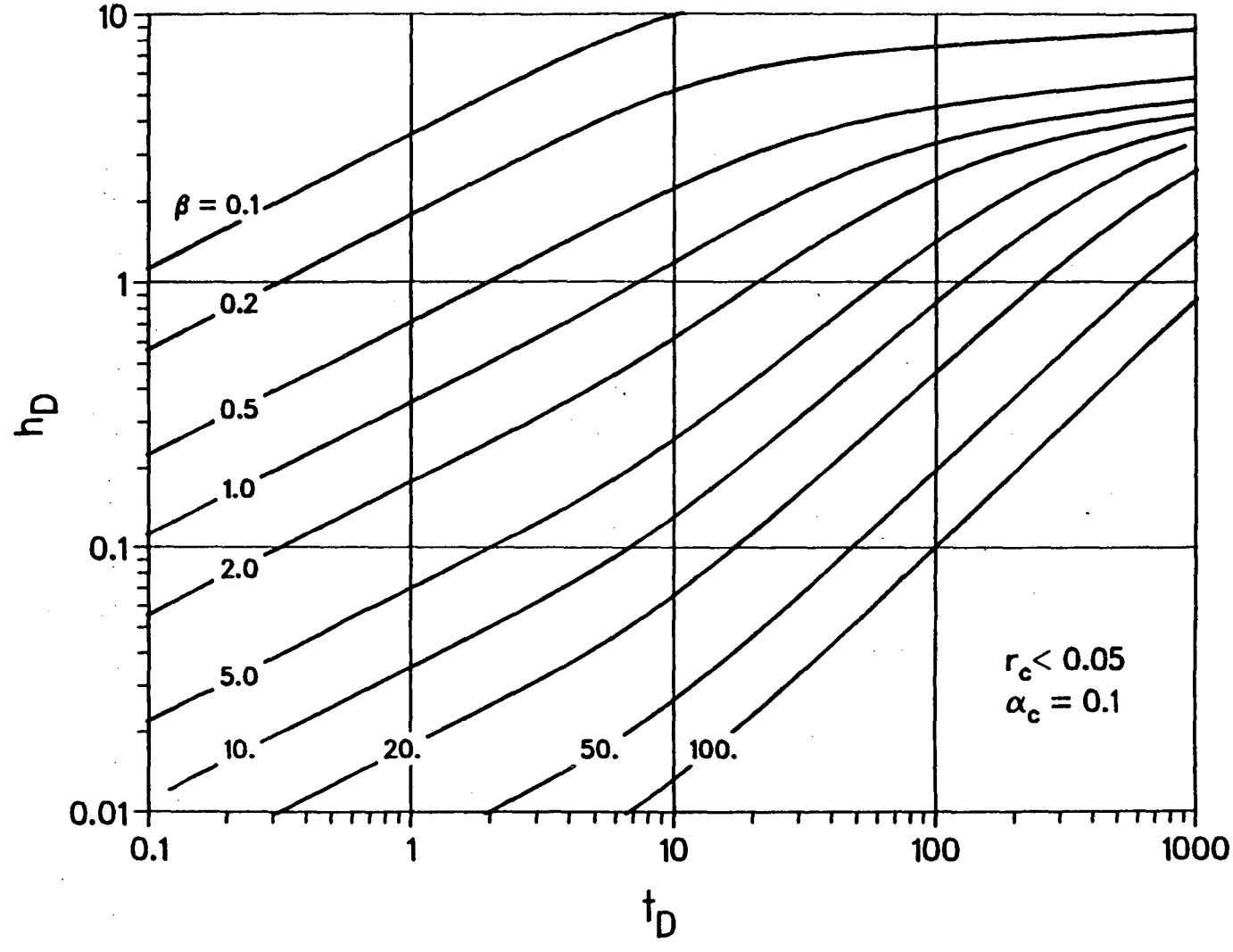

XBL 856-2923A

Figure 3.4a Dimensionless pressure for r_c <0.05 and α_c =0.1.

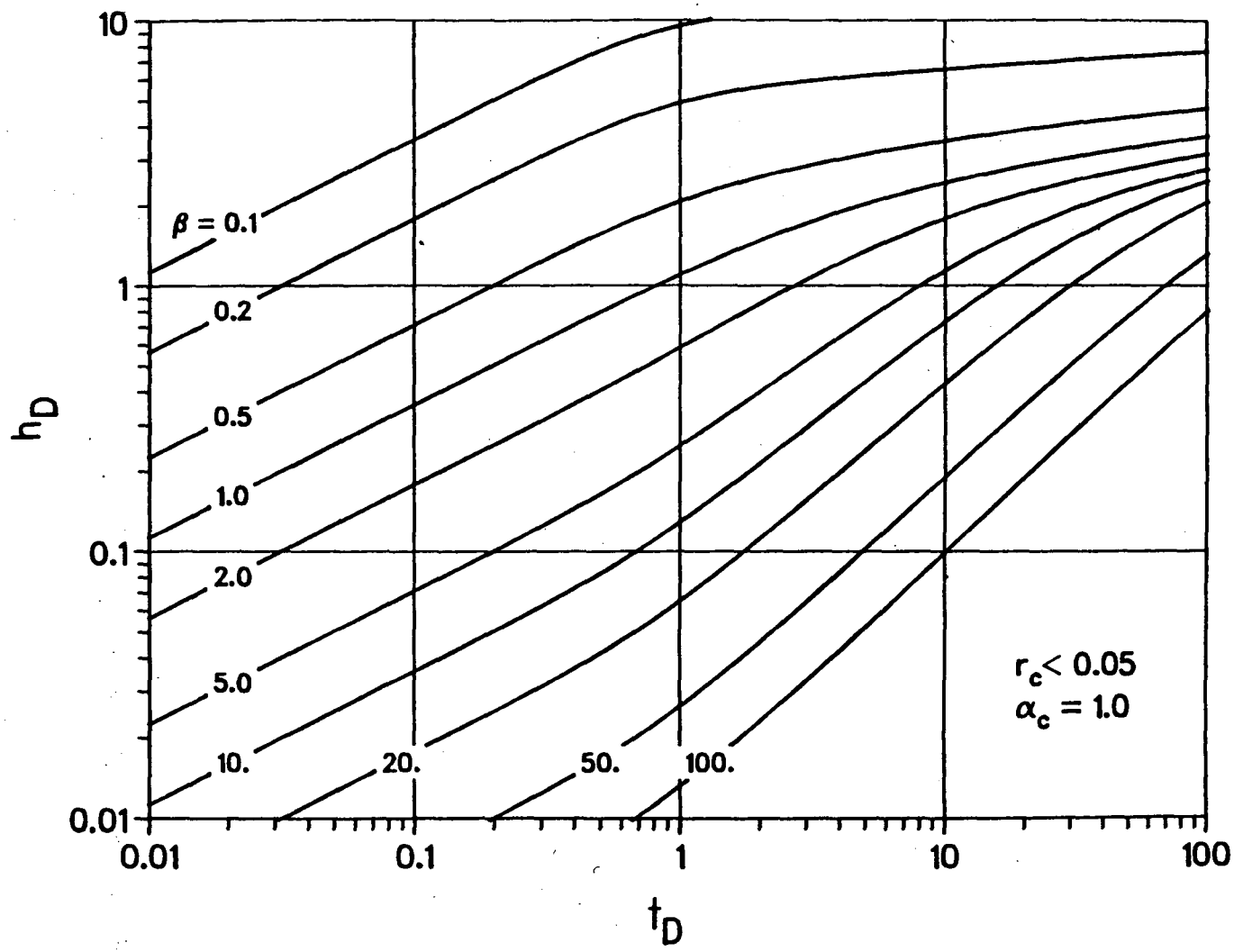

XBL 856-2924A

Figure 3.4b Dimensionless pressure for r_c <0.05 and α_c =1.0.

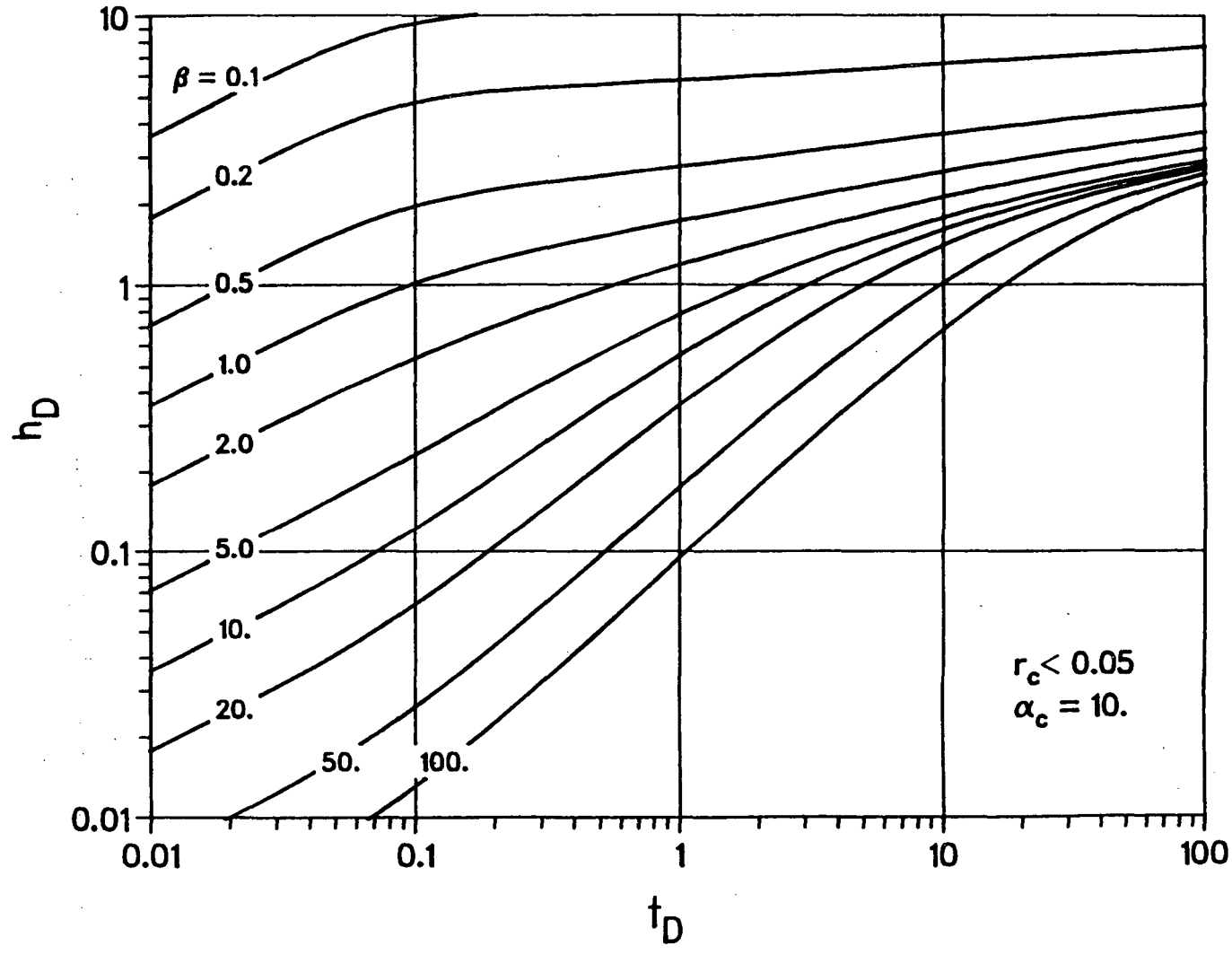

Figure 3.4c Dimensionless pressure for $r_c < 0.05$ and $\alpha_c = 10$.

XBL 856-2925A

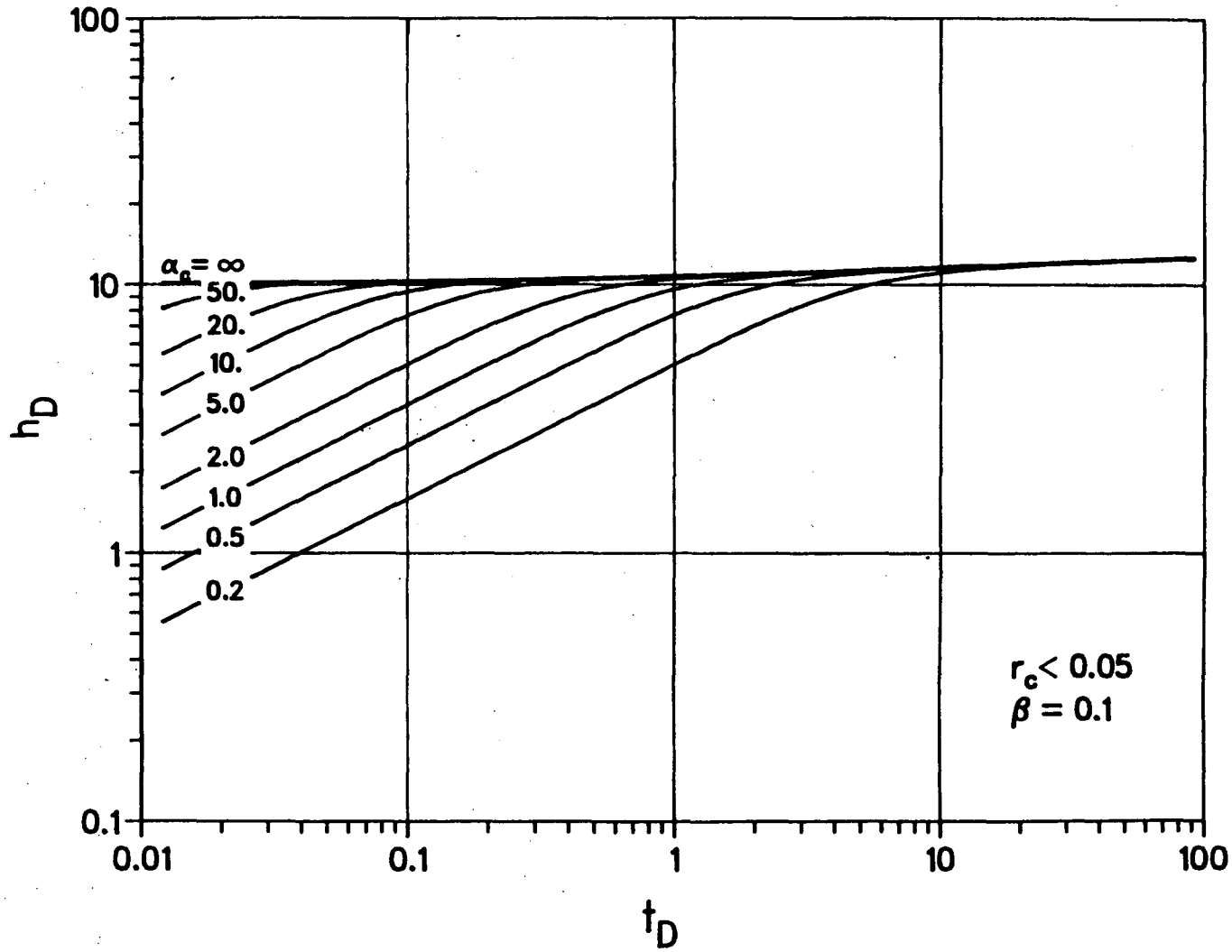

Figure 3.4d Dimensionless pressure for $r_c < 0.05$ and $\beta = 0.1$.

XBL 856-2920A

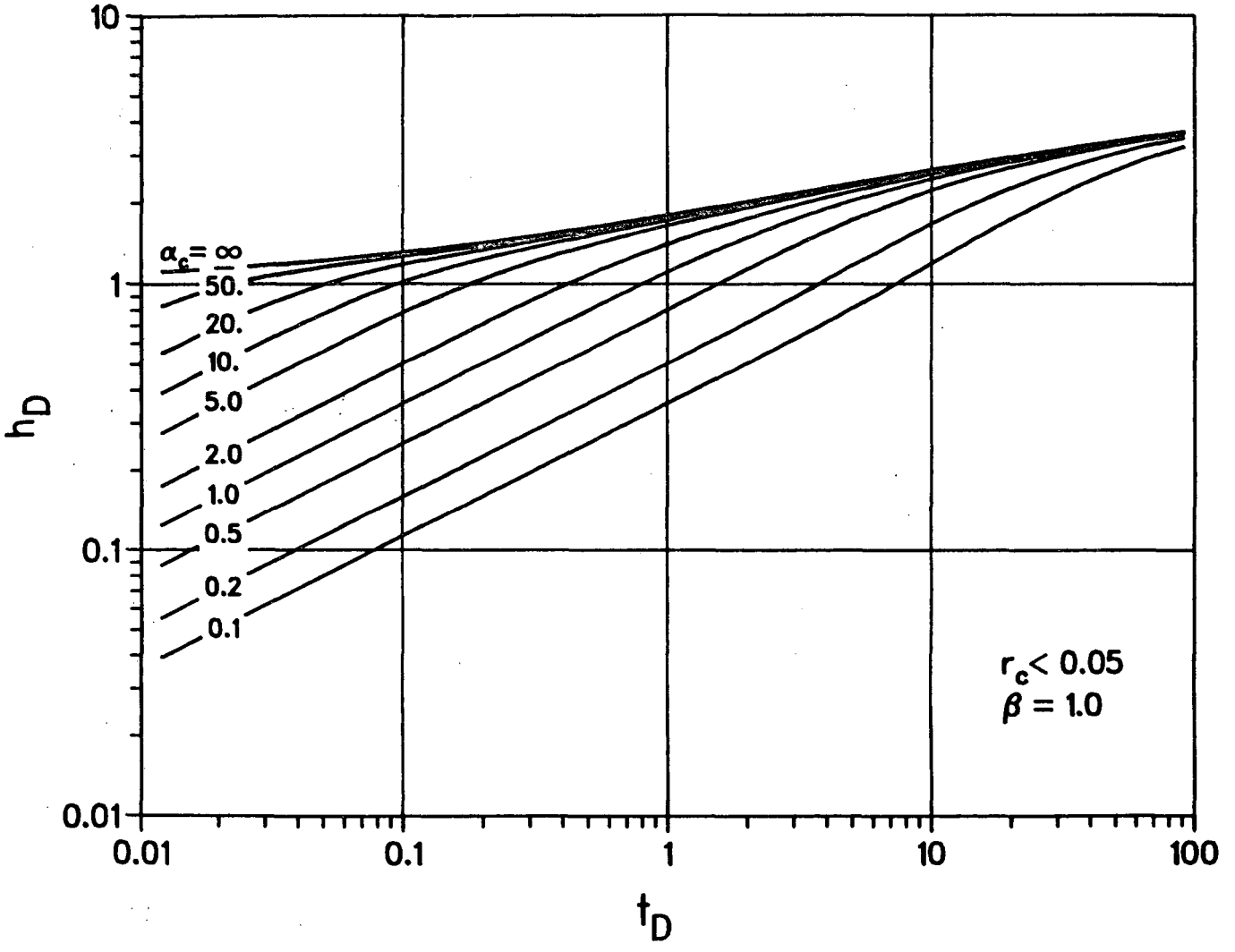

Figure 3.4e Dimensionless pressure for $r_c < 0.05$ and $\beta = 1.0$. XBL 856-2921A

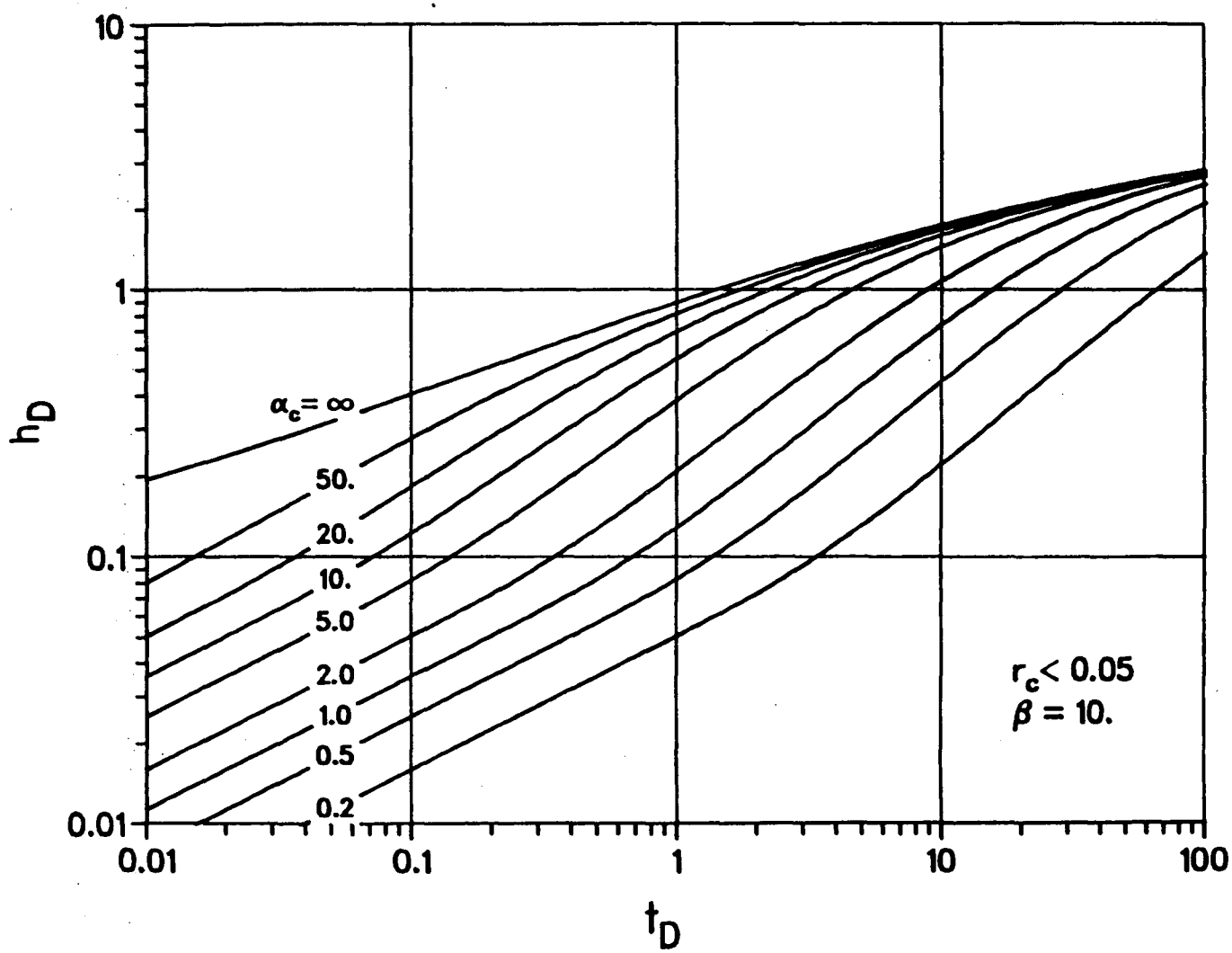

Figure 3.4f Dimensionless pressure for $r_c < 0.05$ and $\beta = 10$. XBL 856-2922A

outer region's capability to supply fluid. Consequently, the drawdown curves exhibit the characteristics of a no flow boundary. Usual curve matching techniques can be used to analyze well test data with such characteristics. However, because the shapes of some of the curves are similar to each other, it may be difficult to find a unique match especially when a long span of data is unavailable. However, if a unique match of the data to one of the curves generated by Equation 3.2.28 can be found, α_c , β and r_c can be determined. The match of pressure and time yields two more equations, Equation 3.2.7a and 3.2.7b, respectively, from which k_2H and $S_{s_2}Hr_f^2$ can be obtained. Using Equations 3.2.7a through 3.2.7f, the unknowns r_f , S_{s_2}, nbk_1 and nbS_{s_1} can all be calculated.

In Figure 3.5, h_{D_1} has been evaluated using Equation 3.2.28 for various values of r_c with α_c=1.0 and β=1.0. Note that when $r_c = 1.0$, which means no fractures are present, the curve is identical to that of the van Everdingen and Hurst (1949) solution for a finite radius well in an infinite medium. As can be seen in Figure 3.5, h_{D_1} is not very sensitive to r_c when $r_c < 0.1$. Therefore, it will be very difficult to determine r_c directly from the match if $r_c = r_w/r_f < 0.1$. That is if the well radius is small compared to the fracture intersecting the well. This is very unfortunate because there will then be only four equations left to analyze. In such a case, either nbS_{s_1}, nbk_1, S_{s_2}, or r_f must be estimated a priori in order to determine the rest of the parameters.

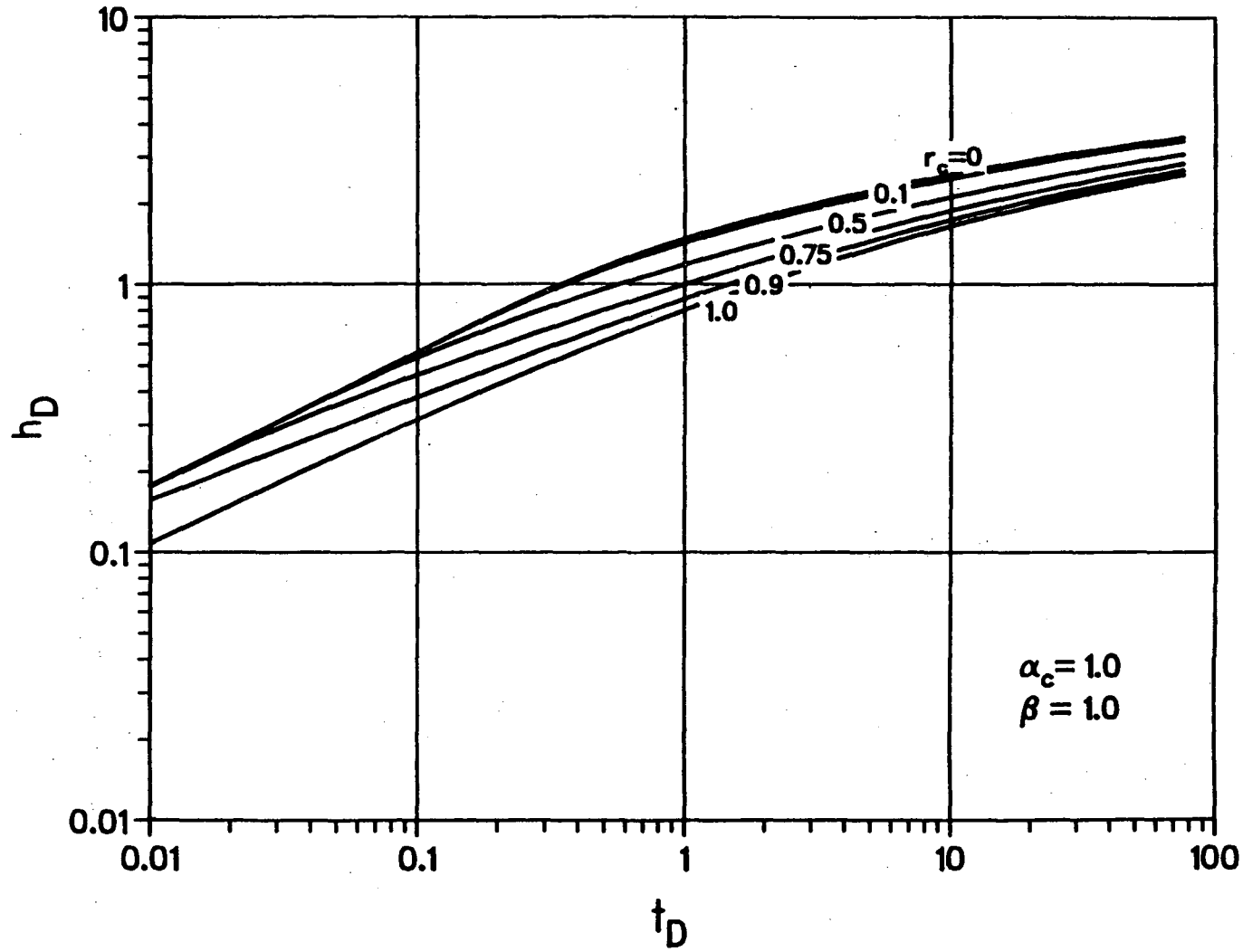

Figure 3.5 Dimensionless pressure for $\alpha_c = 1.0$ and $\beta = 1.0$.

XBL 856-2926A

Large Time Solution for Region 1

For small values of z,

$$K_0(z) \approx -\ln\frac{Ez}{2} - \frac{z^2}{4}\cdot\left(\ln\frac{Ez}{2} - 1\right) + \cdots$$

$$\approx = -\gamma - \ln\frac{z}{2} \tag{3.2.29a}$$

$$K_1(z) \approx \frac{1}{z} + \frac{z}{2}\cdot\left(\ln\frac{Ez}{2} - \frac{1}{2}\right) + \cdots \tag{3.2.29b}$$

$$\cosh z \approx 1 + \frac{z^2}{2} + \cdots \tag{3.2.29c}$$

$$\sinh z \approx z + \frac{z^3}{6} + \cdots \tag{3.2.29d}$$

where $\ln E = \gamma = 0.577215665$ (Euler's constant). Substituing Eq.(3.2.29) into (3.2.24) and rearranging,

$$\bar{h}_{D_1} \approx \frac{1}{p}\left\{\frac{1-r_D}{\beta} - \ln\frac{E\sqrt{p}}{2} + \right.$$

$$\left. + \left[\frac{1-r_D}{\beta} - \frac{1}{2} - \frac{(1-r_D)^2}{\alpha_c}\right]\cdot\frac{p}{2}\cdot\ln\frac{E\sqrt{p}}{2} + \cdots\right\}\times$$

$$\times\left\{1 + p\cdot\left[\frac{1}{2} - \frac{\beta(1-r_c)}{\alpha_c}\right]\cdot\ln\frac{E\sqrt{p}}{2} + \cdots\right\}^{-1}$$

$$\approx \frac{1}{p}\cdot\left\{\frac{1-r_D}{\beta} - \ln\frac{E\sqrt{p}}{2} + \right.$$

$$\left. + p\cdot\left[\frac{1}{2} - \frac{\beta(1-r_c)}{\alpha_c}\right]\cdot\left(\ln\frac{E\sqrt{p}}{2}\right)^2 + \cdots\right\}$$

so that

$$h_{D_1} = L^{-1}\{\bar{h}_{D_1}\}$$

$$\approx \frac{1 - r_D}{\beta} + \frac{1}{2} \cdot \left\{1 + \frac{1}{t_D} \cdot [\frac{1}{2} - \frac{\beta(1 - r_c)}{\alpha_c}]\right\} \times (-\gamma + \ln 4t_D) + \cdots$$

$$\approx \frac{1 - r_D}{\beta} + \frac{1}{2} \cdot (-\gamma + \ln 4t_D) \tag{3.2.30}$$

Therefore, an approximate solution for large time in Region 1 at $r_D = r_c$, i.e., at the wellbore, can be expressed as:

$$h_{D_1} \approx \frac{1 - r_c}{\beta} + \frac{1}{2} \cdot (\ln t_D + 0.80907) . \tag{3.2.31}$$

It is interesting to note that for the particular case of $\beta = 1$ and $r_c << 1$, Equation 3.2.31 becomes identical to that of Gringarten's uniform flux solution for large time:

$$h_{D_1} \approx \frac{1}{2} \cdot (\ln t_{Dxf} + 2.80907) , \tag{3.2.32}$$

Equation 3.2.30 shows that for large t_D, h_{D_1} can be approximated by a logarithmic function of t_D. The lower limit of t_D for which this approximation is valid is a function of β, α, and r_c as can be seen in the derivation of Equation 3.2.30. Recall that

$$t_D = \frac{\alpha_2 t}{r_w^2} \cdot \frac{r_w^2}{r_f^2} . \tag{3.2.7b}$$

Therefore, on a semi-log graph, Equation 3.2.30 would be a straight line

identical to the solution for a homogeneous porous medium except for the pseudo-skin factor:

$$s_f = \frac{(1 - r_w/r_f)}{\beta} + \ln\frac{r_w}{r_f} \quad . \tag{3.2.33}$$

The apparent wellbore radius can then be defined as:

$$r_w' = r_w \cdot e^{-s_f} = r_f \cdot e^{-\frac{(1 - r_w/r_f)}{\beta}} \quad . \tag{3.2.34}$$

Therefore, k_2H can be obtained in the usual manner, i.e., from the slope of the straight line on a semi-log plot, but the calculation of the storage coefficient in such manner, i.e., from the intersect on the time axis, will result in an incorrect value of that parameter by a factor given by

$$\frac{S_{s_2}^*}{S_{s_2}} = \frac{r_f^2}{r_w^2}\exp\left[-\frac{2(1 - r_w/r_f)}{\beta}\right] . \tag{3.2.35}$$

where $S_{s_2}^*$ is the storage coefficient obtained in the conventional manner. Equation 3.2.35 can be used to check the curve match results if the test is run long enough for the data to exhibit a straight line on a semilog plot. Because s_f is a function of the dimensionless conductivity (β) and the dimensionless wellbore radius (r_c), which is related to the fracture spacing, s_f may be used as a parameter to characterize the natural fracture system.

Small Time Solution for Region 1

Remembering for small z,

$$K_\nu(z) = \left(\frac{\pi}{2z}\right)^{1/2} \cdot e^{-z} \cdot \left\{1 + \frac{4\nu^2 - 1}{8z} + O\left(\frac{1}{z^2}\right)\right\}$$

Since $r_c < 1$,

$$\bar{h}_{D_1} \approx \frac{\sqrt{\alpha_c} \cdot e^{-\sqrt{p/\alpha_c}(r_D - r_c)}}{\beta p \sqrt{p}} \times$$

$$\times \left[1 - \frac{\sqrt{\alpha_c} - \beta}{\sqrt{\alpha_c} + \beta} \left(e^{-2\sqrt{p/\alpha_c}(1 - r_D)} + e^{-2\sqrt{p/\alpha_c}(1 - r_c)} \right) + \cdots \right]$$

Then at the pumping well, $r_D = r_c$, the inverse Laplace transform of $\bar{h}_{D_1}$ is,

$$h_{D_1} = L^{-1}\{\bar{h}_{D_1}\}$$

$$\approx \frac{2\sqrt{\alpha_c}}{\sqrt{\pi}\beta} \cdot \sqrt{t_D} \cdot \left[1 - 2 \cdot \frac{\sqrt{\alpha_c} - \beta}{\sqrt{\alpha_c} + \beta} \cdot e^{-(1 - r_c)^2/\alpha_c t_D} \right] +$$

$$+ \frac{4}{\beta} \frac{\sqrt{\alpha_c} - \beta}{\sqrt{\alpha_c} + \beta} \cdot (1 - r_c) \cdot erfc \frac{1 - r_c}{\sqrt{\alpha_c t_D}} + \cdots \qquad (3.2.36)$$

Thererfore, the small time approximate solution for Region 1 is:

$$h_{D_1} \approx \frac{2\sqrt{\alpha_c}}{\sqrt{\pi}\beta} \cdot \sqrt{t_D} \quad . \qquad (3.2.37)$$

From Equation 3.2.37 it is apparent that for small t_D, h_{D_1} will exhibit a half slope straight line on a log-log plot. Equation 3.2.37 is identical to the dimensionless pressure response during the fracture linear flow period of the finite conductivity vertical fracture solution by Cinco-Ley and Samaniego-V (1981) except for the difference in notation. If the definitions of the dimensionless terms from Equations 3.2.7a through 3.2.7f are substituted into Equation 3.2.37, one obtains:

$$(h_i - h_{wf})_{t=t_0} = \frac{2Q\sqrt{t_0}}{nbH\sqrt{\pi k_1 S_{s_1}}} \quad . \qquad (3.2.38)$$

From a log-log plot of field data, one can determine $(h_i - h_{wf})$ at any arbitrary time, t_0, from the straight line portion or an extrapolation of this line. Equation 3.2.38 can be used to find $nb\sqrt{k_1 S_{s_1}}$. If nbk_1 and nbS_{s_1} are already known from curve matching, Equation 3.2.38 can then be used to check the results.

The small time approximate solution for the uniform flux solution is (Gringarten et al., 1972; Gringarten and Ramey, 1974):

$$h_D \approx \sqrt{\pi t_{Dxf}} \quad . \tag{3.2.39}$$

Thus, Equation 3.2.37 becomes identical to Equation 3.2.39 when $\frac{\sqrt{\alpha_c}}{\beta} = \frac{\pi}{2}$. Figure 3.6 illustrates the striking similarity between the uniform flux solution and the solution given by Equation 3.2.28 for $\alpha_c = \frac{\pi^2}{4} = 2.47$ and $\beta = 1$. The two curves are practically indistinguishable. The uniform flux solution provides information about fracture length, but not the parameters of the fracture.

Inversion of $\bar{h}_{D_2}$

It now remains to invert $\bar{h}_{D_2}$ to real space:

$$L^{-1}\{p\bar{h}_{D_2}\} = -\frac{2\sqrt{\alpha_c}}{\pi\beta}\int_0^\infty e^{-\mu^2 t_D}\,\frac{\Theta \cdot J_0(\mu r_D) + \Psi \cdot Y_0(\mu r_D)}{\Psi^2 + \Theta^2}\,d\mu \; .$$

So that

$$h_{D_2} = -\frac{2\sqrt{\alpha_c}}{\pi}\int_0^\infty \frac{1 - e^{-\mu^2 t_D}}{\mu^2} \cdot \frac{\Theta \cdot J_0(\mu r_D) + \Psi \cdot Y_0(\mu r_D)}{\Psi^2 + \Theta^2}\,d\mu$$

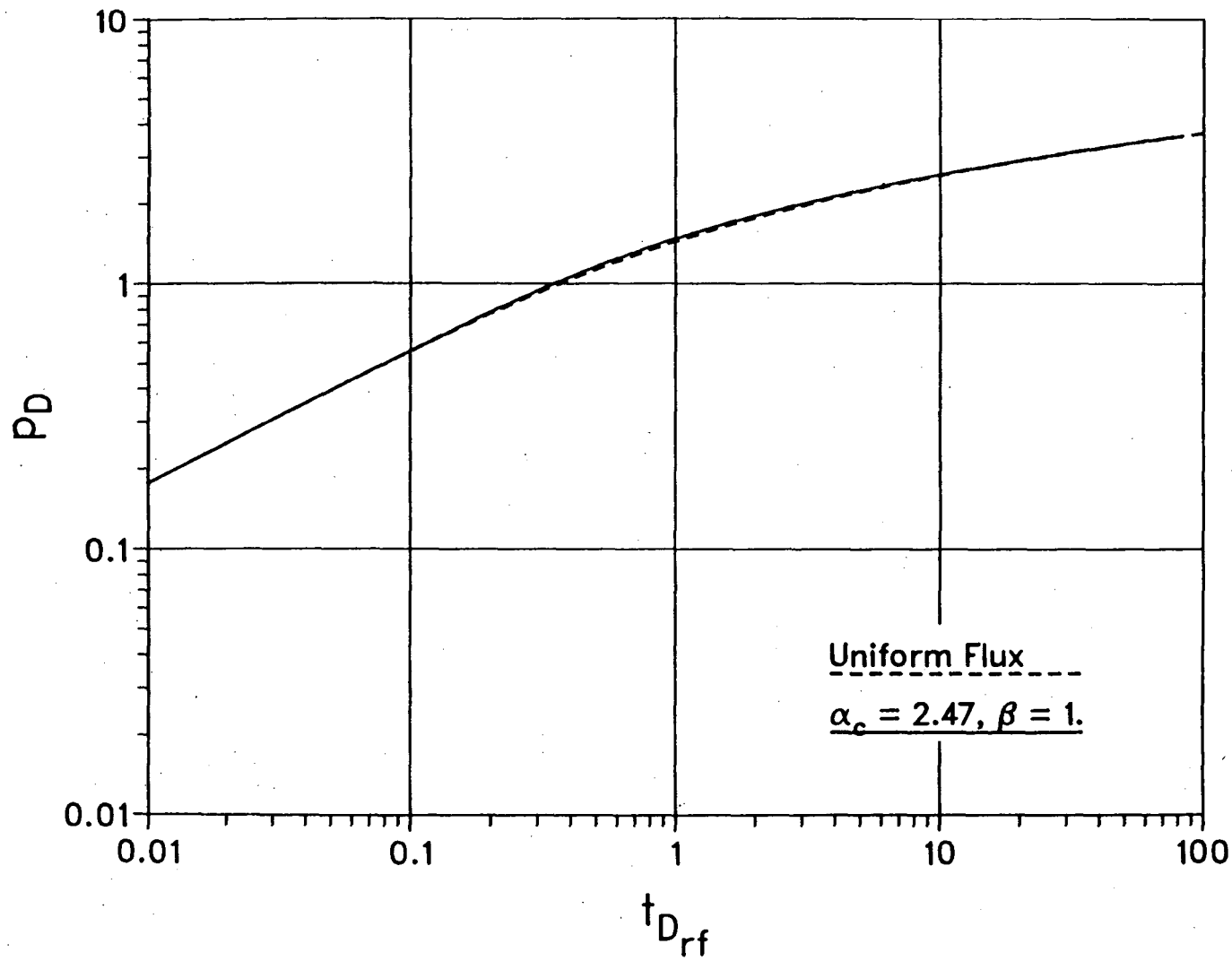

XBL 856-2927

Figure 3.6 Comparison between linear-radial and uniform flux solution.

$$(r_D \geq 1) \ , \tag{3.2.40}$$

where Ψ and Θ are given by Eq.(3.2.27c) and (3.2.27d), respectively.

Large Time Solution for Region 2

Substituting Eqs.(3.2.29) into Eq.(3.2.25),

$$\bar{h}_{D_2} \approx \frac{1}{p}\left\{ -\ln\frac{E\sqrt{p}\,r_D}{2} + \right.$$

$$\left. + p\left[\frac{1}{2} - \frac{\beta(1-r_c)}{\alpha_c}\right] \cdot \ln\frac{E\sqrt{p}\,r_D}{2} \cdot \ln\frac{E\sqrt{p}}{2} + \cdots \right\}$$

Then,

$$h_{D_2} \approx \frac{1}{2}\left\{ 1 + \left[\frac{1}{2} - \frac{\beta(1-r_c)}{\alpha_c}\right]\frac{r_D^2}{t_D} \right\}\left(-\gamma + \ln\frac{4t_D}{r_D^2} \right) + \cdots$$

$$\approx \frac{1}{2}\left(-\gamma + \ln\frac{4t_D}{r_D^2} \right) \tag{3.2.41}$$

It can be readily seen from Equation 3.2.41 that at a large value of time the effect of the inner region is negligible in the outer region. Equation 3.2.41 is identical to the large time solution for a homogeneous medium.

Small Time Solution for Region 2

For large p , noting that $r_c < 1$, Eq3.2.25 becomes

$$\bar{h}_{D_2} \approx \frac{2\sqrt{\alpha_c}}{\sqrt{\alpha_c} + \beta} \cdot \frac{e^{-\sqrt{p/\alpha_c}(1-r_c)}}{p\sqrt{p}} + \cdots ,$$

and now inverting $\bar{h}_{D_2}$, we have:

$$h_{D_2} \approx \frac{2\sqrt{\alpha_c}}{\sqrt{\alpha_c} + \beta} \times$$

$$\times \left[2\left(\frac{t_D}{\pi}\right)^{1/2} e^{-(1-r_c)^2/\alpha_c t_D} - \frac{1-r_c}{\sqrt{\alpha_c}} erfc \frac{1-r_c}{2\sqrt{\alpha_c t_D}} + \cdots \right] \quad (3.2.42)$$

This completes the large and small time solutions.

3.2.3. Example Applications

Two examples are presented to illustrate the application of this work. The first example is a pressure buildup after a long production period and the second example is a pressure falloff after a long injection period. Because the production time and the injection period were sufficiently large, both can be analyzed with the type curves by plotting the pressure difference between flowing bottom-hole pressure and the shut-in bottom-hole pressure, vs shut-in time, Δt. Note that $p = \rho g h$ neglecting the gravity effect.

Example 1

The field data for this example are taken from Gringarten et al. (1972). The reservoir and the build-up data are given in Table 3.1. The match in Gringarten et al. (1972) is shown in Figure 3.7. Using the current solution a slightly better match is obtained for the last three data points (Figure 3.8). Unfortunately, the match for α_c is non-unique and therefore the results shown here are somewhat arbitrary.

Table 3.1 Reservoir and Buildup data for Example 1.

Reservoir Data	
q_o =	5.06×10^{-3} m^3/s
μ_o =	2.3×10^{-4} Pa·s
ϕ =	30 %
c_t =	4.35×10^{-9} Pa^{-1}
H =	70.1 m
B_o =	1.76 RES m^3/ST m^3

Buidup Data	
Δt (sec)	$p_{ws} - p_{wf}$ (MPa)
0.300E+03	0.2137
0.600E+03	0.2965
0.900E+03	0.3723
0.120E+04	0.4551
0.150E+04	0.4551
0.180E+04	0.4964
0.210E+04	0.5378
0.240E+04	0.5723
0.270E+04	0.6137
0.300E+04	0.6895
0.330E+04	0.6895
0.360E+04	0.6895
0.450E+04	0.7860
0.720E+04	0.9377
0.900E+04	1.096
0.144E+05	1.248
0.171E+05	1.420
0.288E+05	1.503

The pressure match point for $p_D = 1$ is $\Delta p = 5.7 \times 10^5$ Pa. Using Equation 3.2.7a and $k = \frac{\tilde{k}\,\rho g}{\mu}$,

$$\tilde{k}_2 = \frac{(5.06 \times 10^{-3}) \cdot (1.76) \cdot (2.3 \times 10^{-4}) \cdot (1)}{2\pi \cdot (7.01 \times 10^1) \cdot (5.7 \times 10^5)}$$

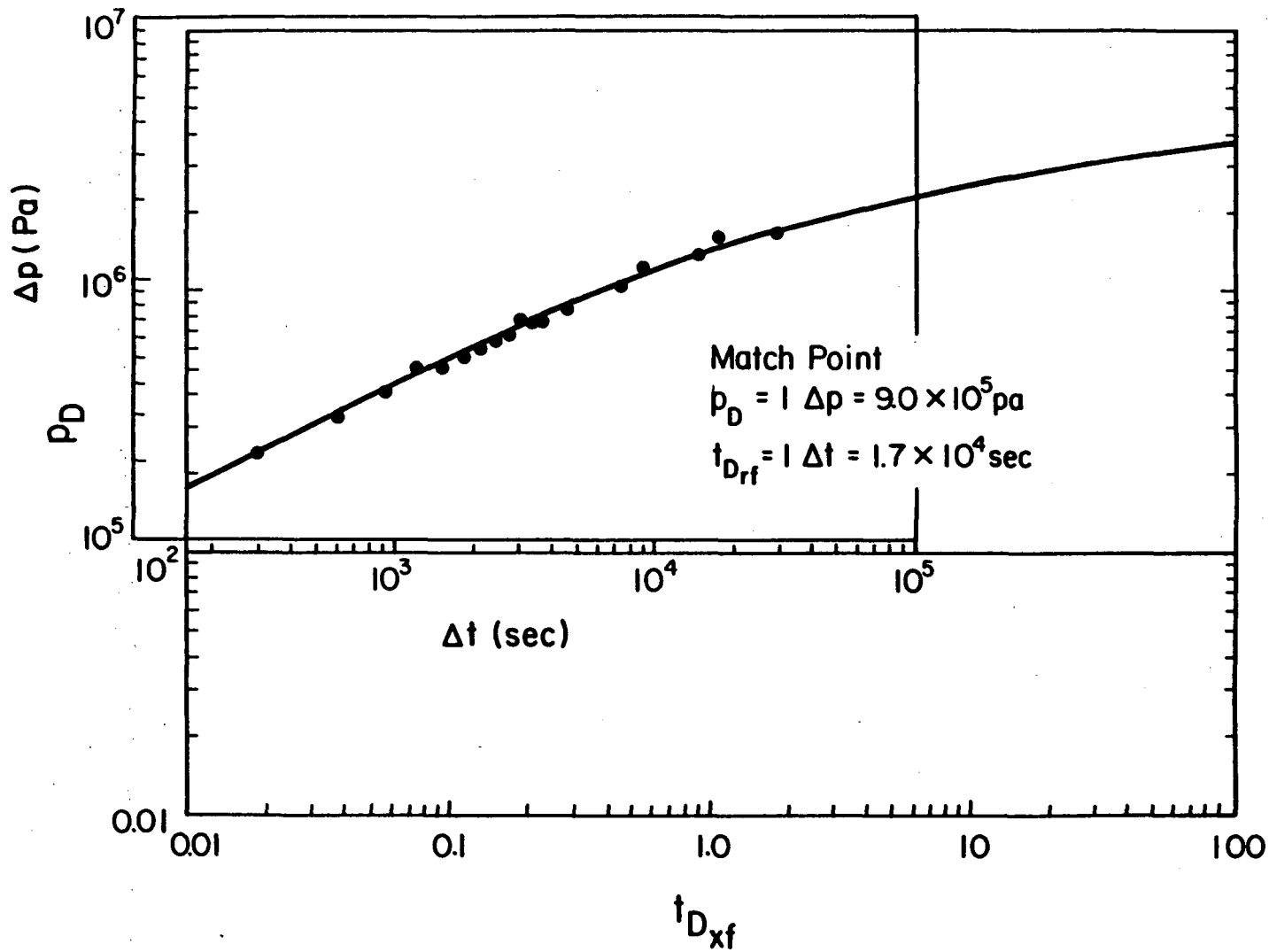

Figure 3.7 Type curve matching with uniform flux solution. XBL 856-10590

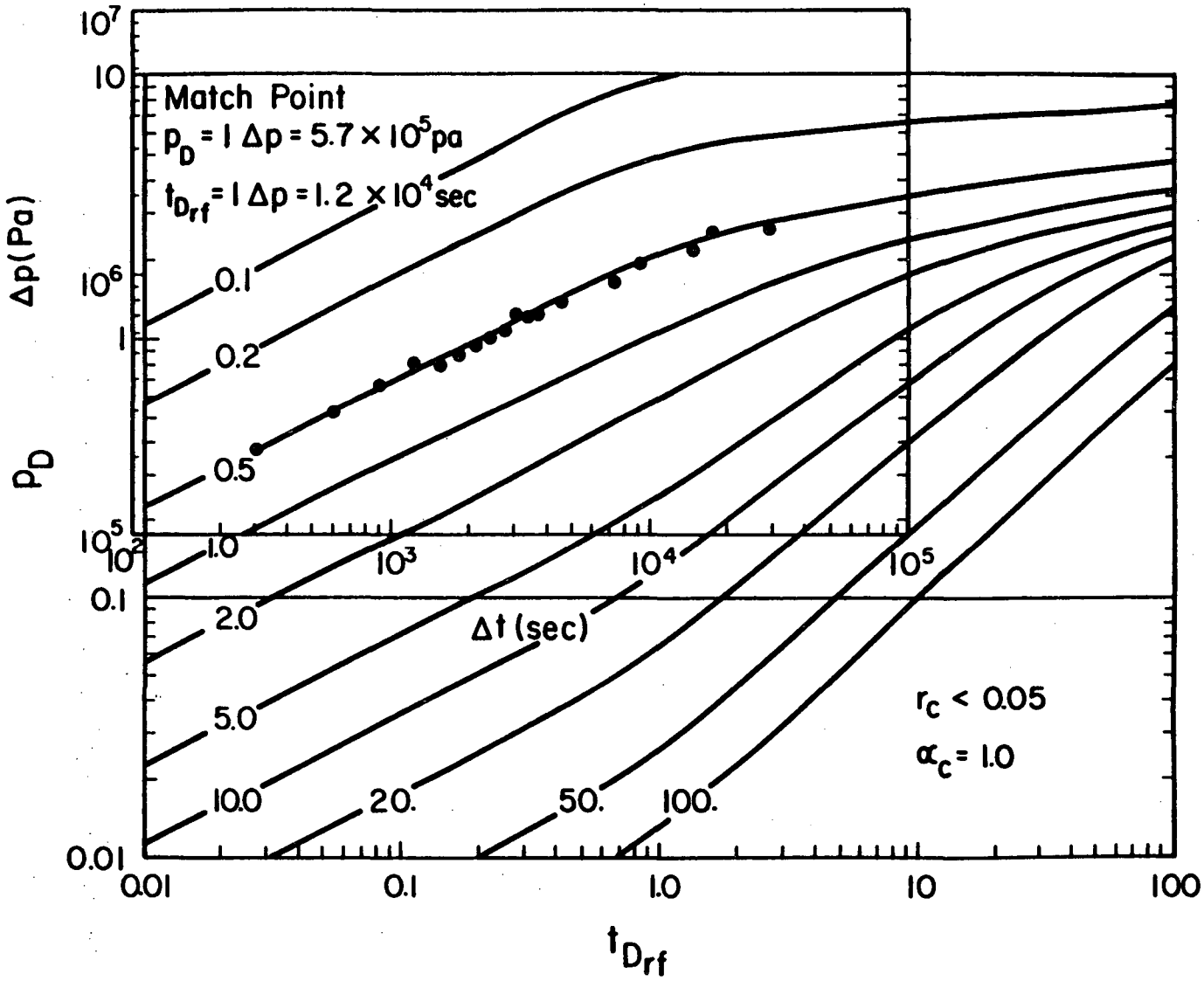

Figure 3.8 Type curve matching with linear-radial solution. XBL 856-10592

$$= 8.16\times10^{-15} \ m^2 \quad .$$

From the time match point, $t_D = 1$ at $\Delta t = 1.2\times10^4$ sec, Equation 3.2.7b, and $S_s = \rho g \, \phi c_t$, where c_t is the total compressibility

$$r_f = \sqrt{\frac{(8.16\times10^{-15}) \cdot (1.2\times10^4)}{(2.3\times10^{-4}) \cdot (0.3) \cdot (4.35\times10^{-9}) \cdot (1)}}$$

$$= 18m \quad .$$

The $\tilde{k}_1$ and x_f values given in Gringarten et al. (1972) are $5.18\times10^{-15} \ m^2$ and 17 m, respectively. It should be kept in mind that our r_f is not necessarily the exact fracture length. Rather, it should be viewed as the distance required before radial flow takes over the total system response. The analysis using the uniform flux solution must stop here. However, from our data match (Figure 3.8), we have also obtained β=0.5. From Equation 3.2.7f,

$$nb\tilde{k}_1 = 2\pi \cdot (18) \cdot (8.16\times10^{-15}) \cdot (0.5) \quad ,$$

$$= 4.6\times10^{-13} \ m^3 \quad .$$

and from $\alpha_c = 1.0$ and Equation 3.2.7e,

$$nb\,(\phi c_t)_1 = \frac{(4.6\times10^{-13}) \cdot (1.31\times10^{-9})}{(1) \cdot (8.16\times10^{-15})}$$

$$= 7.41\times10^{-8} \ \frac{m}{Pa} \quad .$$

This would give a seemingly large value for ϕc_t because nb is expected to be a small value. It must be considered in terms of the total volume of the

inner region. If the storage capacity of the fractures alone is $nbr_f\,(\phi c_t)_1$, then we can introduce a volumetrically averaged storage capacity:

$$(\phi c_t)_{1a} = \frac{nb\,(\phi c_t)_1}{\pi r_f} \tag{3.2.42}$$

$$= \frac{(7.41\times10^{-8})}{\pi\cdot(18)} = 1.31\times10^{-9}\ \mathrm{Pa}^{-1} \quad .$$

Example 2

For the second example, we shall consider the pressure effects of a prolonged period of water injection in a geothermal well in Iceland. Well KJ-20 in the Krafla geothermal field was shut in after 20 days of injection at an average rate of 25.8 liters per second (Gudmundsson et al., 1982). The $(\phi c_t)_2 H$ is 9.12×10^{-9} (O. Sigurdsson, written communication, 1985). Pressure falloff data were collected and are given in Table 3.2. Because the injection period was sufficiently long, the falloff data can be analyzed using type curves and a plot of pressure difference, $p_{wf}-p_{ws}$ vs shut-in time, Δt, as shown on Figure 3.9. It is seen that an excellent match is obtained for the particular type curve where $\alpha_c=2.47$ and $\beta=1$. As discussed above, this type curve is identical to the uniform flux solution. The flattening of the data near the end of the test is probably due to the heating up of the wellbore fluids due to higher reservoir temperature. The pressure match point for $pd=1$ is $\Delta p=2.7\times10^5$ Pa. Using Equation 3.2.7a,

$$\frac{\tilde{k}_2 H}{\mu} = \frac{(2.58\times10^{-2})\cdot(1)}{2\pi\cdot(2.7\times10^5)}$$

Table 3.2 Falloff Data from Krafla Well KJ-20 for Example 2.

Δt (*sec*)	$p_{wf} - p_{ws}$ (MPa)	Δt (*sec*)	$p_{wf} - p_{ws}$ (MPa)
0.600E+02	0.148	0.840E+04	0.742
0.120E+03	0.216	0.900E+04	0.750
0.180E+03	0.260	0.960E+04	0.758
0.240E+03	0.290	0.102E+05	0.766
0.300E+03	0.314	0.108E+05	0.772
0.360E+03	0.338	0.114E+05	0.778
0.420E+03	0.356	0.120E+05	0.785
0.480E+03	0.372	0.126E+05	0.790
0.540E+03	0.388	0.132E+05	0.795
0.600E+03	0.402	0.138E+05	0.800
0.720E+03	0.426	0.144E+05	0.805
0.840E+03	0.444	0.150E+05	0.809
0.960E+03	0.458	0.156E+05	0.814
0.108E+04	0.472	0.162E+05	0.818
0.120E+04	0.486	0.168E+05	0.821
0.132E+04	0.496	0.174E+05	0.825
0.144E+04	0.506	0.180E+05	0.828
0.156E+04	0.516	0.186E+05	0.831
0.168E+04	0.528	0.192E+05	0.834
0.180E+04	0.538	0.198E+05	0.838
0.210E+04	0.558	0.204E+05	0.841
0.240E+04	0.574	0.210E+05	0.844
0.270E+04	0.590	0.216E+05	0.846
0.300E+04	0.604	0.222E+05	0.848
0.330E+04	0.616	0.228E+05	0.850
0.360E+04	0.628	0.234E+05	0.852
0.390E+04	0.638	0.240E+05	0.854
0.420E+04	0.648	0.246E+05	0.856
0.450E+04	0.657	0.252E+05	0.858
0.480E+04	0.666	0.258E+05	0.860
0.510E+04	0.674	0.264E+05	0.862
0.540E+04	0.682	0.270E+05	0.864
0.570E+04	0.689	0.276E+05	0.865
0.600E+04	0.696	0.282E+05	0.867
0.660E+04	0.708	0.288E+05	0.868
0.720E+04	0.719	0.290E+05	0.869
0.780E+04	0.732		

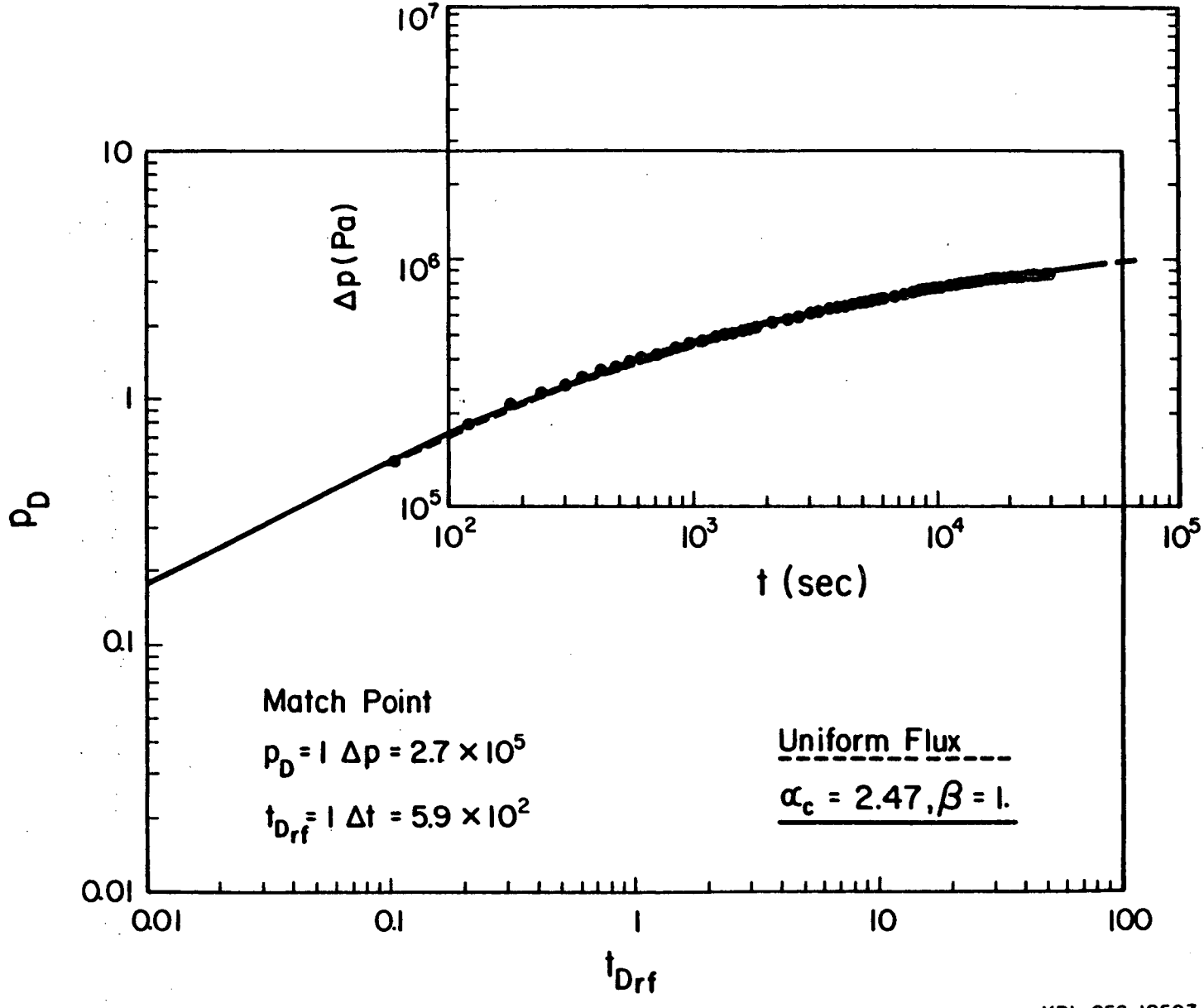

XBL 856-10593

Figure 3.9 Type curve matching for Example 2.

$$= 1.52\times10^{-8} \quad \frac{m^3}{\mathrm{Pa}\cdot s} \quad .$$

From the time match point, $t_D = 1$ at $\Delta t = 5.9\times10^2$sec, and Equation 3.2.7b,

$$r_f = \sqrt{\frac{(1.52\times10^{-8})\cdot(5.9\times10^2)}{(1)\cdot(9.12\times10^{-9})}}$$

$$= 31.3 \quad m \quad .$$

From Equation 3.2.7f,

$$nb \cdot \frac{\tilde{k}_1 H}{\mu} = 2\pi\cdot(31.3)\cdot(1.52\times10^{-8})\cdot(1) \quad ,$$

$$= 2.99\times10^{-6} \quad \frac{m^4}{\mathrm{Pa}\cdot s} \quad .$$

And from $\alpha_c = 2.47$ and Equation 3.2.7e,

$$nb\,(\phi c_t)_1 H = \frac{(2.99\times10^{-6})\cdot(9.12\times10^{-9})}{(2.47)\cdot(1.52\times10^{-8})}$$

$$= 7.18\times10^{-7} \quad \frac{m^2}{\mathrm{Pa}} \quad ,$$

so that the volumetrically averaged storage capacity becomes:

$$(\phi c_t)_{1a} H = 7.3\times10^{-9} \quad \frac{m}{\mathrm{Pa}} \quad .$$

3.3. Composite Model With Radial Flow

In the previous section we considered a case when there exists a region around the well where a linear flow takes place instead of a usual radial flow. We will now consider a case when the flow in the inner and the outer region are both radial and only the flow properties in each region differ. Because naturally fractured reservoirs are often highly heterogeneous it is very possible that the flow properties in the vicinity of the well are not representative of the total system. Thus, a radial composite model may better describe the flow to the well in a fracture medium than a homogeneous model.

Radial composite models have been extensively studied previously. Hurst (1960) solved for a pressure response to a line-source well in a composite medium. Loucks and Guerrero (1961) considered a finite radius well but they assumed a uniform storage coefficient. Larkin (1963) allowed for an arbitrary number of line-source wells at any locations in the inner region, although he did not evaluate his solution. He considered a case when the inner region is very large, in which case a line source approximation of a well is quite adequate.

However, we are interested in a relatively smaller size inner region where a line-source approximation is not appropriate. Ramey (1970) also considered a line-source well and presented approximate solutions for large and small time. Bixel and van Poollen (1967) and Kazemi (1972) used a finite difference method. Sternberg (1973) and Streltsova and McKinley (1984) had a finite radius well condition but used an approximate Laplace inversion method

introduce by Schapery (1961). Satman (1985) included a skin and wellbore storage effects and used a numerical Laplace inversion technique presented by Stehfest (1970) to evaluate the solution in the Laplace space.

To our knowledge, there has not been a fully analytical solution avaliable for a composite medium with different permeabilities and storage coefficients in the two regions that also considers a finite radius well. Because we are interested in a short time behavior of a well in a heterogeneous fracture system, a finite radius well condition is essential. Also we do not know the degree of the error involved with Schapery's approximate Laplace inversion method or with Stehfest's numerical Laplace inversion technique for this particular problem. Therefore we invert the solution in the Laplace domain using Mellin's formula and present the final solution in the real space in an analytical form.

3.3.1. Model Description

An isothermal system in a homogeneously fractured formation of uniform thickness H that is radially symmetric and infinite in extent is considered. The well is pumped at a constant rate Q. It is assumed that all the hydraulic parameters are independent of pressure, and no wellbore storage or damage is considered. We assume that an appropriate measure can be taken to minimize the wellbore storage effect in order to analyze the early time behavior. The system consists of two concentric regions of different flow properties. The pressure head h, the hydraulic conductivity k and the storage

coefficient S_s for the inner and the outer region are denoted by subscripts 1 and 2, respectively. The well is located in the center of the inner region. The radius of the well is r_w, and the radius of the boundary between the inner and outer regions is r_f. Figure 3.10 illustrates the model.

The governing equation for the inner region is:

$$\frac{\partial^2 h_1}{\partial r^2} + \frac{1}{r}\frac{\partial h_1}{\partial r} = \frac{1}{\alpha_1}\frac{\partial h_1}{\partial t} , \tag{3.3.1a}$$

and for the outer region is:

$$\frac{\partial^2 h_2}{\partial r^2} + \frac{1}{r}\frac{\partial h_2}{\partial r} = \frac{1}{\alpha_2}\frac{\partial h_2}{\partial t} . \tag{3.3.1b}$$

The inner boundary condition is:

$$2\pi r_w H \; k_1 \frac{\partial h_1}{\partial r} = Q . \tag{3.3.2}$$

The outer boundary boundary condition is:

$$h_2(\infty, t) = h_i . \tag{3.3.3}$$

The continuity requirements at the interface are:

$$k_1 \frac{\partial h_1}{\partial r} = k_2 \frac{\partial h_2}{\partial r} \quad (r = r_f) , \tag{3.3.4}$$

$$h_1 = h_2 \quad (r = r_f) . \tag{3.3.5}$$

The initial conditions are:

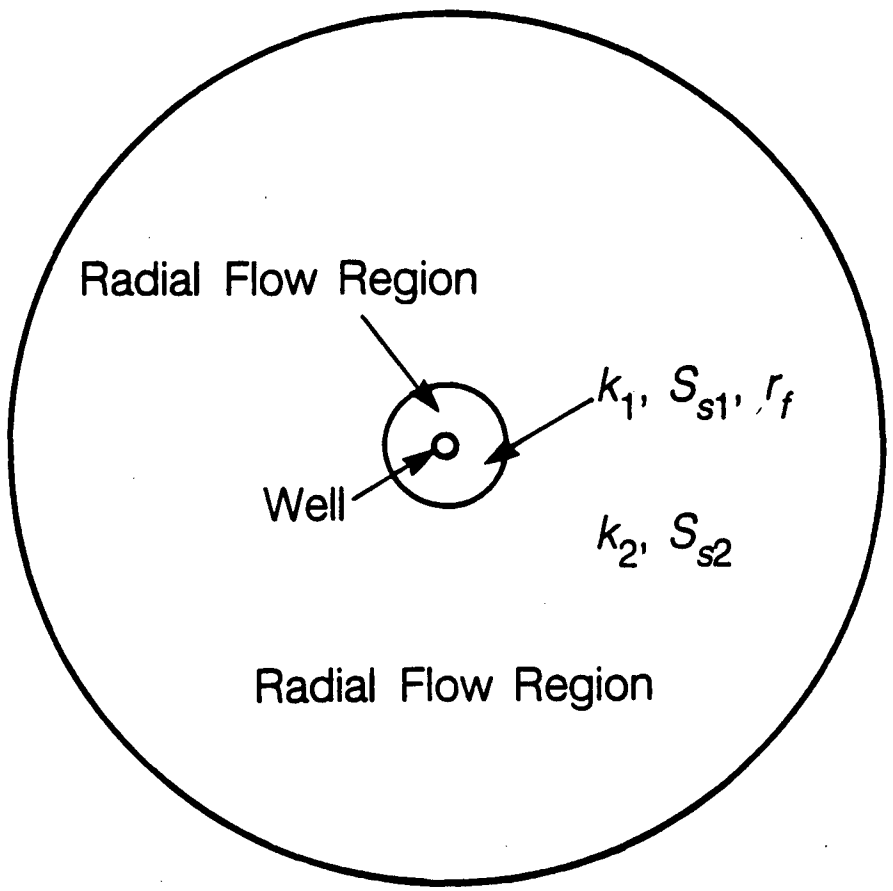

XBL 862-10667

Figure 3.10 Radial composite model.

$$h_1(r,0) = h_i \tag{3.3.6}$$

$$h_2(r,0) = h_i \tag{3.3.7}$$

Defining the following dimensionless parameters:

$$h_D = \frac{2\pi k_2 H(h_i - h)}{Q}, \tag{3.2.8a}$$

$$t_D = \frac{\alpha_2 t}{r_f^2}, \tag{3.3.8b}$$

$$r_D = \frac{r}{r_f}, \tag{3.3.8c}$$

$$k_D = \frac{k_1}{k_2}, \tag{3.3.8d}$$

$$S_{S_D} = \frac{S_{S_1}}{S_{S_2}}, \tag{3.3.8e}$$

$$r_c = \frac{r_w}{r_f}, \tag{3.3.8f}$$

$$\alpha_c = \frac{k_D}{S_{S_D}} \tag{3.3.8g}$$

the governing equations can be written in dimensionless form as follows:

$$\frac{\partial^2 h_{D_1}}{\partial r_D^2} + \frac{1}{r_D}\frac{\partial h_{D_1}}{\partial r_D} = \frac{1}{\alpha_c}\frac{\partial h_{D_1}}{\partial t_D} \tag{3.3.9a}$$

$$\frac{\partial^2 h_{D_2}}{\partial r_D^2} + \frac{1}{r_D}\frac{\partial h_{D_2}}{\partial r_D} = \frac{\partial h_{D_2}}{\partial t_D}. \tag{3.3.9b}$$

In dimensionless form, the boundary conditions and initial conditions become:

$$\frac{\partial h_{D_1}}{\partial r_D} = -\frac{1}{r_c k_D} \quad (r_D = r_c) \tag{3.3.10}$$

$$h_{D_2}(\infty, t_D) = 0 \tag{3.3.11}$$

$$h_{D_1} = h_{D_2} \quad (r_D = 1) \tag{3.3.12}$$

$$\frac{\partial h_{D_1}}{\partial r_D} = \frac{1}{k_D} \frac{\partial h_{D_2}}{\partial r_D} \quad (r_D = 1) \tag{3.3.13}$$

$$h_{D_1}(r_D, 0) = 0 \quad (r_c \leq r_D \leq 1) \tag{3.3.14}$$

$$h_{D_2}(r_D, 0) = 0 \quad (1 \leq r_D < \infty) \tag{3.3.15}$$

3.3.2. Solutions

We will use the Laplace transformation technique to solve the problem. After the Laplace transformations, which require the use of the initial conditions 3.3.14 and 3.3.15, we obtain the subsidiary equations:

$$\frac{d^2\bar{h}_{D_1}}{dr_D^2} + \frac{1}{r_D} \frac{d\bar{h}_{D_1}}{dr_D} = \frac{p}{\alpha_c} \bar{h}_{D_1} , \tag{3.3.16a}$$

$$\frac{d^2\bar{h}_{D_2}}{dr_D^2} + \frac{1}{r_D} \frac{d\bar{h}_{D_2}}{dr_D} = p\bar{h}_{D_2} , \tag{3.3.16b}$$

where the Laplace transformation of a function $f(r_D, t_D)$ is defined as

$$\bar{f}(r_D) = \int_0^\infty e^{-pt_D} f(r_D, t_D) dp \quad .$$

The transformed boundary conditions become:

$$\frac{d\bar{h}_{D_1}}{dr_D} = -\frac{1}{r_c\, k_D\, p} \quad (r_D = r_c) \tag{3.3.17}$$

$$\bar{h}_{D_2} = 0 \quad (r_D = \infty) \tag{3.3.18}$$

$$\bar{h}_{D_1} = \bar{h}_{D_2} \quad (r_D = 1) \tag{3.3.19}$$

$$\frac{d\bar{h}_{D_1}}{dr_D} = \frac{1}{k_D}\frac{d\bar{h}_{D_2}}{dr_D} \quad (r_D = 1) \tag{3.3.20}$$

The general solutions to Equation 3.3.16a and 3.3.16b are:

$$\bar{h}_{D_1} = A\ I_0(\sqrt{p/\alpha_c}\, r_D) + BK_0(\sqrt{p/\alpha_c}\, r_D) \tag{3.3.21a}$$

$$\bar{h}_{D_2} = C\ I_0(\sqrt{p}\ r_D) + DK_0(\sqrt{p}\ r_D) \tag{3.3.21b}$$

From Equation 3.3.19, it can be shown that $C = 0$.

Applying the inner boundary condition Equation 3.3.17:

$$A\sqrt{p/\alpha_c}\, I_1(\sqrt{p/\alpha_c}\, r_c) - B\sqrt{p/\alpha_c}\, K_1(\sqrt{p/\alpha_c}\, r_c) = -\frac{1}{r_c\, k_D\, p} \tag{3.3.22}$$

From Equation 3.3.18:

$$AI_0(\sqrt{p/\alpha_c}) + BK_0(\sqrt{p/\alpha_c}) = DK_0(\sqrt{p}) \tag{3.3.23}$$

From Equation 3.3.20:

$$A\sqrt{p/\alpha_c}\,I_1(\sqrt{p/\alpha_c}) - B\sqrt{p/\alpha_c}\,K_1(\sqrt{p/\alpha_c}) = -D\,\frac{1}{k_D}\sqrt{p}\,K_1(\sqrt{p}) \tag{3.3.24}$$

Solving Equations 3.3.22 through 3.3.24 for A, B and D, we obtain:

$$A = \frac{\sqrt{\alpha_c}}{r_c\,k_D\,p\,\sqrt{p}} \cdot \frac{1}{\Delta} \times$$
$$\times \left\{ k_D \cdot K_0(\sqrt{p}) \cdot K_1(\sqrt{p/\alpha_c}) - \sqrt{\alpha_c} \cdot K_0(\sqrt{p/\alpha_c})K_1(\sqrt{p}) \right\} \tag{3.3.25}$$

$$B = \frac{\sqrt{\alpha_c}}{r_c\,k_D\,p\,\sqrt{p}} \cdot \frac{1}{\Delta} \times$$
$$\times \left\{ k_D \cdot I_1(\sqrt{p/\alpha_c}) \cdot K_0(\sqrt{p}) + \sqrt{\alpha_c} \cdot I_0(\sqrt{p/\alpha_c})K_1(\sqrt{p}) \right\} \tag{3.3.26}$$

$$D = \frac{\sqrt{\alpha_c}}{r_c\,p\,\sqrt{p}} \cdot \frac{1}{\Delta} \cdot$$
$$\times \left\{ I_0(\sqrt{p/\alpha_c}) \cdot K_1(\sqrt{p/\alpha_c}) + I_1(\sqrt{p/\alpha_c}) \cdot K_0(\sqrt{p/\alpha_c}) \right\}, \tag{3.3.27}$$

where

$$\Delta = \sqrt{\alpha_c}\,K_1(\sqrt{p})\left\{ I_1(\sqrt{p/\alpha_c} \cdot r_c)\,K_0(\sqrt{p/\alpha_c}) + I_0(\sqrt{p/\alpha_c})K_1(\sqrt{p/\alpha_c} \cdot r_c) \right\}$$
$$+ k_D \cdot K_0(\sqrt{p})\left\{ I_1(\sqrt{p/\alpha_c}) \cdot K_1(\sqrt{p/\alpha_c}\,r_c) - I_1(\sqrt{p/\alpha_c} \cdot r_c) \cdot K_1(\sqrt{p/\alpha_c}) \right\} \tag{3.3.28}$$

Using the identity;

$$I_0(\sqrt{p/\alpha_c}) \cdot K_1(\sqrt{p/\alpha_c}) + I_1(\sqrt{p/\alpha_c}) \cdot K_0(\sqrt{p/\alpha_c}) = \frac{1}{\sqrt{p/\alpha_c}} \tag{3.3.29}$$

the equation for D simplifies to:

$$D = \frac{\alpha_c}{r_c\, p^2} \cdot \frac{1}{\Delta} \ . \tag{3.3.30}$$

Finally, the solutions in the Laplace space become:

$$\begin{aligned}\bar{h}_{D_1} = & \frac{\sqrt{\alpha_c}}{r_c\, k_D\, p\, \sqrt{p}} \cdot \frac{1}{\Delta} \times \\ & \times \Bigg[k_D \cdot K_0(\sqrt{p}) \Big\{ I_1(\sqrt{p/\alpha_c}) K_0(\sqrt{p/\alpha_c}\, r_D) + I_0(\sqrt{p/\alpha_c}\, r_D) K_1(\sqrt{p/\alpha_c}) \Big\} \\ & + \sqrt{\alpha_c}\, K_1(\sqrt{p}) \Big\{ I_0(\sqrt{p/\alpha_c}) K_0(\sqrt{p/\alpha_c}\, r_D) - I_0(\sqrt{p/\alpha_c}\, r_D) \cdot K_0(\sqrt{p/\alpha_c}) \Big\} \Bigg]\end{aligned} \tag{3.3.31a}$$

and

$$\bar{h}_{D_2} = \frac{\alpha_c}{r_c \cdot p^2} \cdot \frac{1}{\Delta} \cdot K_0(\sqrt{p}\, r_D) \tag{3.3.31b}$$

The Laplace inversion procedures of Equations 3.3.31a and 3.3.31b to the real space are similar to those followed in the previous section and the details can be found in the Appendix B. From the Appendix B, the solutions in the real space are:

$$h_{D_1} = \frac{4\alpha_c}{\pi^2 r_c} \int_0^\infty \frac{1 - e^{-\mu^2 t_D}}{\mu^3} \cdot \frac{C_1 C_3 + C_2 C_4}{\Theta^2 + \Psi^2} \, d\mu \tag{B.9a}$$

for Region 1 and

$$h_{D_2} = \frac{4\alpha_c}{\pi^2 r_c} \int_0^\infty \frac{1 - e^{-\mu^2 t_D}}{\mu^3} \cdot \frac{J_0(\mu r_D)\Theta - Y_0(\mu r_D)\Psi}{\Theta^2 + \Psi^2} \, d\mu \tag{B.9b}$$

for Region 2, where

$$\Theta = k_D \cdot C_4 \cdot Y_0(\mu) + \sqrt{\alpha_c} \cdot C_3 \cdot Y_1(\mu) \tag{B.7c}$$

$$\Psi = k_D \cdot C_4 \cdot J_0(\mu) + \sqrt{\alpha_c} \cdot C_3 \cdot J_1(\mu) \tag{B.7d}$$

and

$$C_1 = J_0(\frac{\mu}{\sqrt{\alpha_c}} r_D) \cdot Y_1(\frac{\mu}{\sqrt{\alpha_c}}) - J_1(\frac{\mu}{\sqrt{\alpha_c}}) \cdot Y_0(\frac{\mu}{\sqrt{\alpha_c}} r_D) \tag{B.8a}$$

$$C_2 = J_0(\frac{\mu}{\sqrt{\alpha_c}} r_D) \cdot Y_0(\frac{\mu}{\sqrt{\alpha_c}}) - J_0(\frac{\mu}{\sqrt{\alpha_c}}) \cdot Y_0(\frac{\mu}{\sqrt{\alpha_c}} r_D) \tag{B.8b}$$

$$C_3 = J_0(\frac{\mu}{\sqrt{\alpha_c}}) \cdot Y_1(\frac{\mu}{\sqrt{\alpha_c}} r_c) - J_1(\frac{\mu}{\sqrt{\alpha_c}} r_c) \cdot Y_0(\frac{\mu}{\sqrt{\alpha_c}}) \tag{B.8c}$$

$$C_4 = J_1(\frac{\mu}{\sqrt{\alpha_c}} r_c) \cdot Y_1(\frac{\mu}{\sqrt{\alpha_c}}) - J_1(\frac{\mu}{\sqrt{\alpha_c}}) \cdot Y_1(\frac{\mu}{\sqrt{\alpha_c}} r_c) \tag{B.8d}$$

Equations B.9a and B.9b have infinite integrals that converge extremely slowly. Therefore, they must be evaluated numerically.

We will now compare Equation B.9a with the solution obtained by an approximate Laplace inversion scheme introduced by Schapery (1961) and the solution obtained by a numerical Laplace inversion scheme introduced by Stehfest (1970). Sternberg (1973) and Streltsova and McKinley (1984) used the approximate inversion scheme in their study, whereas Satman (1985) used the numerical inversion scheme. Comparisons are made in two cases. The parameters used in the two cases are shown in Table 3.3.

Table 3.3 Parameters used to compare inversion methods.

	r_D	r_c	α_c	β
Case 1	1.0	0.1	10.0	1.0
Case 2	0.01	0.01	1.0	10.0

Figure 3.11 and 3.12 show comparison of the three solutions for case 1 and case 2, respectively. As can be seen from the figures, the solution obtained by the numerical inversion scheme is practically identical to the analytically inverted solution for the parameters studied. The calculated error is less than 0.7 per cent, which is negligible for all practical purposes. In fact, it has been shown (Stehfest, 1970) that the numerical inversion scheme is very accurate if an inverted function is monotonic. On the contrary, the solution obtained by the approximate inversion scheme does not compare very well with the other two in either case, especially for small time. The approximation scheme is known to be good for slowly varying

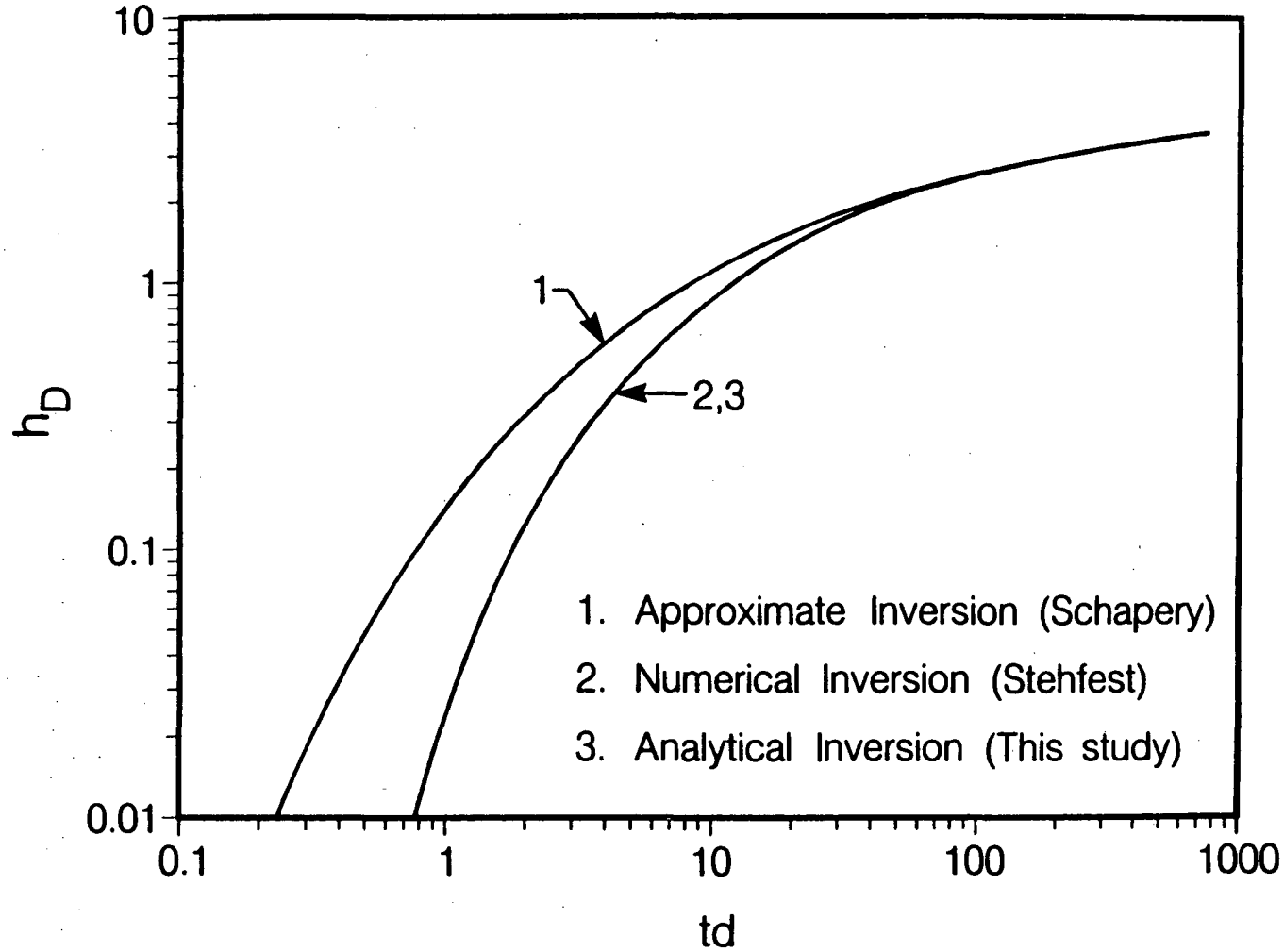

Figure 3.11 Comparison of inversion methods - Case 1.

XBL 862-10681

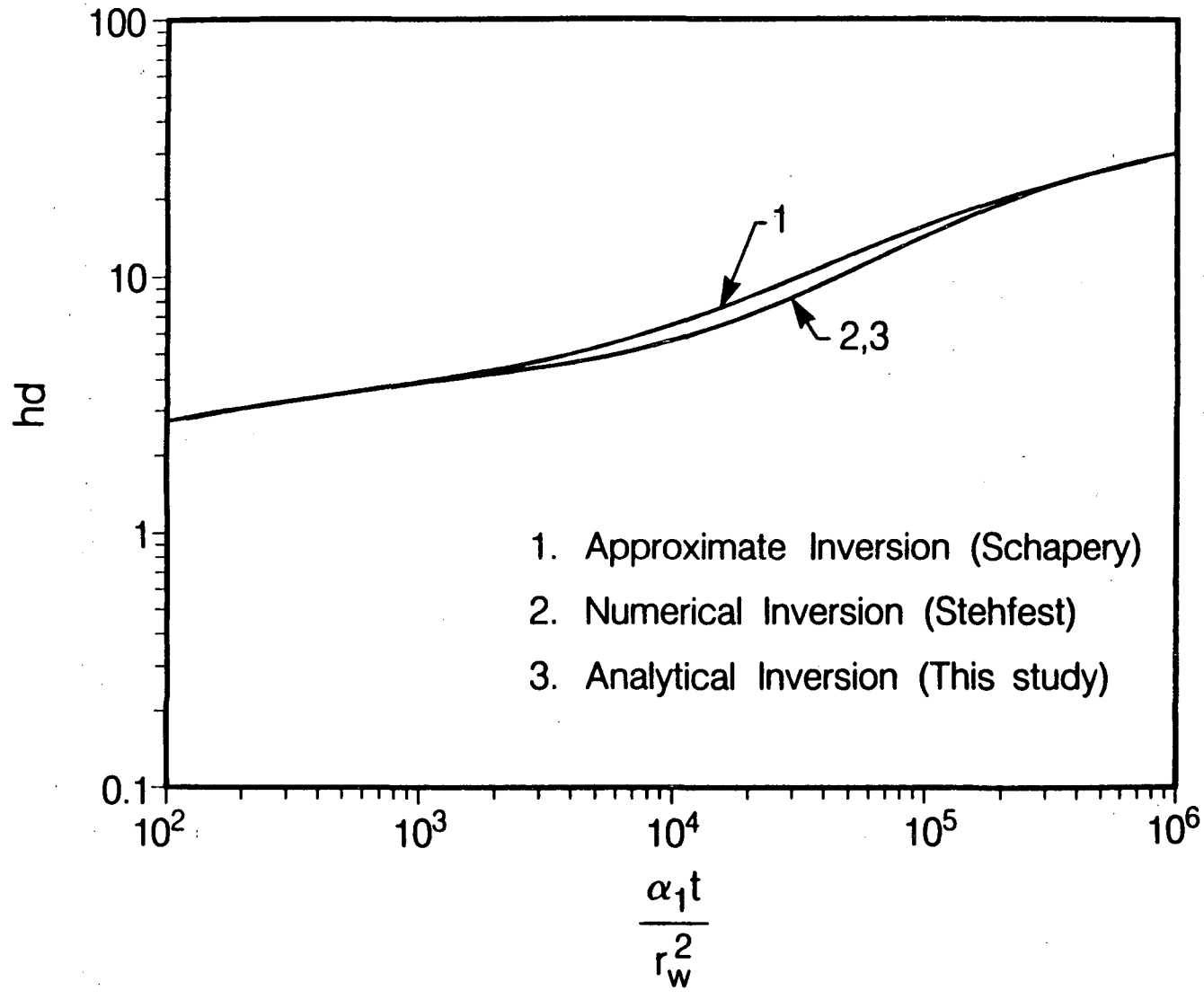

Figure 3.12 Comparison of inversion methods - Case 2.

XBL 862-10684

logarithmic functions (Sternberg, 1973) and therefore for dimensionless time, $t_D > 10$ in common well test problems. In a composite medium, however, a rapid change in dimensionless head may occur, even at a large dimensionless time, if the flow properties of the two regions differ greatly. Therefore, the approximate inversion scheme is not recommended for obtaining type curves for a composite model. One advantage of the approximate inversion over the numerical inversion, however, is that solutions can be expressed in an analytical form.

It should be pointed out that it may require very large amounts of CPU time to evaluate semi-infinite integrals such as Equation B.9a, which is a complex function of Bessel functions. This is because the oscillatory nature of Bessel functions of the first and second kind makes it extremely difficult to achieve convergence. When compared to the numerical inversion scheme, the CPU time required to evaluate the analytical solution, Equation B.9a, may be two to three orders of magnitude larger depending on the values of the parameters.

A similar observation was made for the linear-radial composite medium problem discussed in the previous section, and it should probably be the case for all related well test problems. Therefore, we will use the numerical inversion scheme for the rest of the problems discussed in the present study.

3.4. Composite Model With Spherical Flow

In the previous two sections, we studied two types of composite models. The first model was one in which a linear flow develops to a radial flow (or conversely, radial flow converges to linear flow), and the second model was a classical radial flow model. In this section we will consider a model where a radial flow develops into spherical flow (or conversely, spherical flow converges to radial flow). This situation may arise when a vertical well intersects a non-vertical fracture that is part of a three dimensional, well interconnected fracture network. We assume that all the fluid going into or out of the well flows within this fracture radially. We also assume that the fracture system as a whole can be treated as a porous medium macroscopically. Therefore, at some distance away from the well, the flow is assumed to be spherical.

3.4.1. Model Description

An isothermal system in a homogeneously fractured formation of spherically infinite extent is considered. The system consists of two concentric regions of different flow regimes and flow properties. In the outer region, the flow is spherical, and in the inner region, the flow is assumed to be radial and restricted within the fracture that intersects the well. As in the previous sections, the pressure head h, the hydraulic conductivity k and the storage coefficient S_s for the inner and the outer region are denoted by subscripts 1 and 2, respectively. The hydraulic aperture of the fracture in the inner

region is b. It is assumed that all the hydraulic parameters are independent of pressure, and no wellbore storage or damage is considered. The well is located in the center of the inner region, and it is pumped at a constant rate Q. The radius of the well is r_w, and the radius of the boundary between the inner and outer regions is r_f. The latter is the radius required before the spherical flow regime takes over the system response under well test conditions. Therefore, r_f is again related to, but not exactly equal to, the exact fracture radius. It is also assumed that there is an infinitesimally thin spherical annulus of infinite conductivity between the two regions so that the otherwise incompatible boundaries can be matched. Figure 3.13 illustrates the model.

The governing equation for the inner region is:

$$\frac{\partial^2 h_1}{\partial r^2} + \frac{1}{r}\frac{\partial h_1}{\partial r} = \frac{1}{\alpha_1}\frac{\partial h_1}{\partial t} , \tag{3.4.1}$$

and for the outer region is:

$$\frac{\partial^2 h_2}{\partial r^2} + \frac{2}{r}\frac{\partial h_2}{\partial r} = \frac{1}{\alpha_2}\frac{\partial h_2}{\partial t} . \tag{3.4.2}$$

The inner boundary condition is:

$$Q = 2\pi r_w b k_1 \cdot \left.\frac{\partial h_1}{\partial r}\right|_{r=r_w} . \tag{3.4.3}$$

The outer boundary condition is:

$$h_2(\infty,t) = h_i \tag{3.4.4}$$

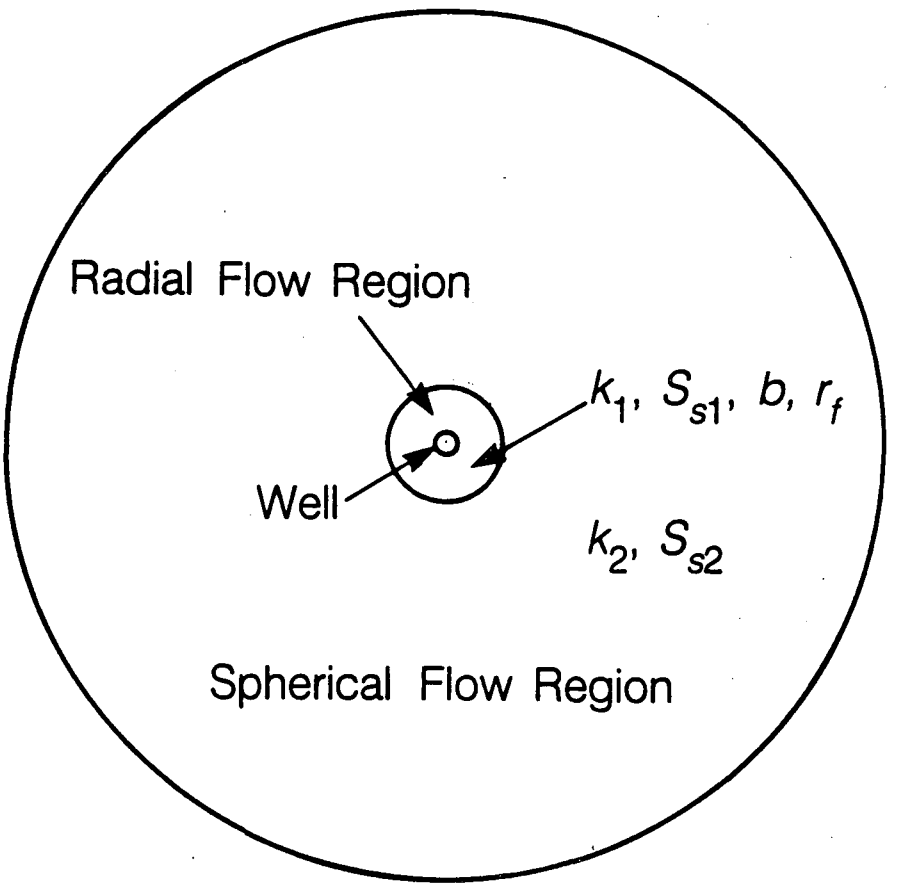

XBL 862-10666

Figure 3.13 Radial-spherical composite model.

The continuity requirements at the interface are:

$$2\pi r_f \cdot b \cdot k_1 \cdot \frac{\partial h_1}{\partial r}\bigg|_{r=r_f} = 4\pi r_f^2 \cdot k_2 \cdot \frac{\partial h_2}{\partial r}\bigg|_{r=r_f} , \tag{3.4.5}$$

$$h_1 = h_2 \Big|_{r=r_f} . \tag{3.4.6}$$

The initial conditions are:

$$h_1(r,0) = h_i \tag{3.4.7}$$

$$h_2(r,0) = h_i \tag{3.4.8}$$

Defining the following dimensionless parameters:

$$h_D = \frac{4\pi r_f \, k_2(h_i - h)}{Q} , \tag{3.4.9a}$$

$$t_D = \frac{\alpha_2 t}{r_f^2} , \tag{3.4.9b}$$

$$r_D = \frac{r}{r_f} , \tag{3.4.9c}$$

$$\beta = \frac{bk_1}{2r_f \, k_2} , \tag{3.4.9d}$$

$$r_c = \frac{r_w}{r_f} , \tag{3.4.9e}$$

$$\alpha_c = \frac{\alpha_1}{\alpha_2} \tag{3.4.9f}$$

In a dimensionless form Equations 3.4.1 and 3.4.2 become:

$$\frac{\partial^2 h_{D_1}}{\partial r_D^2} + \frac{1}{r_D}\frac{\partial h_{D_1}}{\partial r_D} = \frac{1}{\alpha_c}\frac{\partial h_{D_1}}{\partial t_D} \tag{3.4.10}$$

and

$$\frac{\partial^2 h_{D_2}}{\partial r_D^2} + \frac{2}{r_D}\frac{\partial h_{D_2}}{\partial r_D} = \frac{\partial h_{D_2}}{\partial t_D} \tag{3.4.11}$$

In terms of the dimensionless parameters the boundary and initial conditions become

$$\frac{\partial h_{D_1}}{\partial r_D} = -\frac{1}{r_c\,\beta} \qquad (r_D = r_c) \tag{3.4.12}$$

$$h_{D_2}(\infty, t_D) = 0 \tag{3.4.13}$$

$$\frac{\partial h_{D_1}}{\partial r_D} = \frac{1}{\beta}\cdot\frac{\partial h_{D_2}}{\partial r_D} \qquad (r_D = 1) \tag{3.4.14}$$

$$h_{D_1} = h_{D_2} \qquad (r_D = 1) \tag{3.4.15}$$

$$h_{D_1}(r_D, 0) = 0 \qquad (r_c \leq r_D \leq 1) \tag{3.4.16}$$

$$h_{D_2}(r_D, 0) = 0 \qquad (1 \leq r_D \leq \infty) \tag{3.4.17}$$

3.4.2. Solutions

As before, we will use the Laplace transform to solve Equation 3.4.10 and 3.4.11. After the Laplace transformations, which require use of the

initial conditions 3.4.16 and 3.4.17, the governing equations in the Laplace space are:

$$\frac{d^2\bar{h}_{D_1}}{dr_D^2} + \frac{1}{r_D}\frac{d\bar{h}_{D_1}}{dr_D} = \frac{p}{\alpha_c}\bar{h}_{D_1} \tag{3.4.18}$$

$$\frac{d^2\bar{h}_{D_2}}{dr_D^2} + \frac{2}{r_D}\frac{d\bar{h}_{D_2}}{dr_D} = p\bar{h}_{D_2} \tag{3.4.19}$$

The transformed boundary conditions are:

$$\frac{d\bar{h}_{D_1}}{dr_D} = -\frac{1}{r_c\,\beta p} \qquad (r_D = r_c) \tag{3.2.20}$$

$$\bar{h}_{D_2}(\infty) = 0 \tag{3.2.21}$$

$$\bar{h}_{D_1} = \bar{h}_{D_2} \qquad (r_D = 1) \tag{3.2.22}$$

$$\frac{d\bar{h}_{D_1}}{dr_D} = \frac{1}{\beta}\frac{d\bar{h}_{D_2}}{dr_D} \qquad (r_D = 1)\,. \tag{3.2.23}$$

The general solution to Equation 3.4.18 is:

$$\bar{h}_{D_1} = AI_0(\sqrt{p/\alpha_c}\,r_D) + BK_0(\sqrt{p/\alpha_c}\,r_D) \tag{3.4.24}$$

Because Equation 3.4.21 requires Equation 3.4.19 to be bounded, the general solution to Equation 3.4.19 is:

$$\bar{h}_{D_2} = \frac{C}{r_D}\exp(-\sqrt{p}\;\;r_D) \tag{3.4.25}$$

where A, B, and C are constants. By applying the boundary conditions to Equations 3.4.24 and 3.4.25, we obtain the following relations among A, B

and C.

$$\sqrt{p/\alpha_c}\cdot I_1(\sqrt{p/\alpha_c}\,r_c)\cdot A - \sqrt{p/\alpha_c}\,K_1(\sqrt{p/\alpha_c}\,r_c)\cdot B = -\frac{1}{r_c\,\beta p} \tag{3.4.26}$$

$$I_o(\sqrt{p/\alpha_c})\cdot A + K_0(\sqrt{p/\alpha_c})\cdot B - \exp(-\sqrt{p})\cdot C = 0 \tag{3.4.27}$$

$$\sqrt{p/\alpha_c}\,I_1(\sqrt{p/\alpha_c})\cdot A - \sqrt{p/\alpha_c}\,K_1(\sqrt{p/\alpha_c})\cdot B + \\ + \frac{1+\sqrt{p}}{\beta}\cdot\exp(-\sqrt{p})\cdot C = 0 \tag{3.4.28}$$

Solving for A, B and C, we obtain:

$$A = \frac{-1}{r_c\,\beta p\,\Delta}\cdot\left[\frac{1+\sqrt{p}}{\beta}K_0(\sqrt{p/\alpha_c}) - \sqrt{p/\alpha_c}\,K_1(\sqrt{p/\alpha_c})\right] \tag{3.4.29}$$

$$B = \frac{1}{r_c\,\beta p\,\Delta}\cdot\left[\frac{1+\sqrt{p}}{\beta}I_0(\sqrt{p/\alpha_c}) + \sqrt{p/\alpha_c}\,I_1(\sqrt{p/\alpha_c})\right] \tag{3.4.30}$$

$$C = \frac{1}{r_c\,\beta p\,\Delta}\ , \tag{3.4.31}$$

where

$$\Delta = \sqrt{p/\alpha_c}\,I_1(\sqrt{p/\alpha_c}\,r_c)\left[\frac{1+\sqrt{p}}{\beta}K_0(\sqrt{p/\alpha_c}) - \sqrt{p/\alpha_c}\,K_1(\sqrt{p/\alpha_c})\right] + \\ + \sqrt{p/\alpha_c}\,K_1(\sqrt{p/\alpha_c}\,r_c)\left[\frac{1+\sqrt{p}}{\beta}I_0(\sqrt{p/\alpha_c}) + \sqrt{p/\alpha_c}\,I_1(\sqrt{p/\alpha_c})\right] \tag{3.4.32}$$

Therefore, the solution in the Laplace space is

$$\bar{h}_{D_1} = \frac{1}{r_c\,\beta p\,\Delta}\cdot\left\{-I_0(\sqrt{p/\alpha_c}\,r_D)\left[\frac{1+\sqrt{p}}{\beta}K_0(\sqrt{p/\alpha_c}) - \sqrt{p/\alpha_c}\,K_1(\sqrt{p/\alpha_c})\right] + \right. \\ \left. + K_0(\sqrt{p/\alpha_c}\,r_D)\left[\frac{1+\sqrt{p}}{\beta}I_0(\sqrt{p/\alpha_c}) + \sqrt{p/\alpha_c}\,I_1(\sqrt{p/\alpha_c})\right]\right\} \tag{3.4.33}$$

for the inner region and

$$\bar{h}_{D_2} = \frac{1}{r_c \beta p \Delta r_D} \cdot \exp(-\sqrt{p}\ r_D) \tag{3.4.34}$$

for the outer region.

To evaluate dimensionless pressure drops at the well, Equation 3.4.33 must be inverted back to the real space. This can be done by following steps similar to those in the previous sections. We will use the numerical inversion scheme introduced by Stehfest (1970), which gives excellent accuracy for this purpose. Because there are three extra dimensionless parameters, i.e., α_c, β and r_c, it is impractical to plot all the possible dimensionless pressure drop curves. Therefore, we will illustrate the effects of each individual parameter by sequentially varying only that parameter and choosing some representative values for the rest of the parameters. Also, we will plot the curves redefining the dimensionless head to $h_{D_1}' = \frac{2\pi k_1 b (h_i - h)}{Q}$ and the dimensionless time to $t_D' = \frac{\alpha_1 t}{r_w^2}$. These definitions are more convenient to illustrate the deviation from the usual radial flow curve.

Figure 3.14 shows the effects of change in hydraulic conductivity from the inner region to the outer region. For all the curves $r_c = 0.05$ and $\frac{\alpha_c}{\beta} = 1$. Initially, all the curves follow the same curves as radial flow in a homogeneous porous medium, and at later time the curves display a characteristic of a spherical flow. For small values of β, the curves become almost horizontal with little transition period. This can be mistaken for an indication of an

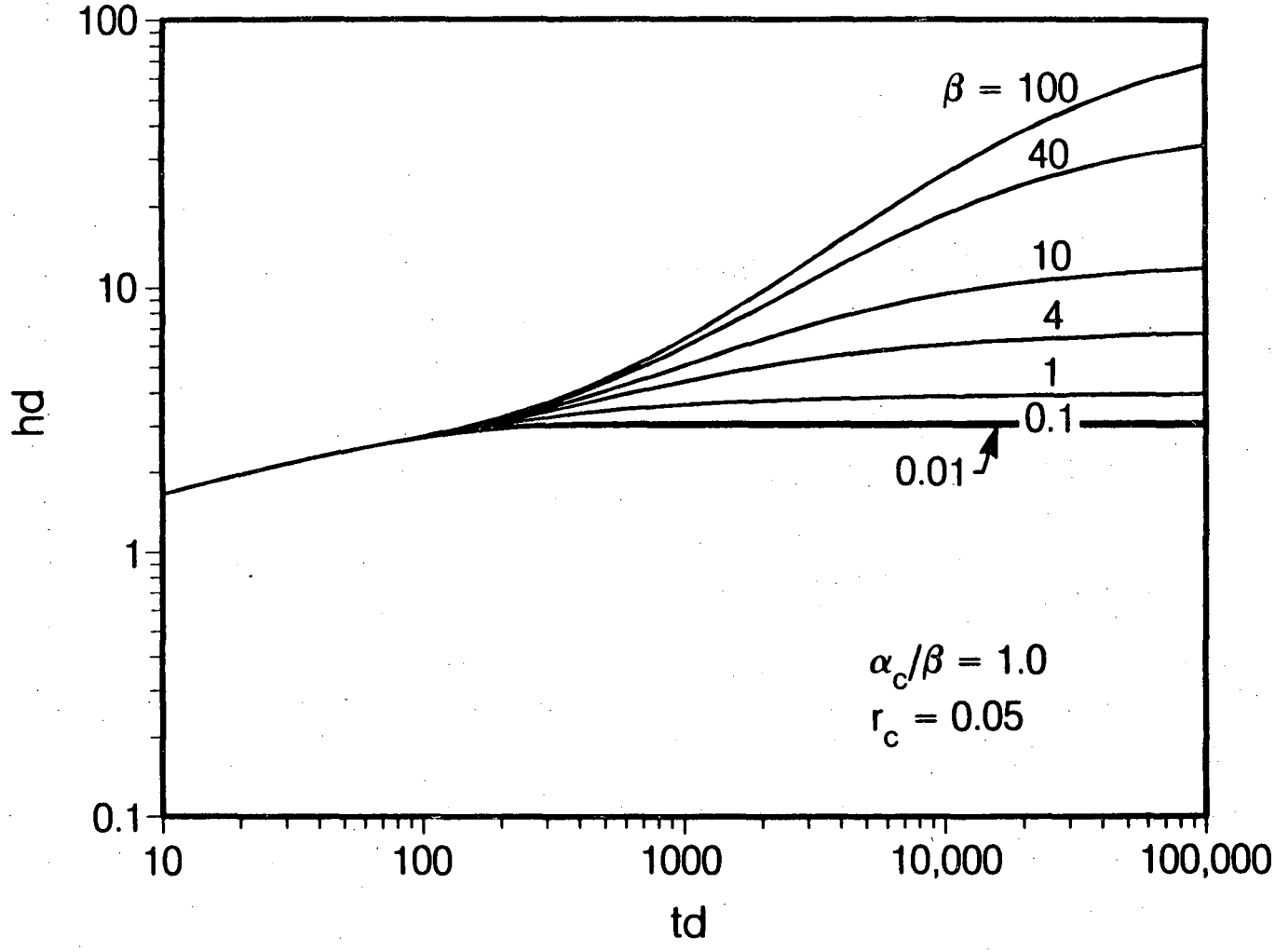

Figure 3.14 h_{D_1} vs. t_D for $\frac{\alpha_c}{\beta}$=1. and r_c =0.05.

XBL 862-10680

open boundary. Furthermore, for $\beta<0.1$, the curves are identical to each other and it would be very difficult to estimate the value of β in curve matching. For large β, the curves bend upward in transition before they flatten. This is because the higher permeability inner region gets drained more quickly than the outer region's capability to supply fluid.

Figure 3.15 illustrates the effects of α_c on a dimensionless pressure. As can be seen from the figure, the larger the values of α_c, the longer the transition period from radial to spherical flow. Although all the curves converge at later time, the effects are much less significant compared to those shown on Figure 3.14 for the effects of β.

Lastly, Figure 3.16 demonstrates the effects of r_c. The curves that deviate upward from the infinite radial flow solution are for $\beta=100$ and those that deviate almost horizontally are for $\beta=0.01$. As can be seen from the figure, the smaller the value of r_c, the longer the radial flow period.

Plots similar to these can be used as type curves for estimating r_c, β and α_c. Unlike the case with the linear-radial composite medium, r_c can be uniquely determined from Figure 3.16, because the shape of the initial flow period is not a straight line. At the same time, one can get estimates of $k_1 b$ and α_1 from the match. Once r_c is determined, which gives an estimate of the extent of the fracture that intersects the well, one can then generate a set of type curves similar to those in Figure 3.14 for different values of β with $\frac{\alpha_c}{\beta}=1$ using the r_c value. After finding a match for β, one can then gen-

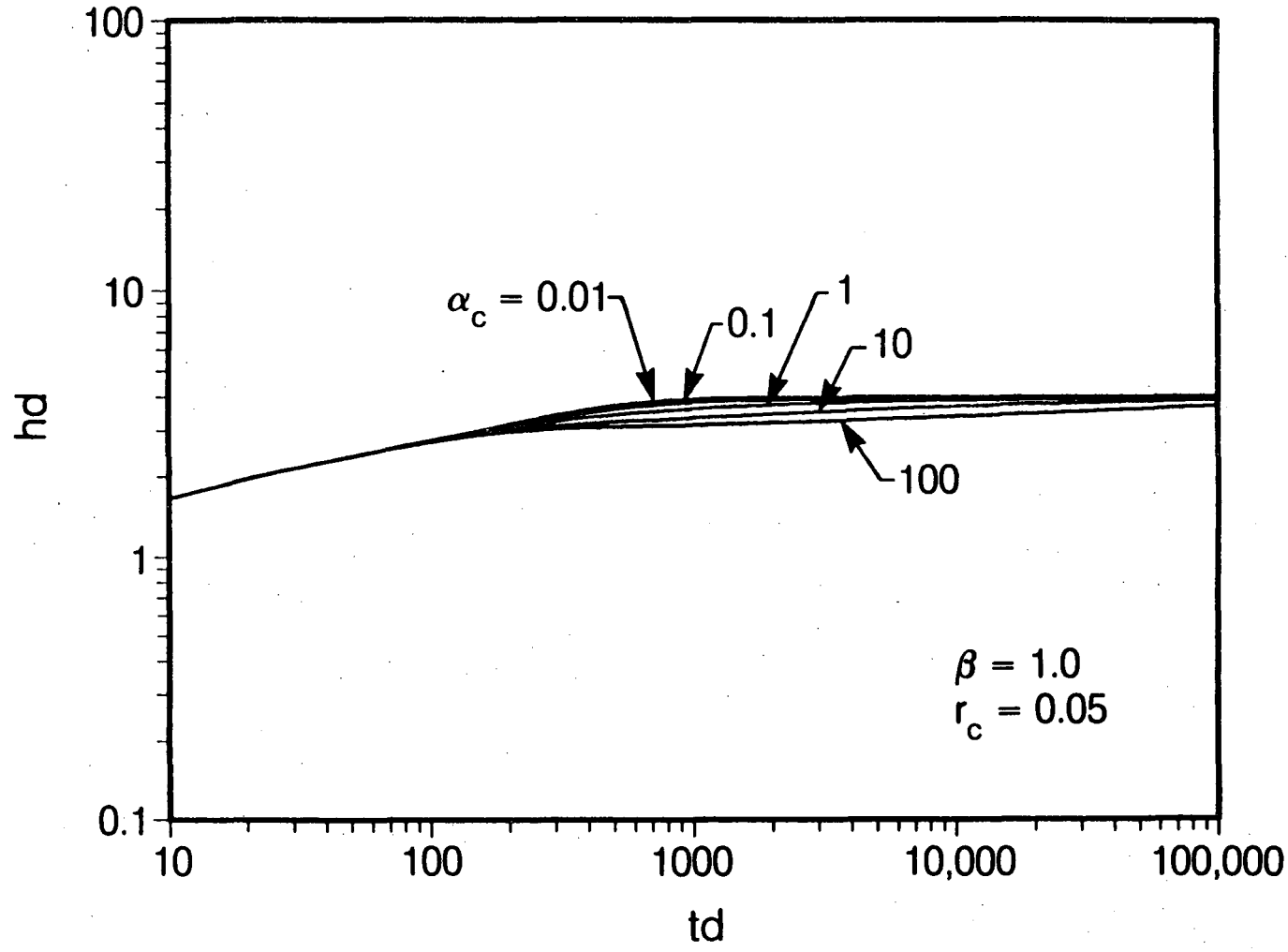

Figure 3.15 h_{D_1} vs. t_D for β=1. and r_c =0.05.

XBL 862-10683

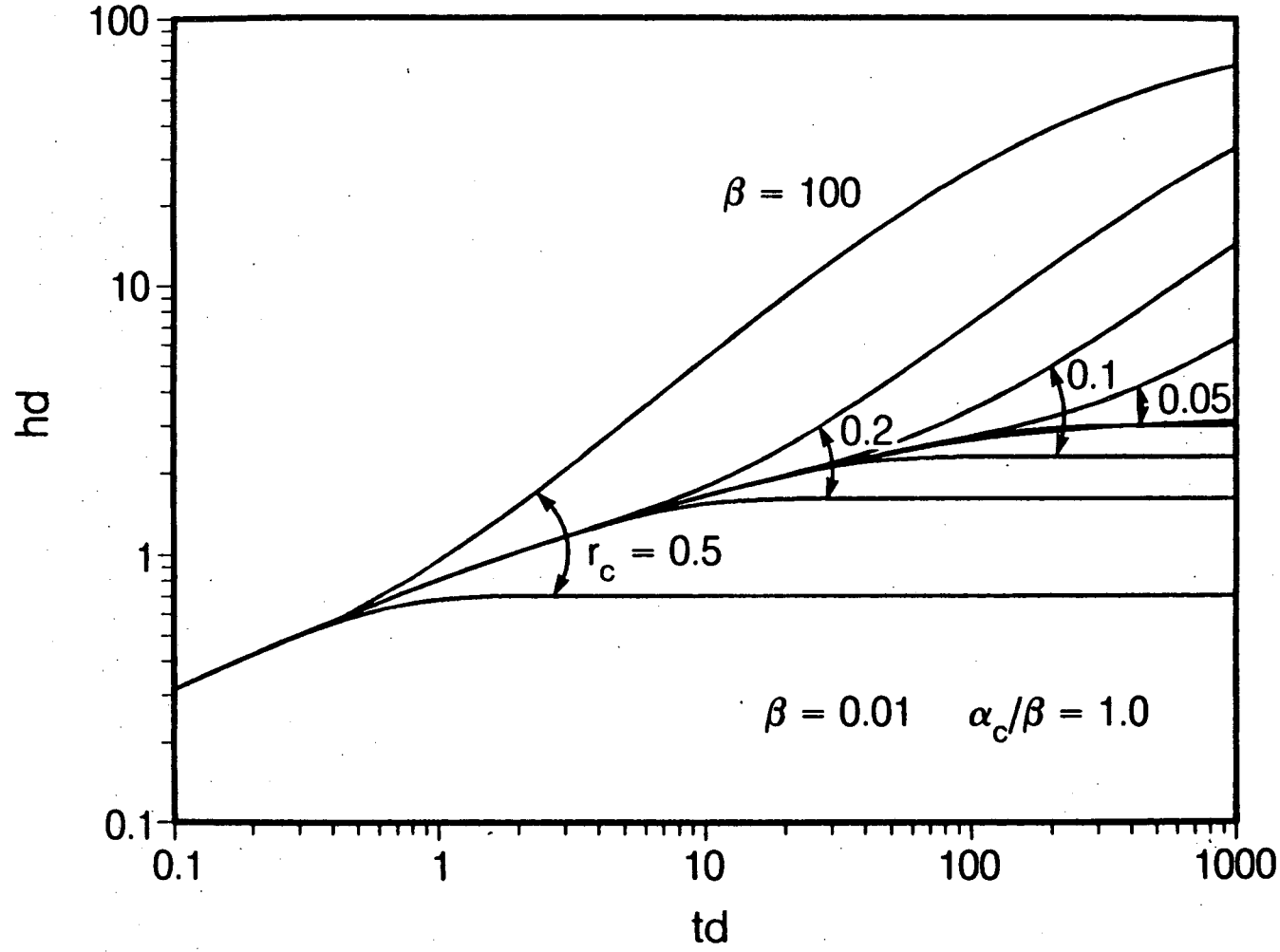

Figure 3.16 h_{D_1} vs. t_D for different values of r_c.

XBL 862-10682

erate type curves for different values of α_c similar to those in Figure 3.15, using the values of β and r_c that have just been determined. In this way, all three parameters r_c, β, and α_c as well as $k_1 b$ and α_1 may be estimated from field data provided that they are free of wellbore storage effects.

3.5. Conclusions

In this chapter, we investigated three types of composite models. The first model was one in which a linear flow develops into a radial flow (or radial flow converging to linear flow), and the second model was a classical radial flow model. Thirdly, we studied a radial-spherical combination. We constructed these models in an attempt to better represent a fracture system under well test conditions.

Many fractured reservoir models are based on the assumption that a fracture system can be treated as one continuum. However, a fracture system is generally highly heterogeneous especially at the fracture scale. The flow characteristic in any given single fracture may be quite different from the macroscopic flow characteristic of the system as a whole. It is probably impossible and may not be necessary to construct an analytical model that accounts for all the heterogeneities. Therefore, the models presented here are based on an assumption that a fracture system can be represented by two concentric regions, i.e., the inner region representing single fracture characteristics and the outer region the average system behavior. Although we have presented three composite models, other combinations may be possible.

We have also shown examples how one of these models may be used to interpret the field data.

In the present chapter, we only considered the case of constant flux. In the next chapter, we will look at slug test models. We will consider models that may be relevant but not limited to fractured medium.

CHAPTER 4

ANALYTICAL MODELS OF SLUG TESTS

4.1. Introduction

Slug tests were originally developed for estimating the flow parameters of shallow aquifers, which are often well approximated as homogeneous porous media. They have also been widely used to estimate the flow parameters of fractured rocks, which are often highly heterogeneous. The attractiveness of slug tests is that they are inexpensive and easy to operate and require a relatively short time to complete. However, available analysis methods for slug tests are limited to a few ideal cases. In this chapter, we will attempt to develop solutions to various models of slug tests that may be applicable in analyzing the results of such tests where existing solutions are inadequate. We then present case studies to demonstrate the use of the new solutions.

Cooper, Bredehoeft and Papadopulos (1967) presented a solution for the change in water level in a finite radius well subjected to a slug test. They obtained the solution from the analogous heat transfer problem in Carslaw and Jaeger (1959). The transient water level $h_s(r_D, t_s)$ at any point in an aquifer normalized to the initial level in the well is:

$$h_s(r_D, t_s) = \frac{2}{\pi} \int_0^\infty e^{-t_s \mu^2/\omega} \frac{\{J_o(\mu r_D) \cdot \Psi(\mu) - Y_o(\mu r_D) \cdot \Phi(\mu)\}}{\Phi^2(\mu) + \Psi^2(\mu)} \cdot d\mu \qquad (4.1.1)$$

where

$$h_s = \frac{h - h_i}{h_0 - h_i} \tag{4.1.2}$$

$$t_s = \frac{2\pi Tt}{C_w} = t_D \cdot \omega \tag{4.1.3}$$

$$\omega = \frac{2\pi r_w^2 S}{C_w} \tag{4.1.5}$$

$$r_D = \frac{r}{r_w} \tag{4.1.6}$$

$$\Phi(\mu) = \mu J_o(\mu) - \omega J_1(\mu) \tag{4.1.7}$$

$$\Psi(\mu) = \mu Y_o(\mu) - \omega Y_1(\mu) \tag{4.1.8}$$

and T is the transmissivity of the formation, S is the storativity of the formation and C_w is the well bore storage. For an open hole slug test, $C_w = \pi r_a^2$ where r_a is the radius of the delivery pipe.

Specifically for $r_D = 1$, or for the water level in the well h_{w_S} is:

$$h_{w_S}(t) = \frac{4\omega}{\pi^2} \int_0^\infty e^{-t_S \mu^2/\omega} \cdot \frac{d\mu}{\mu[\Phi^2(\mu) + \Psi^2(\mu)]} \tag{4.1.9}$$

Cooper et al. evaluated Equation 4.1.9 and presented type curves as shown in Figure 4.1. Figure 4.1 can be used to estimate the transmissivity and the storativity by curve matching.

Some workers have investigated the effects of skin on observed fluid levels (Ramey and Agarwal, 1972; Ramey et al., 1975; and Moench and Hsieh, 1985). Wang et al. (1977) studied cases where tight fractures intersect the

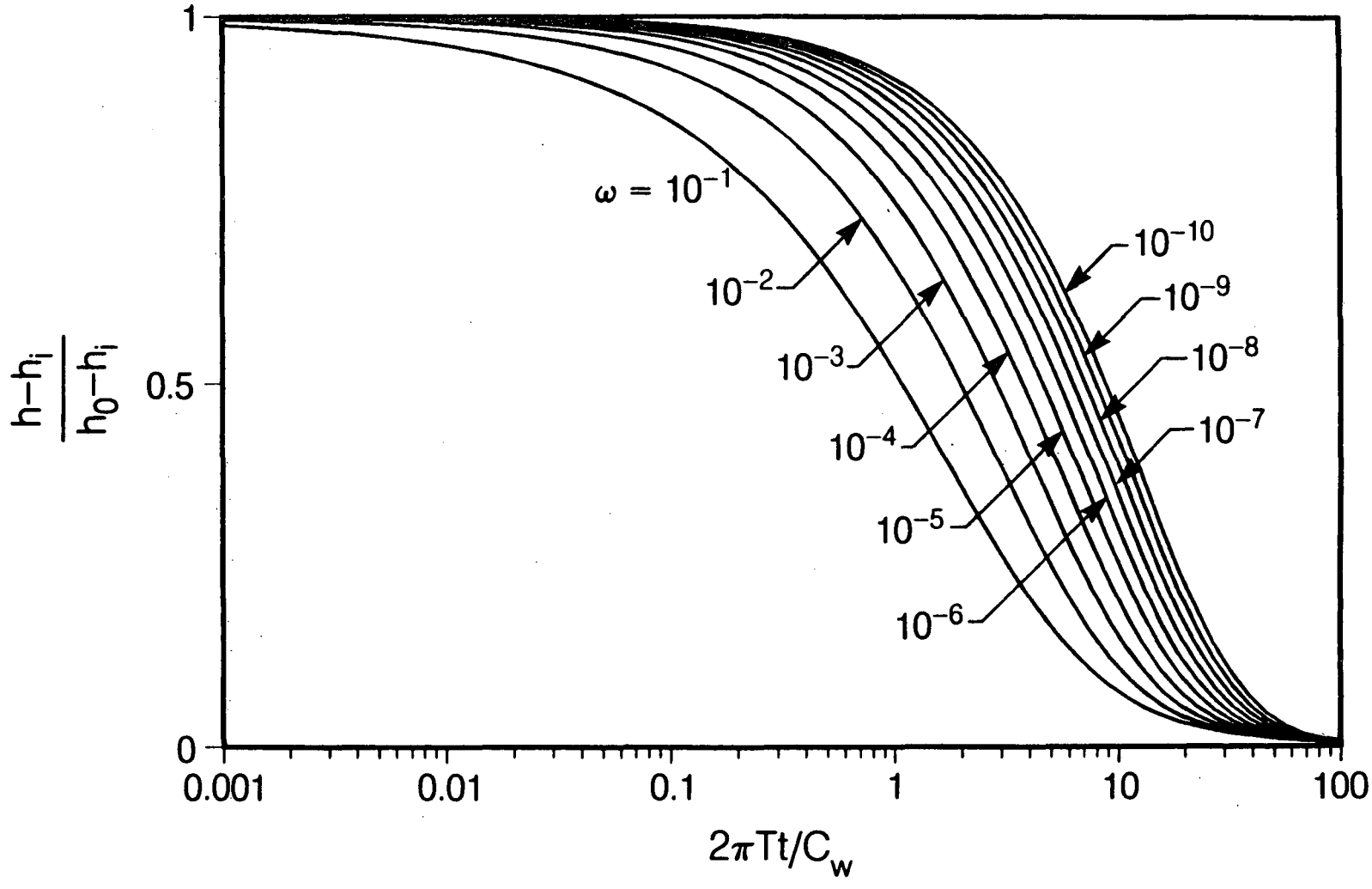

Figure 4.1 Type Curves for radial flow after Cooper et al. (1967).

XBL 861-10565

wellbore. Unlike constant flux tests, however, not many different solutions have been developed for slug tests. In this chapter we will present solutions for various other slug test models.

The Laplace transformation is the analytical tool best suited to problems with the type of inner boundary condition that involve a time derivative as in Equation 2.12. Throughout this chapter, the Laplace transformation is used to eliminate the time variable and solutions are obtained in the Laplace space. Even though analytical inversions are possible following steps similar to those in Chapter 3, the solutions will be in the form of infinite integrals of Bessel functions which converge extremely slowly. Thus, in many cases, solutions must be evaluated numerically, which requires far more intensive computation compared to that needed for a numerical inversion of the solution in Laplace space. In this chapter, therefore, the numerical inversion scheme developed by Stehfest (1970) is used for most cases.

4.2. Linear Flow Model

When a test interval intercepts a large, high-conductivity fracture, the pressure drop along the fracture plane may be negligible, and the flow in the formation may be characterized by one-dimensional flow (Figure 4.2a). One dimensional flow can also occur when the well intersects a vertical fracture (Figure 4.2b) or there is a prevalent channeling within the fracture (Figure 4.2c).

The slug test problem under these conditions can be described by:

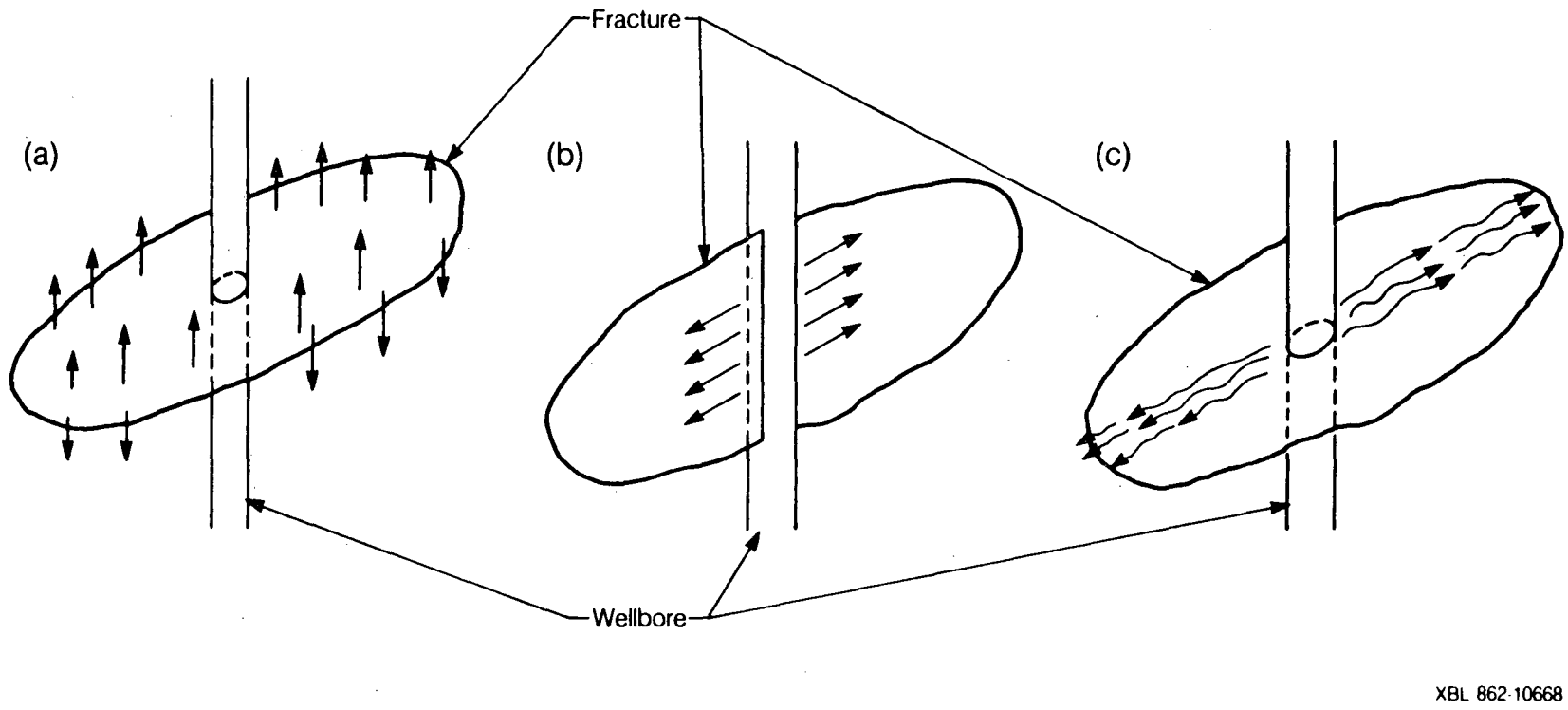

Figure 4.2 Possible geometries that cause a linear flow.

$$\frac{\partial^2 h}{\partial x^2} = \frac{1}{\alpha}\frac{\partial h}{\partial t} \tag{4.2.1}$$

with boundary and initial conditions:

$$kA\frac{\partial h}{\partial x} = C_w \cdot \frac{dh_w}{dt} \qquad (x = 0+,\ t > 0) \tag{4.2.2}$$

$$h(\infty, t) = h_i \tag{4.2.3}$$

$$h(+0, t) = h_w(t) \tag{4.2.4}$$

$$h(x, 0) = h_i \tag{4.2.5}$$

$$h_w(0) = h_0 \tag{4.2.6}$$

The constant A in Equation 4.2.2 describes the area open to flow. The above equations in dimensionless forms are:

$$\frac{\partial^2 h_s}{\partial x_D^2} = \omega\frac{\partial h_s}{\partial t'_s} \tag{4.2.7}$$

$$\frac{\partial h_s}{\partial x_D} = \frac{dh_{w_s}(t_D)}{dt'_s} \qquad (x_D = 0+) \tag{4.2.8}$$

$$h_s(\infty, t'_s) = 0 \tag{4.2.9}$$

$$h_s(+0, t'_s) = h_{w_s}(t'_s) \quad (t'_s > 0) \tag{4.2.10}$$

$$h_s(x_D, 0) = 0 \tag{4.2.11}$$

$$h_{w_s}(0) = 1 \tag{4.2.12}$$

where the dimensionless terms are defined as:

$$x_D = \frac{x}{r_w} \tag{4.2.13}$$

$$t'_s = \frac{kAt}{r_w C_w} \tag{4.2.14}$$

$$\omega = \frac{A \cdot r_w \cdot S_s}{C_w} \tag{4.2.15}$$

After applying the Laplace transformation with respect to time, Eqs. 4.2.7 through 4.2.12 become:

$$\frac{d^2\bar{h}_s}{dx_D^2} = \omega p \bar{h}_s \tag{4.2.16}$$

$$\frac{d\bar{h}_s}{dx_D} = p\bar{h}_s - 1 \qquad (x_D = 0+) \tag{4.2.17}$$

$$\bar{h}_s(\infty) = 0 \tag{4.2.18}$$

The general solution for Equation 4.2.17 is

$$\bar{h}_s = C_1 e^{-\sqrt{\omega p}\, x_D} + C_2 e^{+\sqrt{\omega p}\, x_D} \tag{4.2.19}$$

where C_1 and C_2 are constants.

By applying the boundary condition Equation 4.2.18,

$$\bar{h}_s = C_1 e^{-\sqrt{\omega p}\, x_D} \tag{4.2.20}$$

Using Equation 4.2.17 and solving for C_1,

$$C_1 = \frac{1}{\sqrt{p}\,(\sqrt{p} + \sqrt{\omega})} \tag{4.2.21}$$

Therefore, the solution in Laplace domain becomes

$$\bar{h}_s = \frac{1}{\sqrt{p}\,(\sqrt{p} + \sqrt{\omega})} e^{-\sqrt{\omega p}\, x_D} \tag{4.2.22}$$

The inversion to the real domain can be found in Carslaw and Jaeger (1946) for an analogous problem of heat transfer.

$$h_s = e^{\omega x_D + \omega t'_s} \cdot erfc \left\{ \frac{\sqrt{\omega} x_D}{2\sqrt{t'_s}} + \sqrt{\omega t'_s} \right\} \tag{4.2.23}$$

for $x_D = 0+$, Equation 4.2.23 simplifies to

$$h_D = \frac{h - h_i}{h_0 - h_i} = e^{\omega t'_s} \cdot erfc \sqrt{\omega t'_s} \tag{4.2.24}$$

h_w / h_o versus $\omega t'_s$ is plotted in Figure 4.3. It should be noted that Equation 4.2.24 is a function of $\omega t'_s$ only.

By plotting the observed head normalized to the initial head against time and by superimposing the plot onto Figure 4.3, one would obtain the permeability-storage coefficient product:

$$kS_s = \frac{C_w^2 (\omega t'_s)_{match}}{A^2 \cdot (t)_{match}} \tag{4.2.25}$$

This equation implies that one cannot obtain separate estimates of the permeability and the storage coefficient. Furthermore it will probably be very difficult to estimate the value for A. However, the shape of the pressure response plot is distinctively different from other slug test type curves, i.e., very slow transition occurs from unity to zero, as can be seen in Figure 4.3. Therefore, if such a slow transition is observed, the presence of a linear flow

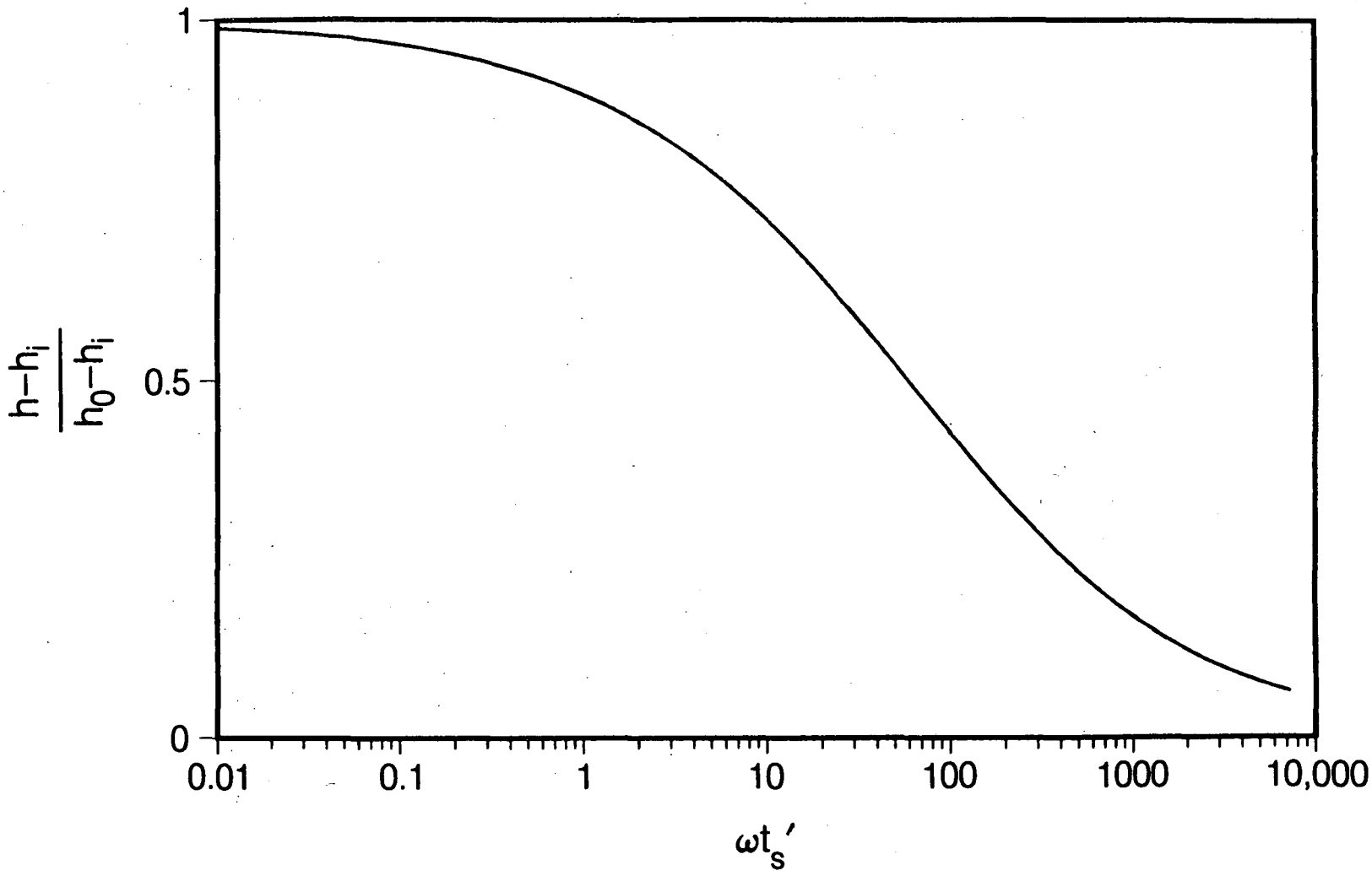

Figure 4.3 Type curve for linear flow.

XBL 861-10581

channel or a large conductivity fracture is could be inferred.

4.3. Radial Flow Models

4.3.1. Interference Analysis of a Slug Test

Cooper et al. (1967) presented a solution which describes the pressure response at any point in a reservoir (Equation 4.1.1). However, they only evaluated the pressure response at the well (Equation 4.1.9). This is because slug tests are ordinarily performed when there is only one well, so that no interference responses are observed. Also, it has been recognized that slug test results reflect the properties of the formation only in the vicinity of the well. As Ferris et al. (1962) stated:

> "the duration of a 'slug' test is very short, hence the estimated transmissivity determined from the test will be representative of only the water-bearing material close to the well"

However, this is not entirely correct. The duration of a slug test and the volume covered by the test are not directly related. As can be seen from Equation 4.1.3, the duration of a slug test is proportional to the wellbore storage and inversely proportional to the transmissivity. The volume of rock that is reflected by well test results does not depend on the time duration of a test but instead it depends on ω, the ratio of formation storativity, S, to the well storage, C_w. Therefore, to be useful a slug test may require a long time to complete in a low transmissivity formation. Yet if the storativity of the formation is large, the results may represent only a small volume of rock. On the other hand, the pressure disturbance could propagate over a fairly

large volume of rock if the storativity is very low. Therefore in some cases interference responses may be observable.

The interference responses to a slug test of wells located at $r_D = 10^2$ and 10^3 are shown in Figure 4.4a and 4.4b, respectively. Figures 4.5a and 4.5b are log-log plots of the same curves. From these figures several observations can be made: (1) Fairly large responses can be observed at a well located as far as 100 meters away for $\omega < 10^{-5}$; (2) In constrast to the responses observed at the injection well, the shapes of the curves are uniquely different from each other even for small values of ω; (3) The transmissivity and the storativity can be estimated independently; (5) A log-log plot enhances the case for a small magnitude response.

Present advances in high sensitivity pressure transducers may permit interference slug tests even in rocks of moderate storativity. Because it would require no additional instrumentation or significant effort, a slug test may be conducted as a supplement to a constant flux test.

The interference response is calculated based on the assumption that the observation well is infinitesimally thin and has no skin. If this assumption does not hold, the observed responses would be different.

4.3.2. Linear Constant Head Boundary

The method of images is commonly used to obtain the dimensionless pressure in a reservoir with linear boundaries. However, a simple superposition of the contributions from the image wells onto the dimensionless pres-

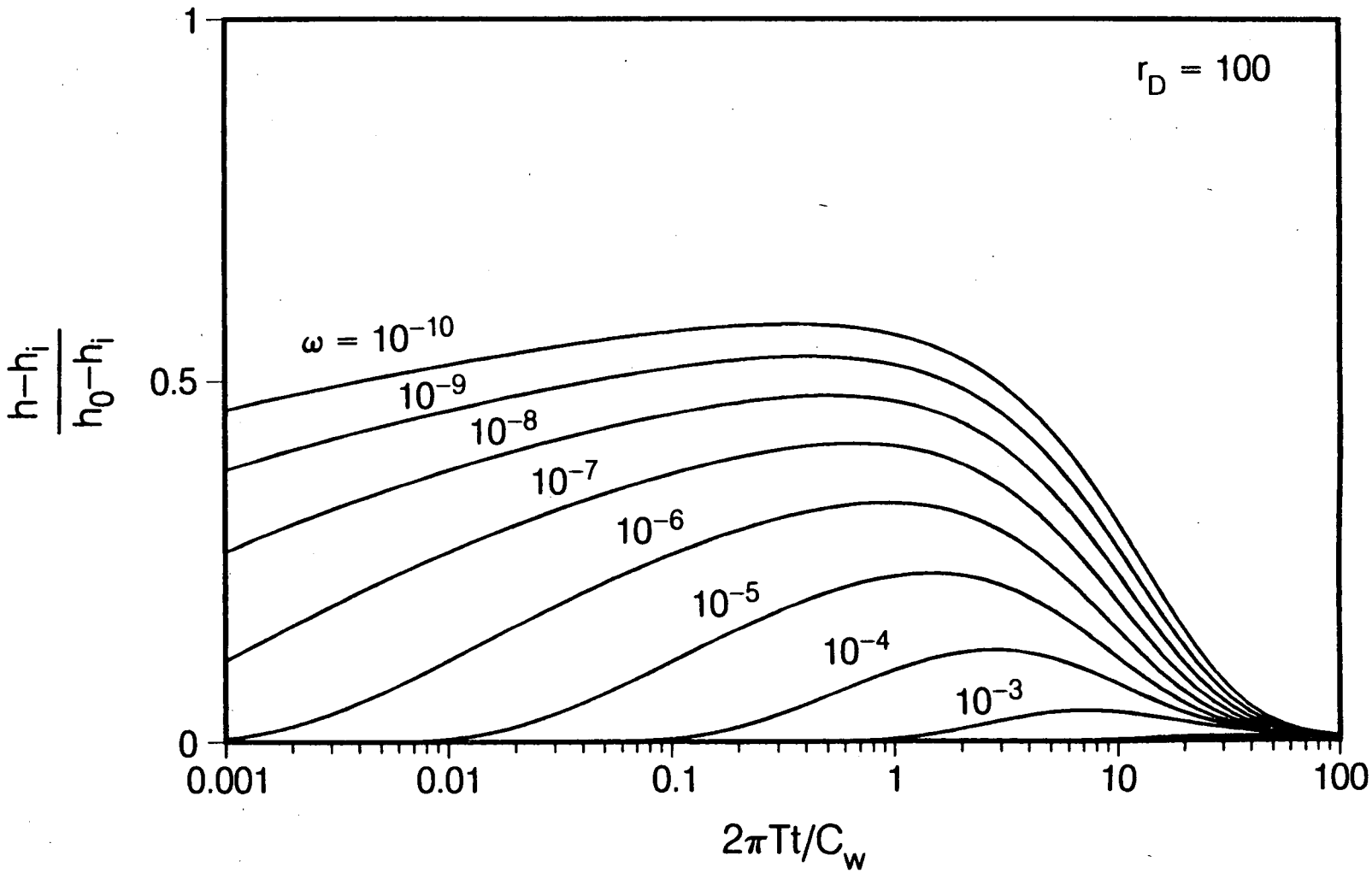

Figure 4.4a Interference responses at $r_D = 10^2$

XBL 861-10570

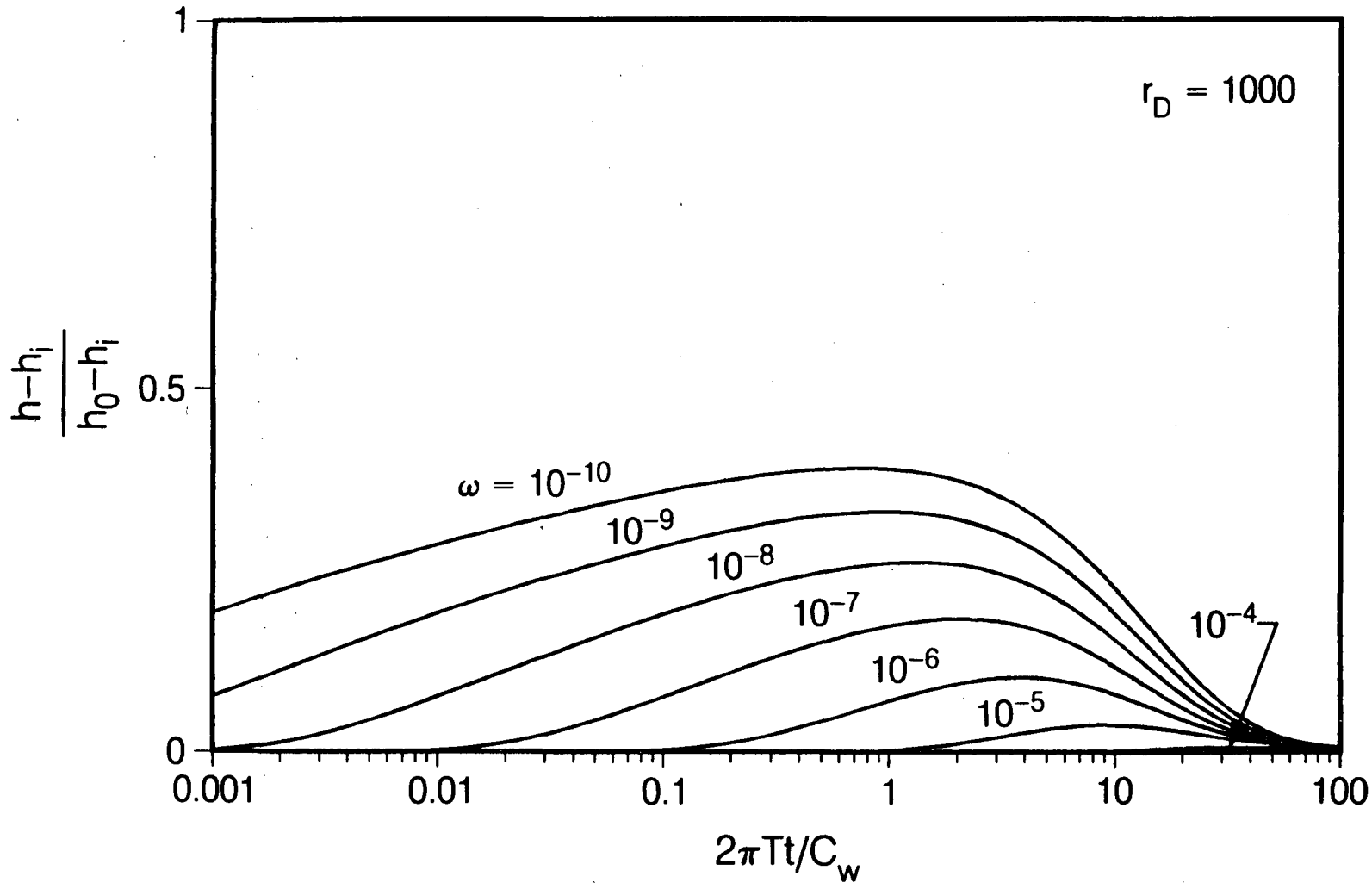

Figure 4.4b Interference responses at $r_D = 10^3$

XBL 861-10571

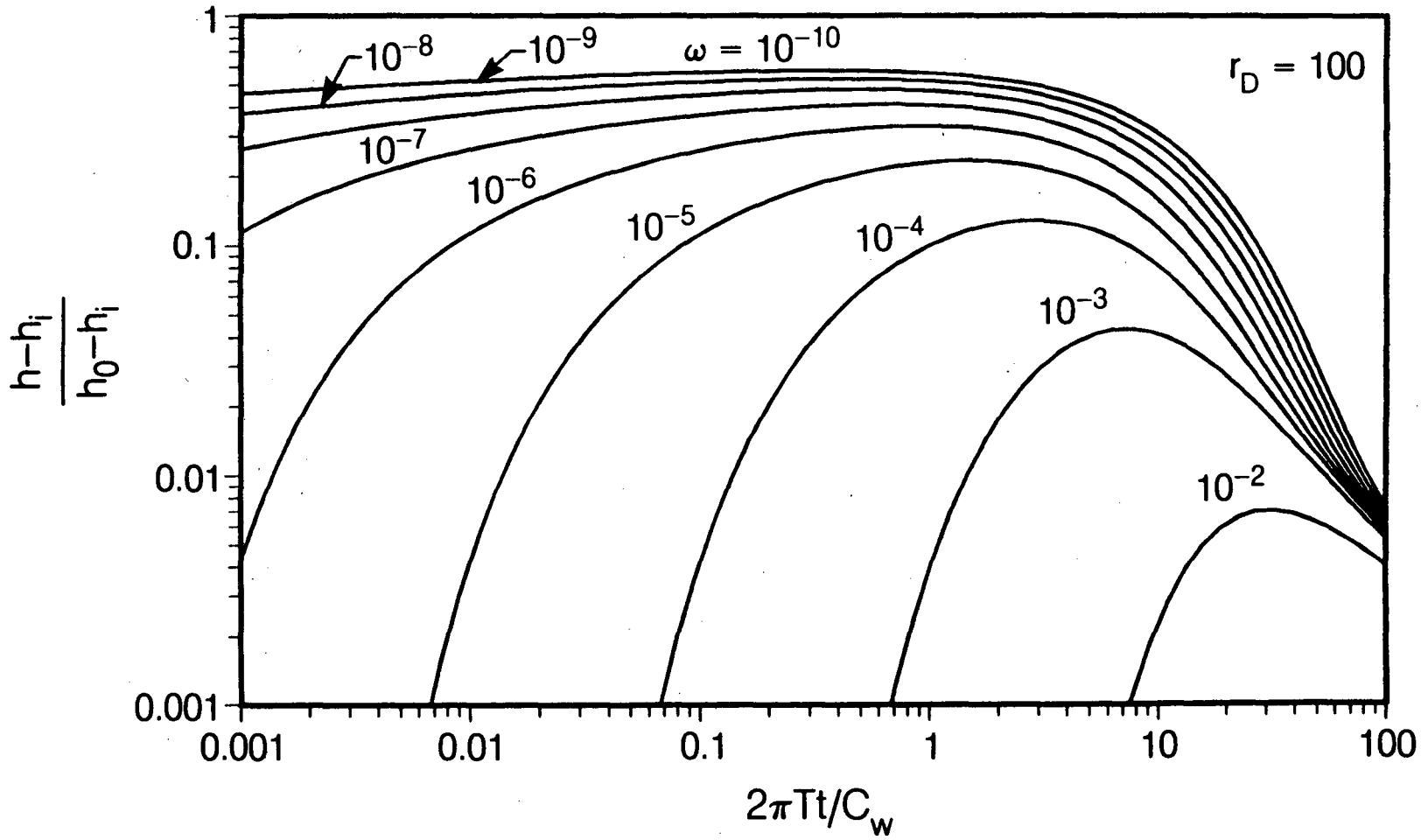

Figure 4.5a Log-log plot of interference responses at $r_D = 10^2$

XBL 861-10572

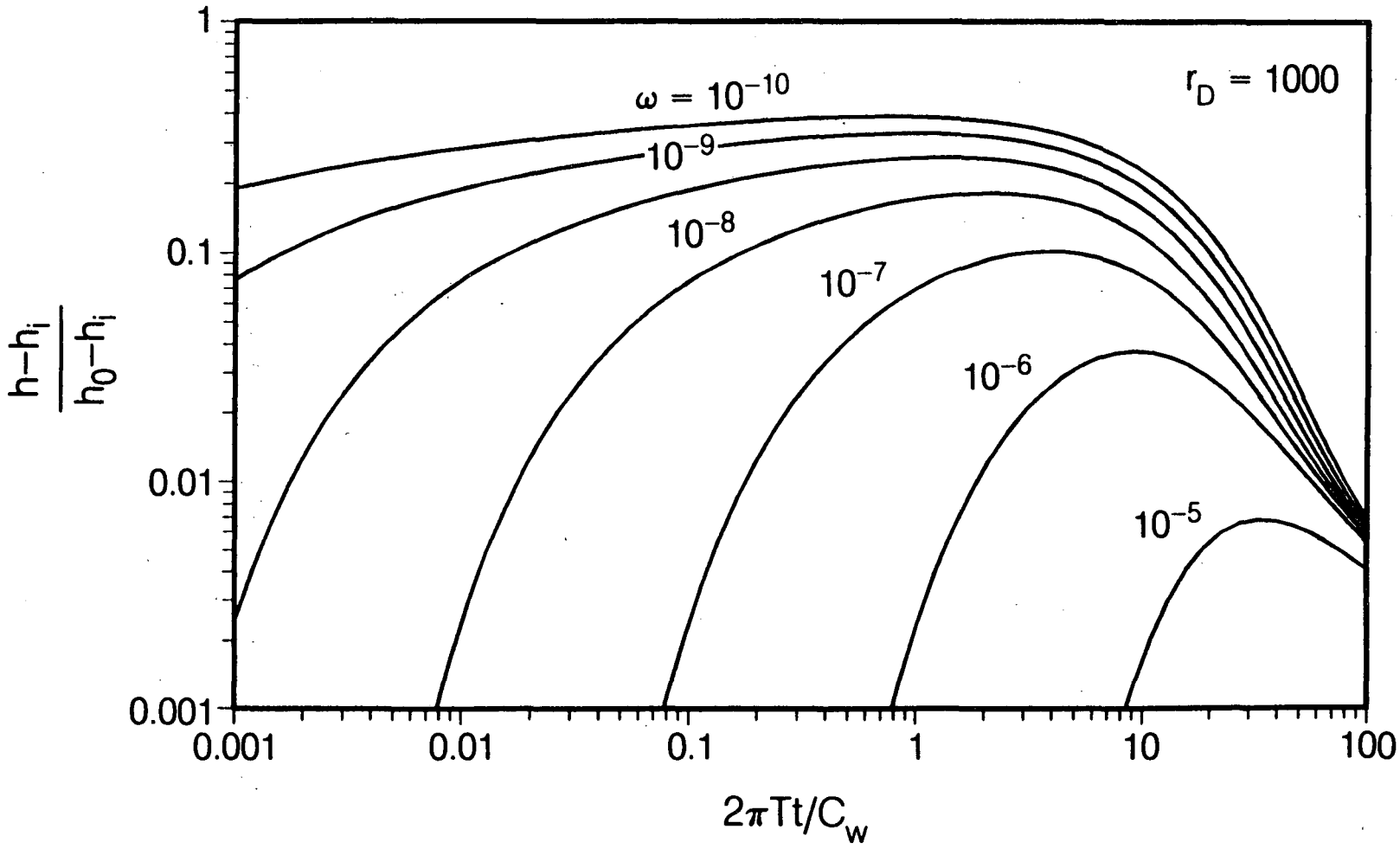

Figure 4.5b Log-log plot of interference responses at $r_D = 10^3$

XBL 861-10569

sure at the real well alone is not theoretically correct when there is an effect of storage at the real well. This is because the real well acts as an observation well with storage in response to the influence of the image wells. Tongpenyai and Raghavan (1981) and Ogbe and Brigham (1984) presented a solution for an interference well with wellbore storage and skin for a constant flux test. An approach similar to theirs can be taken to obtain the water level in slug tests for the case of a linear boundary. The transient water level at the observation well with the same storage as the injection well is superimposed with the solution for an infinite system. The transient pressure response of an aquifer bounded by a linear constant head boundary located at a distance L/r_w can be expressed in Laplace space as:

$$\bar{h}_{w_s} = \frac{K_0(\sqrt{\omega p})}{pK_0(\sqrt{\omega p}) + \sqrt{\omega p}\,K_1(\sqrt{\omega p})} - \frac{\sqrt{\omega p}\,K_1(\sqrt{\omega p})K_0(\sqrt{\omega p}\;2L/r_w)}{[pK_0(\sqrt{\omega p}) + \sqrt{\omega p}\,K_1(\sqrt{\omega p})]^2 - p^2K^2_0(\sqrt{\omega p}\;2L/r_w)} \tag{4.3.1}$$

Equation 4.3.1 is numerically inverted back to real space and evaluated for different values of L/r_w and ω. The results are plotted against t_s in Figures 4.6a-c. As can be seen from the figures, the larger ω and L/r_w are, the smaller the effect of the boundary. However, as ω becomes very small, ($\approx 10^{-9}$), the effect of the boundary can appear even for a large value of L/r_w ($=10^4$). Therefore, if an open hole slug test is used in a formation with very low storativity, a boundary as far as 100 m away could be detected.

The boundary effect can be enhanced if a log-log plot of the pressure

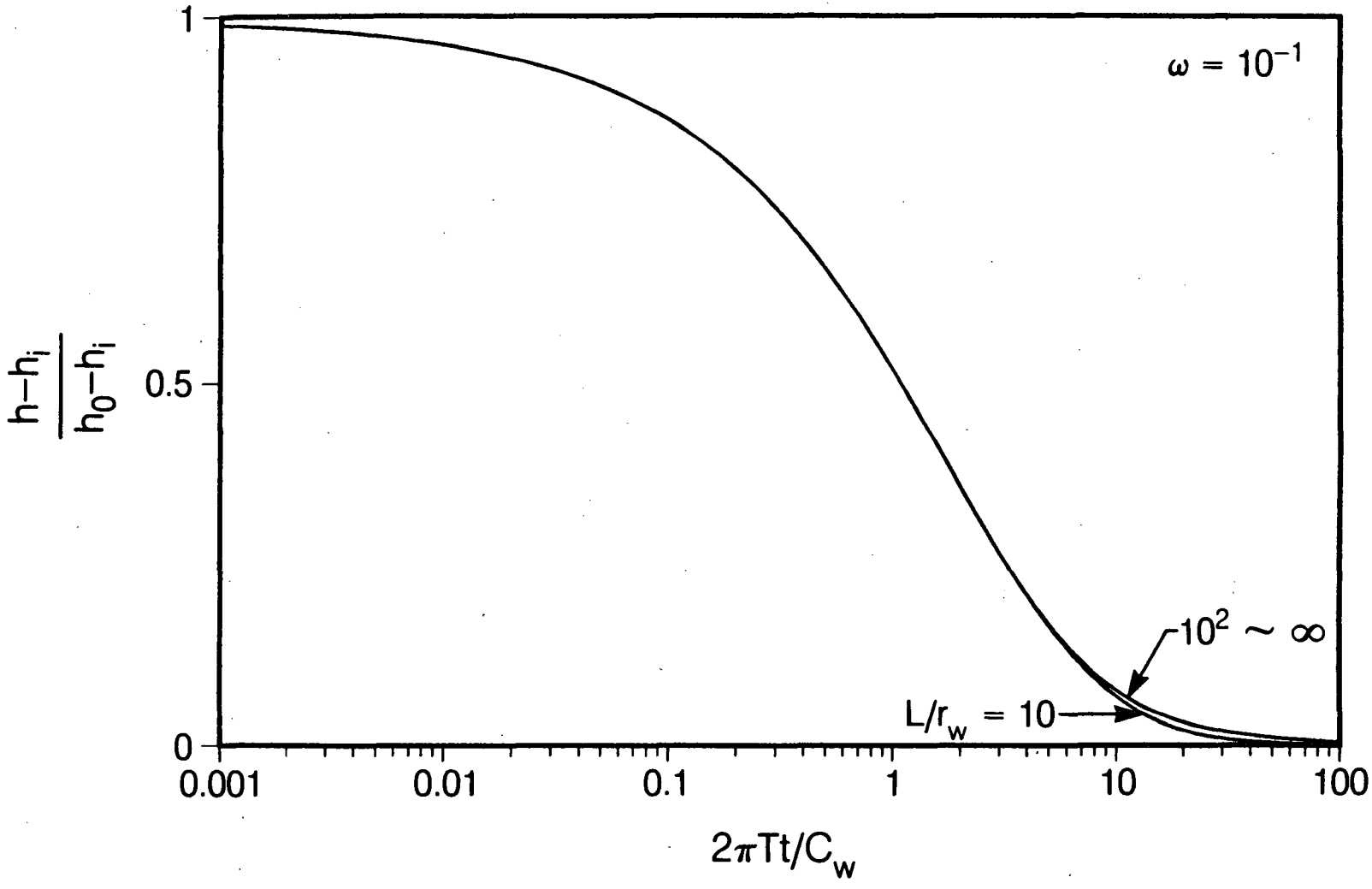

Figure 4.6a Effects of linear constant head boundary for $\omega=10^{-1}$

XBL 861-10566

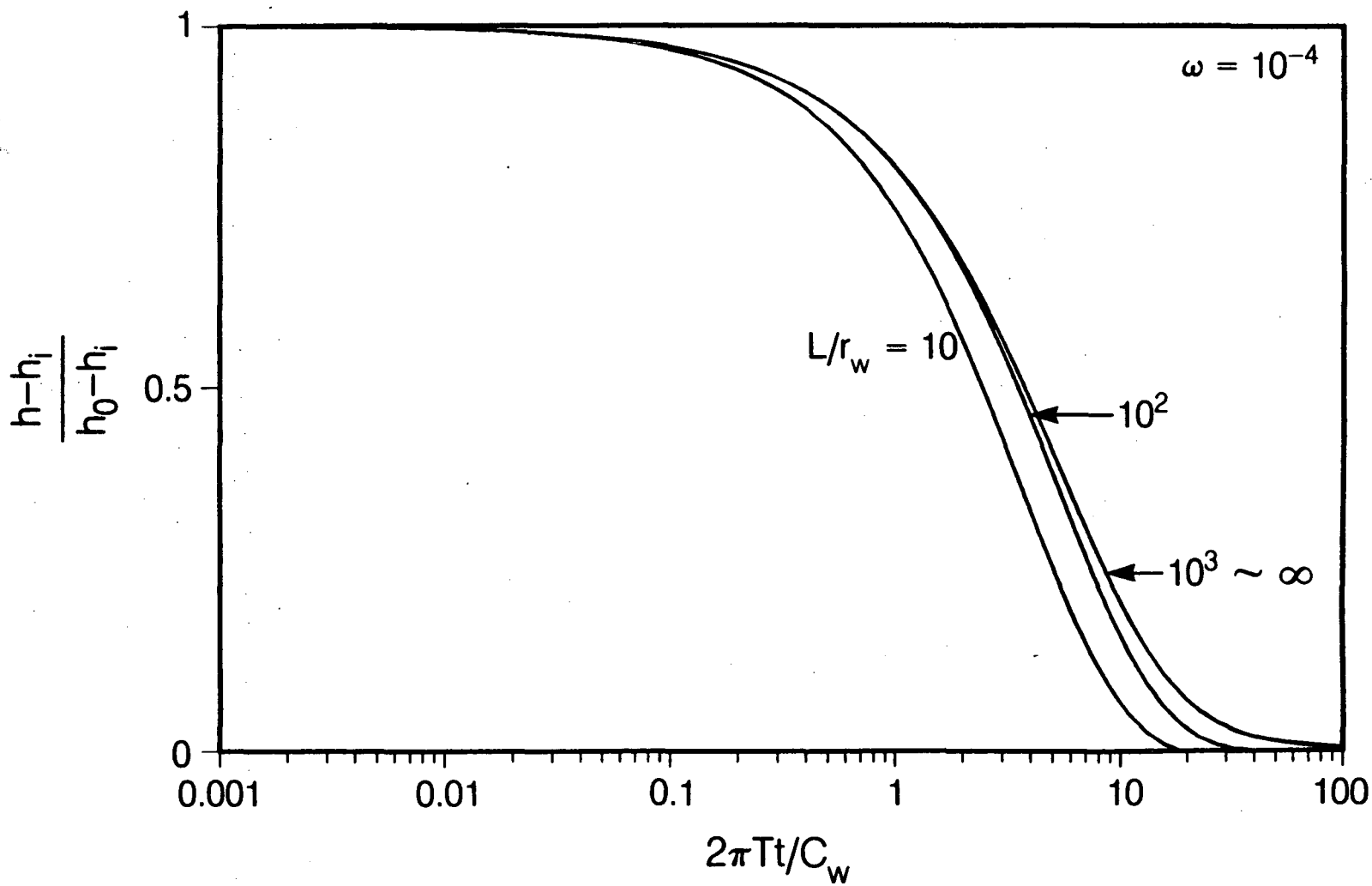

Figure 4.6b Effects of linear constant head boundary for $\omega=10^{-4}$

XBL 861-10564

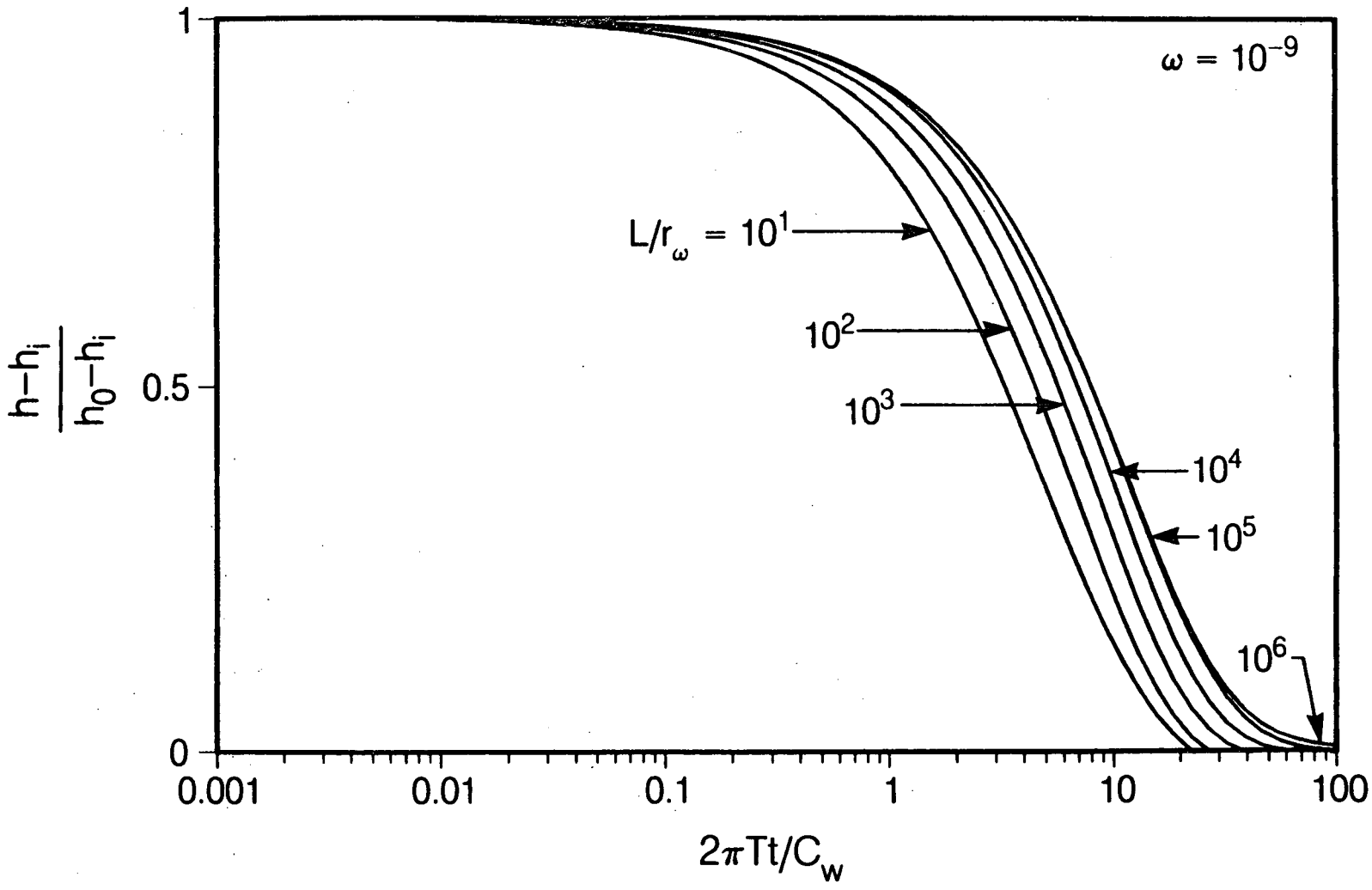

Figure 4.6c Effects of linear constant head boundary for $\omega=10^{-9}$

XBL 861-10568

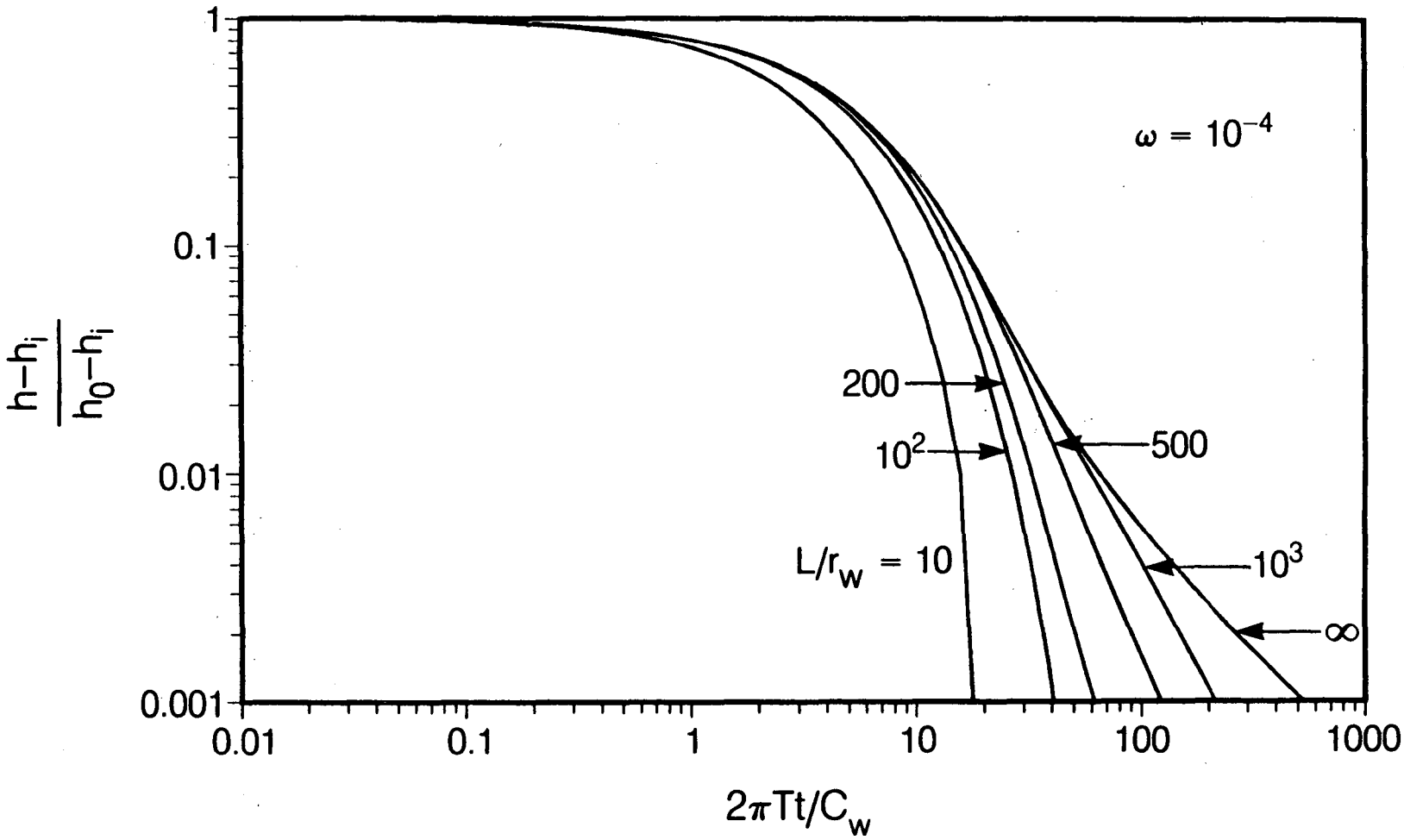

Figure 4.7 Log-log plot of for $\omega=10^{-4}$.

XBL 861-10575

response curve is used as shown in Figure 4.7. Note that for an infinite system, the response curve asymptotes to a slope of minus unity. On the other hand, the curves for a formation with a constant head boundary fall sharply below the unit slope near the end of a test. A log-log plot can generally magnify the effects that occur near the end of the slug test. However, for practical reasons, many tests are terminated before the pressure stabilizes.

4.3.3. Radial Constant Head Boundary

The governing equation and the boundary conditions for a system bounded by a circular constant head boundary are the same as those for an infinite system solved by Cooper et al. (1967) with the exception of the outer boundary condition. The outer boundary condition is now prescribed at the fixed distance R, i.e.,

$$h_s = 0 \quad (r_D = r_e = \frac{R}{r_w}) \tag{4.3.2}$$

The general solution in the Laplace domain becomes

$$\bar{h}_s = A \ K_o(\sqrt{\omega p}\, r_D) + B \ I_o(\sqrt{\omega p}\, r_D) \tag{4.3.3}$$

Applying the inner and outer boundary conditions we obtain:

$$A\,[pK_0(\sqrt{\omega p}\,) + \sqrt{\omega p}\,K_1(\sqrt{\omega p}\,)] + B\,[pI_0(\sqrt{\omega p}\,) - \sqrt{\omega p}\,I_1(\sqrt{\omega p}\,)] - 1 = 0 \tag{4.3.4}$$

$$A \ K_o(\sqrt{\omega p}\, r_e) + B \ I_o(\sqrt{\omega p}\, r_e) = 0 \tag{4.3.5}$$

Solving Equation 4.3.4 and Equation 4.3.5 for A and B, we get

$$A = \frac{-I_o(\sqrt{\omega p}\, r_e)}{K_0(\sqrt{\omega p}\, r_e)[pI_o(\sqrt{\omega p}\,) - \sqrt{\omega p}\,I_1(\sqrt{\omega p}\,)] - I_o(\sqrt{\omega p}\, r_e)[pK_0(\sqrt{\omega p}\,) + \sqrt{\omega p}\,K_1(\sqrt{\omega p}\,)]}$$

(4.3.6)

$$B = \frac{K_o(\sqrt{\omega p}\, r_e)}{K_0(\sqrt{\omega p}\, r_e)[pI_o(\sqrt{\omega p}\,)-\sqrt{\omega p}\, I_1(\sqrt{\omega p}\,)]-I_o(\sqrt{\omega p}\, r_e)[pK_0(\sqrt{\omega p}\,)+\sqrt{\omega p}\, K_1(\sqrt{\omega p}\,)]}$$

(4.3.7)

Therefore, the solution in the Laplace domain becomes:

$$\bar{h}_s = \frac{-I_o(\sqrt{\omega p}\, r_e)\cdot K_0(\sqrt{\omega p}\, r_D)+K_o(\sqrt{\omega p}\, r_e)I_o(\sqrt{\omega p}\, r_D)}{K_0(\sqrt{\omega p}\, r_e)[pI_o(\sqrt{\omega p}\,)-\sqrt{\omega p}\, I_1(\sqrt{\omega p}\,)]-I_o(\sqrt{\omega p}\, r_e)[pK_0(\sqrt{\omega p}\,)+\sqrt{\omega p}\, K_1(\sqrt{\omega p}\,)]}$$

(4.3.8)

Equation 4.3.8 is numerically inverted back to the real space. The normalized pressure responses at the injecting well with a radial constant head boundary at various dimensionless distances (r_e) for ω=10^{-4} and ω=10^{-9} are shown in Figures 4.8a and 4.8b, respectively. As can be seen from these figures, the boundary is undetectable if ω is larger than 10^{-4} and the dimensionless distance to the boundary (r_e) is larger than 500. However, for a much smaller value of ω, (10^{-9}), the boundary effect can be felt at as far as $r_e = 10^5$. Unfortunately, the curves are similar to each other so that it may be difficult to obtain a unique match. If the normalized pressure response is plotted in log-log scale, the late time behavior of a system with a radial constant head boundary can be distinguished from that of an infinite system because the curve for the radial boundary does not follow a straight line of a negative unit slope as can be seen in Figure 4.9.

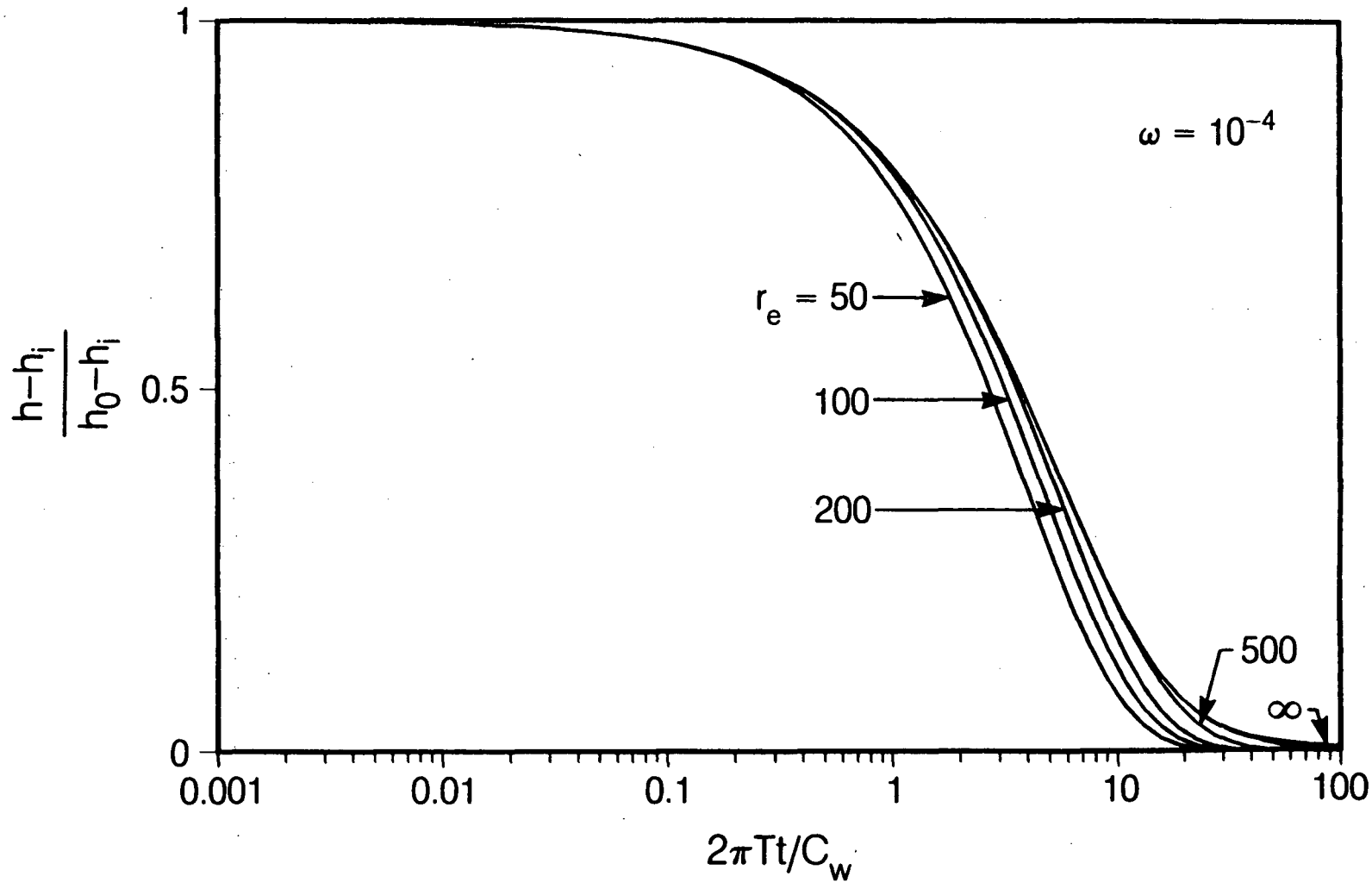

Figure 4.8a Responses to a radial open boundary for $\omega=10^{-4}$.

XBL 861-10573

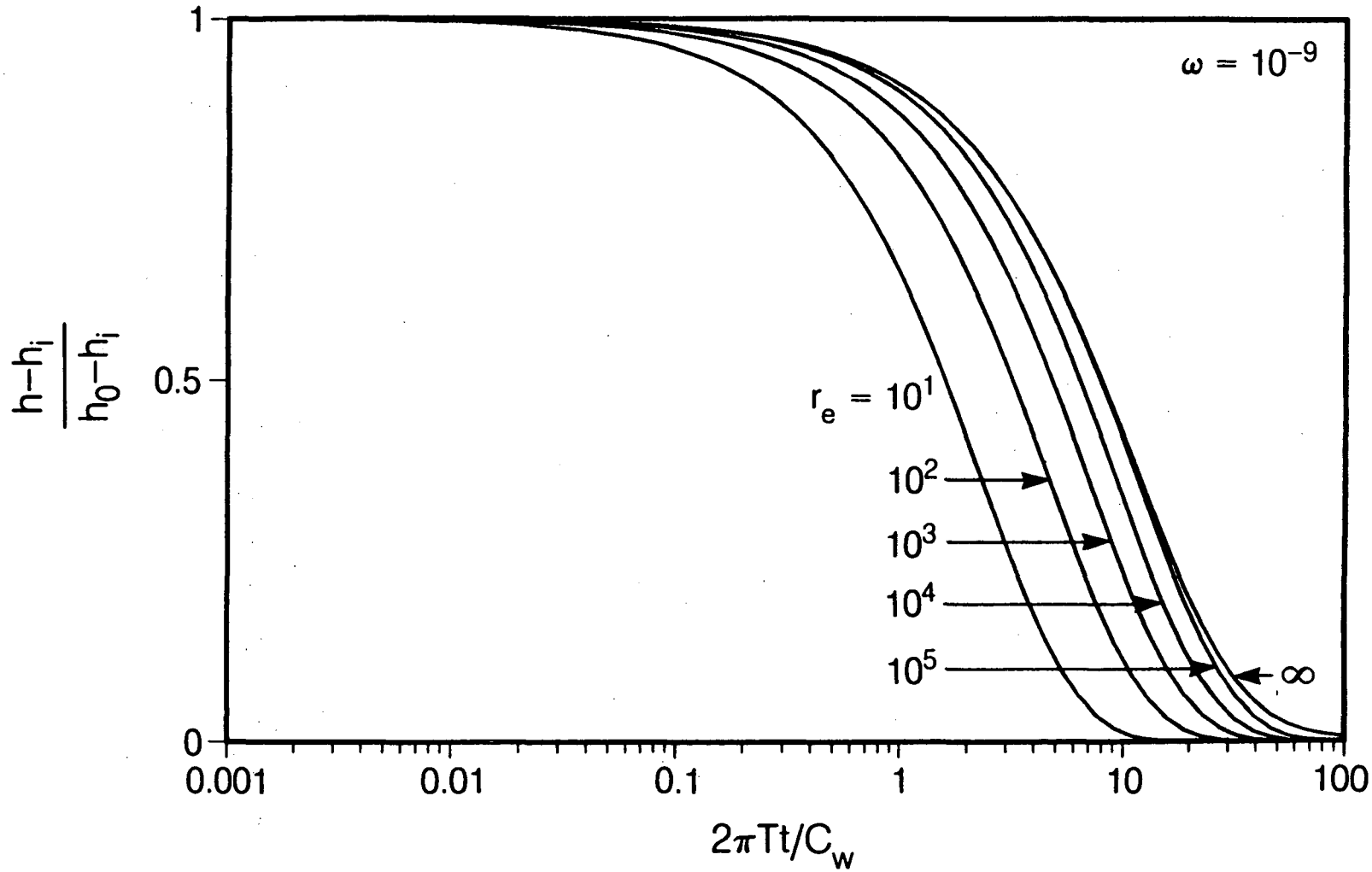

Figure 4.8b Responses to a radial open boundary for $\omega=10^{-9}$.

XBL 861-10567

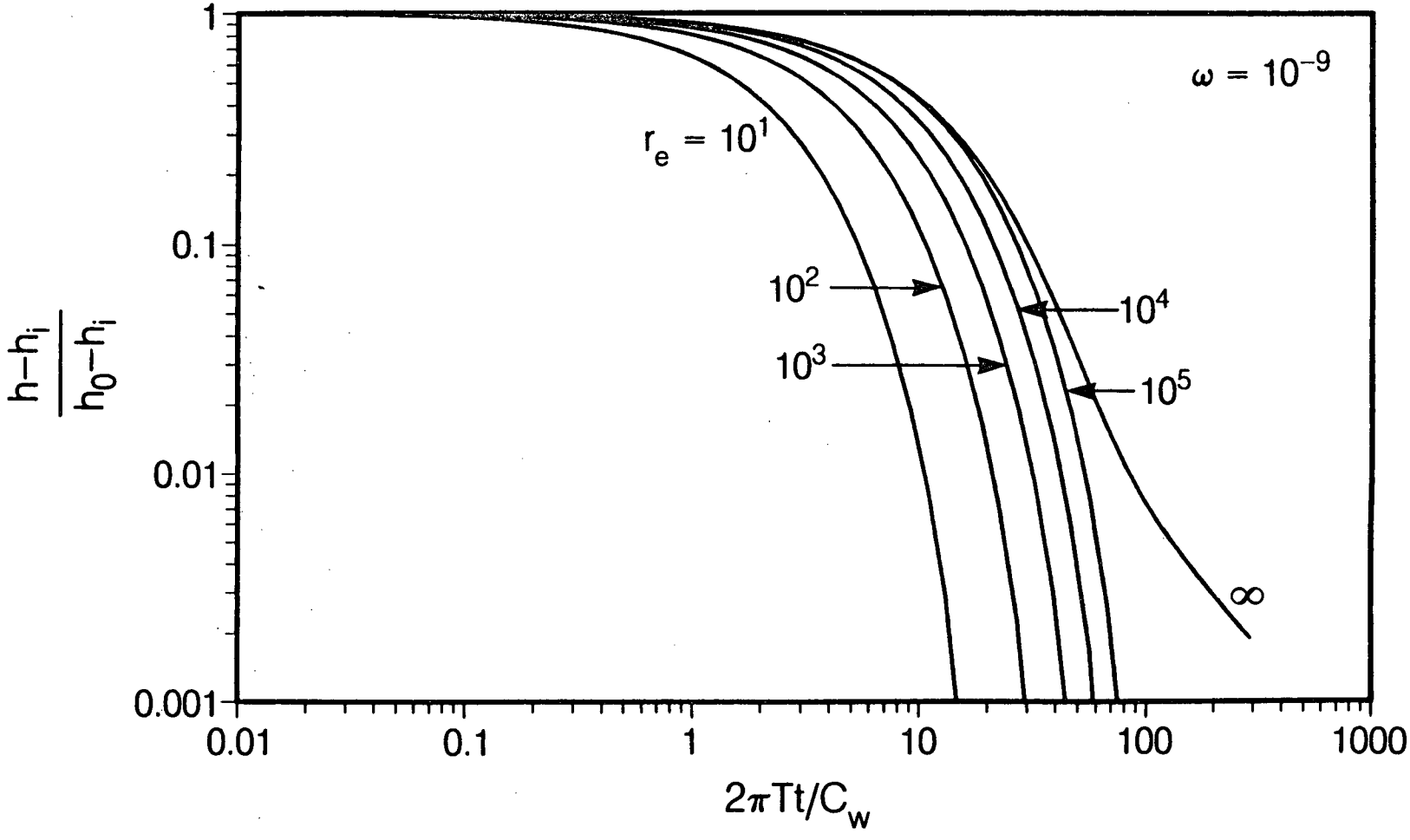

Figure 4.9 Log-log plot for $\omega=10^{-9}$.

XBL 861-10576

4.3.4. Layered Aquifer with No Cross Flow

We consider the pressure response of a well penetrating two layers with different flow properties. The model applies to the case where a well intersects large horizontal fractures or faults that do not have hydraulic connections with each other.

The problem can be cast mathematically as follows.

$$\textit{For layer 1:} \quad \frac{\partial^2 h_1}{\partial r^2} + \frac{1}{r}\frac{\partial h_1}{\partial r} = \frac{1}{\alpha_1}\frac{\partial h_1}{\partial t} \tag{4.3.9}$$

$$\textit{For layer 2:} \quad \frac{\partial^2 h_2}{\partial r^2} + \frac{1}{r}\frac{\partial h_2}{\partial r} = \frac{1}{\alpha_2}\frac{\partial h_1}{\partial t} \tag{4.3.10}$$

The boundary and initial conditions are

$$2\pi r_w T_1 \frac{\partial h_1}{\partial r} + 2\pi r_w T_2 \frac{\partial h_2}{\partial r} = \pi r_a^2 \frac{dh_w}{dt} \quad (r = r_w) \tag{4.3.11}$$

$$h_1(\infty, t) = 0 \tag{4.3.12}$$

$$h_2(\infty, t) = 0 \tag{4.3.13}$$

$$h_1(r_w + 0, t) = h_2(r_w + 0, t) = h_w(t) \quad (t > 0) \tag{4.3.14}$$

$$h_1(r, 0) = h_2(r, 0) = 0 \tag{4.3.15}$$

$$h_w(0) = h_0 \tag{4.3.16}$$

Casting Equations 4.3.9 through Equation 4.3.16 in dimensionless form, we obtain:

$$\frac{\partial^2 h_{s_1}}{\partial r_D^2} + \frac{1}{r_D}\frac{\partial h_{s_1}}{\partial r_D} = \omega \frac{\partial h_{s_1}}{\partial t_D} \tag{4.3.17}$$

$$\frac{\partial^2 h_{s_2}}{\partial r_D^2} + \frac{1}{r_D}\frac{\partial h_{s_2}}{\partial r_D} = \frac{\omega}{\alpha_c}\frac{\partial h_{s_2}}{\partial t_D} \tag{4.3.18}$$

$$\frac{\partial h_{s_1}}{\partial r_D} + \beta \frac{\partial h_{s_2}}{\partial r_D} = \frac{dh_{w_s}}{dt_D} \qquad (r_D = 1) \tag{4.3.19}$$

$$h_{s_1}(\infty, t_D) = 0 \tag{4.3.20}$$

$$h_{s_2}(\infty, t_D) = 0 \tag{4.3.21}$$

$$h_{s_1}(1+0, t_D) = h_{s_2}(1+0, t_D) = h_{w_s}(t_D) \qquad (t_D > 0) \tag{4.3.22}$$

$$h_{s_1}(r_D, 0) = h_{s_2}(r_D, 0) = 0 \tag{4.3.23}$$

$$h_w(0) = 1 \tag{4.3.24}$$

where $\beta = \frac{T_2}{T_1}$, $\alpha_c = \frac{\alpha_2}{\alpha_1} = \frac{\beta}{\gamma}$.

Equation 4.3.17 and Equation 4.3.18 are transformed into the Laplace space using the initial conditions Equation 4.3.23.

$$\frac{d^2 \bar{h}_{s_1}}{dr_D^2} + \frac{1}{r_D}\frac{d\bar{h}_{s_1}}{dr_D} = \omega p \bar{h}_{s_1} \tag{4.3.25}$$

$$\frac{d^2 \bar{h}_{s_2}}{dr_D^2} + \frac{1}{r_D}\frac{d\bar{h}_{s_2}}{dr_D} = \frac{\omega}{\alpha_c} p \bar{h}_{s_2} \tag{4.3.26}$$

Using the boundary condition Equation 4.3.20 and 4.3.21 the general solu-

tions for Equations 4.3.25 and 4.3.26 become

$$\bar{h}_{s_1} = C_1 K_0(\sqrt{\omega p}\, r_D) \tag{4.3.27}$$

$$\bar{h}_{s_2} = C_2 K_0(\sqrt{\omega p / \alpha_c}\, r_D) \tag{4.3.28}$$

From Equation 4.3.22, $\bar{h}_{s_1}(1) = \bar{h}_{s_2}(1)$. Therefore,

$$C_2 = C_1 \frac{K_0(\sqrt{\omega p})}{K_0(\sqrt{\omega p / \alpha_c})} \tag{4.3.29}$$

The inner boundary conditions Equation 4.3.19 and Equation 4.3.24 are transformed to obtain:

$$\frac{d\bar{h}_{s_1}}{dr_D} + \beta \frac{d\bar{h}_{s_2}}{dr_D} = p\bar{h}_{w_s} - 1 \tag{4.3.30}$$

Equation 4.3.27 through 4.3.29 are substituted into 4.3.30 to obtain:

$$\begin{aligned} C_1 = {} & K_0(\sqrt{\omega p / \alpha_c}) \times \\ & \times \Big[pK_0(\sqrt{\omega p})K_0(\sqrt{\omega p / \alpha_c}) + \sqrt{\omega p}\, K_1(\sqrt{\omega p})K_0(\sqrt{\omega p / \alpha_c}) + \\ & + \beta(\sqrt{\omega p / \alpha_c}\, K_0(\sqrt{\omega p})K_1(\sqrt{\omega p / \alpha_c}) \Big]^{-1} \end{aligned} \tag{4.3.31}$$

Therefore, the solution in the Laplace space at $r_D = 1$ becomes

$$\begin{aligned} \bar{h}_{s_1}(1) = \bar{h}_{s_2}(1) = {} & K_0(\sqrt{\omega p})K_0(\sqrt{\omega p / \alpha_c}) \times \\ & \times \Big[pK_0(\sqrt{\omega p})K_0(\sqrt{\omega p / \alpha_c}) + \sqrt{\omega p}\, K_1(\sqrt{\omega p})K_0(\sqrt{\omega p / \alpha_c}) + \\ & + \beta(\sqrt{\omega p / \alpha_c}\, K_0(\sqrt{\omega p})K_1(\sqrt{\omega p / \alpha_c}) \Big]^{-1} \end{aligned} \tag{4.3.32}$$

Equation 4.3.32 is inverted back to the real space using the alogrithm introduced by Stehfest (1970). Figures 4.10a and 4.10b show the normalized

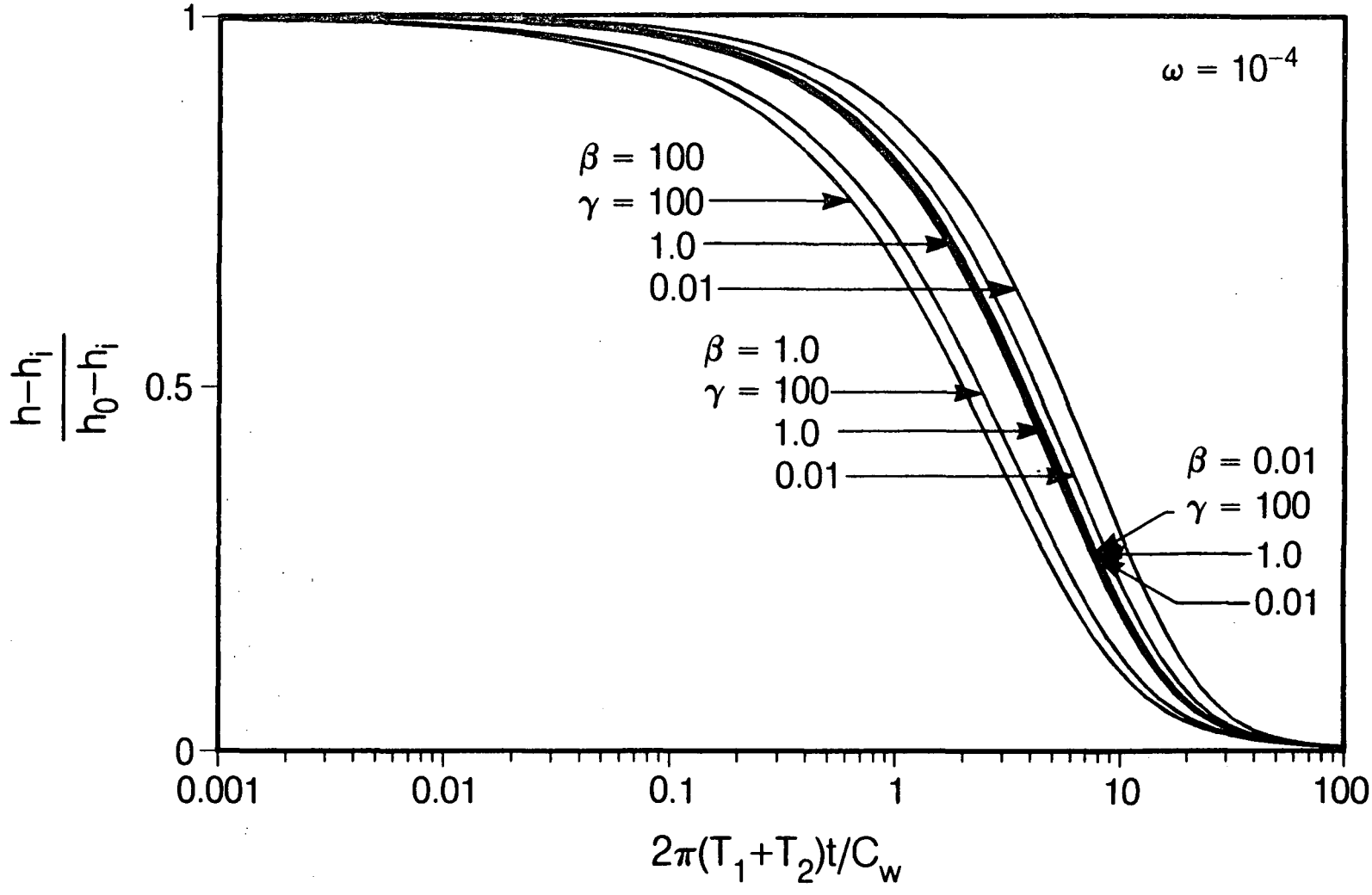

Figure 4.10a Response of a two-layered aquifer for $\omega=10^{-4}$

XBL 861-10577

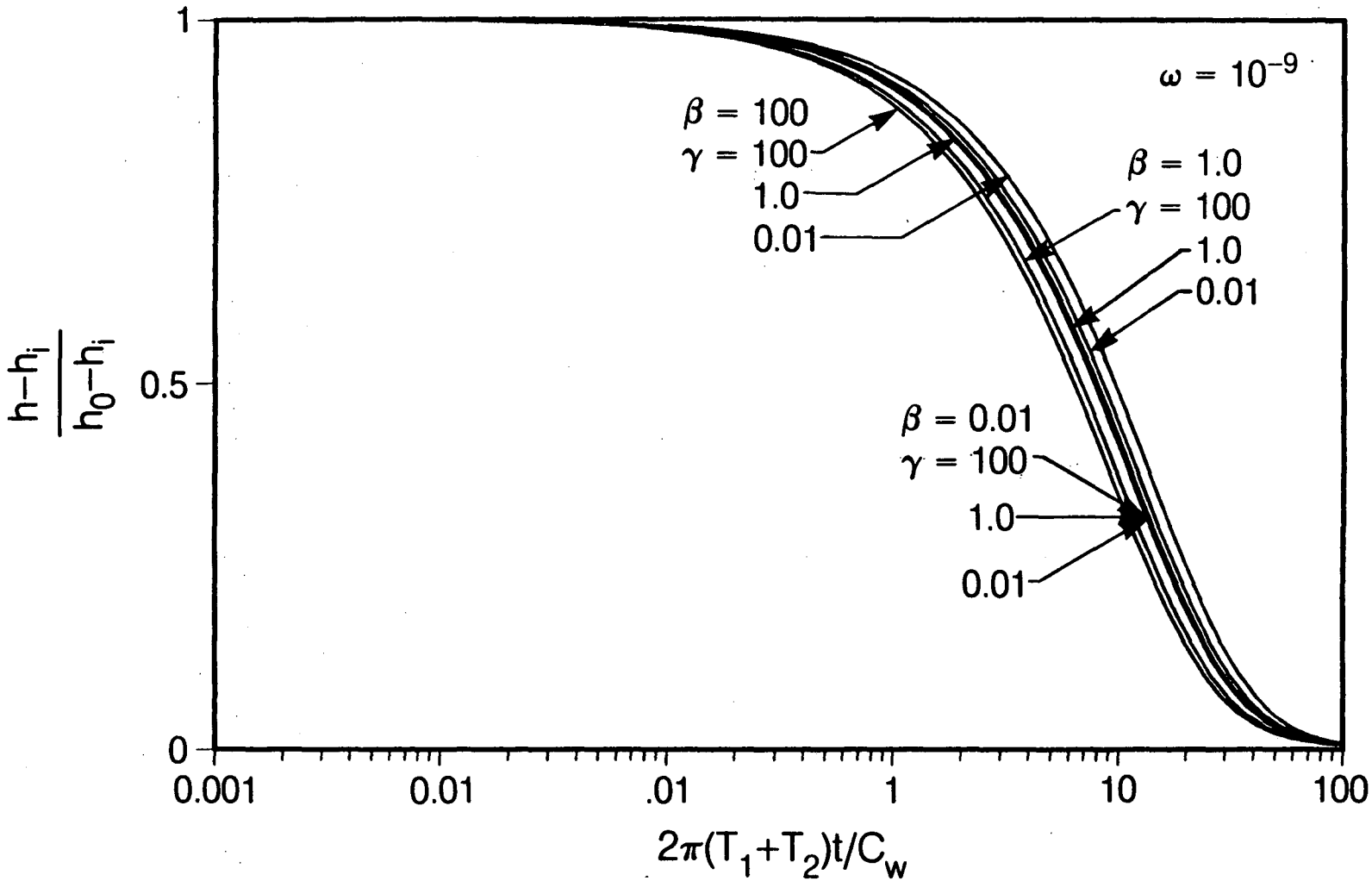

Figure 4.10b Response of a two-layered aquifer for $\omega=10^{-9}$

XBL 861-10578

pressure responses when ω of one of the layers is 10^{-4} and 10^{-9}, respectively. The curves are plotted for different values of β and γ. From these figures, the following observations are pertinent. The behavior of a two layer system is similar to that of one layer system with the equivalent transmissivity equal to the arithmetic sum of the two. The dimensionless storage ω obtained by analysing a two layer system is nearly equal to that of the ω value of the layer with the larger transmissivity if $\beta >> 1$ or $\beta << 1$. For $\beta \approx 1$, ω is the arithmetic average of the two ω values. Therefore, it is probably impossible to distinguish a two layer system from a one layer system. This should hold for multiple layered systems of more than two layers. A similar conclusion has been made for constant flux tests (Lefkovits et al., 1981; Russell and Prats, 1962).

4.3.5. Linear-Radial Flow Model

We will now consider the case when there is a linear flow region around the injection well. A linear flow may be caused by a vertical fracture intersecting the wellbore or by a channeling. Outside of the inner region it is assumed that the flow is, on the average, radial. The model is a linear and radial composite model similar to the problem discussed in Chapter 3.2 for constant rate pumping test. Therefore, the descriptions for the model in Chapter 3.2.1 apply. Only the inner boundary condition is different from the problem statement in Chapter 3.2.1.

Recalling the governing equations for the inner and outer regions in Chapter 3.2.1,

$$\frac{\partial^2 h_1}{\partial r^2} = \frac{1}{\alpha_1}\frac{\partial h_1}{\partial t}, \tag{3.2.1a}$$

$$\frac{\partial^2 h_2}{\partial r^2} + \frac{1}{r}\frac{\partial h_2}{\partial r} = \frac{1}{\alpha_2}\frac{\partial h_2}{\partial t}. \tag{3.2.1b}$$

The inner boundary condition is of the same type as Equation 2.12 involving a time derivative:

$$nk_1 bH \frac{\partial h_1}{\partial r}\bigg|_{r = r_w + 0} = C_w \frac{dh_w}{dt}, \tag{4.3.23}$$

where $C_w = \pi r_a^2$ for an open well test whose casing radius is r_a, in which the water level h_w changes. And the relation between h_1 and h_w is:

$$h_1(r_{w+0}, t) = h_w(t). \tag{4.3.24}$$

The outer boundary condition is that for a infinite medium:

$$h_2(\infty, t) = h_i \tag{4.3.25}$$

The initial conditions are:

$$h_w(0) = h_0 \tag{4.3.26}$$

$$h_1(r, 0) = h_i \qquad (r_w < r \leq r_f) \tag{4.3.27}$$

$$h_2(r, 0) = h_i \qquad (r_f \leq r \leq \infty) \tag{4.3.28}$$

The continuity requirements at the interface of the inner and outer regions

are as follows:

$$h_1 = h_2 \quad (r = r_f) \tag{4.3.29}$$

$$nk_1 b \frac{\partial h_1}{\partial r} = 2\pi r_f \, k_2 \frac{\partial h_2}{\partial r} \quad (r = r_f) \; . \tag{4.3.30}$$

Dimensionless parameters are defined as:

$$h_s = \frac{h - h_i}{h_0 - h_i} \tag{4.1.2}$$

$$t_D = \frac{2\pi T_2 t}{C_w} \cdot \frac{1}{\omega} = \frac{2\pi T_2 t}{C_w} \cdot \frac{C_w}{2\pi r_f^2 S_2} = \frac{\alpha_2 t}{r_f^2} \tag{4.3.31}$$

$$r_D = \frac{r}{r_f} \tag{3.2.7c}$$

$$r_c = \frac{r_w}{r_f} \, , \tag{3.2.7d}$$

$$\alpha_c = \frac{\alpha_1}{\alpha_2} \tag{3.2.7e}$$

$$\beta = \frac{nk_1 b}{2\pi r_f \, k_2} \tag{3.2.7f}$$

$$\omega = \frac{2\pi r_f^2}{C_w} S_2 \, , \tag{4.3.32}$$

Therefore, the governing equations in dimensionless form become:

$$\frac{\partial^2 h_{s_1}}{\partial r_D^2} = \frac{1}{\alpha_c} \frac{\partial h_{s_1}}{\partial t_D} \tag{4.3.33}$$

$$\frac{\partial^2 h_{s_2}}{\partial r_D^2} + \frac{1}{r_D}\frac{\partial h_{s_2}}{\partial r_D} = \frac{\partial h_{s_1}}{\partial t_D} \tag{4.3.34}$$

The boundary, initial, and interface conditions corresponding to Equations 4.3.23 through 4.3.29 are now:

$$\frac{\partial h_{s_1}}{\partial r_D} = \frac{1}{\omega\beta}\frac{dh_{ws}}{dt_D} \qquad (r_D = r_c) \ , \tag{4.3.35}$$

$$h_{s_1}(r_{c+0}, t_D) = h_{ws}(t_D) \ , \tag{4.3.36}$$

$$h_{s_2}(\infty, t_D) = 0 \tag{4.3.37}$$

$$h_{w_s}(0) = 1 \tag{4.3.38}$$

$$h_{s_1}(r_D, 0) = 0 \qquad (r_C < r_D \leq 1) \tag{4.3.39}$$

$$h_{s_2}(r_D, 0) = 0 \qquad (1 \leq r_D \leq \infty) \tag{4.3.40}$$

$$h_{s_1} = h_{s_2} \qquad (r_D = 1) \tag{4.3.41}$$

$$\frac{\partial h_{s_1}}{\partial r_D} = \frac{1}{\beta}\frac{\partial h_{s_2}}{\partial r_D} \qquad (r_D = 1) \tag{4.3.42}$$

The Laplace transformation of the governing equations 4.3.33 and 4.3.34 with the initial conditions in 4.3.39 and 4.3.40 yield the following subsidiary equations:

$$\frac{d^2\overline{h}_{s_1}}{dr_D^2} = \frac{p}{\alpha_c}\overline{h}_{s_1} \tag{4.3.43}$$

$$\frac{d^2\bar{h}_{s_2}}{dr_D^2} + \frac{1}{r_D} \cdot \frac{d\bar{h}_{s_2}}{dr_D} = p\bar{h}_{s_2} \tag{4.3.44}$$

The transformed boundary and interface conditions are:

$$\frac{d\bar{h}_{s_1}}{dr_D} = \frac{1}{\omega\beta}\,[p\bar{h}_{s_1} - 1] \quad (r_D = r_c) \tag{4.3.45}$$

$$\bar{h}_{s_2}(\infty, t_D) = 0 \tag{4.3.46}$$

$$\bar{h}_{s_1} = \bar{h}_{s_2} \qquad (r_D = 1) \tag{4.3.47}$$

$$\frac{d\bar{h}_{s_1}}{dr_D} = \frac{1}{\beta}\,\frac{d\bar{h}_{s_2}}{dr_D} \qquad (r_D = 1) \tag{4.3.48}$$

The general solutions to the Equations 4.3.43 and 4.3.44 are:

$$\bar{h}_{s_1} = A\ \cosh\left(\sqrt{p/\alpha_c} \cdot r_D\right) + B \sinh\left(\sqrt{p/\alpha_c} \cdot r_D\right) \tag{4.3.49}$$

$$\bar{h}_{s_2} = C\ I_0(\sqrt{p} \cdot r_D) + D\ K_0(\sqrt{p} \cdot r_D) \tag{4.3.50}$$

Equation 4.3.46 requires $C=0$ in 4.3.50. Applying the boundary condtions 4.3.45, 4.3.47 and 4.3.48, we obtain:

$$A\sqrt{p/\alpha_c}\ \sinh\left(\sqrt{p/\alpha_c} \cdot r_c\right) + B\sqrt{p/\alpha_c}\ \cosh\left(\sqrt{p/\alpha_c} \cdot r_c\right)$$

$$= \frac{1}{\omega\beta}\left\{p\,[A\ \cosh\left(\sqrt{p/\alpha_c} \cdot r_c\right) + B\ \sinh\left(\sqrt{p/\alpha_c} \cdot r_c\right)] - 1\right\} \tag{4.3.51}$$

$$A\ \cosh\sqrt{p/\alpha_c} + B\ \sinh\sqrt{p/\alpha_c} = DK_0(\sqrt{p}) \tag{4.3.52}$$

$$A\sqrt{p/\alpha_c}\sinh\sqrt{p/\alpha_c}+B\sqrt{p/\alpha_c}\cosh\sqrt{p/\alpha_c}=-\frac{D}{\beta}\sqrt{p}\;K_1(\sqrt{p}) \quad (4.3.53)$$

We now solve Equations 4.3.51 through 4.3.53 for A, B, and D. After a lengthy manipulation, we obtain:

$$A=\frac{\sqrt{\alpha_c}}{\beta\sqrt{p}\,\Delta}\times\left\{\sqrt{\alpha_c}K_1(\sqrt{p})\sinh\sqrt{p/\alpha_c}+\beta K_0(\sqrt{p})\cosh\sqrt{p/\alpha_c}\right\} \quad (4.3.54)$$

$$B=\frac{\sqrt{\alpha_c}}{\beta\sqrt{p}\,\Delta}\times\left\{\sqrt{\alpha_c}K_1(\sqrt{p})\cosh\sqrt{p/\alpha_c}+\beta K_0(\sqrt{p})\sinh\sqrt{p/\alpha_c}\right\} \quad (4.3.55)$$

$$D=\frac{1}{\sqrt{p/\alpha_c}\,\Delta}\;, \quad (4.3.56)$$

where

$$\Delta=\sqrt{\alpha_c}\,[\omega K_1(\sqrt{p})+\sqrt{p}K_0(\sqrt{p})]\cosh\sqrt{p/\alpha_c}(1-r_c)$$
$$+\beta[\frac{\alpha_c}{\beta^2}\sqrt{p}K_1(\sqrt{p})+\omega K_0(\sqrt{p})]\sinh\sqrt{p/\alpha_c}(1-r_c) \quad (4.3.57)$$

Finally, the solutions in the Laplace domain become:

$$\bar{h}_{s_1}=\frac{\sqrt{\alpha_c}}{\beta\sqrt{p}}\cdot\frac{1}{\Delta}\times$$
$$\times\left\{\sqrt{\alpha_c}K_1(\sqrt{p})\sinh[\sqrt{p/\alpha_c}(1-r_D)]+\beta K_0(\sqrt{p})\cosh[\sqrt{p/\alpha_c}(1-r_D)]\right\} \quad (4.3.58)$$

for the inner region and

$$\bar{h}_{s_2}=\frac{1}{\sqrt{p/\alpha_c}\,\Delta}K_0(\sqrt{p}\cdot r_D) \quad (4.3.59)$$

for the outer region, where Δ is expressed by Equation 4.3.57.

To obtain the normalized head at the well, Equation 4.3.58 is inverted back to the real space by a numerical inversion scheme and evaluated at $r_D = r_c$ for various values of α_c, β, and ω. Figures 4.11a through 4.11c show the particular cases of $r_c = 0.005$ for $\omega = 10^{-3}$, 10^{-4}, and 10^{-9}, respectively. Note a new dimensionless time $nbT_1 t / C_w r_w$, and a new storage ratio $w' = nbr_w S_1 / C_w$, that are based on the inner region transmissivity and storativity, are used in plotting these curves. The curves show the effects of changes in the flow properties from the inner to the outer region.

A composite medium behavior is noticeable only when the contribution of the infinite acting period of the inner region on the head change is significant but does not account for all the change (Figure 4.11a). When the transmissivity of the outer region is small compared to that of the inner region (large values of β), the curves display two staged decline. The point of deflection moves to later time as r_c increases. For values of β smaller than 10^{-2}, i.e., when the outer region transmissivity is large compared to that of the inner region, the curves are identical to each other and essentially present the effect of an open boundary.

When the total storage capacity of the inner region is very small, the curves appear to be merely shifted horizontally to the left or right depending on the permeability contrast β (Figure 4.11c). Although the shapes of the curves are different from each other, the differences are minute and may not be distinguishable. The smaller the diameter of the inner region and the smaller the storage coefficient of the inner region, the smaller the total

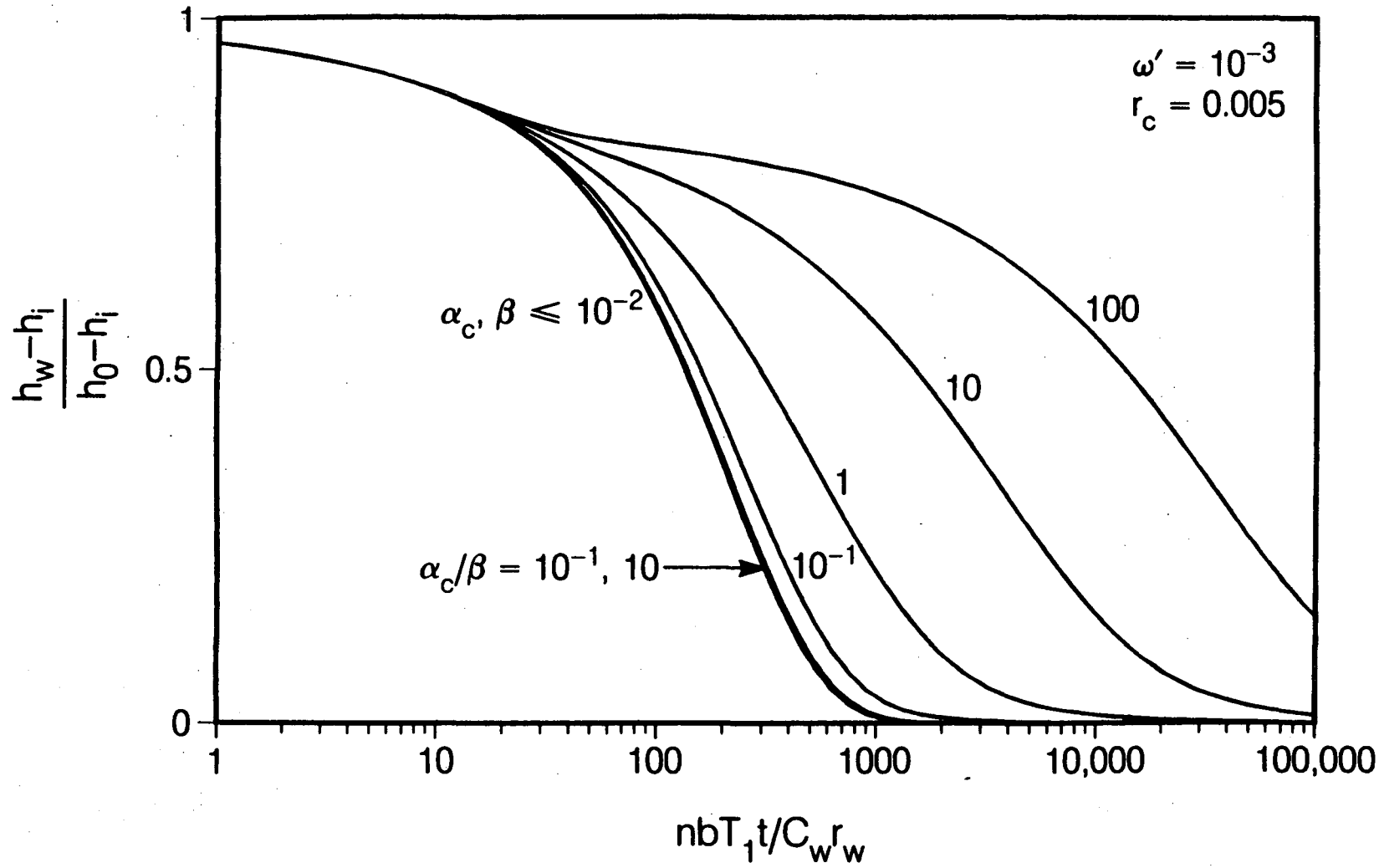

Figure 4.11a Normalized head for linear-radial model ($\omega' = 10^{-3}$).

XBL 862-10677

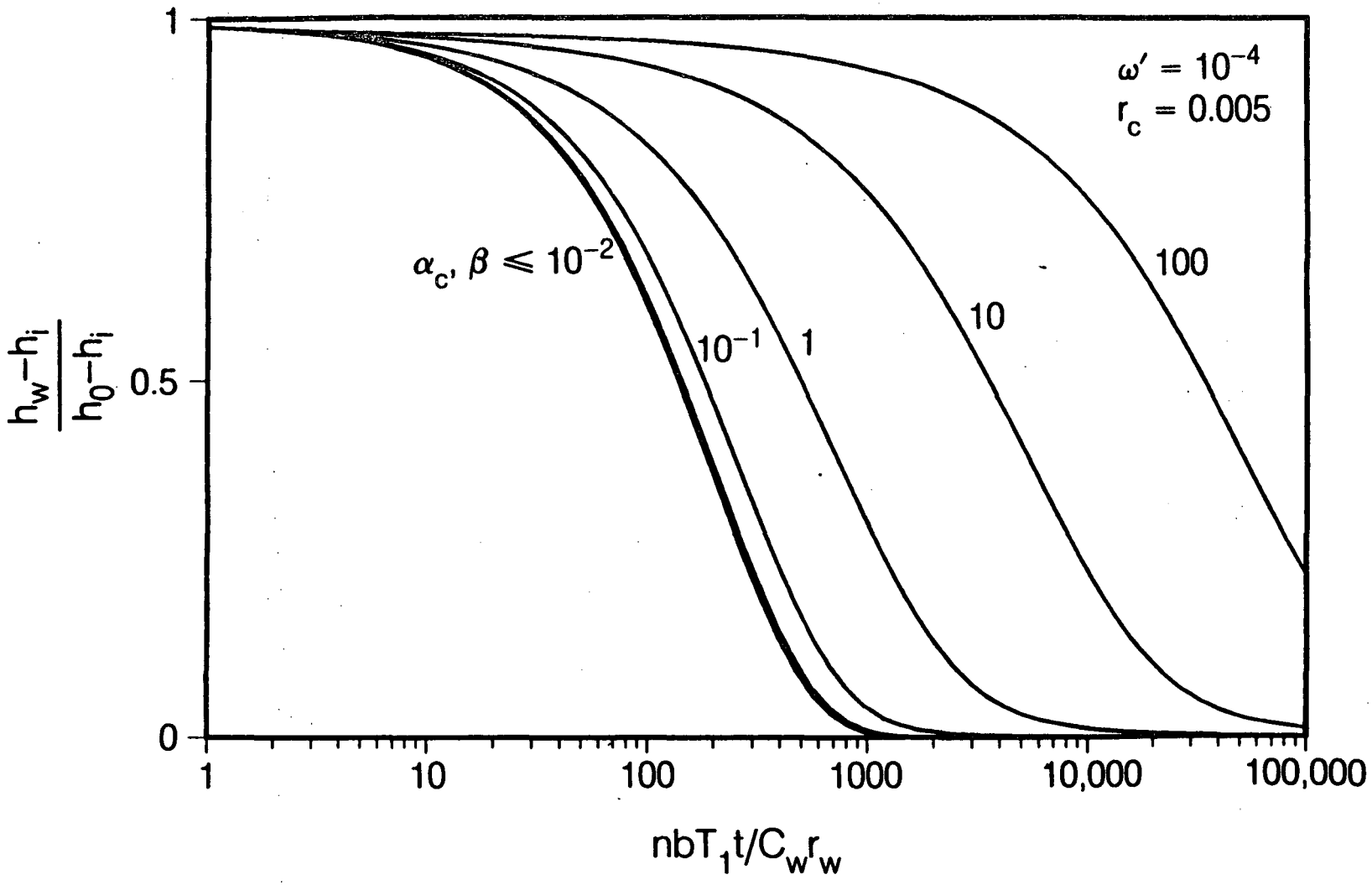

Figure 4.11b Normalized head for linear-radial model ($\omega' = 10^{-4}$).

XBL 862-10679

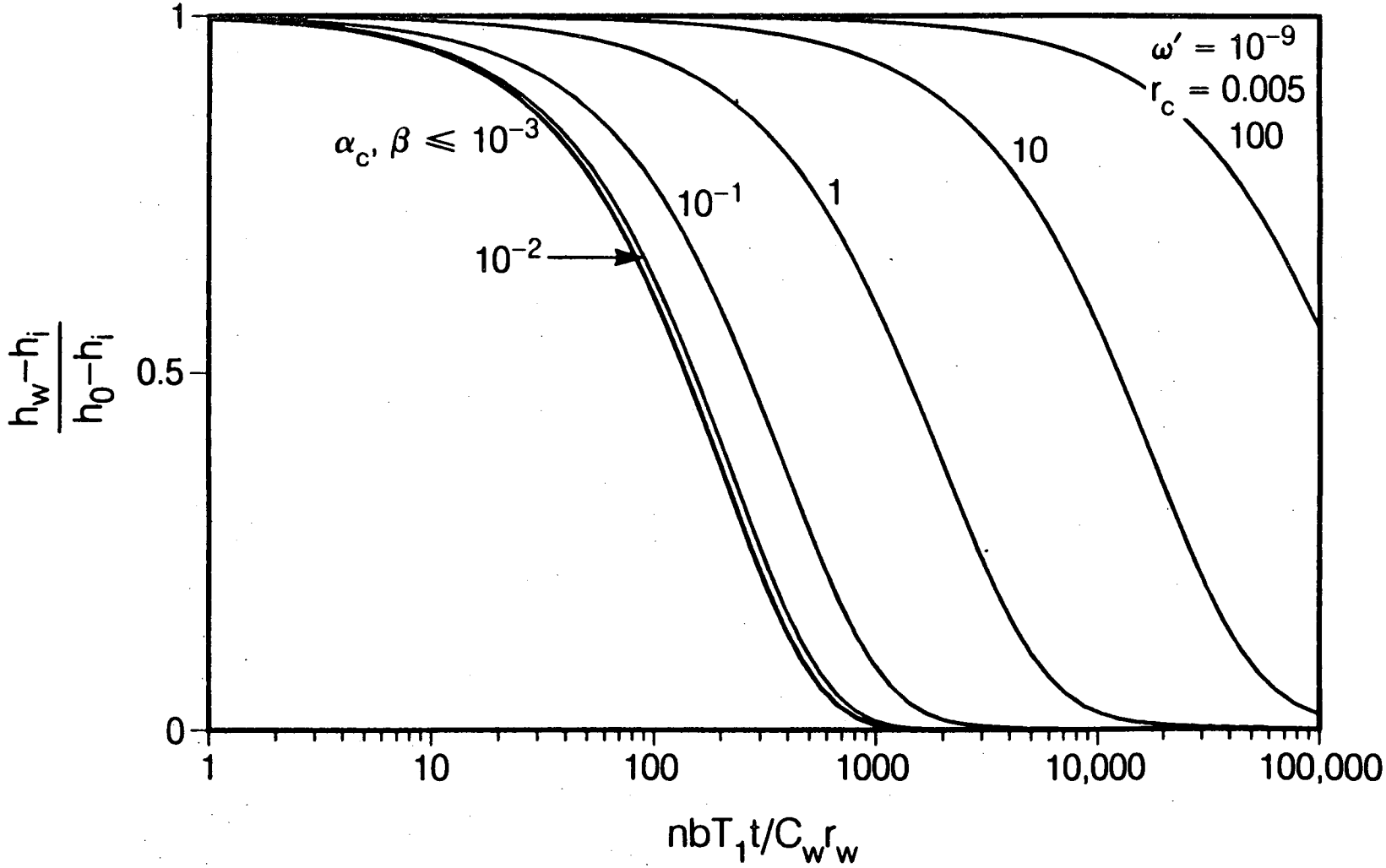

Figure 4.11c Normalized head for linear-radial model ($\omega' = 10^{-9}$).

XBL 862-10678

storage capacity. Conversely, if the total storage capacity of the inner region is large, the inner region would be infinite acting and the effect of the outer region would not be observed. For all cases except in Figure 4.11a, it is assumed that $\alpha_c/\beta=1$. In Figure 4.11a, curves for $\alpha_c/\beta=0.1$ and 10 when $\beta=10^{-2}$ are also shown but the effect of different values of α_c/β is insignificant for the particular case.

4.4. Spherical Flow Models

4.4.1. Spherical Flow in a Homogeneous System

When the length of a well open to flow is much smaller than the thickness of the formation and when the vertical permeability is comparable to the horizontal permeability, the flow may be better approximated by a spherical flow.

The governing equation for spherical flow can be written as:

$$\frac{\partial^2 h}{\partial r^2} + \frac{2}{r}\frac{\partial h}{\partial r} = \frac{1}{\alpha}\frac{\partial h}{\partial t} \tag{4.4.1}$$

The initial conditions are

$$h(r,0) = 0 \tag{4.4.2}$$

$$h(r_w+0,t) = h_w(t) \tag{4.4.3}$$

$$h_w(0) = h_0 \tag{4.4.4}$$

The boundary conditions are

$$4\pi r_w^2 k \left.\frac{\partial h}{\partial r}\right|_{r=r_w} = C_w \frac{dh_w}{dt} \tag{4.4.5}$$

$$h(\infty,t) = 0 \tag{4.4.6}$$

In dimensionless form, they become:

$$\frac{\partial^2 h_s}{\partial r_D^2} + \frac{2}{r_D}\frac{\partial h_s}{\partial h_D} = \omega \frac{\partial h_s}{\partial t_s} \tag{4.4.7}$$

$$h_s(r_D,0) = 0 \tag{4.4.8}$$

$$h_s(1+0,t_s) = h_{w_s}(t_s) \tag{4.4.9}$$

$$\left.\frac{\partial h_s}{\partial r_D}\right|_{r_D=1} = \frac{dh_{w_s}}{dt_s} \tag{4.4.10}$$

$$h_s(\infty,t_s) = 0 \tag{4.4.11}$$

$$h_{w_s}(0) = 1 \tag{4.4.12}$$

with the following definitions for t_s and ω:

$$t_s = \frac{4\pi r_w kt}{C_w} \tag{4.4.13}$$

$$\omega = \frac{4\pi r_w^3 S_s}{C_w} \quad . \tag{4.4.14}$$

After employing the Laplace transformation Equation 4.4.7 and Equation 4.4.8 yield:

$$\frac{d^2\bar{h}_s}{dr_D^2} + \frac{2}{r_D}\frac{d\bar{h}_s}{dr_D} = \omega p \bar{h}_s \tag{4.4.15}$$

The inner boundary condition, Equation 4.4.10 with Equations 4.4.9 and 4.4.12 now becomes

$$\left.\frac{d\bar{h}_s}{dr_D}\right|_{r_D=1} = p\bar{h}_s - 1 \tag{4.4.16}$$

The general solution to Equation 4.4.15 that satisfies the outer boundary condition Equation 4.4.11 is:

$$\bar{h}_s = \frac{C}{r_D} \exp\left[-\sqrt{\omega p}\, r_D\right] \tag{4.4.17}$$

Using Equation 4.4.16 and solving for C,

$$C = \frac{e^{\sqrt{\omega p}}}{1 + \sqrt{\omega p} + p} \tag{4.4.18}$$

Therefore, the solution in Laplace space is now:

$$\bar{h}_s = \frac{1}{r_D} \cdot \frac{e^{\sqrt{\omega p}\,(1-r_D)}}{1 + \sqrt{\omega p} + p} \tag{4.4.19}$$

The inversion of Equation 4.4.19 can be found in Carslaw and Jaeger (1959) for the analogous problem in heat flow. The normalized water level in the well is

$$h_s = \frac{2\omega}{\pi} \int_0^\infty \frac{e^{-t_s \cdot \mu^2/\omega}}{(\mu^2 - \omega)^2 + \omega^2\mu^2}\, d\mu \tag{4.4.20}$$

Equation 4.4.20 is evaluated for a wide range of values of ω ($10^{-10} \leq \omega < 10$) and the resulting normalized fluid levels at the well are shown in Figure 4.12. It can be seen that the transition of the fluid level from unity to zero occurs

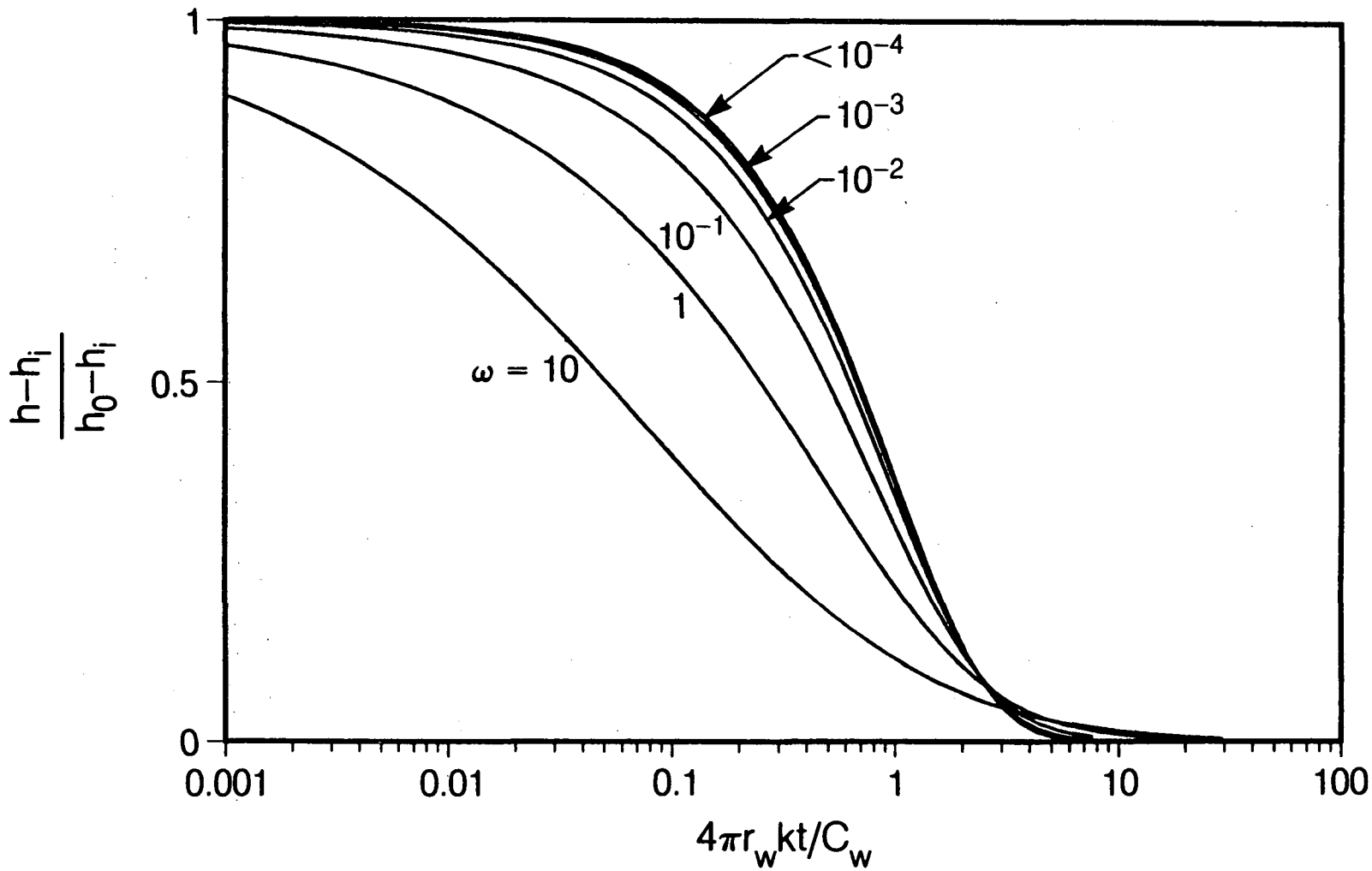

Figure 4.12 Normalized head for spherical flow model.

XBL 861-10579

much faster and the fluid level diminishes to zero more abruptly than when the flow is radial. Therefore if a test result shows such characteristics, spherical flow can be suspected. However, the curves for the values of ω smaller than 10^{-3} are indistinguishable from each other. Therefore it will not be possible to estimate the storage coefficient values smaller than 10^{-3}. For a system with a larger value of ω, the volume of the rock tested would be so small that the reliability of the estimated storage coefficient value would be questionable.

4.4.2. Radial-Spherical Composite Model

We will now consider a problem similar to that discussed in Chapter 3.3, where a well intersects a non-vertical fracture that is part of an interconnected fracture system. We assume that the flow near the wellbore is radial and at some distance from the well the flow becomes spherical. In this section, we investigate a slug test boundary condition. Recalling the governing equations for the composite system,

$$\frac{\partial^2 h_1}{\partial r^2} + \frac{1}{r}\frac{\partial h_1}{\partial r} = \frac{1}{\alpha_1}\frac{\partial h_1}{\partial t} \tag{3.4.1}$$

$$\frac{\partial^2 h_2}{\partial r^2} + \frac{2}{r}\frac{\partial h_2}{\partial r} = \frac{1}{\alpha_2}\frac{\partial h_2}{\partial t} \tag{3.4.2}$$

we solve Equation 3.4.1 and 3.4.2 under the following boundary conditions. The inner boundary condition is now expressed as follows:

$$2\pi r_w \; b \; k_1 \frac{\partial h_1}{\partial r}\bigg|_{r=r_w} = C_w \frac{dh_w}{dt} = C_w \frac{\partial h_1}{\partial t} \quad (r = r_w) \tag{4.4.21}$$

The outer boundary condition is that for a infinite medium:

$$h_2(\infty,t) = h_i \tag{4.4.22}$$

The initial conditions are:

$$h_w(0) = h_0 \tag{4.4.23}$$

$$h_1(r,0) = h_i \qquad (r_w < r \leq r_f) \tag{4.4.24}$$

$$h_2(r,0) = h_i \qquad (r_f \leq r \leq \infty) \tag{4.4.25}$$

The continuity requirements at the interface of the inner and outer regions are as follows:

$$h_1 = h_2 \qquad (r = r_f) \tag{4.4.26}$$

$$2\pi r_f \cdot b \cdot k_1 \cdot \frac{\partial h_1}{\partial r} = 4\pi r_f^2 k_2 \frac{\partial h_2}{\partial r} \quad (r = r_f) \tag{4.4.27}$$

Dimensionless parameters are defined as:

$$h_s = \frac{h - h_i}{h_0 - h_i} \tag{4.1.2}$$

$$t_D = \frac{2\pi T_2 t}{C_w} \cdot \frac{1}{\omega} = \frac{2\pi T_2 t}{C_w} \cdot \frac{C_w}{2\pi r_f^2 S_2} = \frac{\alpha_2 t}{r_f^2} \tag{4.3.31}$$

$$r_D = \frac{r}{r_f} \tag{3.2.7c}$$

$$r_c = \frac{r_w}{r_f}, \tag{3.2.7d}$$

$$\alpha_c = \frac{\alpha_1}{\alpha_2} \tag{3.2.7e}$$

$$\beta = \frac{bk_1}{2r_f\ k_2} \tag{4.4.28}$$

$$\omega = \frac{4\pi r_f^2 r_w}{C_w} S_{s_2} \tag{4.3.32}$$

In dimensionless form Equations 3.4.1 and 3.4.2 become:

$$\frac{\partial^2 h_{s_1}}{\partial r_D^2} + \frac{1}{r_D}\frac{\partial h_{s_1}}{\partial r_D} = \frac{1}{\alpha_c}\frac{\partial h_{s_1}}{\partial t_D} \tag{4.4.29}$$

$$\frac{\partial^2 h_{s_2}}{\partial r_D^2} + \frac{2}{r_D}\frac{\partial h_{s_2}}{\partial r_D} = \frac{\partial h_{s_2}}{\partial t_D} \tag{4.4.30}$$

The boundary conditions are now identical to Equations 4.3.35 through 4.3.42. After the Laplace transformations, the governing equations are:

$$\frac{d^2\overline{h}_{s_1}}{dr_D^2} + \frac{1}{r_D}\frac{d\overline{h}_{s_1}}{dr_D} = \frac{p}{\alpha_c}\overline{h}_{s_1} \tag{4.4.31}$$

$$\frac{d^2\overline{h}_{s_2}}{dr_D^2} + \frac{2}{r_D}\frac{d\overline{h}_{s_2}}{dr_D} = p\overline{h}_{s_2} \tag{4.4.32}$$

The transformed boundary conditions are expressed in Equations 4.3.45 through 4.3.48. The general solution to Equation 4.4.31 is:

$$\overline{h}_{s_1} = AI_0(\sqrt{p/\alpha_c}\, r_D) + BK_0(\sqrt{p/\alpha_c}\, r_D) \tag{4.4.33}$$

Because Equation 4.3.46 requires Equation 4.4.33 to be bounded, the general

solution to Equation 4.4.32 is:

$$\bar{h}_{s_2} = \frac{C}{r_D}\exp(-\sqrt{p}\ \ r_D) \tag{4.4.34}$$

where A, B, and C are constants. Applying the boundary conditions 4.3.45 through 4.3.48, we obtain:

$$A\sqrt{p/\alpha_c}\,I_1(\sqrt{p/\alpha_c}\,r_c) - B\sqrt{p/\alpha_c}\,K_1(\sqrt{p/\alpha_c}\,r_c)$$
$$= \frac{1}{\omega\beta}\left\{p\left[AI_0(\sqrt{p/\alpha_c}\,r_c) + BK_0(\sqrt{p/\alpha_c}\cdot r_c)\right] - 1\right\} \tag{4.4.35}$$

$$AI_0(\sqrt{p/\alpha_c}) + BK_0(\sqrt{p/\alpha_c}) - C\ \exp(-\sqrt{p}\ ) = 0 \tag{4.4.36}$$

$$A\sqrt{p/\alpha_c}\,I_1(\sqrt{p/\alpha_c}) - B\sqrt{p/\alpha_c}\,K_1(\sqrt{p/\alpha_c}) + \frac{C}{\beta}(1+\sqrt{p}\ )e^{-\sqrt{p}} = 0 \tag{4.4.37}$$

Using a recurrence formula of Bessel functions and solving for A, B, and C, we obtain:

$$A = \frac{1}{\Delta}\,\frac{1}{\omega\beta}\left\{\frac{1+\sqrt{p}}{\beta}K_0(\sqrt{p/\alpha_c}) - \sqrt{p/\alpha_c}\,K_1(\sqrt{p/\alpha_c})\right\} \tag{4.4.38}$$

$$B = -\frac{1}{\Delta}\,\frac{1}{\omega\beta}\left\{\frac{1+\sqrt{p}}{\beta}I_0(\sqrt{p/\alpha_c}) + \sqrt{p/\alpha_c}\,I_1(\sqrt{p/\alpha_c})\right\} \tag{4.4.39}$$

$$C = -\frac{e^{\sqrt{p}}}{\omega\beta\Delta}\ , \tag{4.4.40}$$

where

$$\Delta = \left[-\sqrt{p/\alpha_c}\,I_1(\sqrt{p/\alpha_c}\,r_c + \frac{p}{\omega\beta}I_0(\sqrt{p/\alpha_c}\,r_c)\right]\times$$
$$\times\left[\frac{1+\sqrt{p}}{\beta}K_0(\sqrt{p/\alpha_c}) - \sqrt{p/\alpha_c}\,K_1(\sqrt{p/\alpha_c})\right] -$$

$$- \left[\sqrt{p/\alpha_c} K_1(\sqrt{p/\alpha_c}\, r_c) + \frac{p}{\omega\beta} K_0(\sqrt{p/\alpha_c}\, r_c) \right] \times$$

$$\times \left[\frac{1+\sqrt{p}}{\beta} I_0(\sqrt{p/\alpha_c}) + \sqrt{p/\alpha_c}\, I_1(\sqrt{p/\alpha_c}) \right] . \qquad (4.4.41)$$

Finally, the solution for the inner region ($r_c \leq r_D \leq 1$) becomes:

$$\bar{h}_{s_1} = \frac{1}{\omega\beta\Delta} \cdot \left[\frac{1+\sqrt{p}}{\beta} K_0(\sqrt{p/\alpha_c}) - \sqrt{p/\alpha_c}\, K_1(\sqrt{p/\alpha_c}) \right] I_0(\sqrt{p/\alpha_c}\, r_D) -$$

$$- \left[\frac{1+\sqrt{p}}{\beta} I_0(\sqrt{p/\alpha_c}) + \sqrt{p/\alpha_c}\, I_1(\sqrt{p/\alpha_c}) \right] K_0(\sqrt{p/\alpha_c} \cdot r_D) \qquad (4.4.42)$$

and for completeness, we obtain the outer region solution ($r_D \geq 1$).

$$\bar{h}_{s_2} = - \frac{\exp[-\sqrt{p}\,(r_D - 1)]}{r_D\, \omega\beta\Delta} . \qquad (4.4.43)$$

The normalized head at the well can be obtained by inverting Equation 4.4.42 back to the real space using a numerical inversion scheme introduced by Stehfest (1970) and evaluating at $r_D = r_c$ for various values of α_c, β, and ω. Figures 4.13a and 4.13b show the particular case of $r_c = 0.005$ for $\omega = 10^{-3}, 10^{-6}$, respectively. A new dimensionless time $2\pi b k_1 t / C_w$, and a new dimenstionless storage ratio $2\pi b r_w S_{s_1} / C_w$, that are based on the inner region transmissivity and storativity, are used to plot the curves.

Similar observations as in Section 4.3.5 can be made on these figures. The curves show the effects of the change in the flow properties from the inner to the outer region. A composite medium behavior is noticeable only when the contribution of the infinite acting period of the inner region on the head change is significant but does not account for all the change (Figure

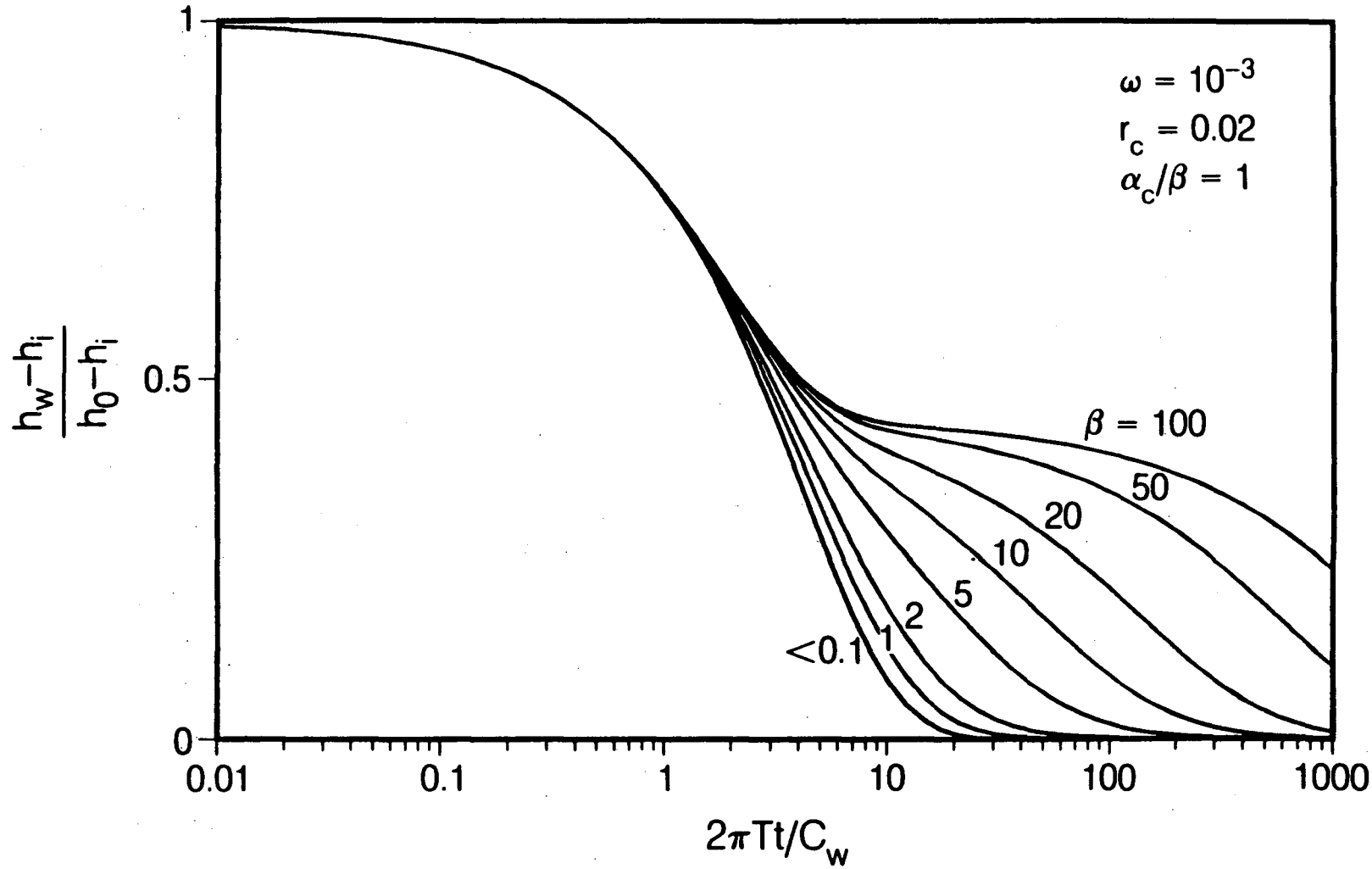

Figure 4.13a Normalized head for radial-spherical model ($\omega' = 10^{-3}$).

XBL 862-10676

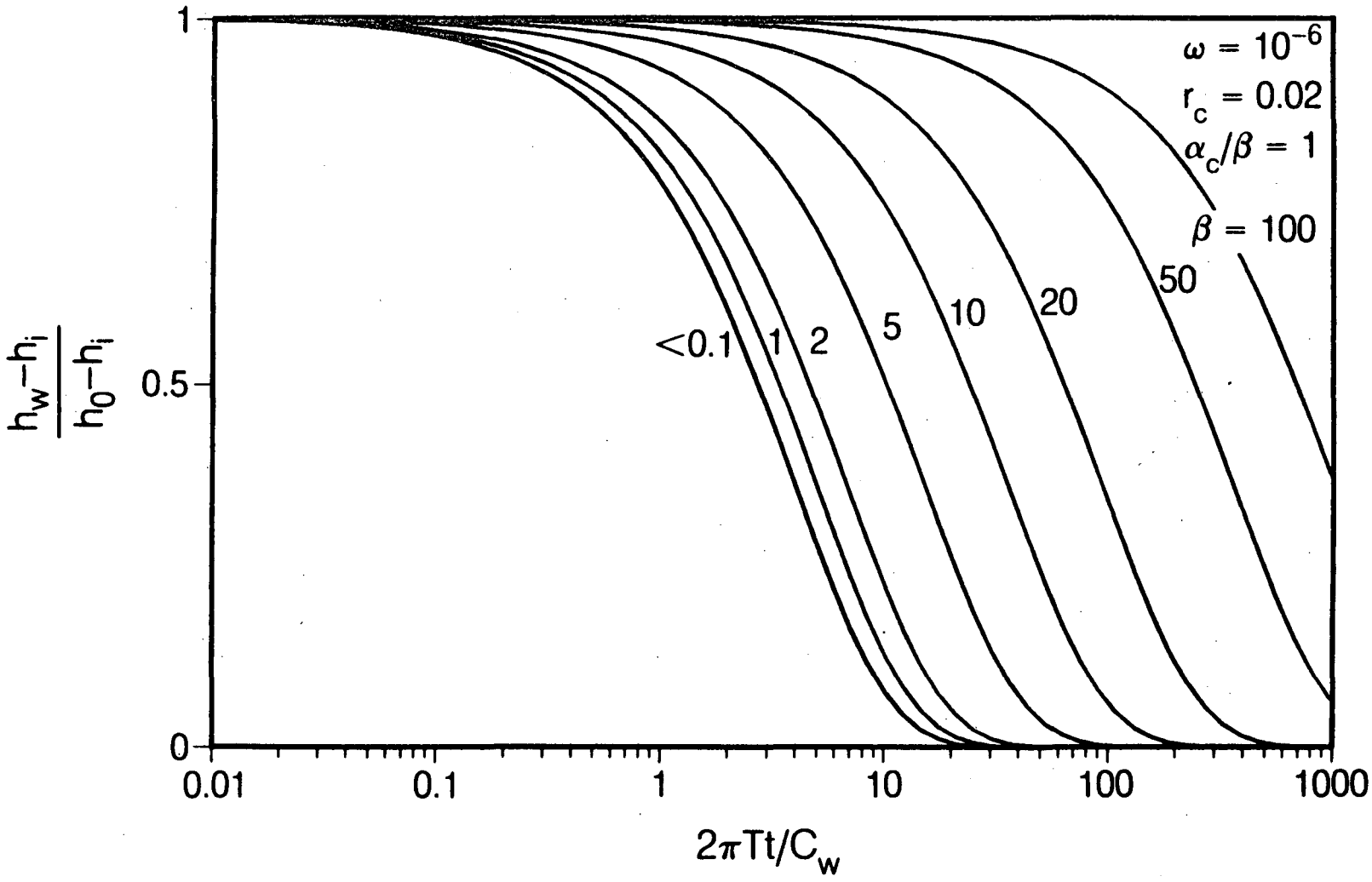

Figure 4.13b Normalized head for radial-spherical model ($\omega' = 10^{-6}$).

XBL 862-10675

4.13a). The early time behavior is that of a radial flow with its shape reflecting the ω' value. However, unlike the constant flux case, the late time behavior does not obviously show the characteristics of a spherical flow. When the transmissivity of the outer region is small compared to that of the inner region (large values of β), the curves display two staged decline. As r_c increases, the point of deflection moves to later time. For values of β smaller than 10^{-2}, i.e., large outer region transmissivity compared to that of the inner region, the curves are identical to each other and essentially present the same effect as an open boundary.

When the total storage capacity of the inner region is very small, the curves appear to be merely shifted horizontally to the left or right depending on the permeability contrast β (Figure 4.13b). The smaller the diameter and the storage coefficient of the inner region, the smaller the total storage capacity of the inner region. The shift to the left is bounded by the curve for β=0.1. The curves for β<0.1 are virtually indistinguishable from each other. Although the shapes of the other curves are different from each other, the differences are small and it may be difficult to distinguish from each other. Conversely, if the total storage capacity of the inner region is large, the inner region would be infinite acting and the effect of the outer region would not be observed. In this case, one can use a homogenous radial flow model. For all curves with the exception of two on Figure 4.13a, it is assumed that α_c/β=1. In Figure 4.13a, curves for α_c/β=0.1and10 when β=10^{-2} are also shown but the effect of different values of α_c/β is insignificant.

4.5. Analysis of slug tests at Nevada Test Site

The fractured volcanic tuff at Yucca Mountain in Nevada is being investigated as one of potential host rocks for a high-level nuclear waste repository. The United States Geological Survey has been conducting a number of well tests at Yucca Mountain area in an effort to characterize the regional hydrologic behavior. Among these tests, a series of open-hole slug tests were performed in the Ue-25c1 well (Figure 4.14). The lengths of the intervals that were packed off varied from 6 to 100 meters, and the depths ranged from 400 to 900 meters from the surface (Figure 4.15). The water table was measured at about 394 meters below the ground surface.

The results of the slug tests are shown in Figure 4.16. The conventional type curves for slug tests (Figure 4.1) developed by Cooper et al. (1967) do not fit any of the slug test data. It is only possible to match the early time portion (Figure 4.17a) or middle portion (Figure 4.17b) of the data to the type curves. The resulting transmissivities differ by as much as two orders of magnitude, depending on which of these match points are used. The late time portion of the curves are too steep to match any of the available type curves. In this section, attempts will be made to give a possible interpretation to this anomalous well test data using the solutions developed in the previous sections.

4.5.1. Well Test Data Analysis

In general, well test data do not match the analytical solution of a par-

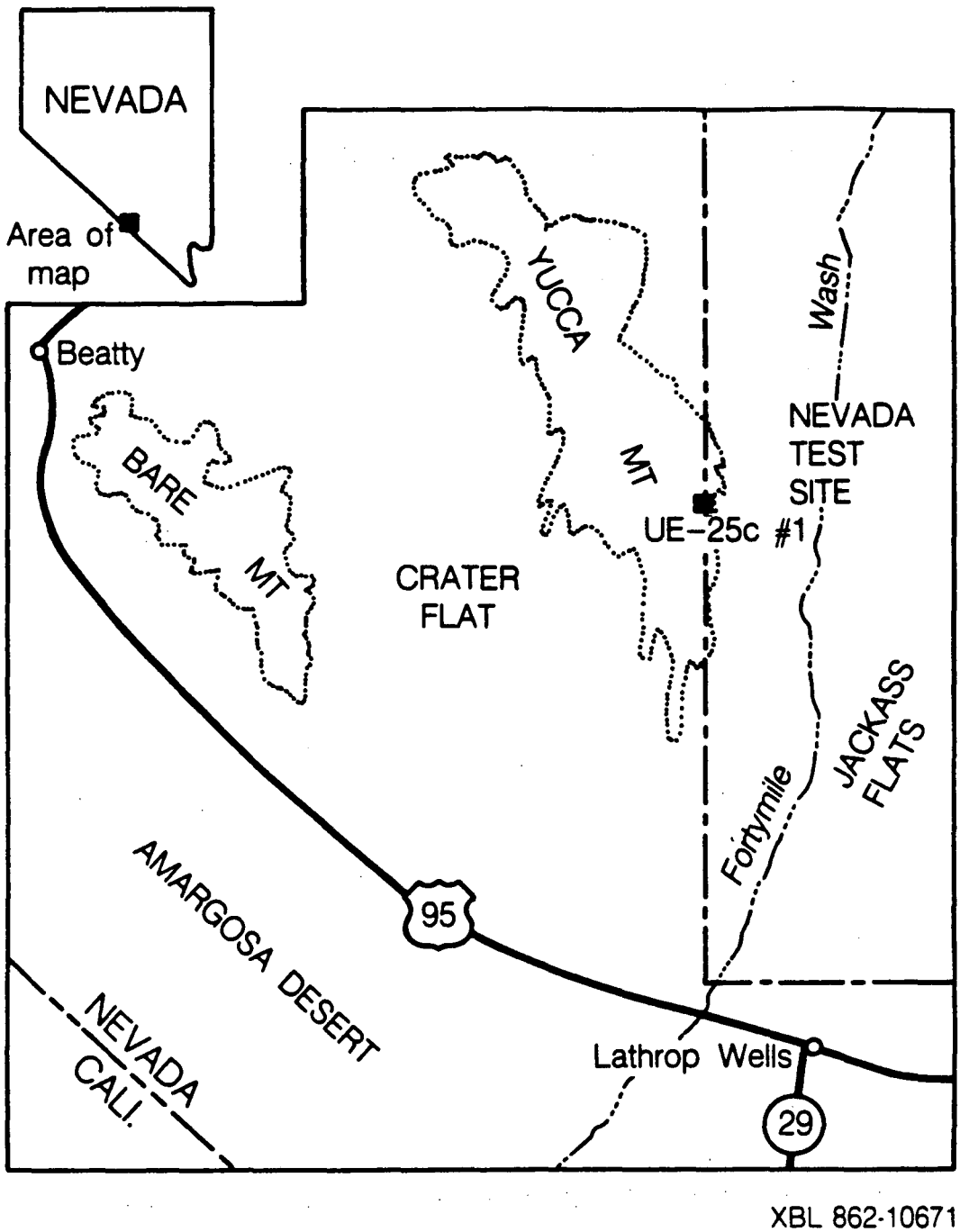

Figure 4.14 Location of Nevada Test Site and Ue-25c1 well.

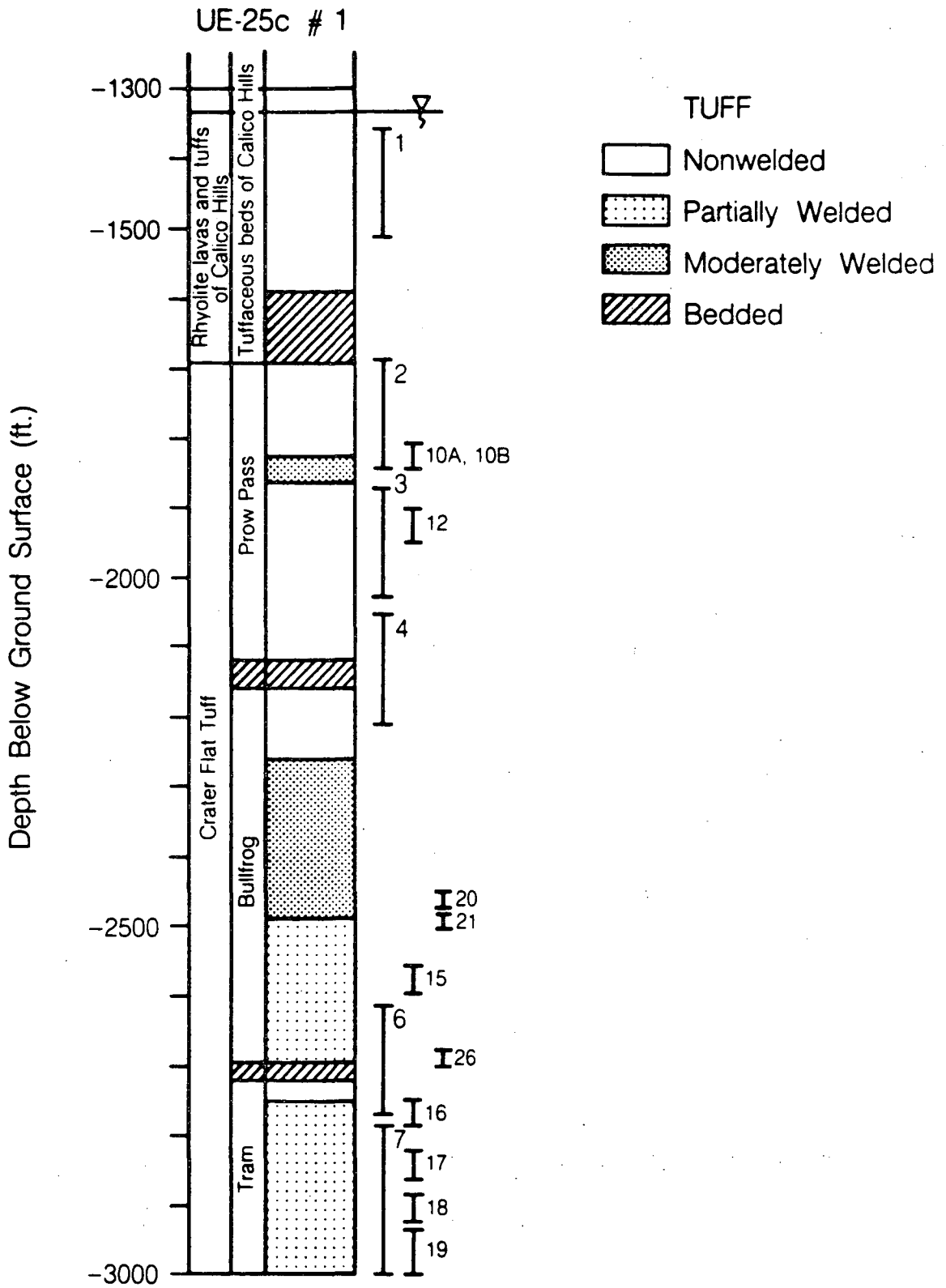

Figure 4.15 Test intervals in Ue-25c1 well.

XBL 862-10672

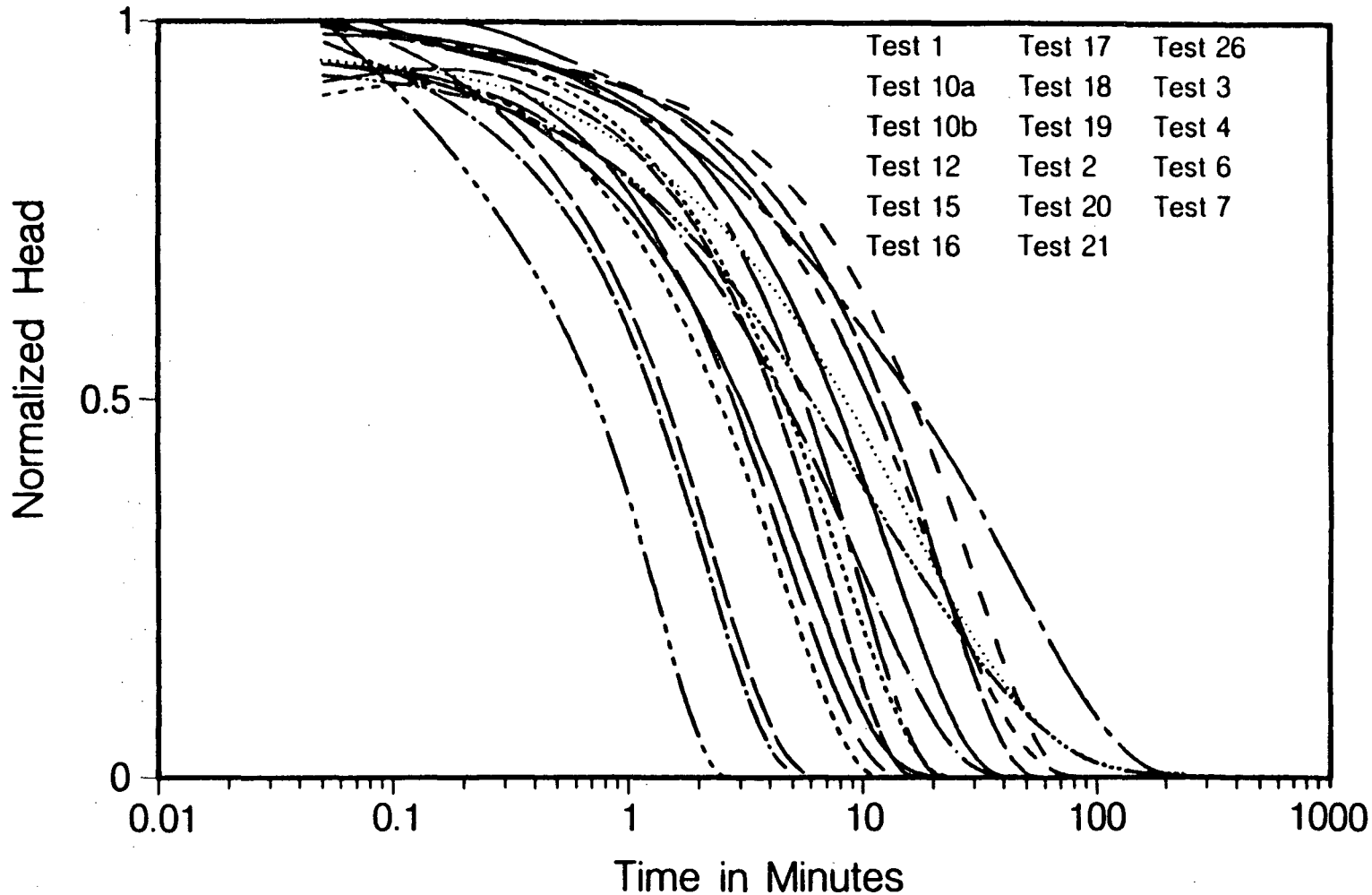

Figure 4.16 Slug test results in Ue-25c1 well.

XBL 862-10674

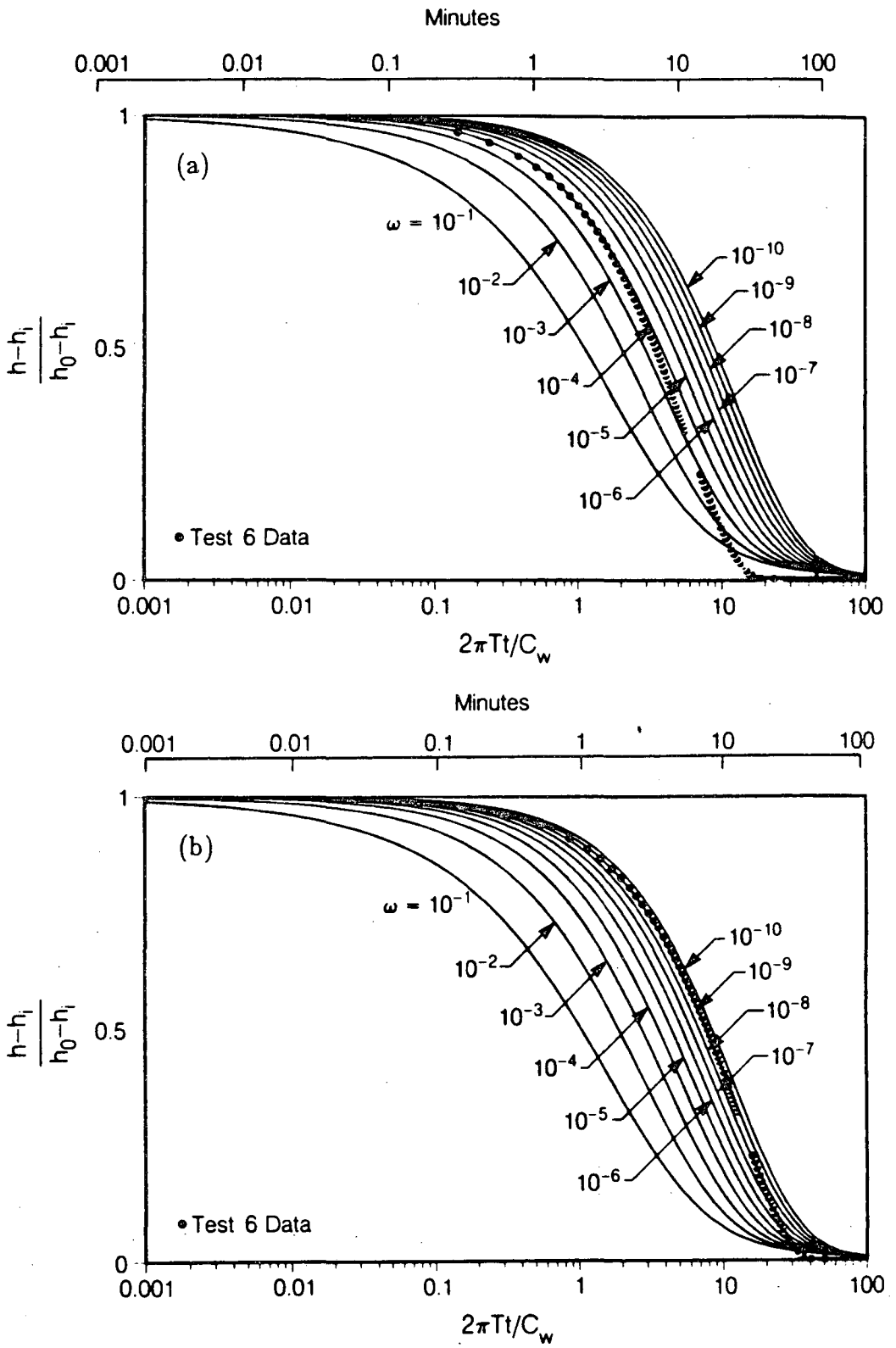

Figure 4.17 Test 6 results matched with type curves after Cooper et al.

ticular type of test because the model does not describe the physical phenomena adequately. Two causes for this can be described, but in practice it may not be possible to distinguish between them. First, recorded test results may not accurately reflect the properties of the geologic medium because the test fails to meet the boundary and initial conditions designated at the wellbore for the particular test. Examples of this include faulty instrumentation, design flaws, and other factors related to the actual test process. These adverse causes can generally be located in the wellbore or in the surface equipment. Second, although the direct responses of the system to the disturbance caused by the well test are monitored correctly, the model on which the analysis scheme is based may not accurately represent the real situation outside of the wellbore. For instance, the model may be based on the assumption that the system is homogeous when, in fact, it is highly heterogeneous.

In the present case, we suspect, under the first category, that the initial head was large enough so that high velocity flow occured inside the wellbore as well as in the formation. This induced large frictional losses in the delivery pipe and at the down-hole valve. For all tests except Test 10b, the initial height of the applied water column was about 180 meters. The value was chosen to obtain strong enough signals for the high range pressure transducer located above the straddle packers. Had a pressure transducer been located within the packed zone, the actual head that was being applied to the zone could have been known. A high velocity flow may also cause non-

linear flow in the formation near the wellbore. Although this occurs outside of the wellbore, and therefore is related to the second category, we consider this as a failure to meet the specifications of the slug test. All of these phenomena can cause a steepening of the curves at late times on the semi-log plot of the normalized head.

To examine the causes that may fall in the second category, we must look at the assumptions used in the Cooper et al model. In their model, it is assumed that the formation is an infinite slab of homogeneous porous medium and that Darcy's law holds. Thus their solution does not account for the following possible conditions:

1. Fracture flow
2. Flow other than radial flow
3. Bounded outer boundary
4. Non-Darcy flow.

In the previous sections we have developed solutions that consider each of the first three conditions. Although a model that incorporates the fourth condition can be constructed, the governing equation will be non-linear and it is probably impossible to obtain an analytical solution. Therefore, although an occurrence of a non-Darcy flow is a strong possibility in the present case, an analysis of the data with a non-Darcy flow model is beyond the scope of the present study. We believe that such non-Darcy flow in slug tests can be avoided through a careful design and execution of the tests as discussed

above, so that we can analyze well test data with a model that is free of such complexities.

As can be seen in Figure 4.16, all the slug test data have characteristically steep slopes at late times, which make the data difficult to fit to the conventional type curves. Using the insights we have gained from the studies in the previous sections, we are able to hypothesize the geometric conditions that may have led to these steep drops. If there exists a zone that has less resistance to flow at some distance from the well, the observed head at the well would show a faster decline at some time during the test depending on the distance to the zone and the storage ratio, ω. More specifically, possible geometric conditions that may cause faster decline of head include:

(a) constant head boundary

(b) larger area available to flow

(c) larger permeability.

The solutions developed in Sections 4.3.2 and 4.3.3 consider Condition (a). For Conditions (b) and (c), the solutions in Sections 4.3.5, 4.4.1 and 4.4.2 apply. We have attempted to match the field data that did not fit well with the conventional curves with the type curves for each model. Although we obtained better matches with all of our solutions than the conventional solution, no solution matched all parts of the data. This suggests that no geometric condition may explain the phenomena conclusively, because We feel that we have exhausted all the extreme geometric conditions that may

give rise to steeper curves. In fact, a diffusion-type equation as in Equation 2.9a may never explain the extremely short 'tails' as observed in Tests 6, 7, 10, 16, 17, 18, 20, 21, and 26 in Figure 4.16. Therefore, we suspect that these anomalies are mainly due to the causes in the first category.

In order to demonstrate their use, two of the solutions that gave better matches than the others are shown in Figures 4.18a and 4.18b for Test 6, which is typical of the tests. The radial constant head boundary model in Figure 4.18a is a slightly better match than the spherical flow model in Figure 4.18b. Figure 4.18a shows that the data from Test 6 matches the type curves of the radial constant head boundary model with $\omega=10^{-4}$. The match point is $\frac{2\pi Tt}{C_w}=1$ at $t=2$ minutes and $r_e=150$. Because the diameter of the delivery pipe, r_a is 6.2 centimeters, we have $C_w = \pi r_a^2 = 3.14\times(3.1\times10^{-2})^2 = 3.02\times10^{-3}m^2$. Therefore, we obatin the transmissivity,

$$T=\frac{1\cdot C_w}{2\pi t}=\frac{1\cdot(3.02\times10^{-3})}{2\cdot 3.14\ 2\times60}=4.0\times10^{-6}(m^2/s).$$

The storativity can be obtained from Equation 4.1.5 using $r_w=14.6cm$, i.e.,

$$S=\frac{\omega\cdot C_w}{2\pi r_w^2}=\frac{(1.\times10^{-4})\cdot(3.02\times10^{-3})}{2\cdot 3.14\cdot(1.46\times10^{-1})^2}=2.25\times10^{-6}$$

Because we have $r_e=150$, we suspect that there may be a constant head boundary about 22 meters away from the well. We obtained similar results with the radial-spherical composite model discussed in Section 4.4.2 when $\beta<0.1$, i.e., the outer region permeability is more than ten times larger than the inner region permeability. This is expected because if the outer region

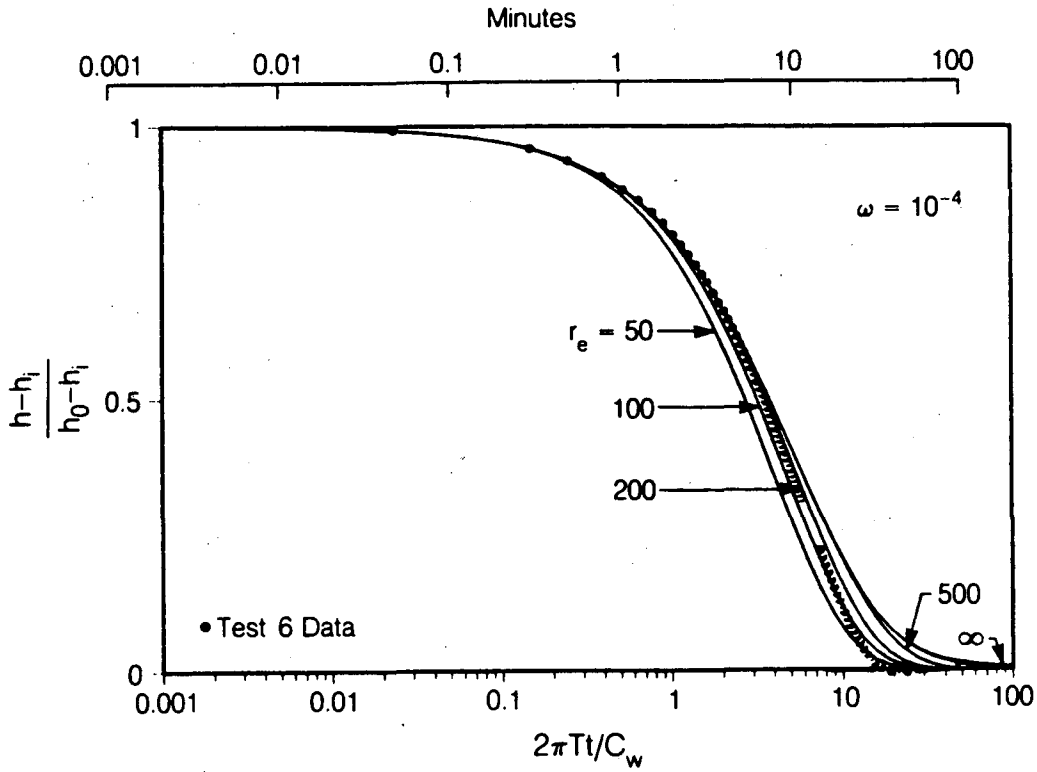

(a)

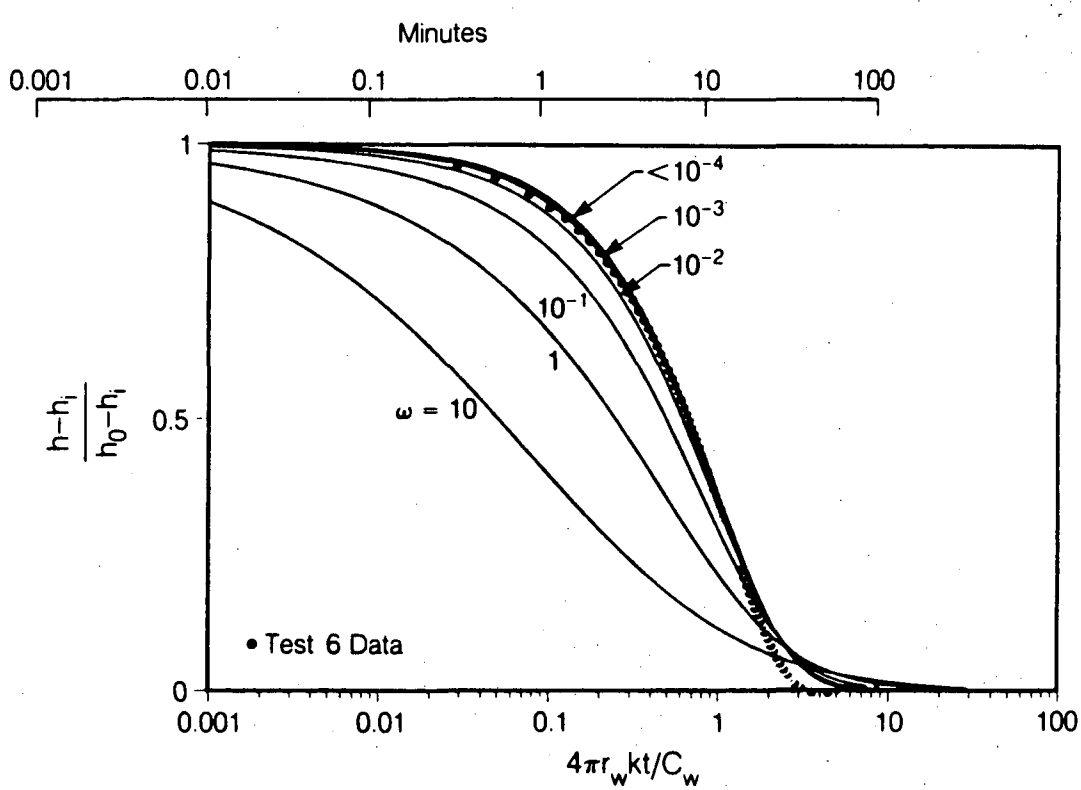

(b)

Figure 4.18 Type curve match with radial constant head boundary model (a) and spherical flow model (b).

permeability is very large and has more area for flow, it should have the same effect on the observed pressure as a constant head boundary. Therefore, r_e may be related to the radius of the fracture intersecting the well.

Figure 4.18b shows the same data fit to type curves for the spherical flow model discussed in 4.4.1. These curves also have steeper late time slopes than Cooper et al.'s curves and thus also give a better fit to the data. The match point in this case is $4\pi r_w kt / C_w = 0.9$ at $t = 10$ minutes and $\omega = 5\times10^{-3}$. Therefore, from Equation 4.4.13 we obtain:

$$r_w k = \frac{0.9 \cdot (3.02\times10^{-3})}{4 \cdot 3.14 \cdot 600} = 3.6\times10^{-7} (m^2/s) \ .$$

It should be noted that r_w is an equivalent spherical radius of the well and may not be equal to the actual well radius. For the ω match, from Equation 4.4.14 we have:

$$r_w^3 S_s = \frac{\omega \cdot C_w}{4\pi} = \frac{(5\times10^{-3}) \cdot (3.02\times10^{-3})}{4 \cdot 3.14} = 1.20\times10^{-6} \ (1/m)$$

4.6. Conclusions

In this chapter, we have presented several solutions that may be used for analyzing slug tests. We have considered the geometric conditions that may be present in fractured media, although they are not limited to such media. The type curves developed for each model can be used to estimate such geometric parameters as the distance to the boundary as well as the flow parameters. However, analyses of slug test results suffer problems of nonuniqueness, more than other well tests. As can be seen from the figures

presented, many curves have unique shapes only for some combination of the flow parameters and the distance. Other sets of type curves are all similar in shape, although log-log plots may emphasize some features that may not be apparent in semi-log plots. Therefore, it is important that one consider all other available information, such as geology and geophysical data, when analyzing results of slug tests. Although we limited our discussion to slug tests, the solutions apply directly to pressurized pulse tests. Pressurized pulse tests may be used to estimate the flow parameters and geometry of an individual fracture.

We also presented a field example of slug tests which do not match with the existing solution for homogeneous porous media. This is an example of the mismatch between well test data and analytical solutions that can occur when the real situation deviates from the assumptions made in the analysis. Although a model could be constructed to include the adverse conditions that may exist in the wellbore, such as wellbore storage effects or pipe resistances, well tests should be designed in advance to minimize those conditions as much as possible. This is because in well tests there is usually only one kind of measurement that can be made, i.e., either pressure or flow rate as a function of time at only a few points in the system. Therefore, the fewer number of variables there are in the solution, the more accurately the flow properties of the system can be estimated. In this case we see that care must be taken not to impose too high an initial head when preforming slug tests.

CHAPTER 5

NUMERICAL ANALYSIS

5.1. Numerical Model

At a large scale of observation, homogeneously fractured rock under natural conditions may or may not behave like a porous medium. However, even when the fracture network behaves like porous medium from the stand point of regional flow, it may not behave like porous medium under well test conditions. The fractures that are intersected by the well are limited in number and undergo a much stronger gradient than the rest of the system. Therefore the characteristics of these fractures may have great influence on the test results. As a result, the well test results may not reflect the average system behavior.

In order to investigate this, well tests have been simulated numerically by calculating flow through each fracture in the network. The modelling is done in two stages. A mesh generator produces random realizations of a fracture system which represents the statistical characteristics of fractures observed in the field. Then the well test boundary conditions are imposed on the mesh and the transient head distribution is solved using a finite element code. The following two sections describe each stage in detail.

5.1.1. Mesh Generator

The method used to create the fracture system was developed by Long

(1983) based on the fracture network model proposed by Baecher et al (1978). First, points are generated randomly in a two dimensional space called the generation region (Figure 5.1a). These points become the center points of fractures. The number of the points generated is determined by the desired fracture density in the generation region (Figure 5.1b,c,d). Then each fracture is assigned an orientation, length, and aperture using probablistic simulation. The above procedure is repeated for each set of fractures and then the sets are superimposed. For each geometric parameter, the type of probability distribution and the distribution parameters are input to the mesh generator. The resulting fracture system may be viewed as a network of two-dimensional vertical fractures. Therefore, a two-dimensional representation of a fracture network may directly apply to field cases where vertical fractures are dominant. It is believed that fractures are primarily vertical in deep formations because the direction of the least stress is usually horizontal. Such is the case at the Nevada Test Site, where the slug tests, whose analysis was discussed in the previous chapter, were performed.

It should be noted that well testing in the field is, in general, a three dimensional problem. However, two dimensional representation of a fracture system is a special case which should provide useful insight into the behavior of well tests in fractured rock.

Using the techniques of Long et al. (1982), we can determine the permeability tensor, K_{ij} under linear flow conditions. We then examine the behavior under well test conditions (Figure 5.2). Circular inner and outer boundaries

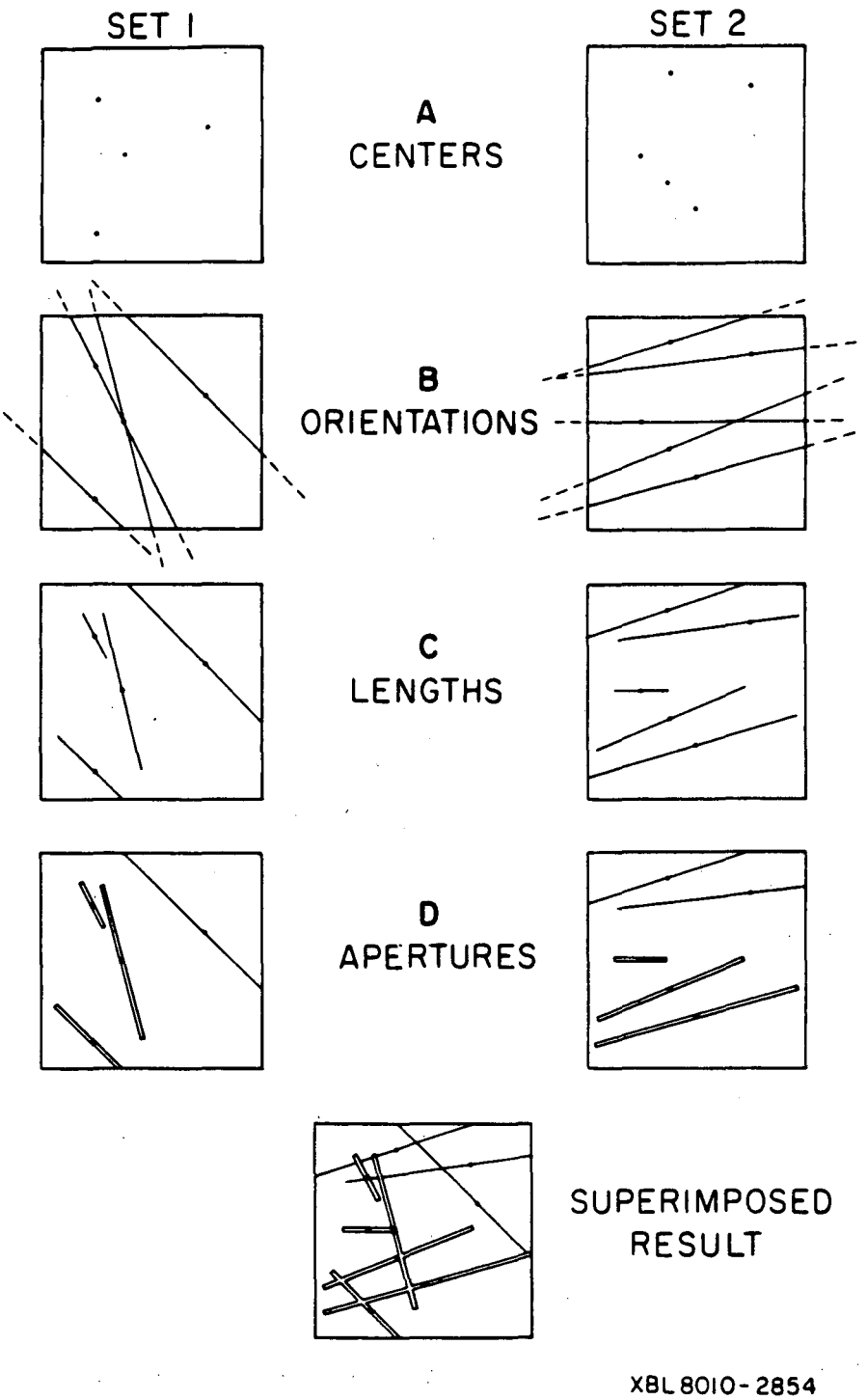

Figure 5.1 Generation of fracture network.

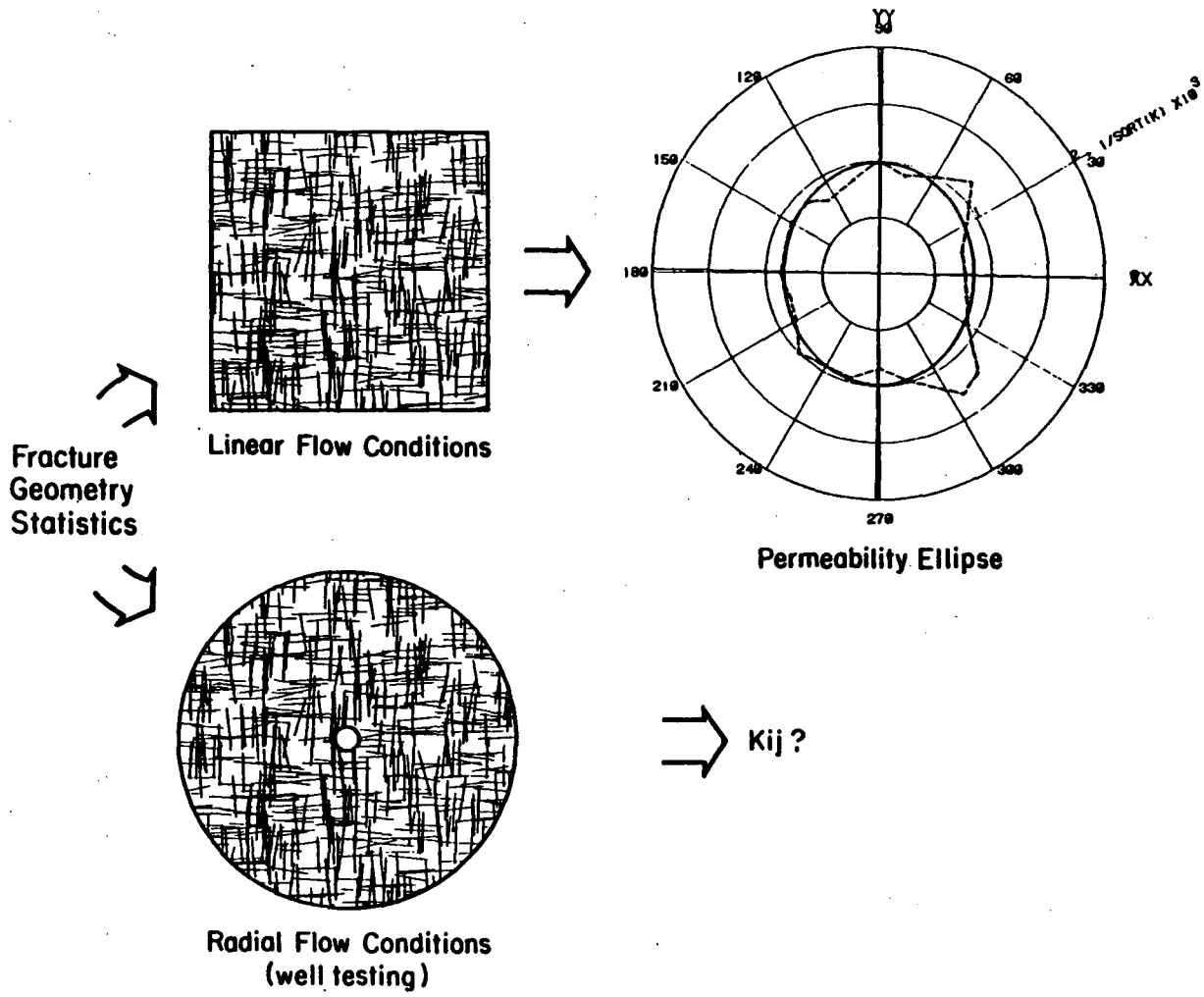

Figure 5.2 Linear flow model in Long (1982) and well test model.

are drawn to define the flow region. The inner boundary is the well. This two-dimensional analysis represents vertical fractures and a vertical well. This is unusual but is representative of the case at the Nevada Test Site, where the slug tests of the previous chapter were performed. Since, in the present study, the rock matrix is assumed to be impermeable, the well must be designed to intersect at least one fracture or no results can be obtained. For a transient analysis, the fractures must be descretized into short segments where the gradient is steep in order to ensure stability as well as accuracy. A node numbering scheme is used to maximize the usable memory space in the computer and to minimize the computing cost. The procedure developed by Cuthill and McGee (1969) is used here.

5.1.2. Fracture Flow Program

The finite element code simulates transient flow in a fracture network. The code is used to solve for the head distribution as a function of time in the fracture mesh created by the mesh generater .

The governing equation of flow for transient flow of slightly compressible water through a fracture is

$$K\frac{\partial^2 h}{\partial x^2} = S_s \frac{\partial h}{\partial t} , \tag{5.1}$$

where h is the water head, x is the direction of the fracture orientation, K is the fracture hydraulic conductivity, and S_s is the storage coefficient of the fracture. It is assumed that the fracture permeability is constant and not a

function of pressure and that the flow is laminar and the fractures are sufficiently open such that the cubic law holds. These assumptions may not be valid under all circumstances, especially where the pressure in the fracture exceeds the overburden pressure or where the fractures are closed by stress or infilling such that channeling occurs within the fracture.

The finite element formulation is based on Galerkin approach. The integration of basis functions is done over the length of a line element and the general form of the resulting element equations in matrix notation is

$$\left(\frac{[A]^t}{\Delta t} + \theta \cdot [B]^t \right) \cdot \{h\}^{t+\Delta t} = \{F\} + \left(\frac{[A]^t}{\Delta t} - (1-\theta) \cdot [B]^t \right) \cdot \{h\}^t , \qquad (5.2)$$

where $[A]$ is the storage coefficient matrix, $[B]$ is the permeability matrix, $\{F\}$ contains boundary conditions, $\{h\}$ is the head vector, and θ is the time weighting parameter. The above equations are solved for the head at each node simultaneously. The solution scheme utilizes a banded symmetric matrix solver. The program is written in FORTRAN and is designed to run on the CRAY-1 system.

The code has been validated against the analytical solution given by Carslaw (1946) for a one dimensional heat flow problem. The results show an exellent match (Figure 5.3). Since there is no analytical solution to be compared against for two dimentional transient problem in a network of fractures, the code has been tested against the steady-state code developed by Wilson (1970). It is observed that the transient profile approaches the steady-state solution with time (Figure 5.4).

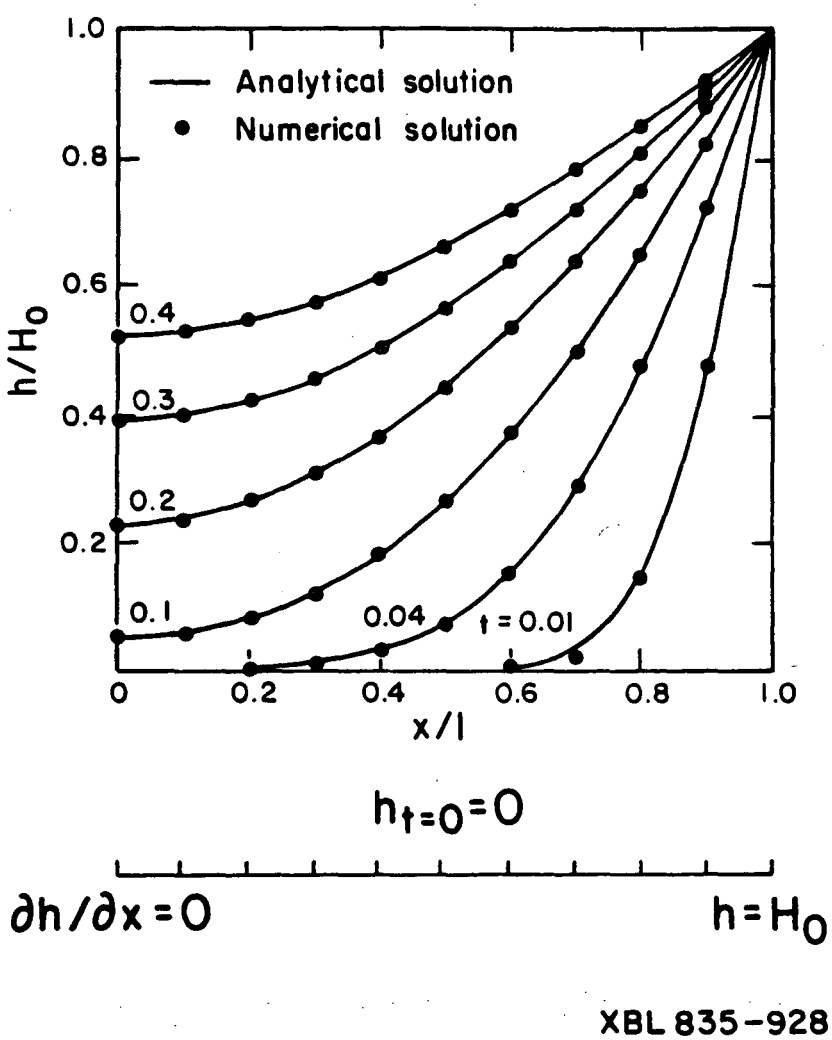

Figure 5.3 Comparison of analytical and numerical solutions.

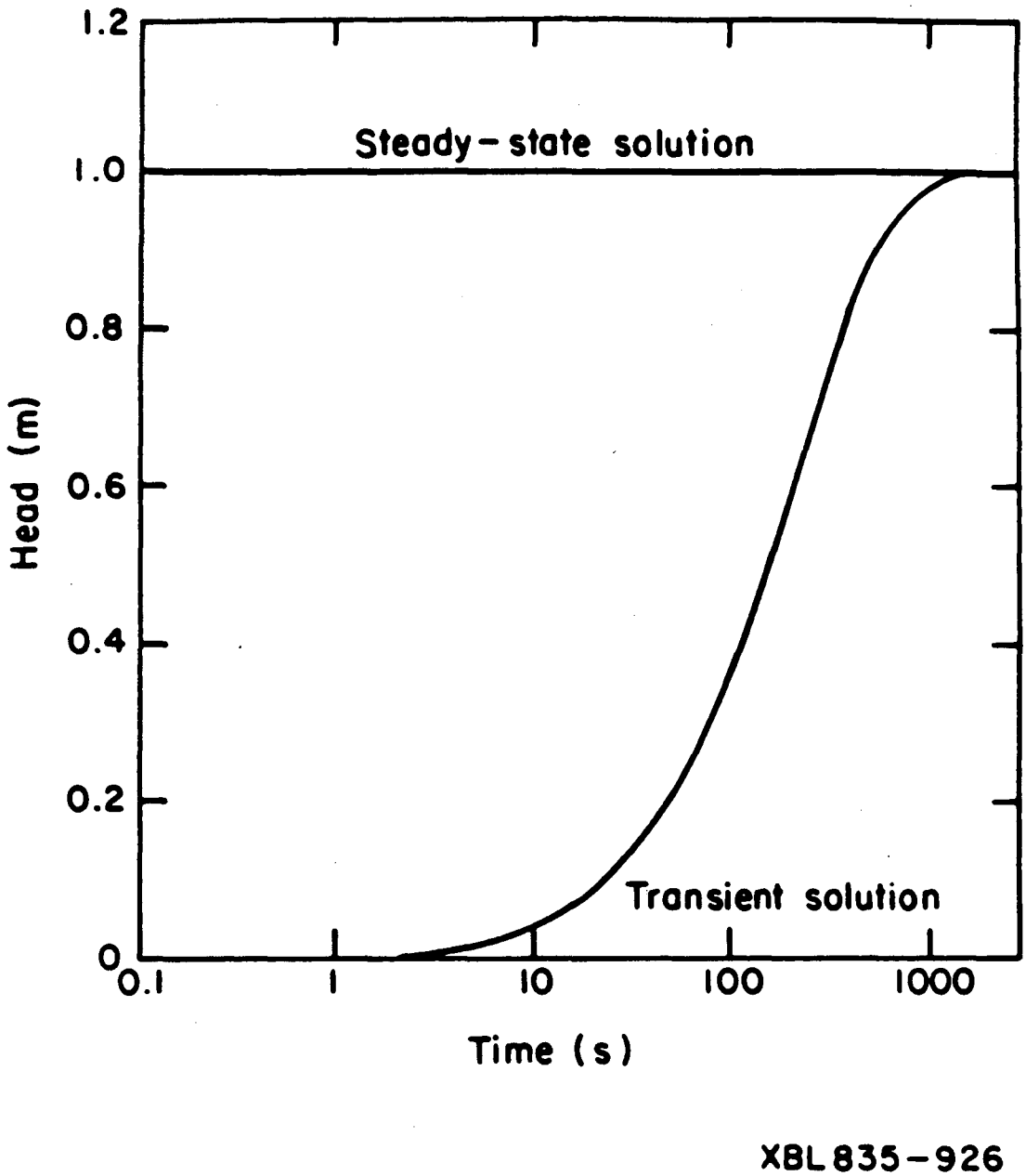

Figure 5.4 Plot of numerical solution approaching steady state solution.

5.2. Numerical Simulation of Well Tests

Numerical simulations of well tests in two dimentional fracture systems have been conducted using the numerical model discussed above. First, systems with two orthogonal sets of continuous fractures with constant spacing were investigated. Snow (1960) showed that such a system behaves like a porous medium under regional flow but he did not consider well test conditions in his study. Since the pressure gradient along a fracture is not constant or even uniform under well test conditions, it is not obvious that such a system always behaves like a porous medium. Next, well tests were performed in discontionuous fracture systems with distributed lengths and orientations. Such systems should be closer representations of actual fracture systems. The study is limited to two-dimensional systems but should provide useful insight especially where vertical fractures are dominant.

5.2.1. Well Tests in Continuous Fracture Systems

Figure 5.5a shows the fracture mesh used in Case-1. The fractures have a constant spacing of $1m$ and a constant aperture of $5\ \mu m$. The storage coefficient of a fracture is set to $1.0\times10^{-5}\ 1/m$, which essentially assumes the fracture is rigid. The theoretical value of the permeability of this system as predicted by Snow's technique, is $1.02\times10^{-10}\ m/s$. The storage coefficient is $1.00\times10^{-10}\ 1/m$, which can be obtained by volumetrically averaging the value for the fracture over a unit volume of rock. The pumping well is located at the center and the pressure transient is monitored at observation wells

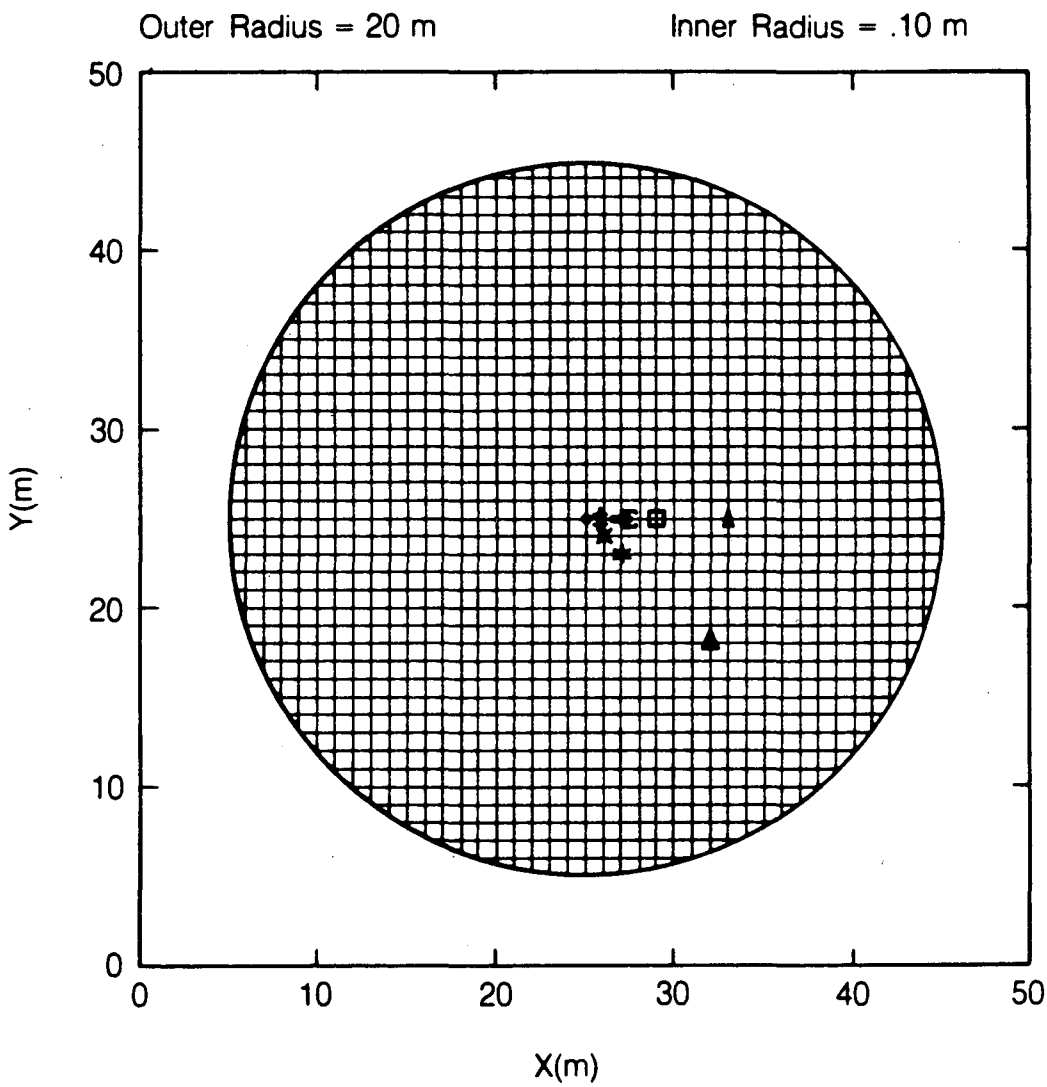

XBL 862-10663

Figure 5.5a Case 1 - pumping well at intersection.

located at various distances and directions from the pumping well. A constant flux injection test was simulated and the pressure heads at various wells were plotted against time over the square of distance on a semi-log graph (Figure 5.5b). The problem is terminated when the pressure pulse reaches the outer boundary because the results no longer reflect the behavior of an infinite system. Thus, the system is infinite-acting during the period of observation. The buildup curve for the equivalent porous medium based on the theoretical values is also plotted. Note that some curves do not coincide with the theoretical curve. They are shifted horizontally either to the right or left of the theoretical curve. The deviation from the theoretical curve becomes smaller as the distance from the pumping well to the observation well becomes larger. The curves for those wells located more than $4m$ away closely agree with the theoretical curve.

All the curves render the same correct value of average permeability since the curves have the same slope. However, the time intersect of the straight lines varies depending on the particular observation well used to produce the curve. Therefore, the storage coefficient calculated using the time intersect depends on the observation well used and may differ from the theoretical value. Especially, the buildup curve at the pumping well gives a considerably larger value of storage ($5.3\times10^{-10}\ 1/m$) than the volume averaged theoretical value. A similar problem was pointed out by Gringarten (1972) for a vertically fractured well.

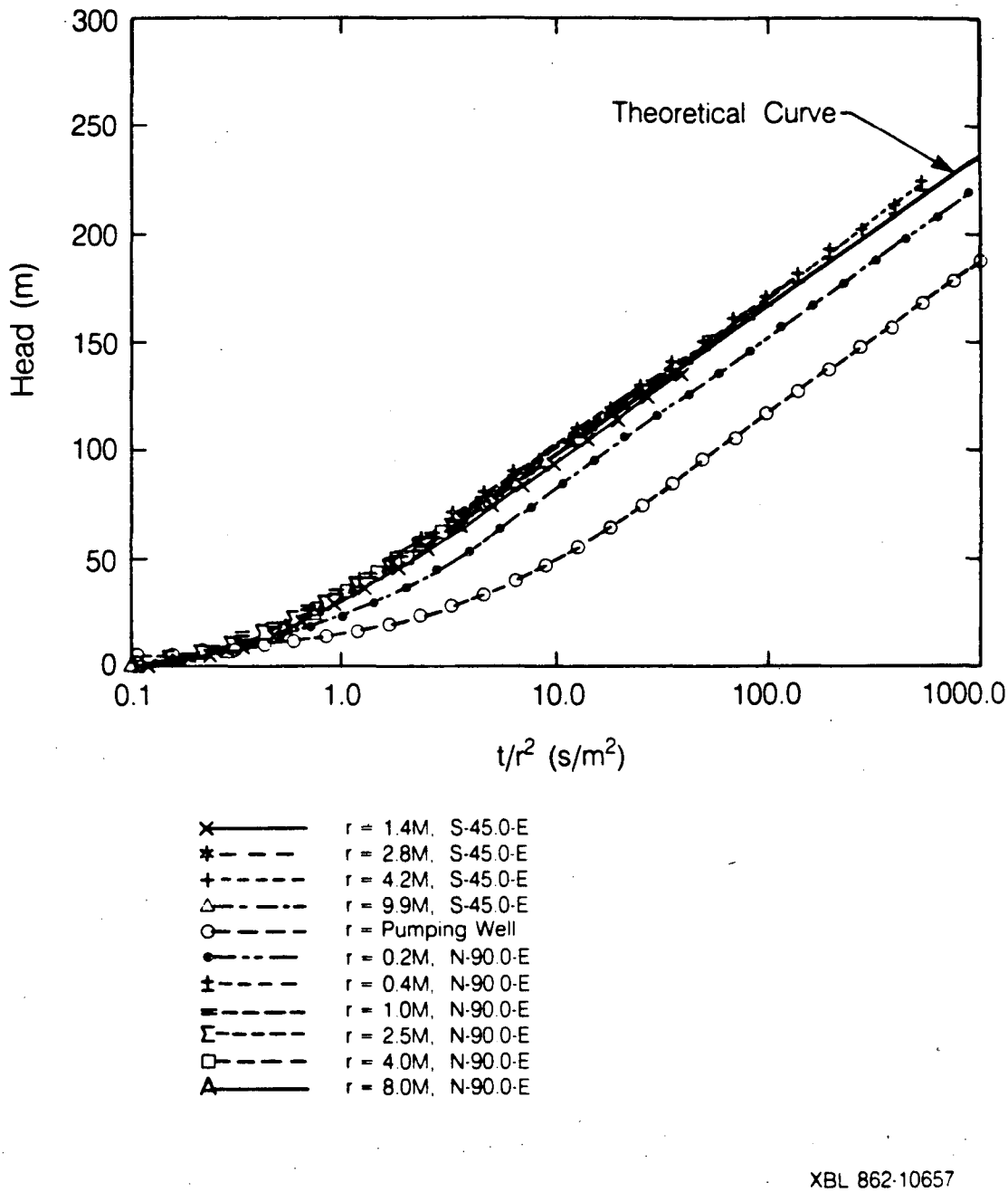

Figure 5.5b Injection test results for Case 1.

In Case-2 the location of the pumping well was changed to the middle of a fracture element (Figure 5.6a) and the same test was conducted. Figure 5.6b shows the similar result as in Case-1, but with less deviation from the theoretical curve at the pumping well.

A pumping well with the radius of $1.5m$ was used in Case-3, which is 1.5 times larger than the fracture spacing, so that twelve fractures were intersected by the well (Figure 5.7a). The results show that the straight line portion of the pumping well data can be extrapolated to obtain a value of storage coefficient which is nearly equal to the volume averaged value despite of the deviation from the theoretical value at early time (Figure 5.7b). Note that the flattening of the curves are due to the open outer boundary condition.

The study indicates that when the pumping well radius is small compared to the fracture spacing, the storage coefficient calculated from the semilog analysis may be much different from the correct value and one has to rely on observation wells that are located far enough from the pumping well to obtain the correct storage coefficient.

5.2.2. Well Tests in Discontinuous Fracture Systems

Two distinct fracture meshes were generated using the same fracture frequency, orientation and aperture distributions (Figure 5.8a,b). However in Case-4, the mean fracture length was longer than in Case-5. Thus Case-4 is a more highly connected fracture network than Case-5 and should behave

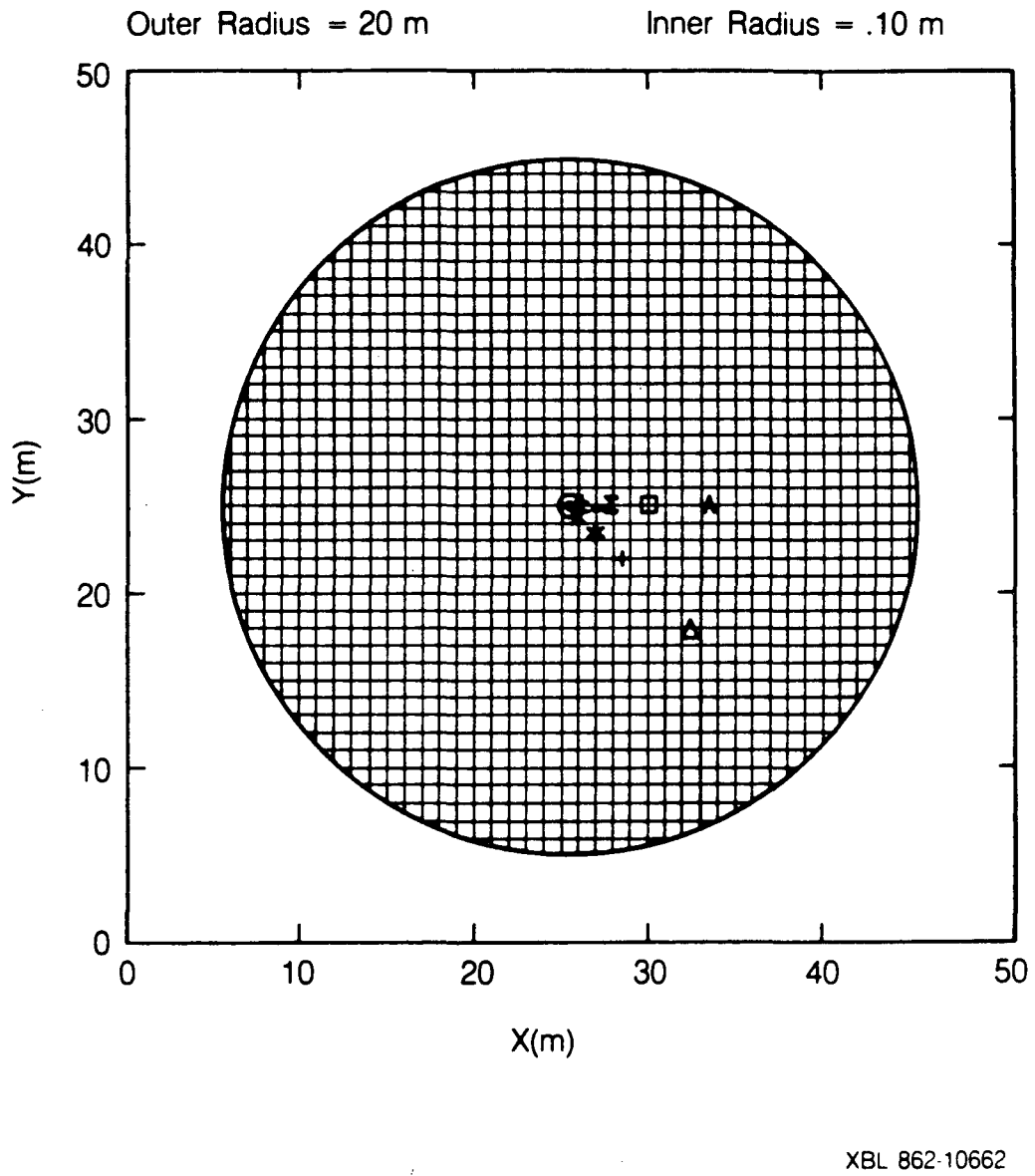

Figure 5.6a Case 2 - pumping well at middle of fracture.

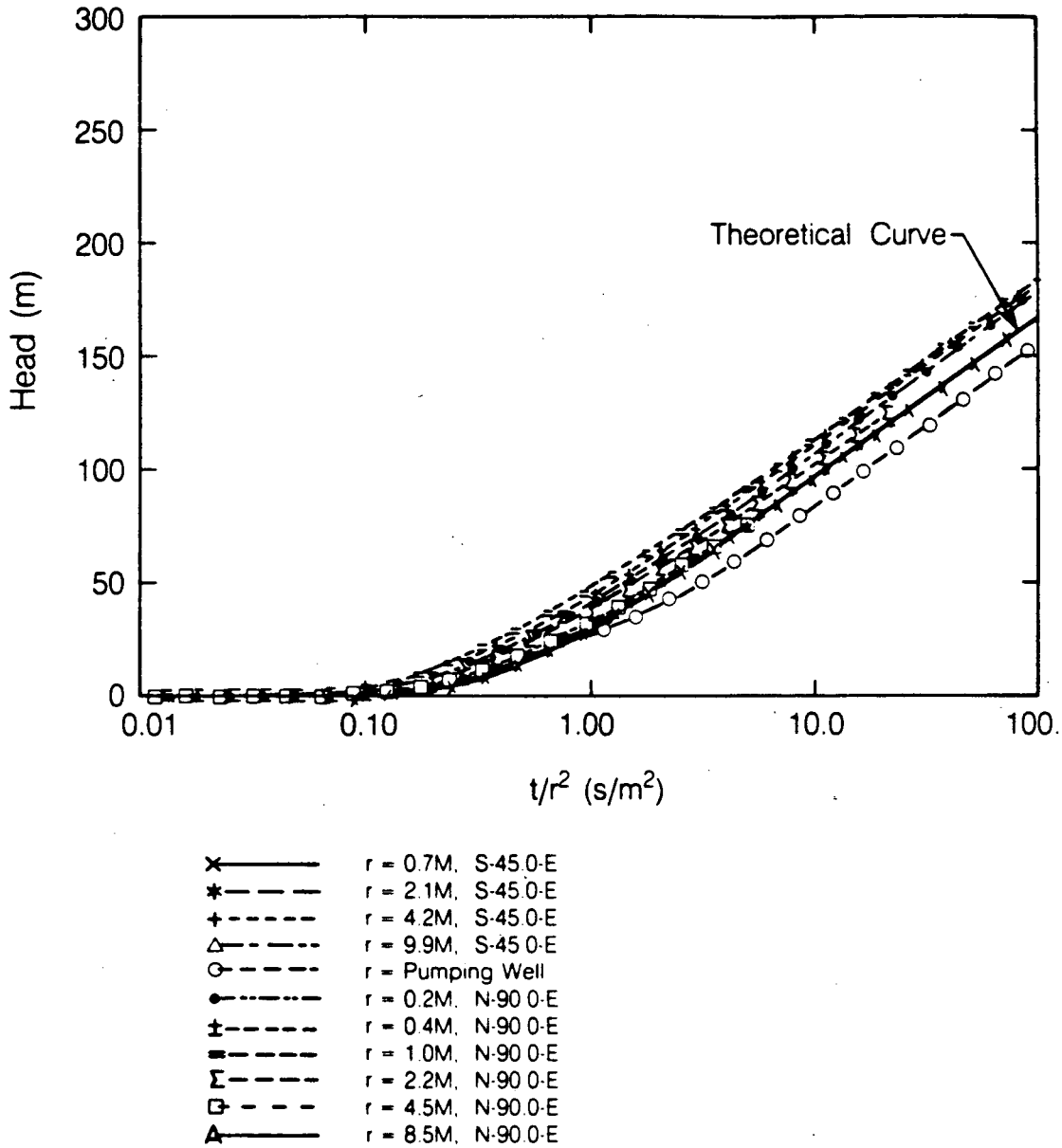

Figure 5.6b Injection test results for Case 2.

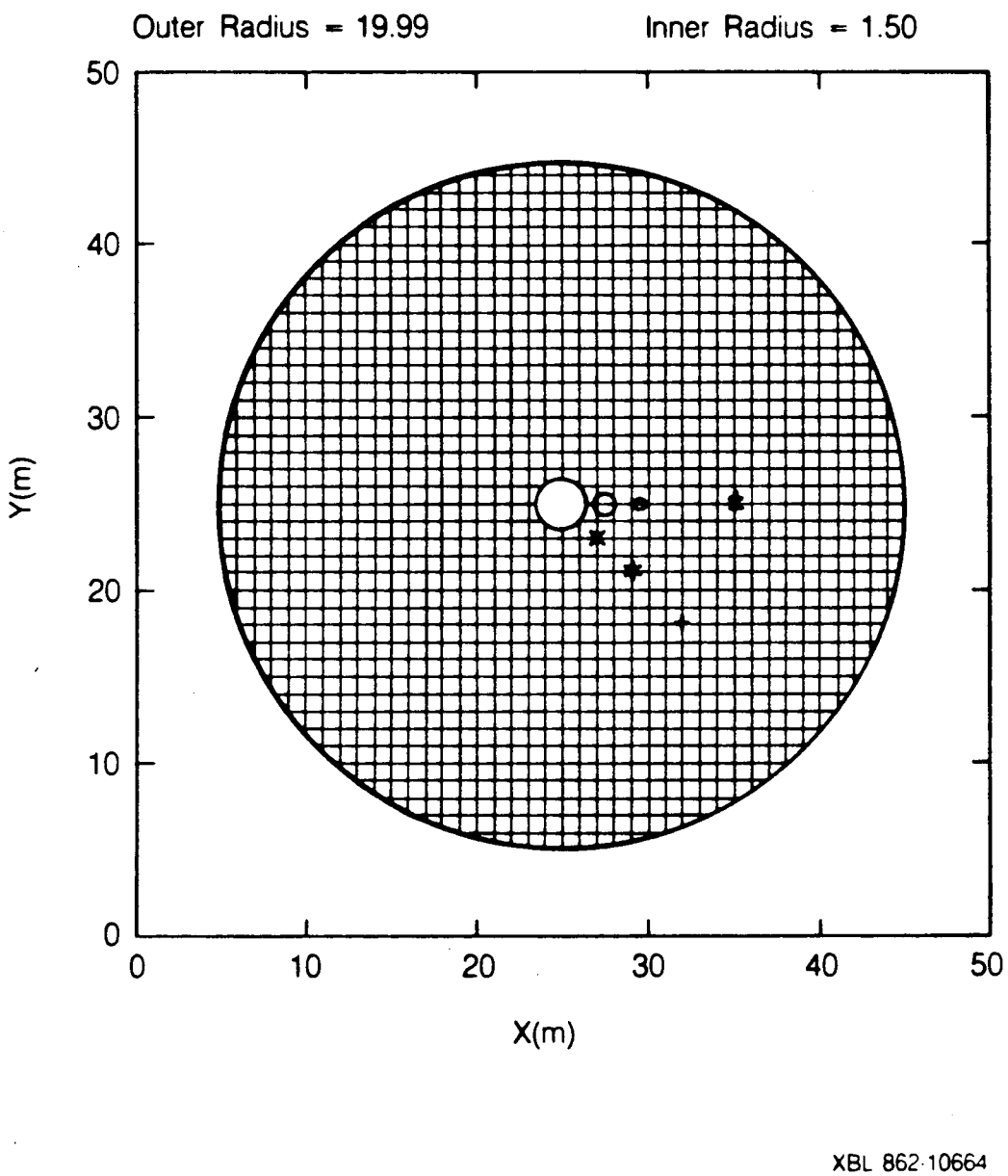

Figure 5.7a Continuous fracture system-large diameter well.

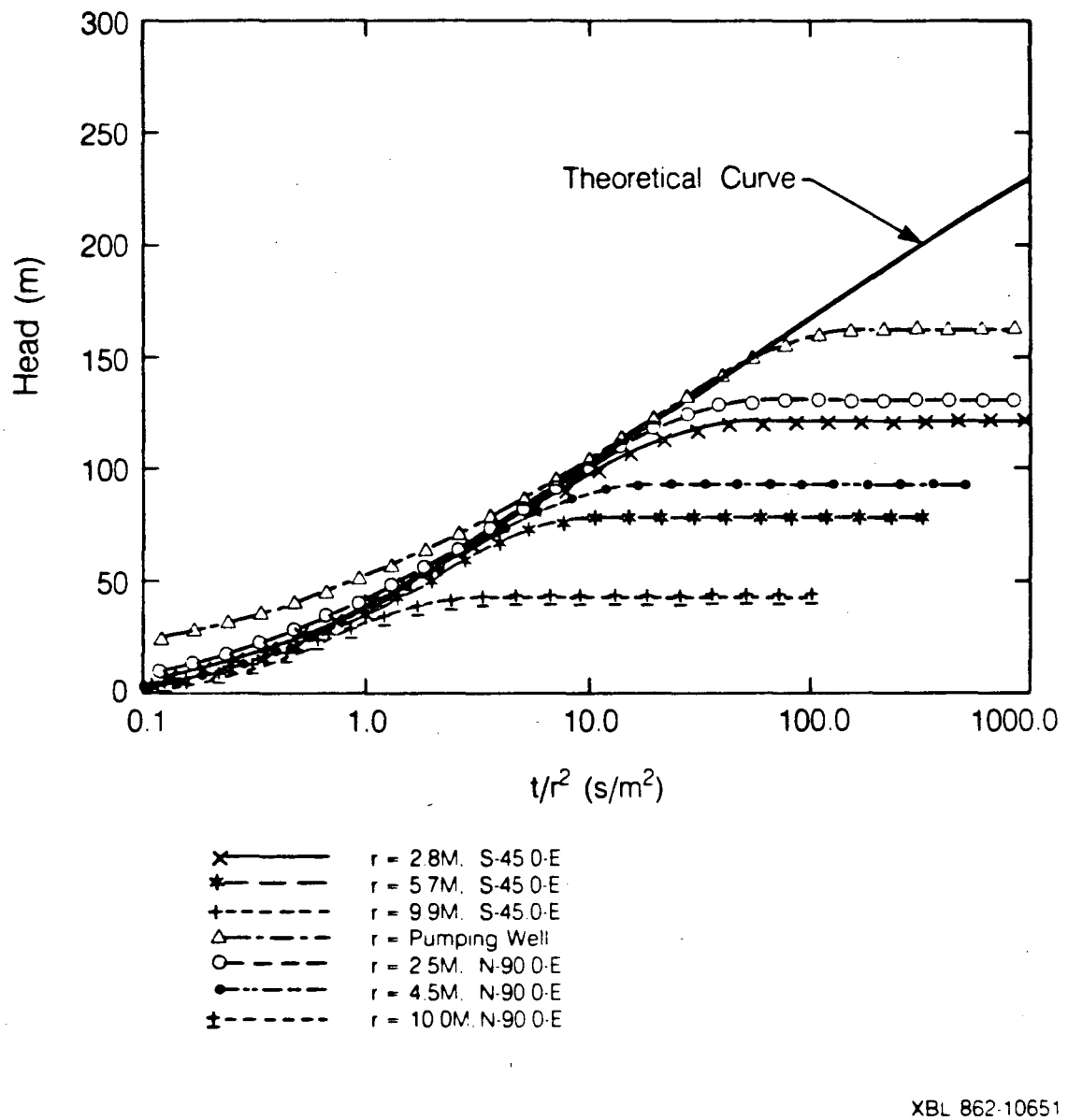

Figure 5.7b Injection test results for the system in Fiugure 5.7a.

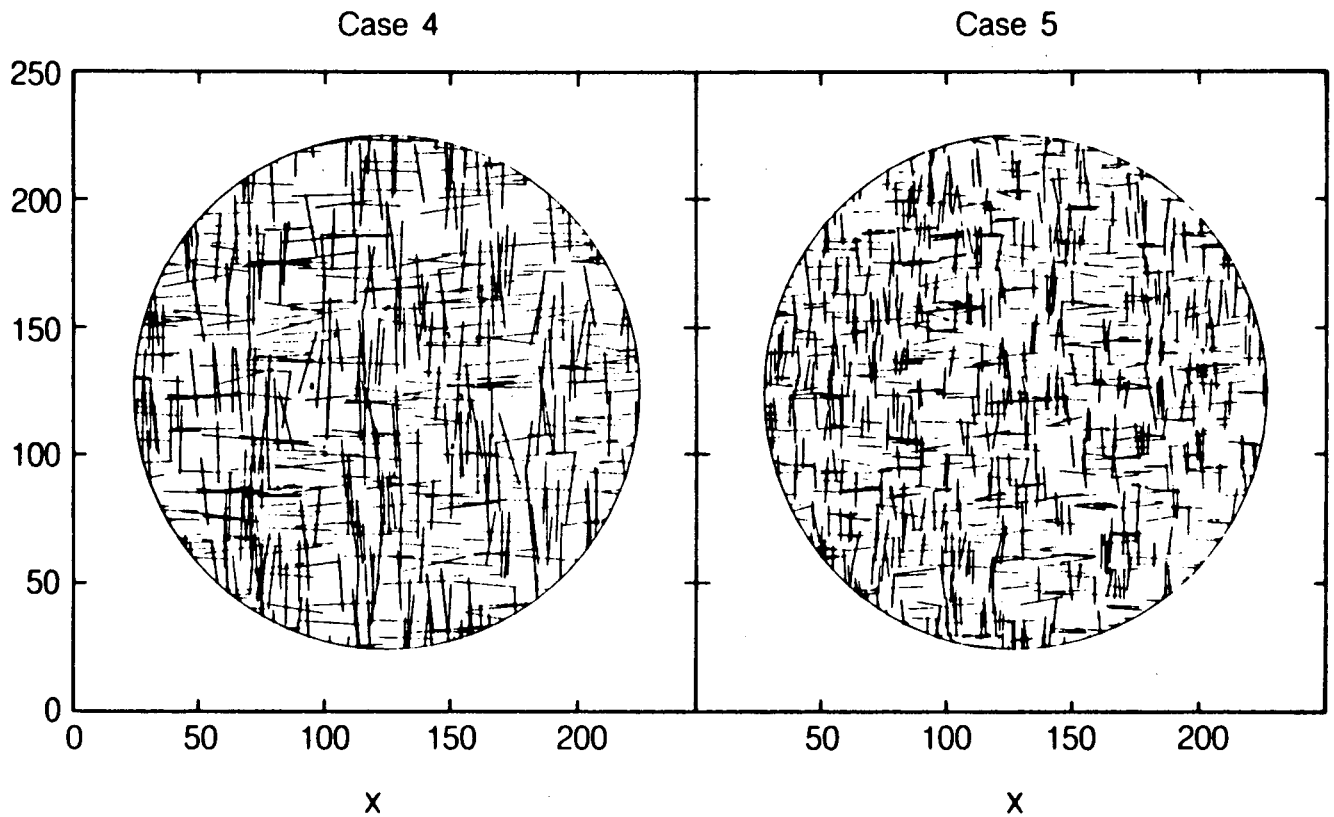

XBL 862-10673

Figure 5.8 Fracture meshes for Case 4 and Case 5.

more like a homogeneous continuum. The input data for the two cases are listed in Table 5.1.

Table 5.1 Geometric Parameters for Case4 and Case5.

	Case 4		Case 5	
Outer boundary radius	100m		100m	
Well radius	0.1m		0.1m	
Set no.	Set 1	Set 2	Set 1	Set 2
Line density (1/m)	0.2	0.2	0.2	0.2
Length (m/σ)	25m/2.5m	25m/2.5m	13m/1.3m	13m/1.3m
Orientation (m/σ)	0°/5°	90°/5°	0°/5°	90°/5°
Aperture (m/σ)	20μm/0μm	20μm/0μm	20μm/0μm	20μm/0μm

m = mean, σ = standard deviation

Statistically, these meshes have isotropic permeability. Constant rate injection tests were performed with the pumping well located at the center. Interference responses were observed at various convenient locations in the system where fractures occured. The results were analyzed based on the method presented by Papadopulos (1965) taking only the portions of the pressure records before the boundary of the system is perturbed.

5.2.2.1. Case-4

Figure 5.9 and Figure 5.10 show semilog plots of interference responses of two different groups of three arbitrarily chosen observation wells each called group A and group B and the permeability ellipses that result from the

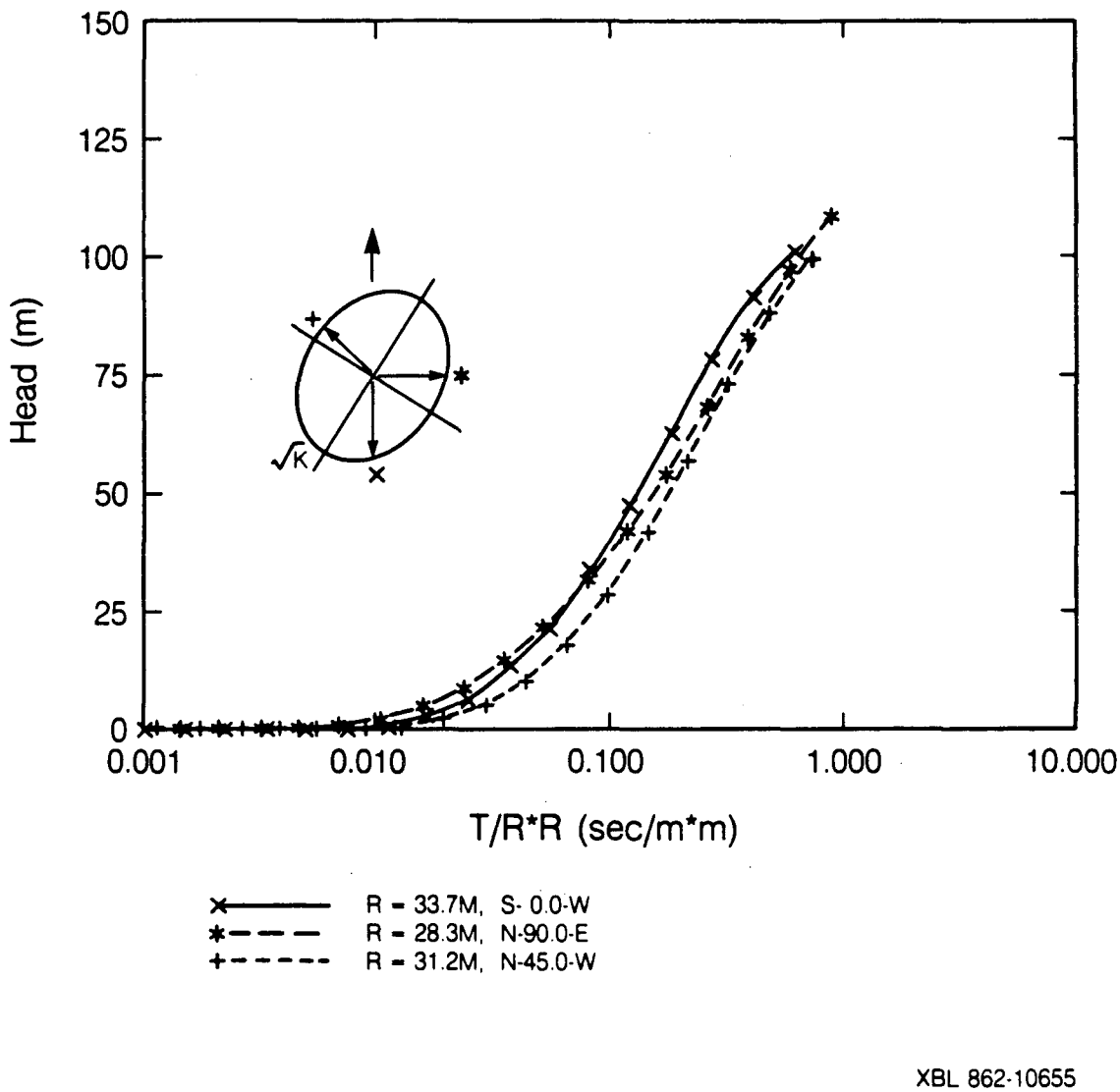

Figure 5.9 Injection test results for Case 4 at Group A observation wells.

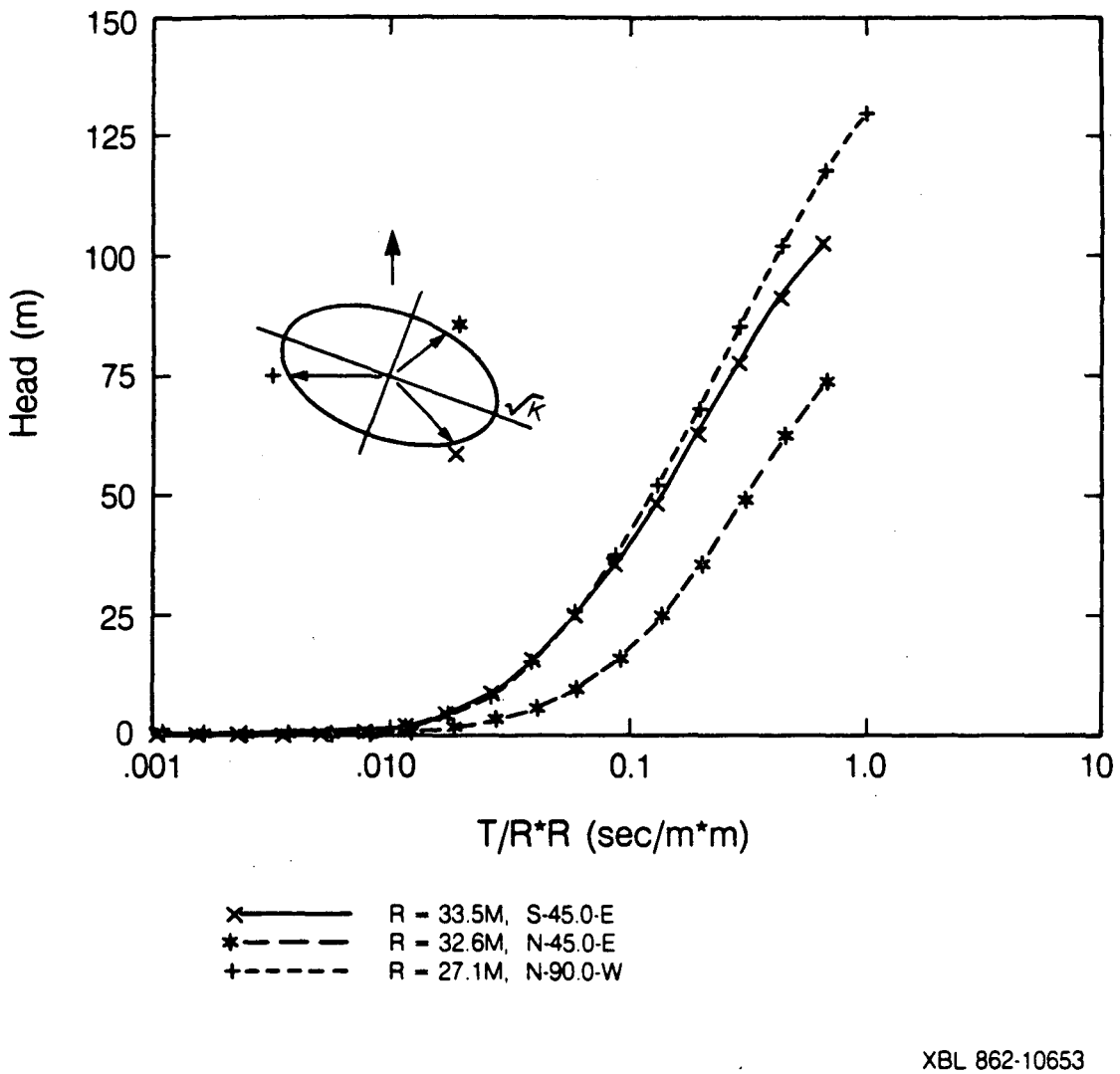

Figure 5.10 Injection test results for Case 4 at Group B observation wells.

analysis of the data in each group. The results are summarized and tabulated in Table 5.2.

Table 5.2 Principal Permeabilities and Axis Orientation for Case 4.

Group	K_X($\times 10^{-10}$ m/s)	K_Y($\times 10^{-10}$ m/s)	θ
Group A	8.3	4.8	N-31 °-E
Group B	13.1	3.1	S-70 °-E

By arbitrarily choosing different groups of wells, totally different pictures of the system anisotropy are observed. Figure 5.11 shows the iso-potential map at a particular time in the duration of the well test and that in fact the system is roughly isotropic as expected.

5.2.2.2. Case-5

In this case the mean fracture length is about one half of and the areal density is twice than that of Case-4. Again, in a porous medium, any three arbitrarily chosen observation wells should determine the anisotropic permeability tensor. First, Group A which consisted of wells located at $9.1m$ S-W, $20.4m$ S, and $12.9m$ E were chosen for the analysis. Semilog plots were generated and three time-axis intersects were obtained. However no single permeability ellipse can account for these three measurements. The fracture system simply does not behave like a porous medium on the scale of observation (Figure 5.12). Two other groups of three observation wells were analyzed (Figure 5.13 and 5.14) and the results are tabulated in Table 5.3.

XBL 862-10659

Figure 5.11 Iso-potential contour map for Case 4.

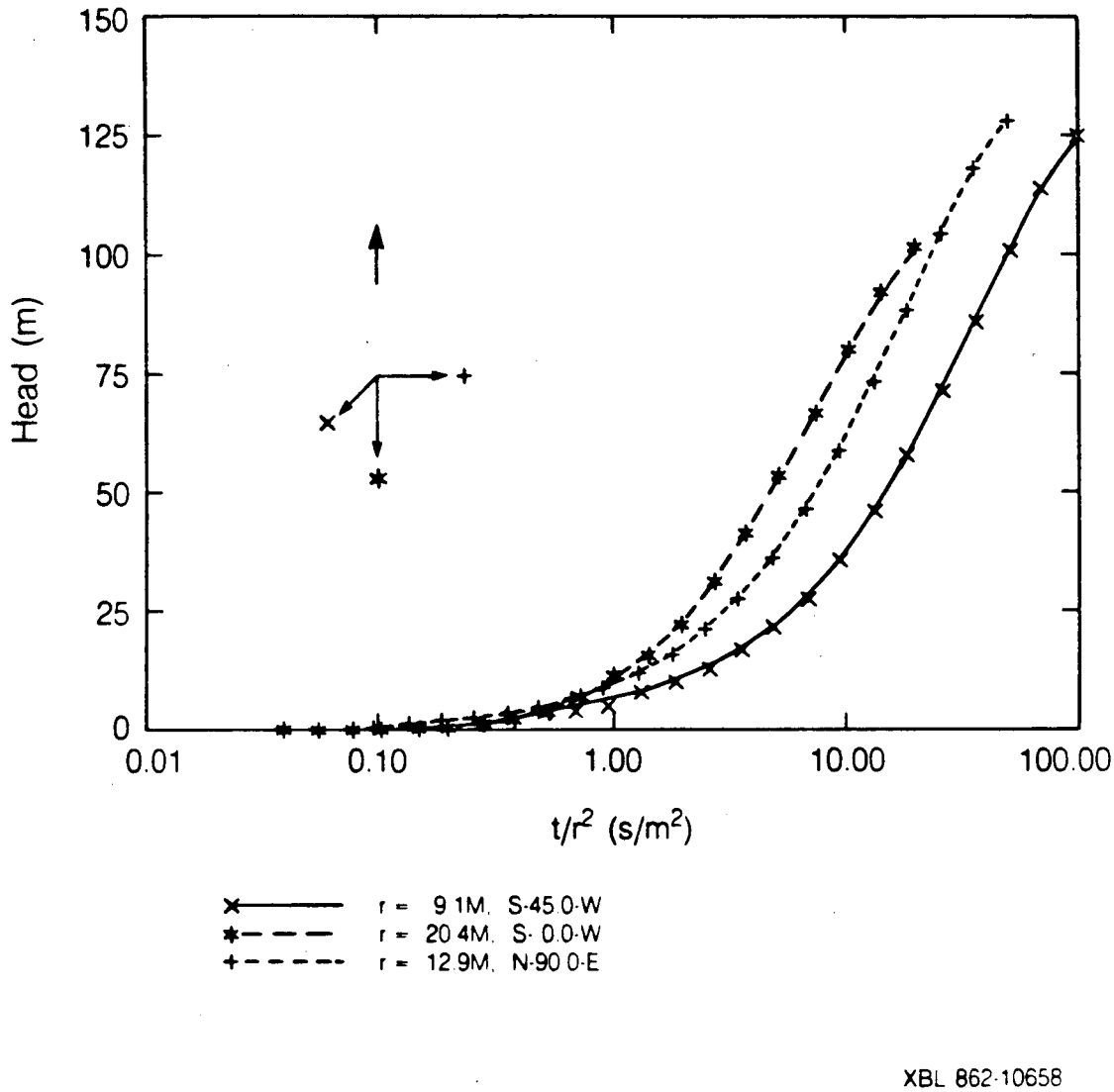

Figure 5.12 Injection test results for Case 5 at Group A observation wells.

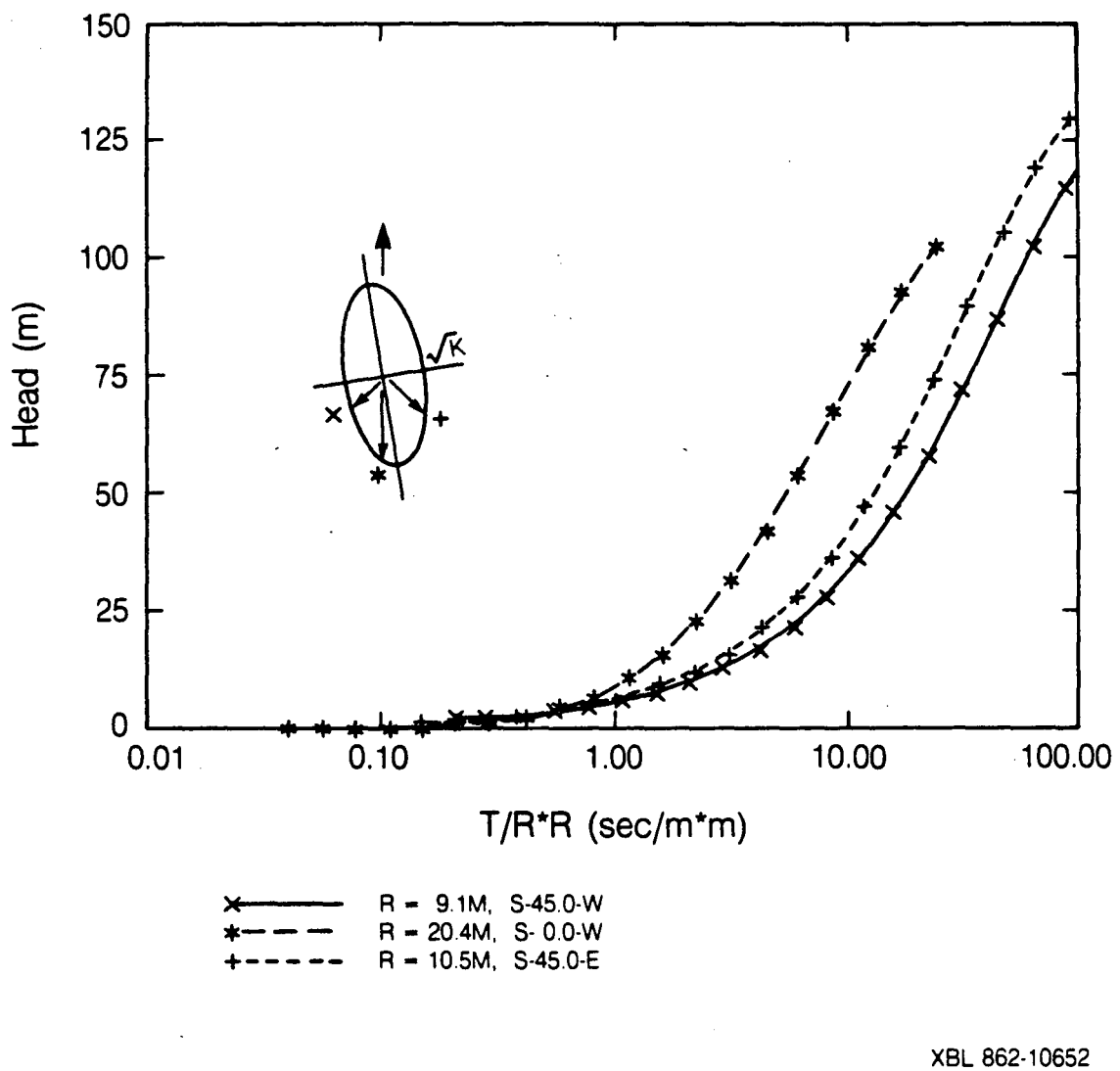

Figure 5.13 Injection test results for Case 5 at Group B observation wells.

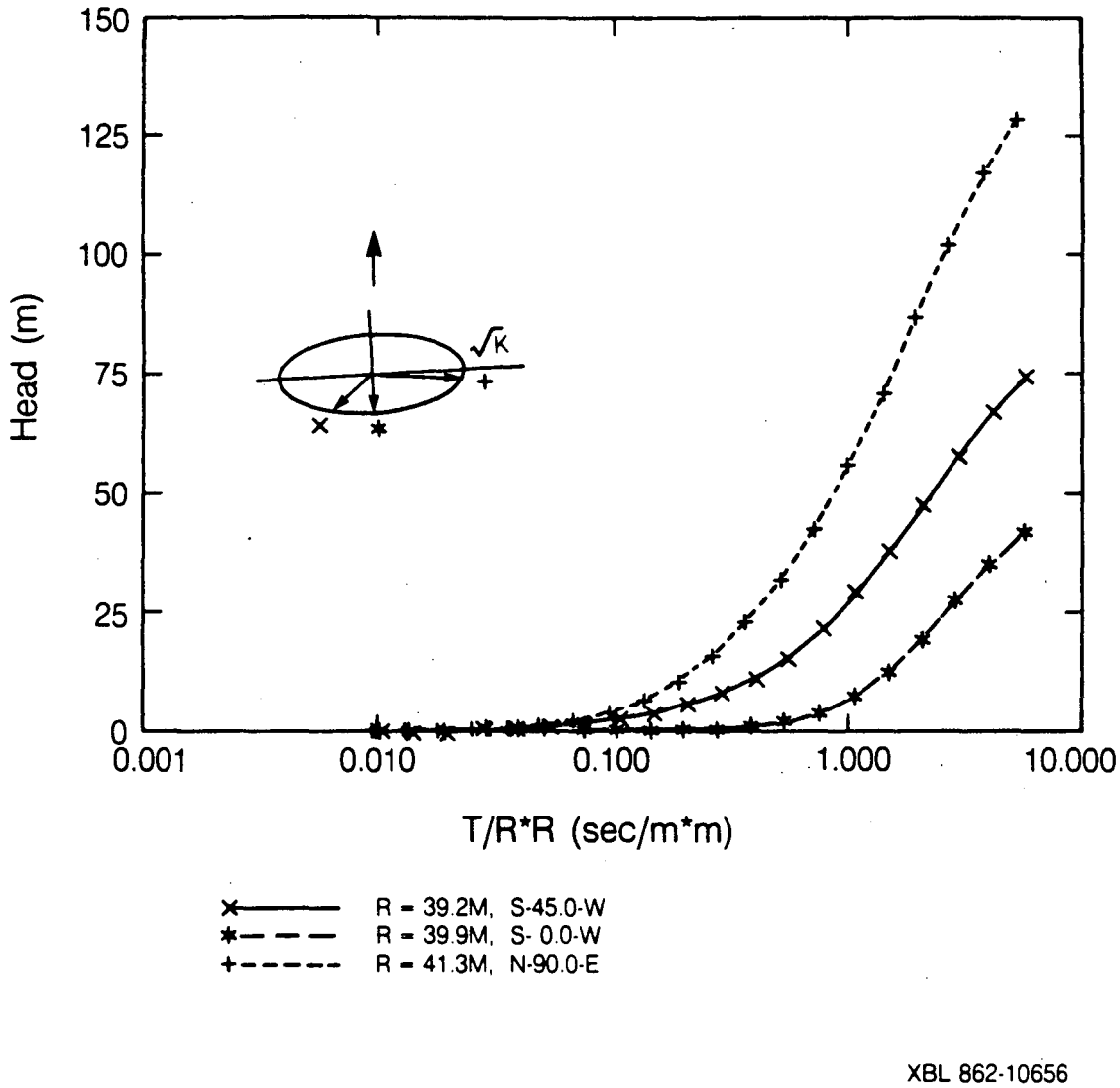

Figure 5.14 Injection test results for Case 5 at Group C observation wells.

Table 5.3 Principal Permeabilities and Axis Orientation for Case 5.

Group	K_X($\times 10^{-11}$ m/s)	K_Y($\times 10^{-11}$ m/s)	θ
Group A	-	-	-
Group B	3.9	0.77	S-9.5 °-E
Group C	4.3	0.70	N-83.7 °-E

From those two groups of observation wells, two different permeability ellipses were obtained with nearly opposite orientations. When dead-end fractures and independent patches are taken out of the fracture mesh plot (Figure 5.15), one can clearly see that the system is poorly connected and thus the results of the anisotropy analysis are rather meaningless. Figure 5.16 shows how the iso-potential lines propagate with time and provides further evidence of the non-radial flow of the system. Lack of connection between fractures may be such that conventional well testing methodology may fail or provide misleading answers.

5.3. Conclusions

The pressure transient at the pumping well during a constant flux pumping or injection test is very sensitive to the local fracture characteristics and therefore the results obtained from analysis by conventional methods may be quite different from the average system parameters. The locations of observation wells must be chosen such that the distance to the pumping well is far enough to include representative volume of rock. For systems with per-

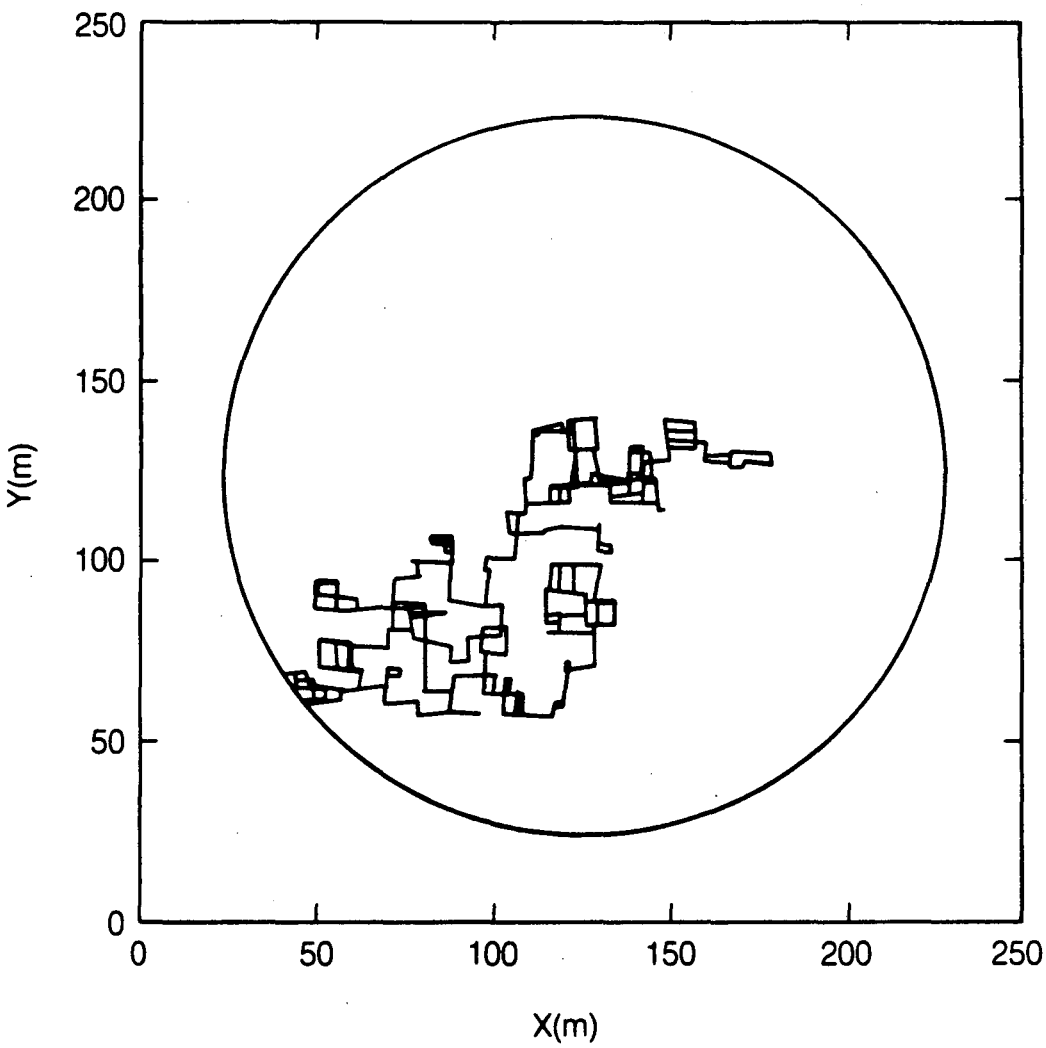

XBL 862-10661

Figure 5.15 Fracture mesh for Case 5 with only connected fractures shown.

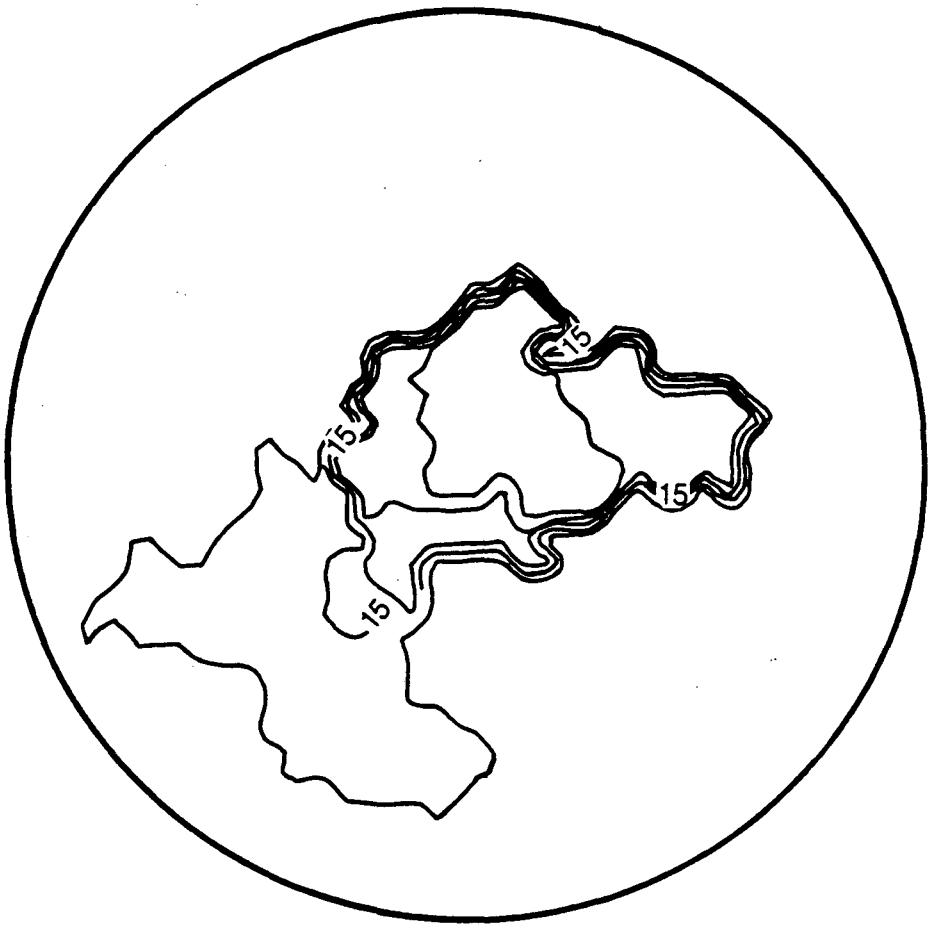

XBL 862-10660

Figure 5.16 Isopotential contour map for Case 5.

meability anisotropy, three observation wells may not be enough to define the permeability tensor because of local heterogeneities. In sparsely fractured rock, the system may not behave like a continuum on any scale of interest and the conventional well testing methodology may fail or provide misleading answers. Hydrologic characterization of such systems will be very difficult.

CHAPTER 6

A NEW FRACTURE AND MATRIX MESH GENERATOR

6.1. Introduction

Analysis of fluid flow behavior in naturally fractured porous media is generally very difficult because of the complex nature of the fracture geometry. Analytical treatment of the problem, therefore, is limited to simple and ideal cases. The double porosity models originated by Barenblatt (1960) and extended by many others (Warren and Root, 1963; Odeh, 1965; Kazemi, 1969; Streltsova, 1983) treat naturally fractured porous systems by superimposing two continua, one for the fracture system and another for the porous matrix. In these models several assumptions must be made. These assumptions include:

1) the fracture system behaves as an equivalent continuum,
2) the permeability of the porous matrix is very small compared to that of the fracture system so through-flow can be neglected in the porous matrix.

It may be very difficult to know a priori whether these assumptions are appropriate for a given system. In fact, the criteria for these assumptions to be valid depend on the conditions the system is subjected to and the phenomena of interest. For example, the criteria for equivalent porous medium behavior for transport phenomena is more restrictive than that for

permeability (Endo, 1985). Also where gradients are changing rapidly, erratic behavior will result from heterogeneities which can not be accounted for by an equivalent continuum.

Complex processes in complex geometries are more amenable to analysis through numerical modeling. However, numerical models require that the domain of interest be partitioned into smaller subdomains and, for the case of a fractured porous medium, this is a painstakingly tedious task if done by hand. There has not been a computer program to do the task automatically. This is one of the reasons why published works on numerical analyses of such problems have been limited to simple fracture geometries with very few fractures or equally spaced, orthogonal sets of fractures under assumptions similar to those discussed above. Computational limitations such as excessive memory requirements and execution time have also limited the case studies.

In the present work a numerical scheme is presented which subdivides arbitrary two-dimensional spaces defined by random, discontinuous line segments into smaller subdomains of controlled shape such as triangles and quadrilaterals. The scheme has direct application to simulation studies of mass and heat flow in fractured porous medium where fractures are represented by line segments, and the porous matrix blocks, by spaces between the line segments. The fracture mesh generator (FMG) developed by Long et al.(1982) is utilized as a pre-processor so that geometric information of the fracture mesh are input into the new mesh generator.

6.2. Code Description

A typical mesh generated by FMG is shown in Figure 6.1. It is a numerical realization of a two-dimensional fracture network, where fractures are represented by line segments. A fracture element is defined by two end nodal points, which are either fracture end points or intersections. For cases where the matrix permeability can be neglected, only the fracture geometries are needed as input to a numerical code. However, if mass or heat flow in the matrix is of importance, the rock matrix volume must be partitioned into smaller subregions of simpler shapes. As can be seen in Figure 6.1, the ends of the fractures protrude into the rock matrix (fracture dead ends) and complicate the shapes of the matrix blocks enclosed by other fractures.

Partitioning of such arbitrary shaped polygons into triangles or quadrilaterals is very difficult. The difficulty is avoided if every fracture ends at an intersection with another fracture. Under such an assumption, the matrix blocks enclosed by fractures are always convex. This may be a good assumption in some cases as field observations have shown (Dershowitz, 1985). However, given the fracture mesh like the one in Figure 6.1, it is not necessary to invoke this approximation because one can artificially make matrix blocks convex. This can be done by extrapolating a line from a fracture dead end until it meets another fracture as shown in Figure 6.2. Although the extended portion of the line will not be treated as a part of the fracture for flow calculation, within the mesh generator, it is convenient to treat it as an imaginary fracture of zero width. The program sequentially repeats the

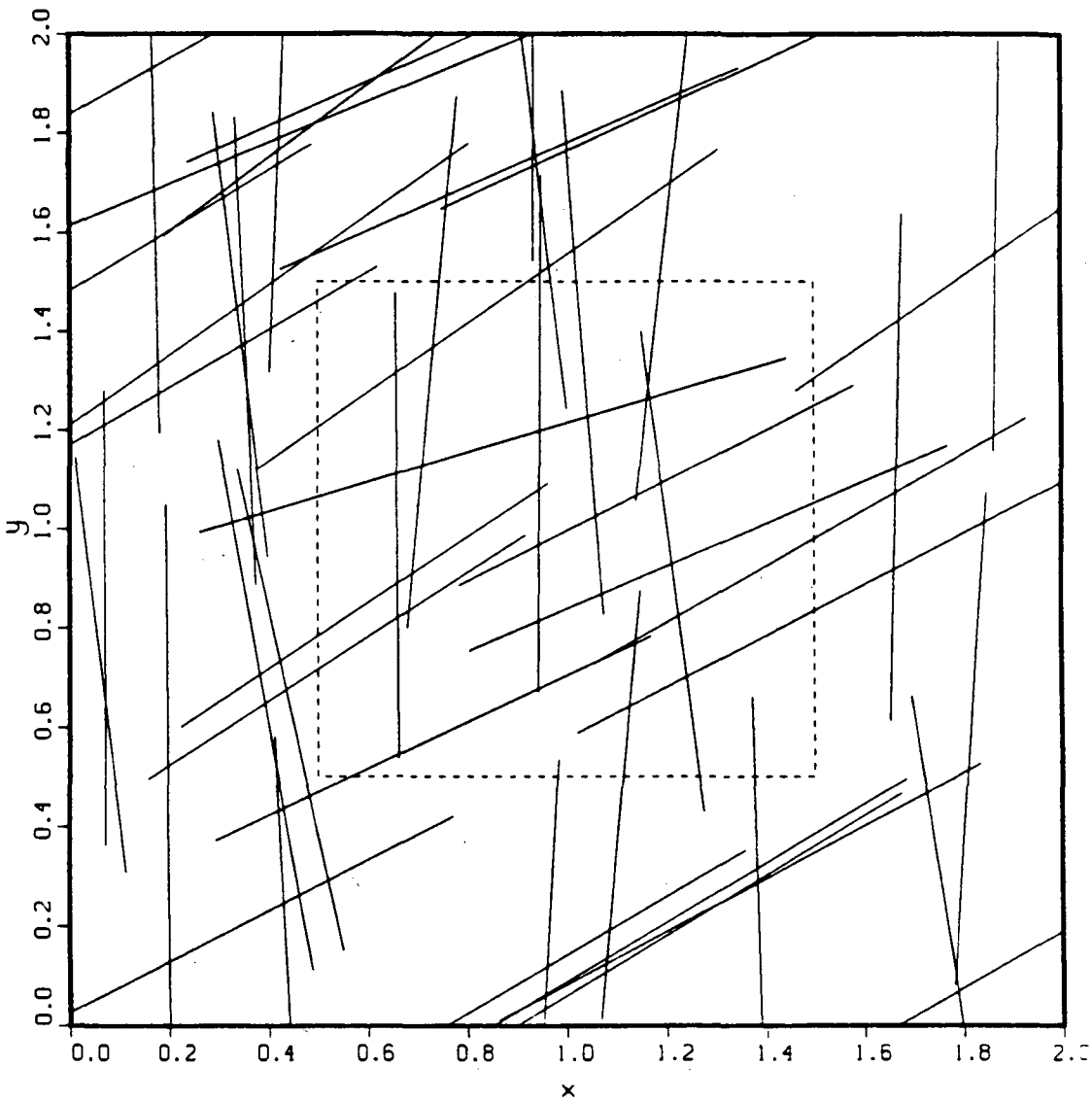

Figure 6.1 Fracture mesh generated by FMG.

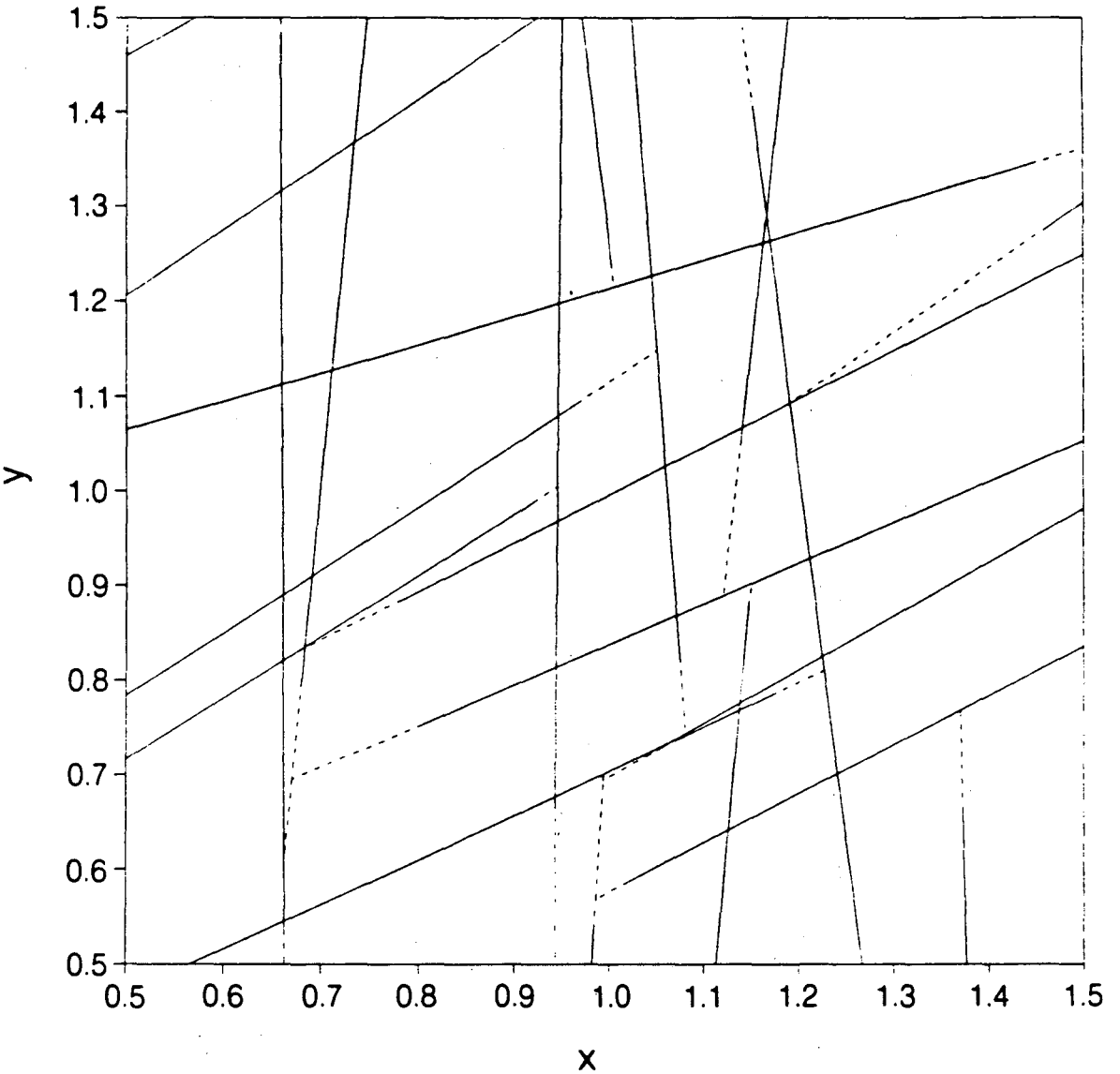

XBL 863-10722

Figure 6.2 Imaginary fracture elements and convex blocks.

operation of search and extrapolation until it does not find any more dead ends. Each successful search results in a new element and nodal points which are added to the element and nodal point catalogues. It is, therefore, quite possible that a fracture that is being extended ends in a previously created imaginary fracture, but, this does not cause any difficulty in generating the mesh.

The next step is to identify each polygon with the fracture elements and the nodal points that form it. This is done by starting with an arbitrary nodal point and following fracture elements clockwise until it arrives at the starting nodal point. This is repeated until all the fracture elements are traced twice, once in each direction. At the same time, the coordinates of the center of gravity and the volume of each polygon are calculated. After all the polygons are identified and numbered, the volume distribution of the polygons is calculated.

It is necessary to further discretize that portion of rock matrix immediately adjacent to fractures because large gradients (e.g. pressure and temperature) are expected near the fractures for transient problems. Thus, element boundary lines are drawn parallel to fractures with the spacing between them increasing as the distance from the fracture become larger. Although the increment ratios are input parameters, logarithmic ratios are recommended for transient flow problems. These boundaries together with the radial rays drawn from the gravity center to each node on the polygon perimeter define element blocks. Figure 6.3 shows the completed grid with the

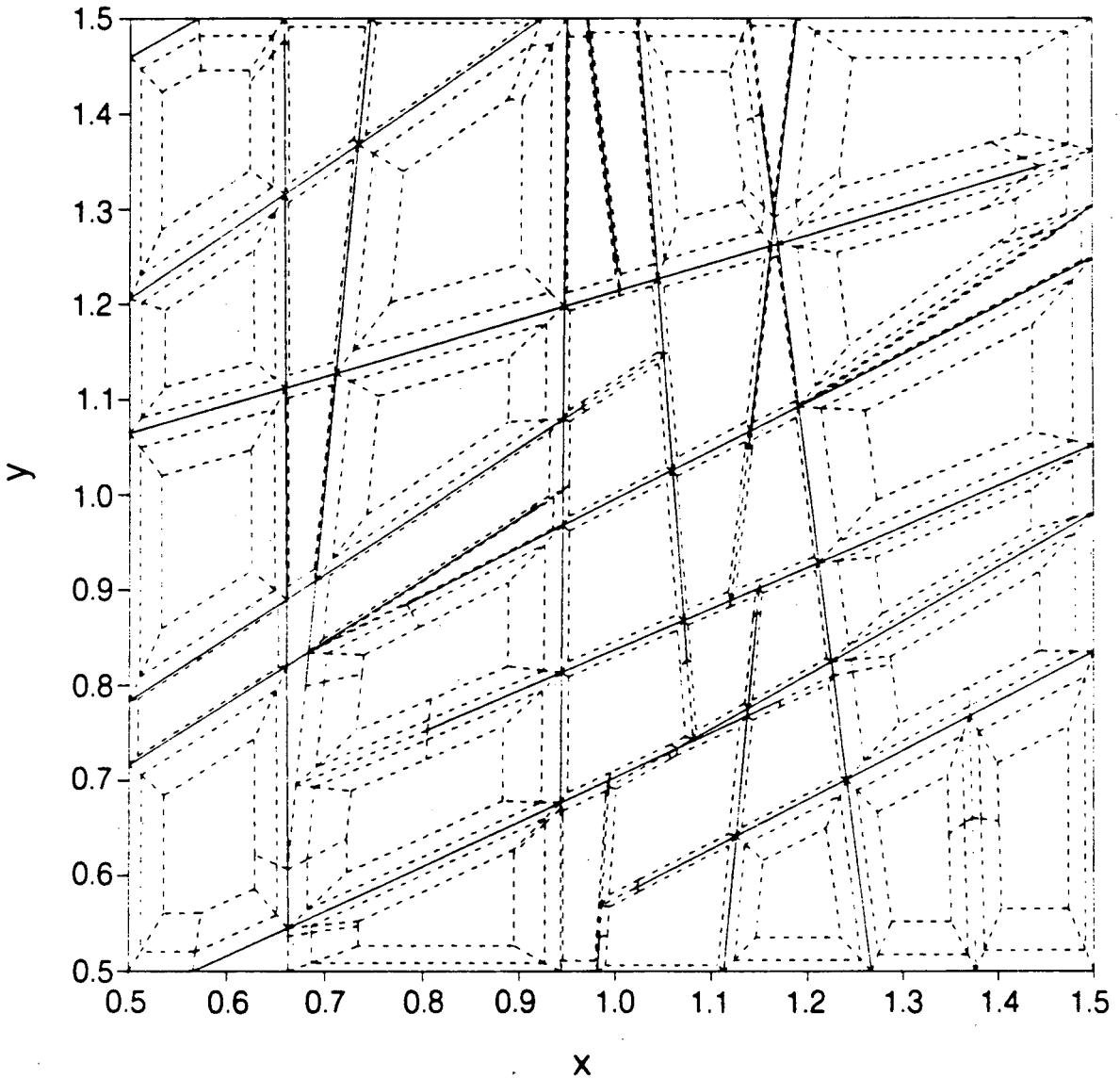

XBL 863-10723

Figure 6.3 Completed fracture-matrix mesh.

fracture mesh in Figure 6.1 and the discretized matrix blocks.

The code is written in FORTRAN-77 and is fully interactive. It includes graphics routines so that on screen graphics as well as a hard copy is readily obtained. The mesh generator has two output schemes, one for finite difference codes and the other for finite element codes. Nodal volumes, connections, interface areas and distances are the output for finite difference codes, whereas nodal coordinates and element catalogues are for finite element codes.

6.3. Example Application

In this section, we will present an example case where we simulate fluid and heat flow in a unit square block of fractured rock shown in Figure 6.1. An integrated finite difference numerical simulator, PT developed by Bodvarsson (1982) is used. The values of input parameters used in the example are listed in Table 6.1.

It is assumed that all the fractures have the same permeability of 1.0×10^{-10} m^2, which is six orders of magnitude larger than that for the rock matrix. We assume that the block is initially under the natural state, i.e., the pressure at $1.0\times10^5 Pa$ and the temperature at 20 $^\circ$ C. Gravity effects are neglected. At time $t=0$, the inlet pressure and temperature are suddenly raised to, and maintained at, $2.0\times10^5 Pa$ and at 100 $^\circ$ C, respectively. The outlet pressure is maintained at the initial state. We assume that the sides of the block are insulated.

Table 6.1 Input parameters for the example case.

	Rock	Fracture
Compressibility	1.0×10^{-10} m^2	1.0×10^{-10} m^2
Density	2650 kg/m^3	2650 kg/m^3
Effective thermal conductivity	2 W/(m·$^\circ$ K)	2 W/(m·$^\circ$ K)
Permeability	1.0×10^{-16} m^2	1.0×10^{-10} m^2
Porosity	0.1	0.999
Specific heat	1000 J/(kg·$^\circ$ K)	1000 J/(kg·$^\circ$ K)

Figure 6.4 shows the transient pressure changes at Node 302 and Node 421. Node 302 is a segment of the rock matrix located at about the center of the mesh and Node 421 is the fracture located downstream from 302 as shown in the Figure 6.4. As can be seen from the figure, the pressure at Node 421 builds up much earlier than at Node 302 even though Node 421 is located downstream of Node 302. This is because the pressure front propagates match faster through fractures than through the low permeability rock matrix. The pressure at Node 421 continues to build up gradually after the initial rapid buildup. However, toward the end of the simulation, the pressure at Node 302 becomes greater than at Node 421 because the system finally reaches the steady state.

Figure 6.5 shows transient temperature profiles at Nodes 302, 421, 466 and 345. Node 466 is located at the outlet, where all the fluids are mixed. Therefore, the temperature at Node 466 is the 'average' temperature of the

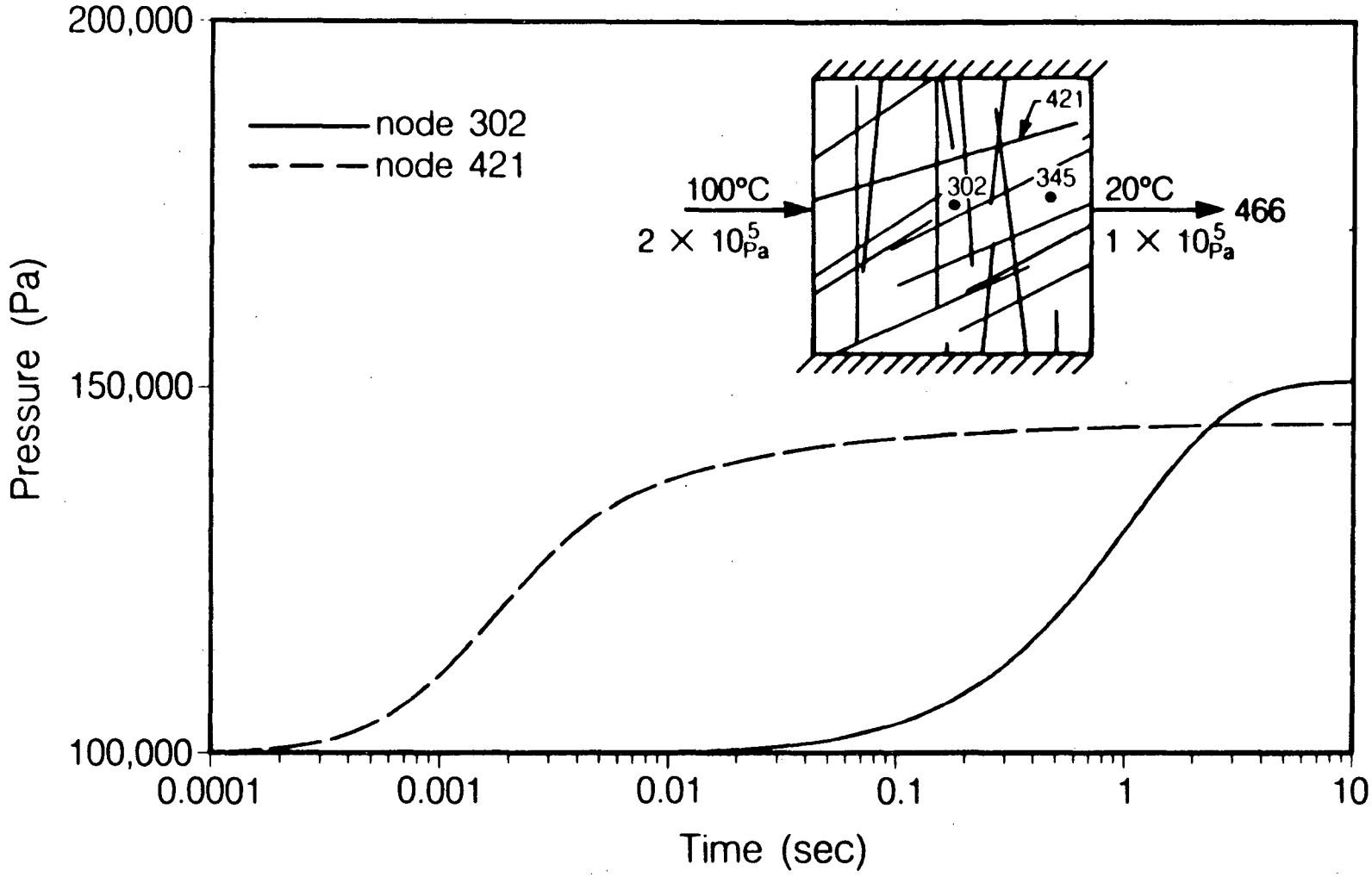

Figure 6.4 Transient pressure profiles at Node 302 and 421.

XBL 863-10687

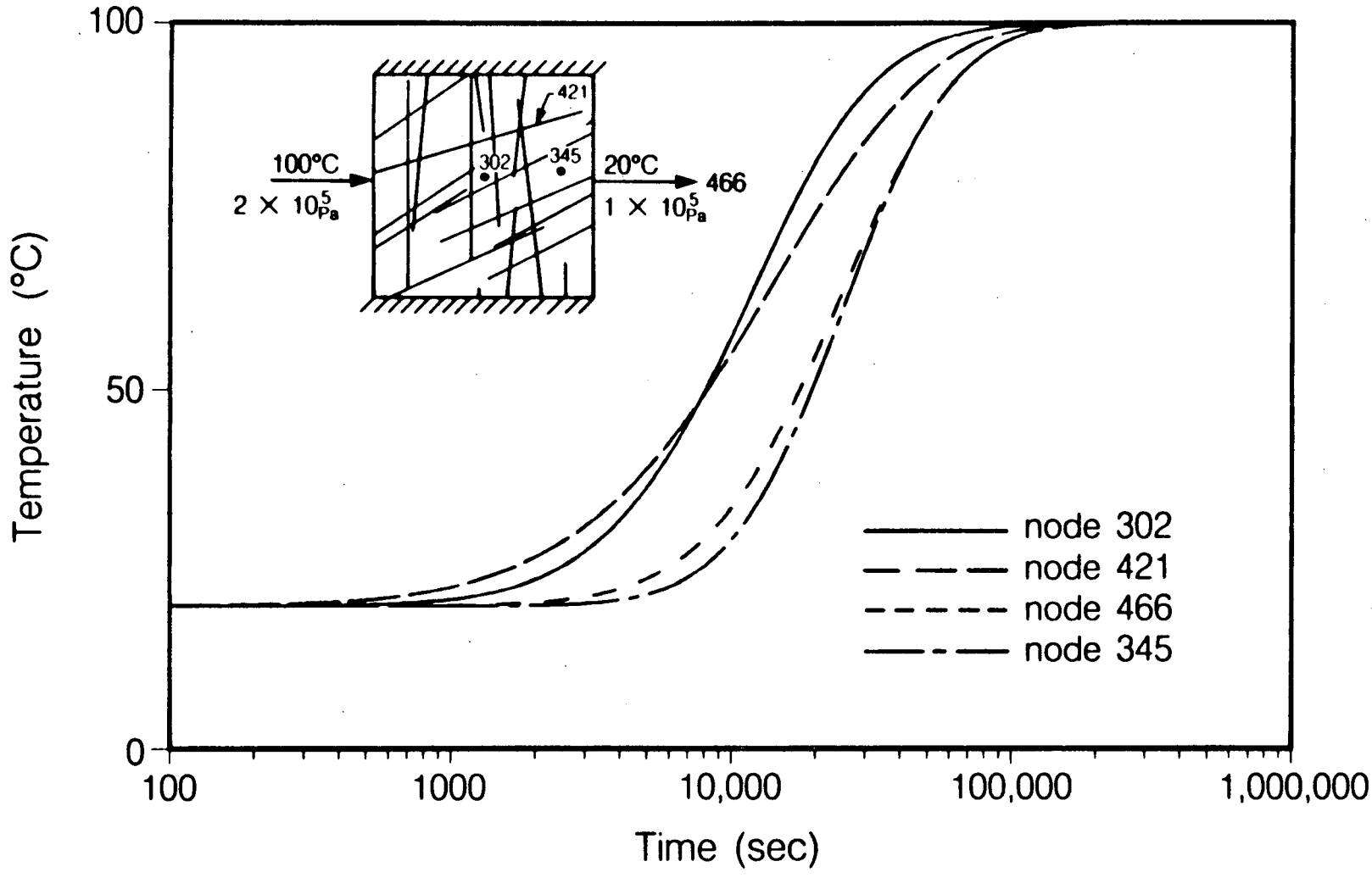

Figure 6.5 Transient temperature profiles at various nodes.

XBL 863-10685

fluids coming out of the system. As can be seen from the figure, the temperature at Node 421 is initially higher than at Node 302. However, at about 8000 seconds, the temperature at Node 302 catches up and becomes higher. This is because the hot water reaches Node 421 initially by convection though the fractures. But at a later time, the conduction front through the rock matrix catches up with the convection front, which attenuates due to the heat loss to the matrix. The shape of the curve of the temperature change in the rock matrix at Node 345, which is located near the exit, is similar to that at Node 466 at the exit, indicating the temperature field is dominated by conduction near the exit. In the conventional double porosity approach, conduction in the rock matrix cannot be modeled rigorously, because no heat or fluid through-flow is allowed in the rock matrix.

Next, we make comparison between the case when the matrix is permeable and conductive and the case when the matrix is not present, i.e. the matrix is impermeable and nonconductive. Figure 6.6 compares the pressure transients at Node 421 in a fracture. The pressure transient behavior when the matrix is permeable shows a much slower transient than when the matrix is not present. Although the rock matrix permeability is six orders of magnitude smaller than that of the fracture, the effect is significant. The effect of the presence of heat conduction though the matrix is even more significant. Figure 6.7 compares the transient temperature profiles at Node 421 and Node 466 for the two cases. When conduction in the rock matrix is neglected, the temperature break-through occurs much earlier and the transients are much

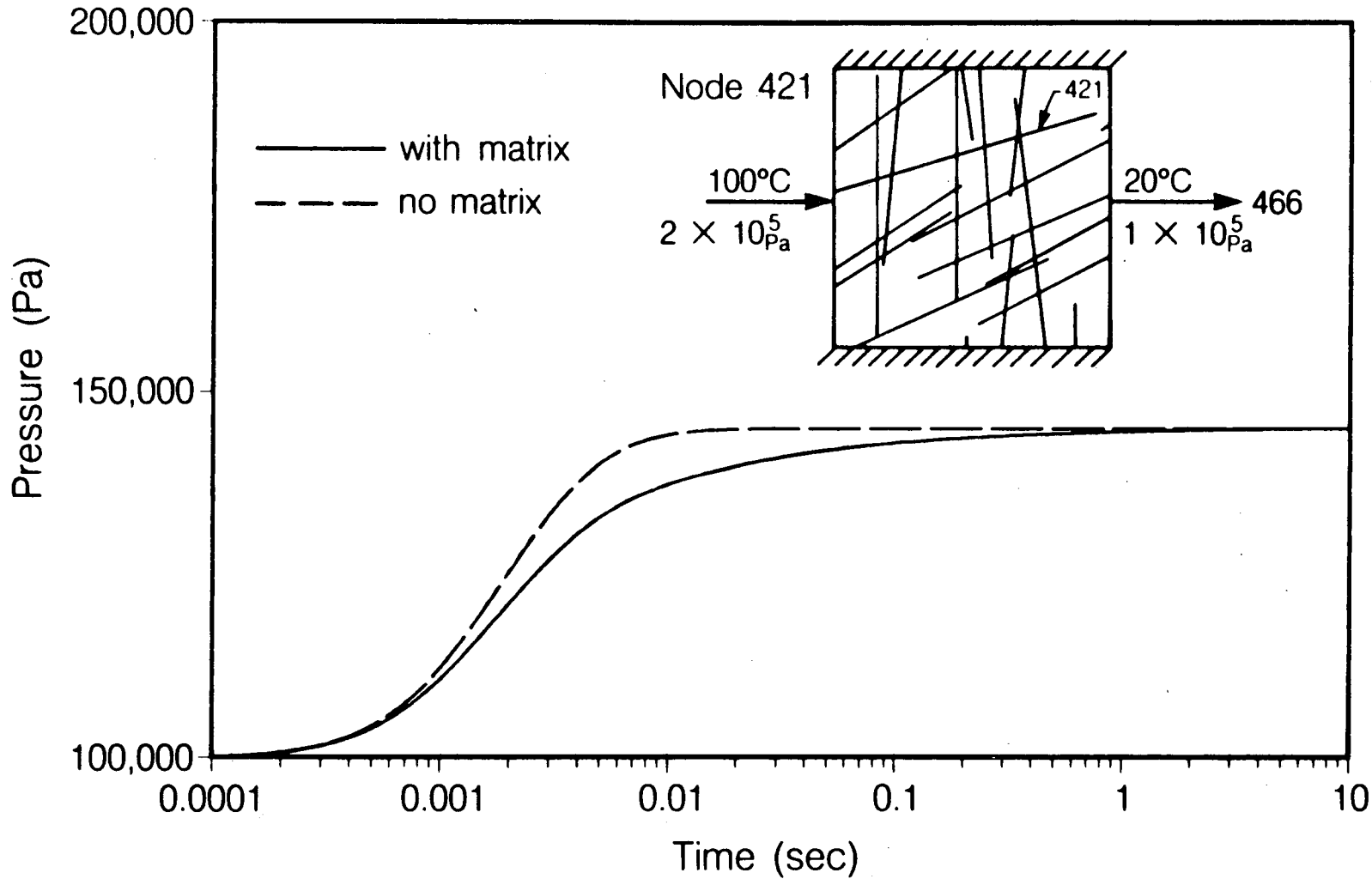

Figure 6.6 Comparison between permeable and impermeable rock matrix.

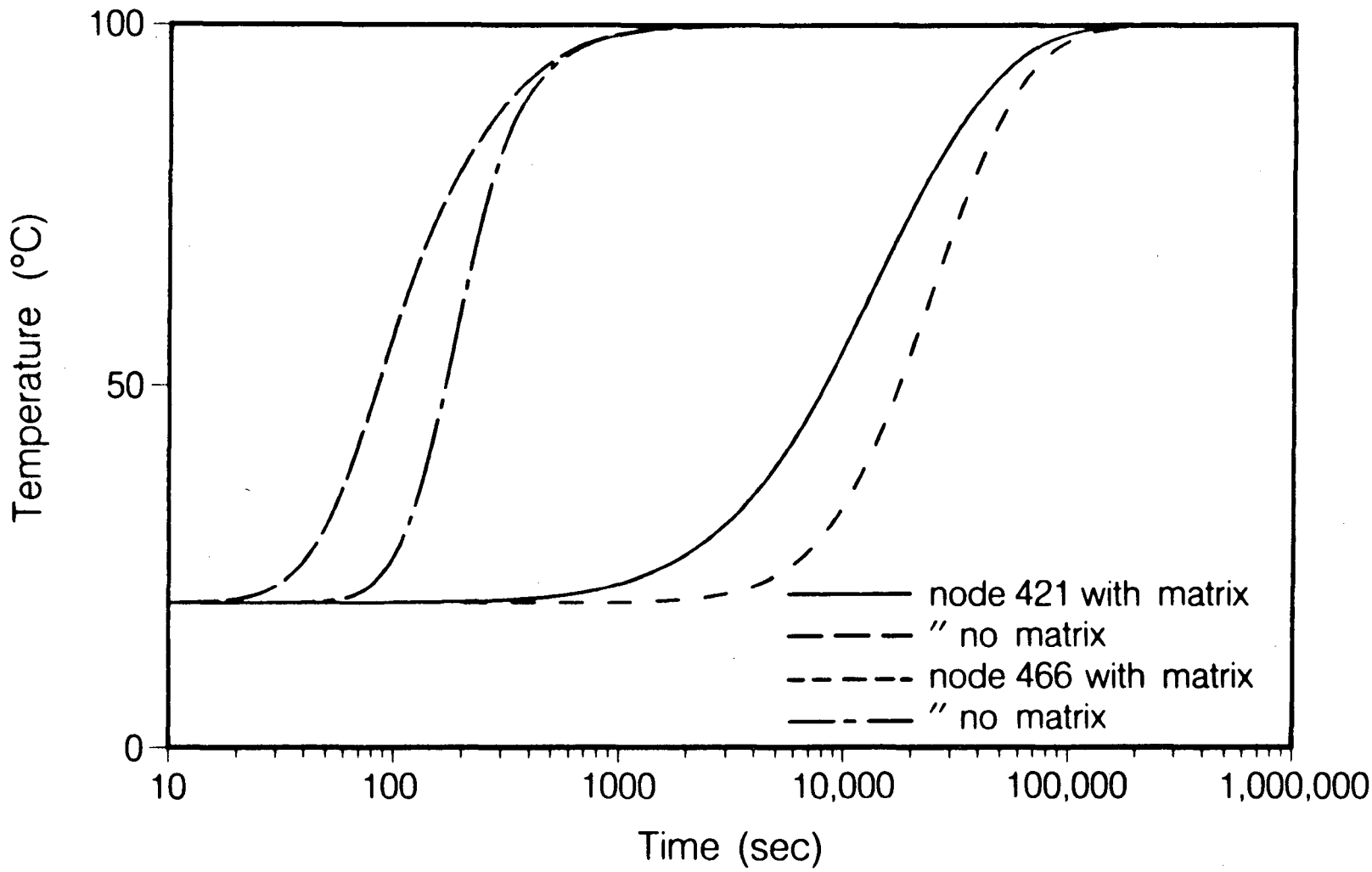

Figure 6.7 Comparison between conductive and non-conductive rock matirx.

shorter compared to the case when the conduction through the rock matrix is allowed.

6.4. Conclusions

In this chapter, we have developed a mesh generator that enables us to model discrete fractures as well as the porous rock matrix. We also presented an example simulation of hot water injection in a fractured porous medium. The fracture-matrix mesh generator can be used to address a wide variety of problems involving mass and heat flow in fractured porous rocks. The model does not require the two important assumptions that are commonly made in double porosity models, i.e., 1) the fracture system behaves as an equivalent continuum and 2) no through-flow occurs in the matrix. Thus we can simulate cases where double porosity models fail. Potential applications include analysis of hydrological and tracer tests for characterization of rocks, and fluid and heat recovery in hydrocarbon and geothermal reservoirs. It is probable, however, that the new numerical scheme will be most useful in determining when simpler fracture matrix models can be applied. It should be noted that for use with the integrated finite difference method, the mesh fails to satisfy the requirement that the line connecting two nodal points be perpendicular to the interface boundary between the nodes. More work is necessary to estimate the error involved, although we feel it is not significant for the case cited in this work.

CHAPTER 7

CONCLUSIONS

7.1. Summary and Conclusions

The primary objectives of this study were to investigate the behavior of fracture systems under well test conditions and to devise methodologies to analyze well test data from fractured media. Several analytical models are developed to be used for analyzing such data. Numerical tools that may be used to simulate mass and heat flow in fractured media are also presented.

In Chapter 3, three types of composite models for constant flux test were investigated. These models were based on the assumption that, in some cases, a fracture system may be better represented by two concentric regions than a single continuum under well test conditions, i.e., the inner region representing single fracture characteristics and the outer region representing the average system behavior. The first model was one in which a linear flow develops into a radial flow (or radial flow converging to linear flow), and the second model was a classical radial flow model. Thirdly, we studied a radial-spherical combination. It was shown for all three types of composite models that the early time pressure behavior represents the inner region characteristics and the late time behavior represents those of the outer region. Type curves are presented that can be used to find the extent and the flow parameters of the fractures near the well and the average values for the entire system provided that wellbore storage effects do not mask the early time data.

Examples were shown how one of these models may be used to interpret the field data. However, it also became clear that, in some cases, it may not be possible to determine all the parameters from one transient pressure test, because some of the type curves are similar to each other.

Three Laplace inversion schemes for the radial composite model were compared, i.e., the approximate inversion scheme introduced by Shapery (1969), the numerical inversion scheme introduced by Stehfest (1970), and the exact analytical inversion scheme. It was found that the approximate inversion scheme was not very accurate in some cases and therefore the use of it is not recommended for well test problems. On the contrary, the numerical inversion scheme was found to be very accurate and it was decided that the scheme should be used for the rest of the problems in the present study. It has an advantage over the analytical scheme because the amount of CPU time required to evaluate the solution is much less than that for the analytical scheme.

In Chapter 4, several solutions that may be used for analyzing slug test results were presented. The geometric conditions that may be present in fractured media were considered, although they are not limited to such media. The type curves developed for each model can be used to estimate such geometric parameters as the distance to the boundary as well as the flow parameters. However, analyses of slug test results suffer problems of nonuniqueness, more than other well tests, i.e., many curves have unique shapes only for some combination of the flow parameters and the geometries,

and other sets of type curves are all similar in shape, although log-log plots may emphasize some features that may not be apparent in semi-log plots. Therefore, it is important that one consider all other available information, such as geology and geophysical data, when analyzing the results of slug tests. The solutions developed in Chapter 4 apply directly to pressurized pulse tests. Pressurized pulse tests may be used to estimate the flow parameters and geometry of an individual fracture.

A field example of slug tests which do not match with the existing solution for homogeneous porous media was presented. Type curve matches with two of the solutions developed in the present study were presented to demonstrate their use. Although better matches were obtained than with the conventional curves, it was not possible to match the entire data. The reason for this was probably that the initial head was too high and caused turbulence in the wellbore. This was an example of the mismatch between well test data and analytical solutions that can occur when the reality is different from the assumptions made in the analysis. Although a model could be constructed to include the adverse conditions such as wellbore storage effects, pipe resistances, or non-Darcy flow, well tests should be designed in advance to minimize those conditions as much as possible. Through the analytical studies in the present work, it became clear that the fewer the number of variables there are in the solution, the more accurately the flow properties of the system can be estimated.

In Chapter 5, a finite element model that can simulate transient fluid flow in fracture networks was presented. The behavior of various two-dimensional fracture systems under well test conditions was investigated using the finite element model. We observed that the pressure transient at the pumping well during a constant flux pumping or injection test is very sensitive to the local fracture characteristics and therefore the results obtained from analysis with the conventional method may be quite different from the average system parameters. Also the locations of observation wells must be chosen such that the distance to the pumping well is far enough to include representative volume of rock. For systems with permeability anisotropy, three observation wells may not be enough to define the permeability tensor because of local heterogeneities. In sparsely fractured rock, the system may not behave like a continuum on any scale of interest and that the conventional well testing methodology may fail or provide misleading answers. Hydrologic characterization of such systems will be very difficult.

In Chapter 6, a mesh generator that can be used to explicitly model fluid flow in a porous matrix as well as in discrete fractures was developed. An algorithm to make any arbitrary shaped polygons bounded by discrete line segments convex was presented. The arbitrary shaped polygons can be partitioned into triangles or quadrilaterals, whichever is required by the particular numerical model. Because the model does not require the two important assumptions that are commonly made in double porosity models, i.e., 1) the fracture system behaves as an equivalent continuum and 2) no through-flow

occurs in the matrix, it can be used to simulate cases where double porosity models fail. A simulation of hot water injection in a fractured porous medium was presented as an example application of the mesh generator. It was shown that the effect of through-flow of heat and mass in porous rock matrix is signigicant. This through-flow is ignored in the conventional double porosity models.

7.2. Recommendations

We have attempted to analytically represent fracture systems under well test conditions by systems that are more complex than a single continuum. Although we presented three types of composite models, other combinations such as linear to spherical flow composite model may be possible depending on the geometry of the fractures. We assumed that the interface region between the inner and outer regions is infinitesimal. However, the change from one flow region to another in fact may occur gradually. The models may be modified by introducing a finite transitional region that accounts for this. Because good early time data is crucial in order to fully utilize the solutions presented, it is recommended that well tests be designed so that the wellbore storage effects are minimized.

As discussed in Chapter 4, the method of images is commonly used to obtain the dimensionless pressure in a reservoir with linear boundaries. However, a simple superposition of the contributions from the image wells onto the dimensionless pressure at the real well may not be theoretically correct

when the well has a wellbore storage and skin. This is because the real well acts as an observation well with storage and skin in response to the influence of the image wells. The dimensionless pressures for reservoirs with a linear fault may have to be recalculated to account for this effect.

In general, we do not recommend the use of slug tests to estimate the flow parameters in fractured media. Fractured media are often highly heterogeneous, and, as discussed previously, the solutions that consider different heterogeneities have similar shapes when plotted. Therefore, it will be very difficult to obtain a unique estimate of parameters by curve matching. We prefer constant flux tests over slug tests.

In Chapter 4, we discussed a spherical flow model. In the solution, we assumed that an equivalent spherical well can be used in place of a cylindrical well. However, this assumption may not be appropriate in the case when the zone open to flow in the well is very long. In this case, the well must be implemented as a cylinder with no flow conditions on the top and bottom surfaces in a three dimensional space. An analytical solution for this problem is probably impossible because of the incompatible coordinate systems. The problem, then, must be solved numerically.

The mesh generator developed in Chapter 6 may be used to address a wide variety of problems involving mass and heat flow in fractured porous rocks. Potential applications include analysis of hydrological and tracer tests for characterization of rocks, and fluid and heat recovery in hydrocarbon and geothermal reservoirs. It may also be used to determine when simpler

fracture matrix models can be applied. Although we only presented the example application using an integrated finite difference model, a finite element model may be better suited for the problems involving such irregular shapes.

In the numerical study, we discussed only two-dimensional fracture systems. However, well testing in fractured medium is, in fact, a three-dimensional problem. Therefore, further research in three dimensional fracture systems such as the network model developed by Long et al. (1985) is needed. We also assumed that a fracture may be represented by two parallel plates. However, a fracture itself is a three dimensional feature. Laboratory experiments as well as numerical study of transient flow in a single fracture with irregular surfaces is also necessary.

REFERENCES

Adams, A. R., H. J. Ramey, Jr., and R. J. Burgess, "Gass Well Testing in a Fractured Carbonate Reservoir," Journal of Petroleum Technology, pp. 1187-1194, AIME, October, 1968.

Agarwal, R. G., R. Al-Hussainy, and H. J. Ramey, Jr., "An Investigation of Wellbore Storage and Skin Effect in Unsteady Liquid Flow: I. Analytical Treatment," Soc. Pet. Eng. J., vol. 10, no. 3, p. 279, 1970.

Baecher, G. B. and N. A. Lanney, "Trace Length Biases in Joint Surveys," in Proceedings of the 19th U.S. Symposium on Rock Mechanics, pp. 56-65, AIME, 1978.

Barenblatt, G. I., Iu. P. Zheltov, and I. N. Kochina, "Basic Concepts in the Theory of Seepage of Homogeneous Liquids in Fissured Rocks," J. Appl. Math. Mech., vol. 24, no. 5, pp. 1286-1303, 1960.

Bennett, C. O., N. D. Rosato, and A. C. Reynolds, Jr., "Influence of Fracture Heterogeneity and Wing Length on the Response of Vertically Fractured Wells," Soc. Pet. Eng. J., pp. 219-230, April 1983.

Benson, S. M. and C. H. Lai, "Analysis of Interference Data in a Highly Heterogeneous Naturally Fractured Geothermal Reservoir," Formation Evaluation, AIME, June 1986.

Bixel, H. C. and H. K. Van Poollen, "Pressure Drawdown and Buildup in the Presence of Radial Discontinuities," Society of Petroleum Engineers Journal, pp. 301-309, AIME, September, 1967.

Blackwell, J. H., "A Transient-Flow Method for Determination of Thermal Constants of Insulating Materials in Bulk," J. Appl. Phys., vol. 25, no. 2, p. 137, 1954.

Bodvarsson, G. S., Mathematical Modeling of the Behavior of Geothermal Systems Under Exploitation, Ph.D. Thesis, University of California, Berkeley, 1982.

Boulton, N. S. and T. D. Streltzova, "Unsteady Flow to a Pumped Well in a Fissured Water-Bearing Formation," J. Hydrology, vol. 35, pp. 257-270, 1977a.

Boulton, N. S. and T. D. Streltzova, "Unsteady Flow to a Pumped Well in a Two-Layered Water-Bearing Formation," J. Hydrology, vol. 35, pp. 245-256, 1977b.

Bourdet, D. P. and A. C. Gringarten, Determination of Fissured Volume and Block Size in Fractured Reservoirs by Type-Curve Analysis. paper SPE 9293, presented at the SPE 55th Annual Technical Conference and Exhibition, Dallas, Texas, Sept. 21-24, 1980

Bourdet, D., T. M. Whittle, A. A. Douglas, and Y. M. Pirard, "A New Set of Type Curves Simplifies Well Test Analysis," World Oil, Gulf Publishing Co., May 1983.

Bremer, R. E., H. Winston, and S. Vela, "Analytical Model for Vertical Interference Tests Across Low-Permeability Zones," Soc. Pet. Eng. J., pp. 407-418, June 1985.

Brigham, W. E., J. M. Peden, and K. F. Ng, The Analysis of Spherical Flow with Wellbore Storage. SPE 9294 presented at 1980 Annual SPE convention, Dallas, Tx.

Brons, F. and V. E. Marting, "The Effect of Restricted Fluid Entry on Well Productivity," J. Pet. Tech., vol. 222, pp. 172-174, Feb. 1961.

Brown, L. P., Pressure Transient Behavior of the Composite Reservoir, 1985. Presented at the 60th Annual Technical Conference and Exhibition of the SPE held in Las Vegas, NV. Sept. 22-25

Calhoun, J. C., Jr., M. Lewis, Jr., and R. C. Newman, "Experiments of the Capillary Properties of Porous Solids," Petroleum Transactions, AIME, pp. 189-196, July, 1949.

Carslaw, H. S. and J. C. Jaeger, in Conduction of Heat in Solids, Clarendon Press, Oxford, 1946.

Carter, R. D., "Pressure Behavior of a Limited Circular Composite Reservoir," Soc. Pet. Eng. J., pp. 328-334, Dec. 1966.

Carter, R. D., Characteristic Behavior of Finite Radial and Linear Gas Flow Systems -Constant Terminal Pressure Case, SPE of AIME, Low Permeability Symposium, Denver, Co., May 27-29, 1981, May 27-29, 1981.

Chen, T. and R. Kry, The Pressure Buildup from a Vertically Fractured Low Permeability Formation, 9889, pp. 553-558, Society of Petroleum Engineers of AIME, Low Permeability Symposium, Denver, Co., May 27-29, 1981, 1981.

Chu, W. C. and R. Raghavan, "The Effect of Noncommunicating Layers on Interference Test Data," J. Pet. Tech., Feb. 1981.

Chu, W. C., J. Garcia-Rivera, and R. Raghavan, "Analysis of Interference Test Data Influence by Wellbore Storage and Skin at the Flowing Well," J. Pet. Tech., pp. 171-178, Jan. 1980.

Cinco-Ley, H.Samaniego-V., F. and N. Dominguez-A., Transient Pressure Behavior for a Well with a Finite Conductivity Vertical Fracture, 1976. paper SPE 6014 presented at the SPE-AIME 51st Annual Fall Technical Conference and Exhibition, New Orleans, Oct. 3-6, 1976

Cinco-Ley, H., Samaniego-V., F. and N. Dominguez-A., "Transient Pressure Behavior for a Well With a Finite Conductifity Vertical Fracture," Society of Petroleum Engineers Journal, pp. 253-264, Society of Petroleum Engineers of AIME, August 1978.

Cinco-Ley, H., Ramey, H. J. Jr., Effect of Non-Darcy Flow on the Constant-Pressure Production of Fractured Wells, pp. 390400, Society of Petroleum Engineers Journal, June 1981.

Cinco-Ley, H., Samaniego-V., F., "Transient Pressure Analysis for Fractured Wells," J. Pet. Tech., vol. 33, pp. 1749-1766, Sept. 1981.

Cinco-Ley, H.Samaniego-V, F., The Pressure Transient Behavior for Naturally Fractured Reservoirs With Multiple Block Size, 1985. paper SPE 14168, presented at the 60th Annual Technical Conference and Exhibition of the SPE held in Las Vegas, NV Sept. 22-25

Cooper, H. H., Jr., J. D. Bredehoeft, and I. S. Papadopulos, "Response of a Finite Diameter Well to an Instanteneous Charge of Water," Water Resour. Res., vol. 3, pp. 263-269, 1967.

Cooper, H. H., Jr. and C. E. Jacob, "A Generalized Graphical Method for Evaluating Formation Constsnts and Slummarizing Well-Field History," Trans., American Geophysical Union, vol. 27, No.4, August 1946.

Cooper, H. H., Jr., J. D. Bredehoeft, and I. S. Papadopulos, "Response of a Finite-Diameter Well to an Instantaneous Change of Water," Water Resources Research, vol. 3. No. 1, pp. 263-269, First Quarter 1967.

Culham, W.E., "Pressure Buildup Equations fos Spherical Flow Regime Problems," Society of Petroleum Engineers Journal, pp. 545-555, December 1974.

Cuthil, E., and J. McKee, "Reducing the Bandwidth of Sparce Symmetric Matrices," Proc. 24th Nat. Conf. Assoc. Comput. Math., ACM Publ P-69, New York, 1969.

Da Prat, G., Cinco-Ley, H. and H. J. Ramey, Jr., "Decline Curve Analysis Using Type Curves for Two-Porosity Systems," Society of Petroleum Engineers Journal, pp. 354-362, Society of Petroleum Engineers of AIME, 1981.

Denson, A. H., J. T. Smith, and W. M. Cobb, "Determining Well Drainage Pore Volume and Porosity from Pressure Buildup Tests," Soc. Pet. Eng. J., vol. 261, pp. 209-216, Aug. 1976. Trans., AIME

Dershowitz, W. S., Rock Joint Systems, pp. 1-7, Golder Associates, 1985.

de Swaan O., A., "Analytic Solutions for Determining Naturally Fractured Reservoir Properties by Well Testing," Society of Petroleum Engineers Journal, pp. 112-122, AIME, June 1976.

Dietz, D. N., "Determination of Average Reservoir Pressure From Build-up Surveys," J. Pet. Tech., vol. 261, pp. 955-959, Aug. 1965. Trans., AIME

Doe, T. and J. Remer, "Analysis of Constantead Tests in Nonporous Fractured Rock," Proc. 3rd. Invitational Well-Testing Symposium, Berkeley, California, March 26-28, 1980.

Duguid, J. O. and J. F. Abel, Finite Element Galerkin Method for Analysis of Flow in Fractured Porous Media, pp. 599-615.

Earlougher, R. C., H. J. Ramey, Jr., F. G. Miller, and T. D. Mueller, "Pressure Distributions in Rectangular Reservoirs," J. Pet. Tech., pp. 199-207, Feb. 1968.

Earlougher, R. C., K. M. Kersch, and H. J. Ramey, Jr., "Wellbore effects in Injection Well Testing," J. Pet. Tech., pp. 1244-1250, Nov. 1973.

Earlougher, R. C. and K. M. Kersch, "Analysis of Short-Time Transient Test Data by Type Curve Matching," J. Pet. Tech., vol. Trans., AIME, July 1974.

Earlougher, R. C., K. M. Kersch, and W. J. Kunzman, "Some Characteristics of Pressure Bulidup Behavior in Bounded MultipleLayered Reservoirs Without Crossflow," J. Pet. Tech., Oct. 1974.

Earlougher, R. C., Advances in Well Test Analysis, Monograph Series, Society of Petroleum Engineers of AIME, Dallas, 1977.

Ehlig-Economides, C. A. and J. A. Joseph, A New Test for Determination of Individual Layer Properties in a Multilayered Reservoir, 1985. Presented at the 60th Annual Technical Conference and Exhibition of the SPE held in Las Vegas, NV Sept. 22-25

Ershaghi, I. and R. Aflaki, "Problems in Characterization of Naturally Fractured Reservoirs from Well Test Data," Soc. Pet. Eng. J., vol. 25, pp. 445-450, June 1985.

Endo, H. K., Mechanical Transport in Two-Dimensional Networks of Fractures, 1984. Ph.D. Thesis

Falade, Gabriel K. and William E. Brigham, The Dynamics of Vertical Pulse Testing in a Slab Reservior. paper SPE 5055A presented at the SPE-AIME 49th Annual Fall Meeting, Houston, Oct.6-9, 1974

Faust, C. R. and J. W. Mercer, "Evaluation of Slug Tests in Wells Containing a Finite-thickness Skin," Water Resour. Res, vol. 4, no. 20, pp. 504-506, 1984.

Freeze, R. A. and J. A. Cherry, Groundwater, p. 604, Prentice-Hall, New York, 1979.

Gringarten, A. C. and P. A. Witherspoon, "A Method of Analyzing Pump Test Data from Fractured Aquifers," in Proceedings, Symposium on Percolation in Fissured Rock, vol. 3, pp. B1B9, Int. Soc. Rock Mech., Stuttgart, 1972.

Gringarten, A. C. and H. J. Ramey, Jr., "The Use of Source and Green's Functions in Solving Unsteady-Flow Problems in Reservoirs," Soc. Pet. Eng. J., vol. 13, no. 5, p. 285, Oct. 1973.

Gringarten, A. C. and H. J. Ramey, Jr., "Unsteady-State Pressure Distributions Created by a Well With a Single Horizontal Fracture, Partial Penetration, or Recstrcted Entry," Soc. Pet. Eng. J., vol. 14, no. 4, pp. 413-426, AIME, Aug. 1974.

Gringarten, A. C., H. J. Ramey, Jr., and R. Raghavan, "UnsteadyState Pressure Distributions Created by a Well With a Single Infinite-Conductivity Vertical Fracture," Soc. Pet. Eng. J., vol. 14, no. 4, pp. 347-360, AIME, Aug. 1974.

Gringarten, A. C., D. P. Bourdet, P. A. Landel, and V. Kniazeff, A Comparison between Different Skin and Wellbore Storage Type-Cureves for Early Time

Transient Analysis, Society of Petroleum Engineers of AIME, 1979. paper SPE 8205, presented at the 54th Annual Fall Technical Conference and Exhibition of the SPE, held in Las Vegas, NV, Sept. 23-26

Gringarten, A. C., T. M. Burgess, D. Viturat, J. Pelissier, and M. Aubry, Evaluating Fissured Formation Geometry from Well Test Data: a Field Example, Society of Petroleum Engineers of AIME, 1981. paper SPE 10182, presented at the 56th Annual Fall Technical Conference and Exhibition of the SPE, held in San Antonio, Texas, Oct. 5-7, 1981

Gringarten, A. C., "Interpretation of Tests in Fissured and Multilayered Reservoirs With Double-Porosity Behavior: Theory and Practice," Journal of Petroleum Technology, pp. 549-564, Society of Petroleum Engineers of AIME, April 1984.

Guppy, K. H., H. Cinco-Ley, and H. J. Ramey, Jr., Effect of NonDarcy Flow on the Constant Pressure Production of Fractured Wells. paper SPE 9344, presented at the SPE 55th Annual Technical Conference and Exhibition, Dallas, Texas, Sept. 21-24, 1980

Hantush, M. S. and C. E. Jacob, Nonsteady Radial Flow in an Infinite Strip of Leaky Aquifers, Trans., 36, pp. 95-100, Amer. Geophys. Union, 1955.

Hantush, M. S., "Nonsteady Flow to a Well Partiallly Penetrating an Infinite Leaky Aquifer," Proc. Iraqi Scientific Soc., vol. 1, pp. 10-19, 1957.

Hantush, M. S., "Nonsteady Flow to Flowing Wells in Leaky Aquifers," J. Geophys. Res., vol. 64, no. 8, pp. 1043-1052, Aug. 1959.

Hantush, M. S., "Modification of the Theory of Leaky Aquifers," J. Geophys. Res., vol. 65, p. 3713, 1960.

Hantush, M. S., "Drawdown Around a Partially Penetrating Well," J. of Hydraulics Div., pp. 83-98, ASCE, July 1961.

Hantush, M. S., "Wells in Homogeneous Anisotropic Aquifers," Water Resour. Res., vol. 2, no. 2, pp. 273-279, 1966a.

Hantush, M. S., "Analysis of Data from Pumping Tests in Anisotropic Aquifers," Jour. Geophys. Res., vol. 71, no. 2, pp. 421-426, 1966b.

Hantush, M. S. and R. G. Thomas, "A Method for Analyzing a Drawdown Test in Anisotropic Aquifers," Water Resour. Res., vol. 2, no. 2, pp. 281-285, 1966.

Horner, D. R., "Pressure Build-Up in Wells," in Proc., ed. E. J. Brill, vol. 2, p. 503, Leiden, 1951. Third Word Pet. Cong.

Hirasaki, George J., "Pulse Tests and Other Early Transient Pressure Analyses for In-Situ Estimation of Vertical Permeability," Soc. Pet. Eng. J., pp. 75-90, Feb. 1974. Trans,. AIME, 257

Holditch, S. A., W. J. Lee, and R. Gist, An Improved Technique for Estimating Permeability, Fracture length and Fracture Conductivity from Pressure Buildup Tests in Low Permeability Gas Wells, pp. 493-497, SPE of AIME, Low Permeability Symposium, Denver, Co., May 27-29, 1981.

Holzer, T. L., "Comments of 'Determination of the Hydraulic Diffusivity of a Heterogeneous Confining Bed' by Roger G. wolff and Stavros S. Papdopulos," Water Resources Research, pp. 1104-1106, August 1973.

Hsieh, P. A., S. P. Neuman, and E. S. Simpson, "Pressure Testing of Fractured Rocks A Methodology Employing ThreeDimensional Cross-Hole Tests," NUREG/CR-3213, Dept. of Hydrology and Water Resources, Univ. of Arizona, July, 1983.

Hubbert, M. K., "The Theory of Groundwater Motion," J. Geol., vol. 48, pp. 785-944, 1940.

Hurst, W., "Establishment of the Skin Effect and its Impediment to Fluid Flow in a Wellbore," Petroleum Engineering, vol. 25, pp. B-6, 1953.

Hurst, W., Interference Between Oil Fields, Trans., 219, p. 175, AIME, 1960.

Jacob, C. E., "On the Flow of Water in an Elastic Artesian Aquifer," Trans. Amer. Geophys. Union, vol. 2, pp. 574-586, 1940.

Jacob, C. E. and S. W. Lohman, "Nonsteady Flow to a Well of Constant Drawdown in an Extensive Aquifer," Trans., pp. 559569, AGU, Aug. 1952.

Jaeger, J. C., "Some Problems Involving Line Sources in Conduction of Heat," Phil. Mag., vol. 35, no. 7, p. 169, 1944.

Jargon, J. R., "Effect of Wellbore Storage and Wellbore Damage at the Active Well on Interference Test Analysis," J. Pet. Tech., pp. 851-858, Aug. 1976.

Javandel, I. and P. A. Witherspoon, "Application of the Finite Element Method to Transient Flow in Porous Media," Soc. Pet. Eng. J., vol. 8, no. 3, p. 241, Sept. 1968.

Javandel, I. and P. A. Witherspoon, "A Semi-Analitical Solution for Partial Penetration in Two Layer Aquifers," Water Resour. Res., vol. 16, no. 6, pp. 1099-1106, 1980.

Javandel, I., "Analytical Solutions in Subsurface Fluid Flow," in Recent Trends in Hydrogeology, ed. T. N. Narasimhan, GSA, 1982.

Javandel, I. and P. A. Witherspoon, "Analitical Solution of a Partially Penetrating Well in a Two Layer Aquifer," Water Resour. Res., vol. 19, no. 2, pp. 567-578, 1983.

Johnson, C. R., R. A. Greenkorn, and E. G. Woods, "Pulse Testing: A New Method for Describing Reservoir Flow Properties Between Wells," J. Pet. Tech., pp. 33-45, Dec. 1973.

Jones, P., "Reservoir Limit Test on Gas Wells," J. Pet. Tech., pp. 613-619, June 1962.

Joseph, J. A. and L. F. Koederitz, Unsteady-State Spherical Flow With Storage and Skin, SPE of AIME, Sept. 16-19, 1984. Presented at the 59th Annual Technical Conference and Exhibition held in Huston, Texas.

Kamal, M. M., "Interference and Pulse Testing - A Review," J. Pet. Tech., pp. 2257-2270, Dec. 1983.

Kanehiro, B. Y., C. R. Wilson, and K. Karasaki, "Transient Analysis of Groundwater Flow in Fracture Networks," Lawrence Berkeley Laboratory Report LBL-15500, July 1983.

Karasaki, K., J. C. S. Long, and P. A. Witherspoon, A New Model for Well Test Analysis in Purely Fractured Media, Stanford, January 1985. Presented at Tenth Geothermal Reservoir Engineering Workshop at Stanford

Kazemi, H. and M. S. Seth, "Effect of Anisotropy and Stratification on Pressure Transient Analysis of Wells with Restricted Flow Entry," J. Pet. Tech., vol. 21, no. 5, pp. 639-647, May 1969.

Kazemi, H., "Pressure Transient Analysis of Naturally Fractured Reservoirs with Uniform Fracture Distribution," Soc. Pet. Eng. J., vol. B246, pp. 451-462, AIME, Dec. 1969.

Kazemi, H. and M. S. Seth, "The Interpretation of Interference Tests in Naturally Fractured Reservoirs with Uniform Fracture Distribution," Soc. Pet. Eng. J., vol. 246, pp. 463472, AIME, Dec. 1969.

Kazemi, H., "Pressure Buildup in Reservoir Limit Testing of Stratified Systems," J. Pet. Tech., April 1970.

Kazemi, H., L. S. Merrill, and J. R. Jargon, "Problems in Interpretation of Pressure Fall-Off Tests in Reservoirs With and Without Fluid Banks," J. Pet. Tech., pp. 1147-1156, Sept. 1972.

Kazemi, H., L. S. Merrill, Jr., and P. R. Zeman, Numerical Simulation of Water-Oil Flow in Naturally Fractured Reservoirs, American Institute of Mining, Metallurgical, and Petroleum Engineers, Inc., December 1976.

Kazemi, H. and L. S. Merrill, "Numerical Simulation of Water Imbibition in Fractured Cores," Society of Petroleum Engineers Journal, pp. 175-182, Society of Petroleum Engineers of AIME, 1979.

Kucuk, F. and W. E. Brigham, "Transient Flow in Elliptical Systems," Soc. Pet. Eng. J., pp. 401-410, Dec. 1979.

Kuo, M. C. T., Predicting Pressure Distribution in Irregularly Shaped Bounded Reservoirs. Presented at the 60th Annual Technical Conference and Exhibition of the Society of Petroleum Engineers held in Las Vegas, NV Sept. 22-25, 1985

Lai, C. H., G. S. Bodvarsson, C. F. Tsang, and P. A. Witherspoon, "A New Model for Well Test Data Analysis for Naturally Fractured Reservoirs," Presented at the 1983 California Regional Meeting, Ventura, CA, March 23-25, 1983.

Larkin, Bert K., "Solutions to the Diffusion Equation for a Region Bounded by a Circular Discontinuity," Soc. Pet Eng. J. Trans., vol. 228, pp. 113-115, AIME, June 1963.

Lee, W. J. and S. A. Holdich, Application of Pseudo-Time to Buildup Test Analysis of Low Permeability Gas Wells with Long Duration Wellbore Storage Distortion, SPE of AIME, Low Permeability Symposium, Denver, Co., May 27-29, 1981.

Lefkovits, H. C., P. Hazebroek, E. E. Allen, and C. S. Matthews, "A Study of the Behavior of Bounded Reservoirs Composed of Stratified Layers," Soc. Pet. Eng. J., pp. 43-58, March 1961.

Long, J. C. S., J. S. Remer, C. R. Wilson, and P. A. Witherspoon, "Porous media equivalents for network of discontinuous fractures," Water Resour. Res., vol. 3, no. 18, pp. 645-658, 1982.

Long, J. C. S., H. K. Endo, K. Karasaki, L. Pyrak, P. Maclean, and P. A. Witherspoon, Hydrologic Behavior of Fracture Networks, 1985. paper presented at the I.A.H. 17th International Congress on "Hydrology of Rocks of Low Permeabili- ty," Tucson, Arizona, Jan. 7-12, 1985

Long, J. C. S. and P. A. Witherspoon, "The Relationship of the Degree of Interconnection to Permeability in Fracture Networks," Journal of Geophysical Research, no. 90 No.B4, pp. 3087-3097, March 10, 1985.

Long, J. C. S., P. Gilmour, and P. A. Witherspoon, A Model For Steady Fluid Flow in Random Three Dimensional Networks of Disc Shaped Fractures, pp. 1-46, Water Resources Research, March 1985.

Loucks, T. L. and E. T. Guerrero, "Pressure Drop in a Composite Reservoir," Soc. Pet. Eng. J., pp. 170-176, Sept. 1961.

Marine, I. W., The Permeability of Fractured Crystalline Rock at the Savannag River Plant Near Aiken, South Carolina, Geological Survey Research, 1967.

Matthews, C. S., F. Brons, and P. Hazebroek, "A Method for Determination of Average Pressure in a Bounded Reservoir," in Trans., vol. 201, pp. 182-191, AIME, 1954.

Matthews, C. S. and D. G. Russell, Pressure Buildup and Flow Tests in Wells, Monograph Series, 1, Society of Petroleum Engineers of AIME, Dallas, 1967. Chapter 2.

Mavor, M. L. and H. Cinco-Ley, Transient Pressure Behavior of Naturally Fractured Reservoirs. paper SPE 7977 presented at the SPE California Regional Meeting, Ventura, Ca., April 18-20, 1979

McKinley, R. M., "Wellbore Transmissibility from Afterflow Dominated Pressure Buildup Data," J. Pet. Tech., vol. 251, pp. 863-872, AIME, July 1971.

Merrill, L. S., H. Kazemi, and W. B. Gogarty, "Pressure Falloff Analysis in Reservoirs With Fluid Banks," J. Pet. Tech., pp. 809-818, July 1974.

Miller, C. C., A. B. Dyes, and C. A. Hutchinson, The Estimation of Permeability and Reservoir Pressure From Bottom-Hole Pressure Build-up Characteristics, Trans., 189, pp. 91-104, AIME, 1950.

Moench, A. F., "Double-Porosity Models for a Fissured Groundwater Reservoir With Fracture Skin," Water Resour. J., vol. 20, no. 7, pp. 831-846, July 1984.

Moench, A. F. and P. A. Hsieh, Analysis of Slug Test Data in a Well with Finite Thickness Skin, Tucson, Arizona, Jan. 7-12, 1985. Presented at the I.A.H. 17th International Congress on "Hydrology of Rocks of Low Permeability"

Moran, J. H. and E. E. Finklea, "Theoretical Analysis of Pressure Phenomena Associated with the Wireline Formation Tester," J. Pet. Tech., pp. 899-908, AIME, Aug. 1962.

Mueller, T. D. and P. A. Witherspoon, "Pressure Interference Effects Within Reservoirs and Aquifers," J. Pet. Tech., pp. 251-271, April, 1965.

Najurieta, H. L., "A Theory for Pressure Transient Analysis in Naturally Fractured Reservoirs," J. Pet. Tech., pp. 12411250, July 1980.

Narasimhan, T. N., "A Unified Numerical Model for SaturatedUnsaturated Groundwater Flow," in Ph.D. dissertation, University of California, Berkeley.

Narasimhan, T. N., "Physics of Saturated-Unsaturated Subsurface Flow," in Recent Trends in Hydrogeology, ed. T. N. Narasimhan, GSA, 1982.

Neuman, S. P., P. A. Witherspoon, and Theory of Flow in Aquicludes Adjacent to Slightly Leaky Aquifers, Water Resour. Res., vol. 4, no. 1, p. 103, Feb. 1968.

Neuman, S. P. and P. A. Witherspoon, "Theory of Flow in a Confined Two Aquifer System," Water Resour. Res., vol. 5, no. 4, pp. 803-816, Aug. 1969a.

Neuman, S. P. and P. A. Witherspoon, "Applicability of Current Theories of Flow in Leaky Aquifers," Water Resour. Res., vol. 5, no. 4, pp. 817-829, Aug. 1969b.

Odeh, A. S., "Unsteady-State Behavior of Naturally Fractured Reservoirs," Soc. Pet. Eng. J., vol. 234, pp. 60-64, AIME, March 1965.

Odeh, A. S., "Steady-State Flow Capacity of Wells With Limited Entry to Flow," Soc. Pet. Eng. J., pp. 43-51, AIME, March 1968.

Odeh, A. S., "Flow Test Analysis for a Well With Radial Discontinuity," J. Pet. Tech., pp. 207-210, Feb. 1969.

Ogbe, D. O. and W. E. Brigham, A Model for Interference Testing With Wellbore Storage and Skin Effects at Both Wells, SPE of AIME, Sept. 16-19, 1984. Presented at the 59th Annual Technical Conference and Exhibition held in Huston, Texas.

Onyekonwu, M. O. and R. N. Horne, "Pressure Response of a Reservoir With Spherically discontinuous Properties," J. Pet. Tech., vol. 35, no. 12, Nov. 1983.

Papadopulos, I. S., "Nonsteady Flow to a Well in an Infinite Anisotropic Aquifer," Proc. Symp. Internat. Assoc. Sci. Hydrology, no. 73, pp. 21-31, Dubrovnik, Yugoslavia, 1965.

Papadopulos, I. S., "Drawdown Distribution around a LargeDiameter Well," Proc. Nat. Symp. on Groundwater Hydrology, San Francisco, Calif., pp. 157-168, 1967.

Papadopulos, I. S. and H. H. Cooper, "Drawdown in a Well of Large Diameter," Water Resour. Res., vol. 3, no. 1, pp. 241-244, 1967.

Papadopulos, S. S., J. D. Bredehoeft, and H. H. Cooper, Jr., On the Analysis of 'Slug Test' Data, 9. No.4, pp. 1087-1089, August 1973.

Raghavan, R. and H. J. Ramey, Jr., "Well-Test Analysis for Vertically Fractured Wells," J. Pet. Tech., pp. 1014-1020, Aug. 1972.

Raghavan, R., H. N. Topaloglu, W. M. Cobb, and H. J. Ramey, Jr., "Well-Test Analysis for Wells Producing From Two Commingled Zones of Unequal Thickness," J. Pet. Tech., Sept. 1974.

Raghavan, R. and K. K. Clark, "Vertical Permeability from Limited Entry Flow Tests in Thick Formations," Soc. Pet. Eng. J., pp. 65-73, Feb. 1975.

Raghavan, R., "Pressure Behavior of Wells Intercepting Fractures," in Proc.. International Well-Testing Symposium, Berkeley, CA, Oct. 19-21, 1977

Raghavan, R., A. Uraiet, and G. W. Thomas, "Vertical Fracture Height: Evvect on Transient Flow Behavior," Society of Petroleum Engineers Journal, pp. 265-277, Society of Petroleum Engineers of AIME, August 1978.

Raghavan, R., R. Prijambodo, A. C. Reynolds, and Well Test Analysis for Wells Producing Layered Reservoirs with Crossflow, Soc. Pet. Eng. J., June 1985.

Ramey, H. J., Jr., "Non-Darcy Flow and Wellbore Storage Effects in Pressure Buildup and Drawdown of Gaswells," J. Pet. Tech., pp. 223-233, Feb., 1965.

Ramey, H. J., Jr., "Approximate Solutions for Unsteady Liquid Flow in Composite Reservoirs," Journal of Canadian Petroleum Technology, pp. 32-37, March 1970.

Ramey, H. J., Jr. and W. M. Cobb, "A General Buildup Theory for a Well in a Closed Drainage Area," J. pet. Tech., pp. 14931505, Dec. 1971. Trans. AIME, 251

Ramey, H. J., Jr. and R. G. Agarwal, "Annulus Unloading Rates as Influenced by Wellbore Storage and Skin effect," Trans., vol. 253, pp. 453-462, A.I.M.E., 1972.

Ramey, H. J., Jr., R. G. Agarwal, and I. Martin, "Analysis of "Slug Test" or DST Flow Period Data," J. Can. Pet. Tech., pp. 37-47, 1975.

Ramey, H. J., Jr., "Interference Analysis for Anisotropic Formations A Case Histoty," J. Pet. Tech., vol. 27, October, 1975.

Ramey, H. J., Jr., "Well-Loss Function and the Skin Effect: A Review," in Recent Trends in Hydrogeology, ed. T. N. Narasimhan, GSA, 1982.

Reynolds, A. C., W. L. Chang, N. Yeh, and R. Raghavan, "Wellbore Pressure Response in Naturally Fractured Reservoirs," Journal of Petroleum Technology, pp. 908-920, Society of Petroleum Engineering, May 1985.

Rodriguez-Nietro, R.Carter, R. D., Unsteady Three-Dimensional Gas Flow in Thick Reservoirs. Paper SPE 4266 was submitted for publication consideration but not preprinted. Available from SPEIME.

Rosato, N. D., C. O. Bennett, and A. C. Reynolds, Jr., "Analysis of Short-Time Buildup Data for Finite Conductivity Fractures," J. Pet. Tech., pp. 2413-2422, Oct. 1982.

Russell, D. G. and M. Prats, "Performance of Layered Reservoirs With Crossflow Single-Compressible-Fluid Case," Soc. Pet. Eng. J., pp. 53-67, March 1962.

Russell, D. G. and N. E. Truitt, "Transient Pressure Behavior in Vertically Fractured Reservoirs," J. Pet. Tech., pp. 11591170, Oct. 1964.

M.Sandal, H., Interference Testing with Wellbore Storage and Skin Effect at the Produced Well., presented at the 1978 SPE Annual and Technical Conference and Exhibition, Houston, Oct. 1-4.

Satman, A., "An Analytical Study of Interference in Composite Reservoirs," Soc. Pet. Eng. J., pp. 281-290, April 1985.

Serra, K. V., A. C. Reynolds, and R. Raghavan, "New Pressure Transient Analysis Methods for Naturally Fractured Reservoirs," J. Pet. Tech., pp. 2271-2283, Dec. 1983.

Shapery, R. A., "Approximate Methods of Transform Inversion for Viscoelastic Stress Analysis," in Proceedings of the Fourth U.S. National Congress of Applied Mechanics, pp. 1075-1085, 1969.

Snow, D. T., A Parallel Plate Model of Fractured Permeable Media, Univ. of California, Berkeley. Ph. D. dissertation

Stehfest, H., Numerical Inversion of Laplace Transforms, Communications of ACM., Vol. 13, 47-49, 1970.

Sternberg, Yaron M., Theory and Application of the Skin Effect Concept to Groundwater Wells, Madras, India, Nov. 26-29, 1973. Presented at International Symposium on Development of Ground Water Resources

Streltsova, T. D., "Unsteady Flow To A Pumped Well In A TwoLayered Water-Bearing Formation," Journal of Hydrology, pp. 245-270, 1977.

Streltsova, T. D., "Well Pressure Behavior of a Naturally Fractured Reservoir," Soc. Pet. Eng. J., pp. 769-780, Oct. 1983.

Streltsova, T. D., "Buildup Analysis for Interference Tests in Stratified Formantions," J. Pet. Tech., pp. 301-310, Feb. 1984.

Streltsova, T. D. and R. M. McKinley, "Effect of Flow Time Duration on Buildup Pattern for Reservoirs With Heterogeneous Properties," Soc. Pet. Eng. J., vol.

24, no. 3, June, 1984.

Tongpenyai, Y. and R. Raghavan, "The Effect of Wellbore Storage and Skin on Interference Test Data," J. Pet. Tech., pp. 151-160, Jan. 1981.

Tsang, Y. W. and P. A. Witherspoon, "Hydromechanical Behavior of a Deformable Rock Fracture Subject to normal Stress," the Journal of Geophysical Research, vol. LBL-12297 Preprint, January 1981.

van Everdingen, A. F., Hurst, W., "The Application of the Laplace Transformation to Flow Problems in Reservers," in Trans., vol. 186, pp. 305-324, AIME, 1949.

van Everdingen, A. F., "The Skin Effect and its Influence on the Productive Capacity of a Well," Trans., vol. 198, pp. 171176, A.I.M.E., 1953.

Walter, G. R., "A Three-Well Technique for Determining Formation Anisotropy at the Waste Isolation Pilot Plant (WIPP) Southeast New Mexico," SAND83-7011, Sandia National Laboratories, Albuquerque, May 1983.

Wang, J. S. Y., T. N. Narasimhan, C. F. Tsang, and P. A. Witherspoon, "Transient Flow in Tight Fractures," in Proceedings, Invitational Well Testing Symposium, Berkeley, Ca., Oct. 19-21, 1977.

Warren, J. F. and P. J. Root, "The Behavior of Naturally Fractured Reservoirs," Soc. Pet. Eng. J., vol. 228, pp. 245-255, AIME, Sept. 1963.

Wattenbarger, R. A. and H. J. Ramey, Jr., "An Investigation of Wellbore Storage and Skin Effect in Unsteady Liquid Flow: I. Analytical Treatment," Soc. Pet. Eng. J., vol. 10, no. 3, p. 279, 1970.

Weeks, E. P., "Aquifer Tests The State of the Art in Hydrology," Proc. International Well-Testing Symposium, Berkeley, California, October 19-21, 1977.

Wijesinghe, A. M. and W. E. Culham, Single-Well Pressure Testing Solutions for Naturally Fractured Reservoirs With Arbitrary Fracture Connectivity, 1984. paper SPE 13055, presented at the 59th Annual Technical Conference and Exhibition held in Huston, Texas, Sept. 16-19

Wilson, C. R. and P. A. Witherspoon, "An Investigation of Laminar Flow in Fractured Rocks," Geotechnical report no. 70-6, University of California, Berkeley, 1970.

Witherspoon, P. A., T. D. Mueller, and R. W. Donovan, Evaluation of Underground Gasstorage Conditions in Aquifers through Investigations of Groundwater Hydrology, Trans., 225, p. 555, AIME, 1962.

Witherspoon, P. A. and S. P. Neuman, Evaluating a Slightly Permeable Caprock in Aquifer Gas Storage, 1. Caprock of Infinite Thickness, Trans., 240, p. 949, AIME, 1967.

Witherspoon, P. A., I. Javandel, S. P. Neuman, and R. A. Freeze, in Interpretation of Aquifer Gas Storage Conditions from Water Pumping Tests, p. 273, American Gas Association, New York, 1967.

Witherspoon, P. A., J. S. Y. Wang, K. Iwai, and J. E. Gale, "Validity of Cubic Law for Fluid Flow in a Deformable Rock Fracture," Water Resour. Res., pp. 1016-1024.

Witherspoon, P. A., N. G. W. Cook, and J. E. Gale, "Geologic Storage of Radioactive Waste Field Studies in Sweden," Science, vol. 211, pp. 894-900, 1981.

Witherspoon, P. A., Y. W. Tsang, J. C. S. Long, and J. Noorishad, "New Approaches to Problems of Fluid Flow in Fractured Rock Masses," LBL-12511, paper presented at the 22nd U. S. Symposium on Rock Mechanics, Massachusetts Institute of Technology, June 29-July 2, 1981.

Witherspoon, P. A., I. Javandel, and L. V. Martin, Hydrology of Brine Disposal in Caprock of Barbers Hill Salt Dome, Chambers County, Texas, 1985. presented at AGU annual meeting at San Francisco, CA

Woods, E. G., "Pulse-Test Response of a Two-Zone Reservoir," Soc. Pet. Eng. J., Sept. 1970.

APPENDIX A

PROOF OF $\lim_{\epsilon \to 0} \int_{D}^{E} = 0$ IN CHAPTER 3.2

We will prove that the integral around the origin tends to zero as the radius of the inner circle ϵ in Figure 3.3 approaches zero.

We have

$$\lim_{\epsilon \to 0} \int_{D}^{E} = \lim_{\epsilon \to 0} \int_{\pi}^{-\pi} p\bar{h}_{D_1} \cdot e^{t_D p} \, dp \tag{A.1}$$

By letting $p = \epsilon e^{i\theta}$, we have $dp = \epsilon \cdot i \cdot e^{i\theta} d\theta$, and

$$\begin{aligned}
\lim_{\epsilon \to 0} \int_{D}^{E} = \lim_{\epsilon \to 0} \int_{\pi}^{-\pi} \alpha_c^{-1/2} \Big\{ & \alpha_c^{1/2} K_1(\epsilon^{1/2} \cdot e^{i\theta/2}) \sinh[\epsilon^{1/2} e^{i\theta/2 - 1/2} \alpha^{1/2} \cdot (1 - r_D)] + \\
& + \beta K_0(\epsilon^{1/2} \cdot e^{i\theta/2}) \cosh[\epsilon^{1/2} e^{i\theta/2} \cdot \alpha^{-1/2} (1 - r_D)] \Big\} \times \\
\times \beta \epsilon^{1/2} e^{i\theta/2} \Big\{ & \alpha_c^{1/2} K_1(\epsilon^{1/2} e^{i\theta/2}) \cosh[\epsilon^{1/2} e^{i\theta/2} \alpha_c^{-1/2} (1 - r_c)] + \\
& + \beta K_0(\epsilon^{1/2} e^{i\theta/2}) \sinh[\epsilon^{1/2} e^{i\theta/2} \cdot \alpha^{-1/2} \cdot (1 - r_c)] \Big\}^{-1} \cdot e^{t_D \cdot \epsilon e^{i\theta}} \cdot \epsilon \cdot i e^{i\theta} d\theta
\end{aligned} \tag{A.2}$$

In Eq. A.2, we may reverse the order of taking the limit and integration. Let us consider the limit of the integrand as $\epsilon \to 0$. Remembering that for a small value of z.

$$K_1(z) \sim \frac{1}{2}$$

$$K_0(z) \sim -\ln \frac{Ez}{z} \quad (lnE = 0.577215665)$$

$$\cosh z \sim 1$$

$$\sinh z \sim z$$

Substituting into the integrand of Eq. A.2 and taking the limit, we have

$$\frac{\alpha_c \{\alpha_c^{1/2}\{\epsilon^{-1/2}\cdot e^{-i\theta/2}\cdot\epsilon^{1/2}\cdot e^{i\theta/2}\alpha^{-1/2}\cdot(1-r_D) - \beta \ln(\frac{E}{2}\cdot\epsilon^{1/2}\cdot e^{i\theta/2})\}\epsilon e^{i(\theta+\frac{\pi}{2})}}{\beta\epsilon^{1/2}\cdot e^{i\theta/2}\{\alpha_c^{1/2}\cdot\epsilon^{-1/2}e^{-i\theta/2}-\beta \ln(\frac{E}{2}\cdot\epsilon^{1/2}\cdot e^{i\theta/2})\cdot\epsilon^{1/2}\cdot e^{i\theta/2}\cdot\alpha^{-1/2}\cdot(1-r_c)\}}$$

$$= \frac{\alpha_c^{1/2}\{1-r_D-\beta(\ln\frac{E}{2} + \frac{i\theta}{2} + \frac{1}{2}\ln\epsilon)\}\epsilon e^{i(\theta+\frac{\pi}{2})}}{\beta\{\alpha_c^{1/2}-\beta\alpha_c^{-1/2}(1-r_c)e^{i\theta}\cdot\epsilon(\ln\frac{E}{2} + \frac{i\theta}{2} + \frac{1}{2}\ln\epsilon)\}}$$

For simplicity, collect and group the constants in a convenient manner. After further simplification

$$\lim_{\epsilon\to 0}\int_D^E = \int_\pi^{-\pi} \lim_{\epsilon\to 0}\left(\frac{e^{i(\theta+2\frac{\pi}{2})}\cdot\epsilon\ln\epsilon}{C_1+C_2e^{i\theta}\cdot\epsilon\ln\epsilon}\right) d\theta$$

Consider $\lim_{\epsilon\to 0}\epsilon\ln\epsilon$. From the L'Hospital's rule,

$$\lim_{\epsilon\to 0}\epsilon\ln\epsilon = \lim_{\epsilon\to 0}\frac{(\ln\epsilon)'}{(\frac{1}{\epsilon})'} = \lim_{\epsilon\to 0}\frac{\frac{1}{\epsilon}}{-\epsilon^{-2}} = \lim_{\epsilon\to 0}(-\epsilon) = 0$$

Therefore,

$$\lim_{\epsilon\to 0}\int_D^E = \int_\pi^{-\pi}\lim_{\epsilon\to 0}\frac{0}{C_1+0}\, d\theta = 0. \tag{A.3}$$

This completes the proof.

APPENDIX B

INVERSION OF $\bar{h}_D$ IN CHAPTER 3.3

The equations to be inverted are:

$$\bar{h}_{D_1} = \frac{\sqrt{\alpha_c}}{r_c\, k_D\, p\, \sqrt{p}} \cdot \frac{1}{\Delta} \times$$
$$\times \left[k_D \cdot K_0(\sqrt{p}) \left\{ I_1(\sqrt{p/\alpha_c}) K_0(\sqrt{p/\alpha_c}\, r_D) + I_0(\sqrt{p/\alpha_c}\, r_D) K_1(\sqrt{p/\alpha_c}) \right\} \right.$$
$$\left. + \sqrt{\alpha_c} K_1(\sqrt{p}) \left\{ I_0(\sqrt{p/\alpha_c}) K_0(\sqrt{p/\alpha_c}\, r_D) - I_0(\sqrt{p/\alpha_c}\, r_D) \cdot K_0(\sqrt{p/\alpha_c}) \right\} \right] \tag{3.3.31a}$$

and

$$\bar{h}_{D_2} = \frac{\alpha_c}{r_c \cdot p^2} \cdot \frac{1}{\Delta} \cdot K_0(\sqrt{p_D}) \ , \tag{3.3.31b}$$

where

$$\Delta = \sqrt{\alpha_c} K_1(\sqrt{p}) \left\{ I_1(\sqrt{p/\alpha_c} \cdot r_c)\, K_0(\sqrt{p/\alpha_c}) + I_0(\sqrt{p/\alpha_c}) K_1(\sqrt{p/\alpha_c} \cdot r_c) \right\}$$
$$+ k_D \cdot K_0(\sqrt{p}) \left\{ I_1(\sqrt{p/\alpha_c}) \cdot K_1(\sqrt{p/\alpha_c}\, r_c) - I_1(\sqrt{p/\alpha_c} \cdot r_c) \cdot K_1(\sqrt{p/\alpha_c}) \right\} \tag{3.3.28}$$

We first look at the inversion of $\bar{h}_{D_1}$. It is more convenient to invert $p\bar{h}_{D_1}$ than to invert $\bar{h}_{D_1}$ directly for the same reason discussed in Chapter 3.2.2.

From the Mellin's inversion theorem we have:

$$L^{-1}\{p\bar{h}_{D_1}\} = \frac{1}{2\pi i}\int_{\gamma-i\infty}^{\gamma+i\infty} p\bar{h}_{D_1} e^{pt_D}\, dp$$

$$= \frac{1}{2\pi i}\int_{\gamma-i\infty}^{\gamma+i\infty} \frac{\sqrt{\alpha_c}}{r_c\, k_D\, p\sqrt{p}} \cdot \frac{dp}{\Delta} \times$$

$$\times \left[k_D \cdot K_0(\sqrt{p}) \left\{ I_1(\sqrt{p/\alpha_c}) K_0(\sqrt{p/\alpha_c}\, r_D) + I_0(\sqrt{p/\alpha_c}\, r_D) K_1(\sqrt{p/\alpha_c}) \right\} \right.$$

$$\left. + \sqrt{\alpha_c} K_1(\sqrt{p}) \left\{ I_0(\sqrt{p/\alpha_c}) K_0(\sqrt{p/\alpha_c}\, r_D) - I_0(\sqrt{p/\alpha_c}\, r_D) \cdot K_0(\sqrt{p/\alpha_c}) \right\} \right] . \tag{B.1}$$

We consider the same contour Γ in Figure 3.2.3 as in Chapter 3.2 because the integrand also has a branch point at $p=0$. Since there are no singularities within Γ, the Cauchy's theorem states:

$$\oint_{\Gamma} = \int_A^B + \int_B^C + \int_C^D + \int_D^E + \int_E^F + \int_F^A = 0 .$$

So that

$$\int_A^B = -\left(\int_B^C + \int_C^D + \int_D^E + \int_E^F + \int_F^A \right) .$$

Therefore,

$$L^{-1}\{p\bar{h}_{D_1}\} = \lim_{\substack{R\to\infty \\ \epsilon\to 0}} \frac{1}{2\pi i}\int_A^B$$

$$= -\frac{1}{2\pi i}\lim_{\substack{R\to\infty\\ \epsilon\to 0}}\left[\int_B^C + \int_C^D + \int_D^E + \int_E^F + \int_F^A\right],$$

where R is the radius of the outer circle and ϵ the radius of the inner. It can be shown that

$$\lim_{R\to\infty}\int_B^C = \lim_{R\to\infty}\int_F^A = 0 .$$

Also, by letting $p = \epsilon e^{i\theta}$ and taking the limit as $\epsilon \to 0$,

$$\lim_{\epsilon\to 0}\int_D^E = 0 .$$

The proof is similar to the one given in Appendix A. Therefore, we only need to evaluate the integral along the negative real axis in both directions.

On CD, let $p = \mu^2 e^{i\pi}$ and recall the following identities:

$$I_0(iz) = J_0(z) \tag{B.2a}$$

$$I_1(iz) = iJ_1(z) \tag{B.2b}$$

$$K_0(iz) = \frac{\pi i}{2}\left\{-J_0(z) + iY_0(z)\right\} \tag{B.2c}$$

$$K_1(iz) = \frac{\pi}{2}\left\{-J_1(z) + iY_1(z)\right\} \tag{B.2d}$$

Also, we have

$$dp = -2\mu\, d\mu \quad , \tag{B.3}$$

so that

$$\frac{1}{2\pi i} \lim_{\substack{\epsilon \to 0 \\ R \to \infty}} \int_c^D e^{t_D p} \cdot p \cdot \bar{h}_{D_1}\, dp = \frac{\sqrt{\alpha_c}}{\pi r_c k_D} \int_0^\infty e^{-t_D \mu^2} \cdot \frac{\Lambda - i\Omega}{\Theta + i\Psi}\, d\mu \quad . \tag{B.4}$$

Similarly, on EF, let $p = \mu^2 e^{-i\pi}$ and using:

$$I_0(-iz) = J_0(z) \quad , \tag{B.5a}$$

$$I_1(-iz) = -iJ_1(z) \quad , \tag{B.5b}$$

$$K_0(-iz) = \frac{\pi i}{2}\left\{ J_0(z) + iY_0(z) \right\} \quad , \tag{B.5c}$$

$$K_1(-iz) = \frac{\pi i}{2}\left\{ J_1(z) + iY_1(z) \right\} \quad , \tag{B.5d}$$

and Equation B.3, we obtain:

$$\frac{1}{2\pi i} \lim_{\substack{\epsilon \to 0 \\ R \to \infty}} \int_E^F e^{t_D p} \cdot p\bar{h}_{D_1}\, dp = \frac{\sqrt{\alpha_c}}{\pi r_c k_D} \int_0^\infty e^{-t_D \mu^2} \cdot \frac{\Lambda + i\Omega}{\Theta - i\Psi}\, d\mu \quad , \tag{B.6}$$

where

$$\Lambda = k_D \cdot C_1 \cdot J_0(\mu) - \sqrt{\alpha_c} \cdot C_2 \cdot J_1(\mu) \tag{B.7a}$$

$$\Omega = k_D \cdot C_1 \cdot Y_0(\mu) - \sqrt{\alpha_c} \cdot C_2 \cdot Y_1(\mu) \tag{B.7b}$$

$$\Theta = k_D \cdot C_4 \cdot Y_0(\mu) + \sqrt{\alpha_c} \cdot C_3 \cdot Y_1(\mu) \tag{B.7c}$$

$$\Psi = k_D \cdot C_4 \cdot J_0(\mu) + \sqrt{\alpha_c} \cdot C_3 \cdot J_1(\mu) \tag{B.7d}$$

and

$$C_1 = J_0(\frac{\mu}{\sqrt{\alpha_c}} r_D) \cdot Y_1(\frac{\mu}{\sqrt{\alpha_c}}) - J_1(\frac{\mu}{\sqrt{\alpha_c}}) \cdot Y_0(\frac{\mu}{\sqrt{\alpha_c}} r_D) \tag{B.8a}$$

$$C_2 = J_0(\frac{\mu}{\sqrt{\alpha_c}} r_D) \cdot Y_0(\frac{\mu}{\sqrt{\alpha_c}}) - J_0(\frac{\mu}{\sqrt{\alpha_c}}) \cdot Y_0(\frac{\mu}{\sqrt{\alpha_c}} r_D) \tag{B.8b}$$

$$C_3 = J_0(\frac{\mu}{\sqrt{\alpha_c}}) \cdot Y_1(\frac{\mu}{\sqrt{\alpha_c}} r_c) - J_1(\frac{\mu}{\sqrt{\alpha_c}} r_c) \cdot Y_0(\frac{\mu}{\sqrt{\alpha_c}}) \tag{B.8c}$$

$$C_4 = J_1(\frac{\mu}{\sqrt{\alpha_c}} r_c) \cdot Y_1(\frac{\mu}{\sqrt{\alpha_c}}) - J_1(\frac{\mu}{\sqrt{\alpha_c}}) \cdot Y_1(\frac{\mu}{\sqrt{\alpha_c}} r_c) \tag{B.8d}$$

Therefore,

$$L^{-1}\{p\bar{h}_{D_1}\} = -\frac{1}{2\pi i} \lim_{\substack{\epsilon \to 0 \\ R \to \infty}} \left(\int_C^D + \int_E^F \right)$$

$$= \frac{2\sqrt{\alpha_c}}{\pi r_c k_d} \int_0^\infty e^{-t_D \mu^2} \frac{\Omega\Psi - \Lambda\Theta}{\Theta^2 + \Psi^2} \, d\mu \ .$$

Further simplifying and using the identity:

$$J_0(z) - Y_1(z) - J_1(z) Y_0(z) = -\frac{2}{\pi z} \ ,$$

we have

$$L^{-1}\{p\bar{h}_{D_1}\} = \frac{4\alpha_c}{\pi^2 r_c} \int_0^\infty \frac{e^{-t_D \mu^2}}{\mu} \frac{C_1 C_3 + C_2 C_4}{\Theta^2 + \Psi^2} \, d\mu$$

Using the convolution theorem, we finally obtain:

$$h_{D_1} = L^{-1}\{\bar{h}_{D_1}\} = \frac{4\alpha_c}{\pi^2 r_c} \int_0^{t_D} \int_0^\infty \frac{e^{-t_D \mu^2}}{\mu} \frac{C_1 C_3 + C_2 C_4}{\Theta^2 + \Psi^2} \, d\mu \, dt_D$$

$$= \frac{4\alpha_c}{\pi^2 r_c} \int_0^\infty \frac{1 - e^{-\mu^2 t_D}}{\mu^3} \cdot \frac{C_1 C_3 + C_2 C_4}{\Theta^2 + \Psi^2} \, d\mu \quad . \tag{B.9a}$$

Similarly, for $\bar{h}_{D_2}$ we obtain:

$$L^{-1}\{\bar{h}_{D_1}\} = \frac{4\alpha_c}{\pi^2 r_c} \int_0^\infty \frac{1 - e^{-\mu^2 t_D}}{\mu^3} \cdot \frac{J_0(\mu r_D)\Theta - Y_0(\mu r_D)\Psi}{\Theta^2 + \Psi^2} \, d\mu \quad . \tag{B.9b}$$

This report was done with support from the Department of Energy. Any conclusions or opinions expressed in this report represent solely those of the author(s) and not necessarily those of The Regents of the University of California, the Lawrence Berkeley Laboratory or the Department of Energy.

Reference to a company or product name does not imply approval or recommendation of the product by the University of California or the U.S. Department of Energy to the exclusion of others that may be suitable.

LAWRENCE BERKELEY LABORATORY
TECHNICAL INFORMATION DEPARTMENT
UNIVERSITY OF CALIFORNIA
BERKELEY, CALIFORNIA 94720